

Magazine of Civil Engineering

113(5), 2022

ISSN
2712-8172



Magazine of Civil Engineering

ISSN 2712-8172

Online peer-reviewed open-access scientific journal in the field of Civil and Construction Engineering

Founder and Publisher: Peter the Great St. Petersburg Polytechnic University

This journal is registered by the Federal Service for Supervision of Communications, Information Technology, and Mass Media (ROSKOMNADZOR) in 2020. Certificate EI No. FS77-77906 issued February 19, 2020.

Periodicity: 8 issues per year

Publication in the journal is open and free for all authors and readers.

Indexing: Scopus, Web of Science (ESCI, RSCI), DOAJ, Compendex, EBSCO, Google Academia, Index Copernicus, ProQuest, Ulrich's Serials Analysis System, CNKI

Corresponding address: 29 Polytechnicheskaya st., Saint Petersburg, 195251, Russia

Chief science editor: associate member of RAS, Sc.D. in Engineering, Vitaly V. Sergeev

Deputy chief science editor:

Sc.D. in Engineering, Galina L. Kozinetc

Executive editor: Ekaterina A. Linnik

Translator, editor: Darya Yu. Alekseeva

DT publishing specialist:

Anastasiya A. Kononova

Contacts:

E-mail: mce@spbstu.ru

Web: <http://www.engstroy.spbstu.ru>

Date of issue: 12.08.2022

© Peter the Great St. Petersburg Polytechnic University. All rights reserved.

© Coverpicture – Ilya Smagin

Editorial board:

T. Awwad, PhD, professor, Damascus University, Syrian Arab Republic

M.I. Balzannikov, D.Sc., professor, Samara State University of Economics, Russia

A.I. Belostotsky, D.Sc., professor, StaDyO Research & Engineering Centre, Russia

A.I. Borovkov, PhD, professor, Peter the Great St. Petersburg Polytechnic University, Russia

A. Borodinecs, Dr.Sc.Ing., professor, Riga Technical University, Latvia

M. Veljkovic, PhD, professor, Delft University of Technology, The Netherlands

R.D. Garg, PhD, professor, Indian Institute of Technology Roorkee (IIT Roorkee), India

M. Garifullin, PhD, postdoctoral researcher, Tampere University, Finland

T. Gries, Dr.-Ing., professor, RWTH Aachen University, Germany

T.A. Datsyuk, D.Sc., professor, Saint-Petersburg State University of Architecture and Civil Engineering, Russia

V.V. Elistratov, D.Sc., professor, Peter the Great St. Petersburg Polytechnic University, Russia

T. Kärki, Dr.-Ing., professor, Lappeenranta University of Technology, Russia

G.L. Kozinetc, D.Sc., professor, Peter the Great St. Petersburg Polytechnic University, Russia

D.V. Kozlov, D.Sc., professor, National Research Moscow State Civil Engineering University, Russia

S.V. Korniyenko, D.Sc., professor, Volgograd State Technical University, Russia

Yu.G. Lazarev, D.Sc., professor, Peter the Great St. Petersburg Polytechnic University, Russia

M.M. Muhammadiev, D.Sc., professor, Tashkent State Technical University, Republic of Uzbekistan

H. Pasternak, Dr.-Ing.habil., professor, Brandenburgische Technische Universität, Germany

F. Rögner, Dr.-Ing., professor, Technology Arts Science TH Köln, Germany

V.V. Sergeev, D.Sc., professor, Peter the Great St. Petersburg Polytechnic University, Russia

T.Z. Sultanov, D.Sc., professor, Tashkent Institute of Irrigation and Agricultural Mechanization Engineers, Republic of Uzbekistan

M.G. Tyagunov, D.Sc., professor, National Research University "Moscow Power Engineering Institute", Russia

M.P. Fedorov, D.Sc., professor, Peter the Great St. Petersburg Polytechnic University, Russia

D. Heck, Dr.-Ing., professor, Graz University of Technology, Austria

A.G. Shashkin, D.Sc., "PI Georekonstruktsiya", LLC, Russia

V.B. Shtilman, D.Sc., JSC "B.E. Vedeneev VNIIG", Russia

Contents

Levchenko, A.V., Polikutin, A.E. Rubber concrete beams under the action of transverse bending	11301
Avsyukevich, D.A., Shishkin, E.V., Litvinova, N.B., Mirgorodskiy, A.N. Thermoeconomic model of a building's thermal protection envelope and heating system	11302
Vatin, N., Korniyenko, S.V. Energy performance of buildings made of textile-reinforced concrete (TRC) sandwich panels	11303
Pikus, G.A., Lebed, A.R., Bondar, A.A. Thermal stresses at the early stage of the hardening of steel-fiber reinforced concrete	11304
Vidyadhara, V., Saurabh, B., Ranganath, R.V. Impact of pond ash as fine aggregate on mechanical and microstructural properties of geopolymer concrete	11305
Larsen, O., Samchenko, S., Naruts, V. Blended binder based on Portland cement and recycled concrete powder	11306
Kotov, P.I., Stanilovskaya, J.V. Long-term strength of frozen saline soils	11307
Arulmoly, B., Konthesingha, K.M.C., Nanayakkara, S.M.A., Premasiri, H.M.R. Metamorphic rocks for manufactured sand and coarse aggregate for concrete and mortar	11308
Lotfi Omran, N., Rajaei, K., Marandi, S.M. Effect of temperature on permanent deformation of polymer-modified asphalt mixture	11309
Ilina, L.V., Kudryakov, A.I., Rakov, M.A. Aerated dry mix concrete for remote northern territories	11310
Mitina, N.A., Revva, I.B., Mitina A. Magnesia cement in the MgO-CO ₂ -H ₂ O system	11311
Kozinetc, G.L., Kozinetc, P.V. The calculation of the dynamic characteristics of the spillway of the dam	11312
Belous, A.N., Kotov, G.A., Belous, O.E., Garanzha, I.M. Calculation of heat resistance of external enclosing structures with heat-conducting inclusions	11313
Klochkov, Yu.V., Nikolaev, A.P., Vakhnina, O.V., Sobolevskaya, T.A., Klochkov, ИМ. Yu. Physically nonlinear shell deformation based on three-dimensional finite elements	11314



Research article

UDC 624:691.34

DOI: 10.34910/MCE.113.1



Rubber concrete beams under the action of transverse bending

A.V. Levchenko , A.E. Polikutin 

Voronezh State Technical University, Voronezh, Russian Federation

✉ Alevchenko@vgasu.vrn.ru

Keywords: concretes, polymers, rubber, strength, reinforced concrete, concrete construction, finite element method, rubcon

Abstract. Bending elements made of rubber polymer concrete (rubcon), which was invented at the Department of Reinforced Concrete and Stone Constructions of the Voronezh Civil Engineering Institute, are a promising direction in the development of the construction industry for industrial buildings due to their high load-bearing capacity combined with universal resistance to aggressive environments. One of the primary building materials today is cement concrete, despite its disadvantages associated with the complexity of the maintenance of reinforced concrete structures in aggressive environments. The previous research on rubcon bending elements of the rectangular cross-section was carried out without implementing numerical studies that consider the nonlinear properties of the materials. Based on the conducted physical experiments, a deformation model of the resistance of the normal cross-sections to the action of transverse bending is developed, which allows estimating the strength of rubcon beams with the greatest deviation of 18%. The accepted prerequisites in the calculation model allow a more correct description of the deformation of polymer concrete in reinforced structures. The proposed analysis method is validated by numerical studies in the ANSYS® software. Due to the obtained excellent convergence with experimental values, physical studies can be replaced by numerical studies.

Funding: The experimental studies have been carried out using the facilities of the Collective Research Center named after Professor Yu.M. Borisov, Voronezh State Technical University, which is partly supported by the Ministry of Science and Education of the Russian Federation, Project No 075-15-2021-662.

Acknowledgments: We would like to express gratitude to professors Potapov and Figovskiy for scientific advice.

Citation: Levchenko, A.V., Polikutin, A.E. Rubber concrete beams under the action of transverse bending. Magazine of Civil Engineering. 2022. 113(5). Article No. 11301. DOI: 10.34910/MCE.113.1

1. Introduction

In this study, we consider bending elements made of rubber polymer concrete (rubcon) invented at the Department of Reinforced Concrete and Stone Constructions of the Voronezh Civil Engineering Institute. The optimal composition of the polymer concrete was obtained by prof. Potapov and Figovskiy [1, 2]. It was somewhat optimized later to obtain the best deformation characteristics [3].

One of the primary building materials today is concrete, despite its disadvantages associated with the complexity of using this material in conditions different from residential and civil housing construction without special protective measures, which can be corrected by polymers introduced directly into the concrete composition. The pioneers in the creation of polymer concrete are Oster-Volkov and Itinsky, who obtained a sample of polymer concrete based on furfural acetone monomer in 1956. Further, in 1961-1962, studies of these polymer concretes were carried out at Voronezh Institute of Civil Engineering, Moscow Institute of Transport Engineers and other organizations, on the basis of which the "Guide for the design

and use of structures made of reinforced polymer concrete in construction" was developed, while abroad recommendations for the design of polymer concrete structures are reflected in ACI 548 documents, including recommendations for the selection of compositions, and also in the work of prof. Figovsky [4]. Authors propose, in addition to the existing methods for calculating polymer concrete structures, to take into account the pre-fracture zone above the crack tip since, as the theory of fracture mechanics shows, at the crack tip, stresses that exceed the limiting ones arise. A similar assumption is put forward for reinforced concrete elements, which is stated in [5], while the additional consideration of the zone of extreme deformation above the crack seems relevant, especially in polymer concrete elements due to the greater ductility compared to traditional cement concrete and higher maximum stresses corresponding to the ultimate tensile strength compared to traditional cement-based concrete.

Polymer materials used as a binder have a rather high cost; therefore, in the manufacture of concretes based on them, it is necessary to strive to reduce the consumption of polymer, obtaining effective materials with filler and aggregate content up to 90–95% of the mass. It is important to note that with such a small consumption of polymer binder (less than 10% of the mass); polymer concretes have high strength characteristics and high chemical resistance. Due to the presence of a large volume of production of synthetic rubbers on the territory of the Russian Federation, their use as a binder in the manufacture of polymer concrete is of practical interest.

The study of the properties of rubber concrete was carried out by the authors of [1, 2, 6], based on which its physical and mechanical parameters and their dependence on variations in compositions were established. A distinctive feature of this material is its high chemical resistance. In the article [7] Borisov obtained and analyzed the coefficients of chemical resistance by for environments that are found in industrial enterprises of various kinds. Chmykhov, in his dissertation work, somewhat expanded the boundaries of this study, thereby proving that rubcon has universal resistance to particularly aggressive media, for example, its chemical resistance coefficient in water is 1. Rubber concrete has high tensile strength, while the modulus of elasticity corresponds to heavy concretes of the class B25-B30, which is an undoubted advantage in comparison with most of the currently known polymer concretes [4], [8]. Which indicates the promising use of rubcon as a material for the manufacture of bending structures. The study of structures made of rubber concrete was carried out by the authors [9–11], including reinforced-rubcon bending T-section elements [11]. Research on reinforced concrete elements with a 5 mm thick rubber concrete coating was carried out by Pinaev in order to provide protection from an aggressive environment [9]. There were also works on the study of a double-layered bending structure with a rubcon in a tensile zone and with ordinary concrete in the compressed zone [10], where it was established that the strength of the "rubcon-concrete" joint is higher than the shear strength of concrete. In the study of rectangular beams [12], it was found that the ultimate strength of inclined sections is achieved when deflections are higher than the maximum permissible, which indicates the expediency of studying the work of normal sections of rubcon beams under load. In view of the presence of fly ash in the rubcon composition, it should be noted that its influence on the strength characteristics and durability was also studied in concretes based on polyester resins [13], as a result of which the effectiveness of its application was proved to reduce the cost of the material. In a separate group of studies, we would like to single out studies of beams made of geopolymer concrete [14]. This type of concrete does not use cement in its composition [15], like most polymer concretes, which is also an advantage because about 7% of the world's greenhouse gases are formed during the production of cement gases [16] and about 1 ton of CO₂ per 1 ton of cement [17]. Among the set of properties of rubcon, it is also worth highlighting high adhesion to materials of various types. Based on research described in the dissertation of Pinaev, it was determined that the adhesion value of the rubcon, for example to a surface made of steel, is 0.8 R_{kt} (almost 9.0 MPa) for comparison adhesion value for the ordinary cement concrete is less than 1.0 MPa. Some properties of the rubcon are given in Table 1.

Table 1. Physical and mechanical properties of rubcon.

Properties	Indicators for rubcon
Compressive strength, MPa	70...80
Tensile strength, MPa	9...11
Elastic modulus, MPa	24000
Poisson's ratio	0.25-0.26
Shrinkage, mm / m	0.0

Numerical modeling in software packages allow to reduce or completely avoid physical experiments on structural and non-structural components. This direction is especially interesting in the study of innovative (non-traditional) materials. To date, many works are devoted to the problems of studying structures in such software systems as Midas®, ANSYS® and others, while the vast majority of works,

including experimental ones, are devoted to structures made of traditional materials, such as steel or cement concrete [18], recently, composite reinforcement and carbon fiber lamellas have been added to this list [19]. As for polymer concretes, the bulk of research is focused on epoxy and polyester polymer concretes [13], [20].

It is important to note that at the moment, the study of rubcon bending elements of the rectangular cross-section was carried out without the implementation of numerical studies that take into account the nonlinear properties of materials [3, 10-12]. Based on experimental studies, it is necessary to develop a deformation model that will allow to evaluate the strength of normal sections of rubcon beams. Implement a finite element model in ANSYS® that takes into account the nonlinear properties of the material, allow to expand the boundaries of the study, change the size and shape of the cross-section, and reduce the number of field experiments conducted. To do this, we need to determine the actual strength characteristics of the reinforcement and polymer concrete used, as well as to assess the adequacy of the finite element model in comparison with the experiments conducted.

2. Methods

2.1. Theoretical studies

The prerequisites for the method for calculating the strength of normal sections of rubcon bending elements, which differ from the traditional method for calculating the strength, are based on the analysis of their stress-strain state, established on the basis of physical experimental studies and the information published in [3], [10], [21].

In view of the greater ductility and higher maximum stresses at the ultimate strength of rubber concrete in comparison with the regular cement concrete, it is proposed to include in the calculation the forces from the resistance of polymer concrete to crack propagation, i.e. taking into account the formation of a zone of plastic deformation above the crack tip.

Thus, the following prerequisites of the method for calculating the strength of normal sections of rubcon bending elements were established:

1. The sections above the crack tip remain plane after deformation and are perpendicular to the curved axis of the beam;
2. The calculation is carried out according to the stage of destruction ;
3. The compressed zone stresses are determined from a multilinear deformation diagram. The compressive stress-strain diagram has a nonlinear outline;
4. The part of the rubcon above the crack resists tensile forces;
5. The stresses in the tensile reinforcement during the destruction of the beam do not exceed the yield strength;
6. Inelastic deformations in the tensile zone of concrete at the crack tip are modeled by the pre-fracture zone, which is considered in the work of Irwin [22]. The pre-fracture zone means an area equal to two radii of plasticity at the crack tip in which the stresses at the crack tip tend to have values higher than the ultimate strength of the material.

The distribution of the calculated internal forces and deformations in the normal section of a bending element made of rubber concrete, taking into account the above prerequisites, is shown in Figure 1.

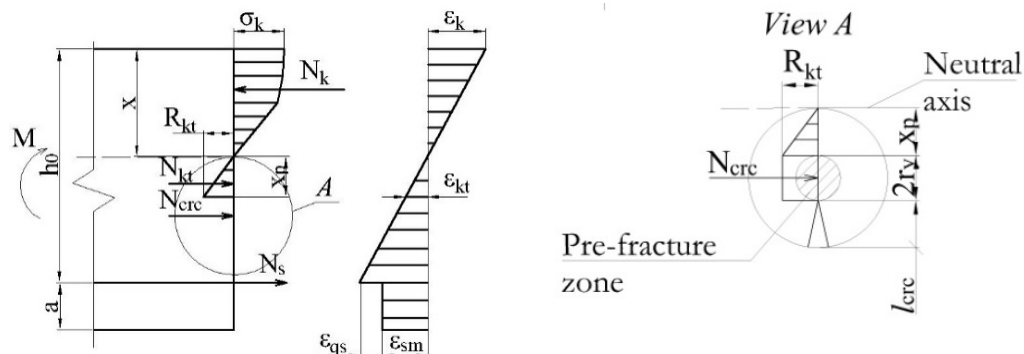


Figure 1. Distribution of calculated internal forces in a normal section.

The force in the reinforcement is determined by the formula:

$$N_s = \sigma_s \cdot A_s, \quad (1)$$

where A_s is rebar area;

σ_s are rebar stresses:

$$\sigma_s = \frac{\varepsilon_k (h_0 - x)}{x} E_s, \quad (2)$$

E_s is elastic modulus.

The force in the rubcon tensile zone is determined by the formula:

$$N_{kt} = \frac{1}{2} R_{kt} \cdot x_p \cdot b, \quad (3)$$

where $x_p = \frac{\varepsilon_{kt}}{\varepsilon_k} x$;

ε_{kt} are tensile rubcon strains;

ε_k are relative compressive rubcon strains;

R_{kt} is tensile strength;

b is section width.

The force in the rubcon compressed zone is determined by the formula:

$$N_k = \omega \cdot \sigma_k \cdot x \cdot b, \quad (4)$$

where ω is the coefficient of completeness of the compressed zone epure, obtained on the basis of the established parameters of the multilinear diagram (Figure 2):

$$\omega = \begin{cases} 0.5 & \varepsilon_k \leq \varepsilon_{k1} \\ 1 - 0.5 \frac{\sigma_{k1} \varepsilon_{k1}}{\sigma_k \varepsilon_k} - \left(\frac{\sigma - \sigma_{k1}}{\sigma} \right) \cdot \left(\frac{\varepsilon_{k1}}{\varepsilon_k} + 0.5 \cdot \left(1 - \frac{\varepsilon_{k1}}{\varepsilon_k} \right) \right) & \varepsilon_{k1} < \varepsilon_k < \varepsilon_{k0} \\ 1 - 0.5 \frac{\sigma_{k1} \varepsilon_{k1}}{\sigma_k \varepsilon_k} - \left(\frac{\sigma - \sigma_{k1}}{\sigma} \right) \cdot \left(\frac{\varepsilon_{k1}}{\varepsilon_k} + 0.5 \cdot \left(\frac{\varepsilon_{k0} - \varepsilon_{k1}}{\varepsilon_k} \right) \right) & \varepsilon_{k0} \leq \varepsilon_k \leq \varepsilon_{k2} \end{cases} \quad (5)$$

σ_k is the maximum compressed zone stress determined from a multilinear diagram, which is obtained from testing of control samples (Figure 2); σ_{k0} , σ_{k1} , σ_{k2} are compressive stresses at various stages of loading and ε_{k0} , ε_{k1} , ε_{k2} are relative compressive strains at different stages of loading.

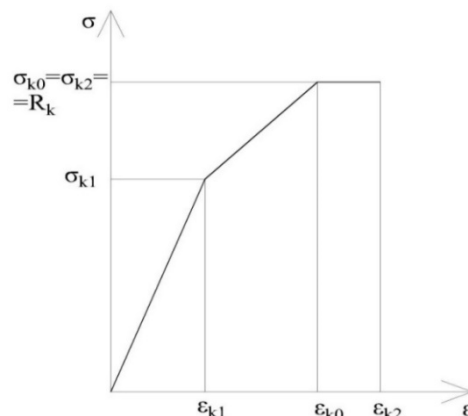


Figure 2. Multilinear stress-strain diagram of rubcon.

Resistance to crack propagation is determined taking into account the J.R. Irwin's correction to the plastic zone above the crack tip [23]:

$$N_{crc} = 2 \cdot r_y \cdot R_{kt} \cdot b, \quad (6)$$

where r_y is the radius of the plastic zone at the crack tip, determined from the solution of the following system of equations:

$$\begin{cases} K_{IC} = k_0 \cdot R_{kt} \cdot \sqrt{r_y} \\ K_{IC} = R_{kt} \cdot \sqrt{\pi l_{crc}} \\ 2r_y = h_0 - x - x_p - l_{crc} \end{cases} \quad (7)$$

K_{IC} is the critical value of the stress intensity factor;

k_0 is empirical coefficient according to [23];

l_{crc} is crack height.

As a result, it was found that the radius of the plastic zone at the crack tip is:

$$r_y = \gamma \cdot h_0 - \gamma \cdot x \left(1 + \frac{\varepsilon_{kt}}{\varepsilon_k}\right), \quad (8)$$

where $\gamma = \left(\frac{\pi}{k_0^2}\right) / \left(\frac{2\pi}{k_0^2} + 1\right)$.

The compressed zone height is determined from the sum of the projections of the internal forces on the longitudinal axis of the element:

$$\omega \cdot \sigma_k \cdot x \cdot b - \frac{1}{2} R_{kt} \cdot \frac{\varepsilon_{kt}}{\varepsilon_k} \cdot x \cdot b - \varepsilon_k \cdot E_s \cdot \frac{(h_0 - x)}{x} \cdot A_s - 2R_{kt} \cdot b \cdot \gamma \cdot h_0 + 2R_{kt} \cdot b \cdot \gamma \cdot \left(1 + \frac{\varepsilon_{kt}}{\varepsilon_k}\right) \cdot x = 0. \quad (9)$$

We transform this equation to find the height of the compressed zone:

$$A \cdot x^2 + B \cdot x - \varepsilon_k \cdot h_0 \cdot E_s \cdot A_s = 0, \quad (10)$$

$$\text{where } A = \omega \cdot \sigma_k \cdot b - \frac{1}{2} R_{kt} \cdot \frac{\varepsilon_{kt}}{\varepsilon_k} \cdot b + 2R_{kt} \cdot b \cdot \gamma \cdot \left(1 + \frac{\varepsilon_{kt}}{\varepsilon_k}\right) = 0, \quad (11)$$

$$B = \varepsilon_k \cdot E_s \cdot A_s - 2R_{kt} \cdot b \cdot \gamma \cdot h_0. \quad (12)$$

The bending moment is determined from the equilibrium of moments of all internal forces relative to the center of gravity of the tensioned rebar:

$$M_u = N_k \cdot (h_0 - y_t) - N_{kt} \cdot \left(h_0 - x - \frac{2}{3} x_p\right) - N_{crc} \cdot (h_0 - x - x_p - r_y), \quad (13)$$

where $y_t = S_{red} / A_{red}$ – the center of gravity of the stress diagram of the compressed zone.

2.2. Experimental studies

To study normal sections of reinforced rubcon beams of rectangular cross-section, experimental specimens with longitudinal bar reinforcement were manufactured and tested for pure bending. Reinforcing bars were grade A500C and B500 per GOST 34028-2016. The percentage of longitudinal reinforcement varied in the range from 0.8% to 6.3%. Beams in the experiment were designed as the beams, which failure starts with the reinforcement reaching its yield stress.

The tests were carried out at the Center for Collective Use (CCU) of the Voronezh State Technical University, Russia. The beams were loaded with two equal concentrated loads applied vertically in thirds of the span. With this type of load application, the value of the bending moment arising in the beam

increases from zero at the support to the maximum value under the point of load application. Between the points of application of the load, the shear force is zero, and the value of the bending moment is constant and equal to the maximum value - the zone of pure bending. The diagram of load application on specimen-beams and their reinforcement are shown in Figure 3. Beam-samples were tested on a laboratory press "INSTRON 600KN" (60 tons). The tests were carried out at a constant speed; the movement of the press traverse was 1 mm/min.

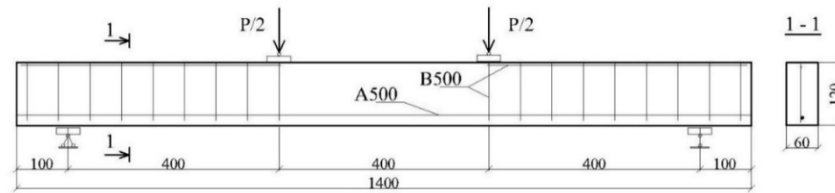


Figure 3. Loading scheme, section and reinforcement of bending elements.

To study the stress-strain state of normal sections, strain gauges were glued along the height of the beam section (Figure 4).

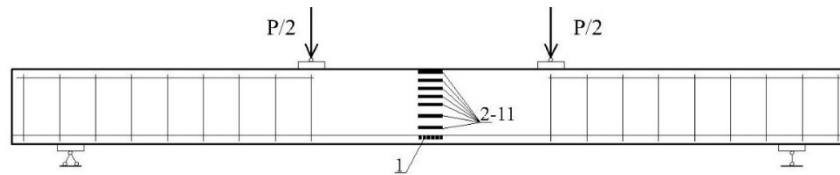


Figure 4. Strain gauges scheme.

Strain gauge № 1 for measuring the deformation of the reinforcing bar, strain gauges №2-11 to measure the strain on the section height. The value of the ultimate load was taken as the maximum value of the press force, indicated by the force sensor, at which the yield strength of the reinforcement is reached. Figure 5 shows a general view of a ready-to-test beam installed to a testing machine.



Figure 5. General view of the beam BRR-2x14 prepared for testing.

With each series of beams, three concrete prism samples and three rebar samples were tested to determine the compressed strength of concrete and rebar mechanical properties. Reinforcing bars were grade A500 per GOST 34028-2016. Based on the test results, the actual strength characteristics of the materials were obtained (Table 2) and used in the calculations. Table 2 also shows the values of the ultimate bending moment and the height of the compressed and tensile zones.

Table 2. Test results.

Beam designation	Reinforcement percentage $\mu, \%$	R_k , MPa	σ_y , MPa	M_u^e , kNm	x^e , mm	x_p^e , mm
BRR - 1x8	0.8	81	565	2.96	32	22
BRR - 1x10	1.25	81	600	4.28	38	18
BRR - 1x12	1.8	80	600	5.80	46	16
BRR - 2x10	2.5	75	600	7.82	44	16
BRR - 2x12	3.6	79	600	10.30	61	15
BRR - 2x14	4.95	79	635	14.00	62	11
BRR - 2x16	6.3	80	550	15.32	60	10

Note: Beam designation BRR-NxM means that rectangular beams are made of rubcon, N – number of reinforcing bars, M – diameter of reinforcing bars. M_u^e is ultimate bending moment according to test results; x^e , x_p^e are height of compressed and tensile zones according to test results.

2.3. The FEM simulations

ANSYS® software package was used for finite element analysis of rubcon beams using nonlinear properties of materials. On the right support of the beam, a roller was set, prohibiting only vertical displacements, but allowing all rotations and horizontal displacements. A pinned support was set on the left side. The length of the support zone was 60 mm, the cantilevers of the beam were 75 mm. Two concentrated forces act on the beam, located similar to the test scheme (Figures 6 and 7).

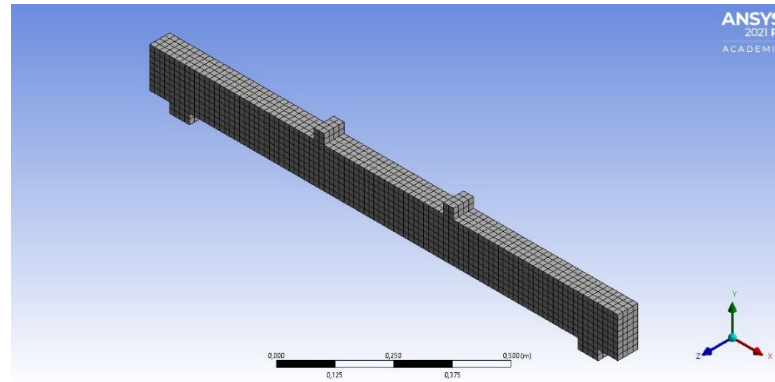


Figure 6. Finite element model of the element under research.

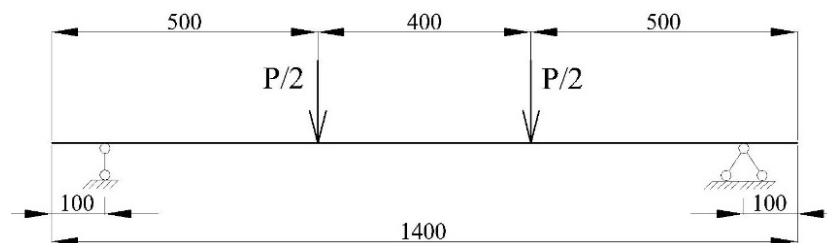


Figure 7. Design scheme of the element under research.

The eight nodal finite element Solid65 was used to model concrete. This element type is capable of simulating plastic deformations, cracking in tension and crushing in compressed. This finite element implements the “Willam-Warnke” concrete deformation model [24]. The model includes the following parameters: the stress-strain relationship for compression, elastic modulus E_k , compressive strength R_k and tensile strength R_{kt} , Poisson's ratio ν , shear transfer coefficient for closed and open cracks β_t and β_c . To model the longitudinal and transverse reinforcement, the finite element Beam 188 was used, which is a linear spatial finite element. The support and load plates have a thickness of 20 mm and are made of steel, the contact zone is rigid. The mesh size of the finite element model was chosen in such a way that the nodes of the rod element modeling the reinforcement bar match with the nodes of the solid elements to ensure a rigid contact between the polymer concrete body and the reinforcement.

To describe the mechanical characteristics of polymer concrete, a multilinear diagram of the relationship between stress and strain is used, which is shown in Figure 2, $\varepsilon_{k1} = 0.2\%$, $\sigma_{k1} = 48.0$ MPa, this point means that the beginning of microcracking occurs, $\varepsilon_{k0} = 0.45\%$, this point means that the beginning of macrocracking occurs, $\varepsilon_{k2} = 0.55\%$, $\sigma_{k0} = \sigma_{k2} = 80.0$ MPa. For the rubcon, the coefficient of transfer of shear forces for closed cracks, β_t , is taken equal to 0.4, for open cracks, β_c , 0.9 in accordance with [25], [26].

For A500 rebar and B500 transverse rebar, bilinear stress-strain diagrams were used. The first parametric point is the elastic limit, the second is the limit of plastic deformation, which was taken as 2.5%.

The mechanical characteristics of the B500 rebars are taken in account with the normative documents (Russian State Standard GOST 34028-2016). The relative longitudinal deformations of the first point are $\varepsilon_{s0} = 0.25\%$. The stress values for the first and second points are taken equal to σ_y , the yield point = 500 MPa. When modeling bars, the relative longitudinal deformations of the second point are $\varepsilon_{s2} = 2.5\%$. The stress-strain relationship are assumed to be identical for tension and compression. The diagrams are taken ignoring hardening beyond the yield point.

3. Results and Discussion

Figure 8 shows the results of vertical displacements of the BRR-2x12 beam under the action of a load, obtained experimentally and according to the results of finite element analysis.

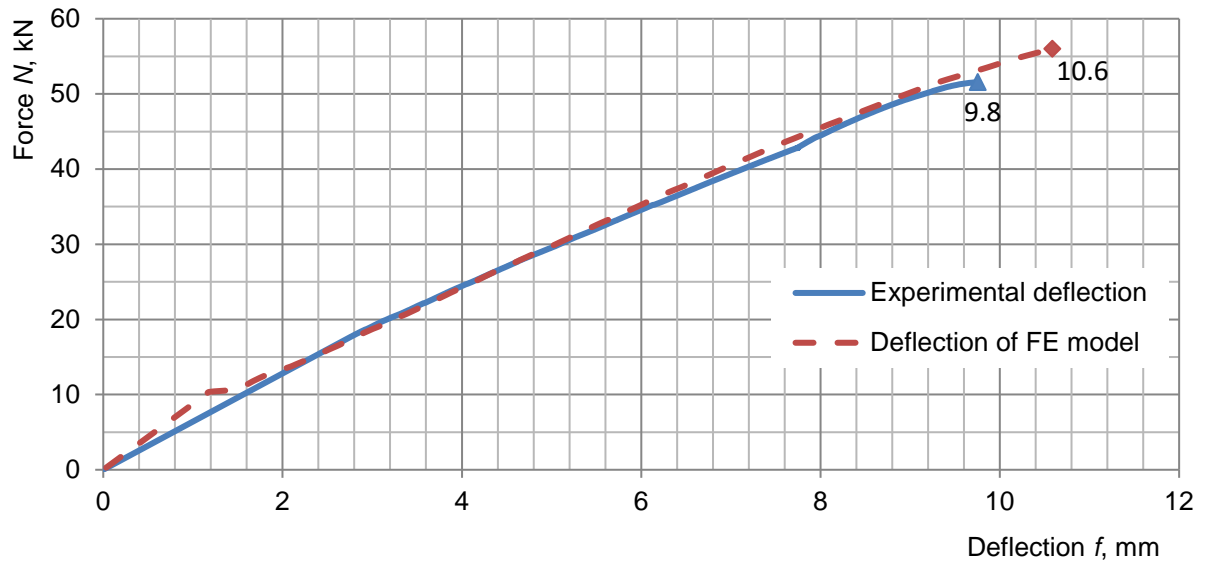


Figure 8. Deflection of a beam with $\mu = 3.6\%$ reinforcement.

This indicates an excellent convergence of the experiment and the FE model, but Figure 9 shows the results of the stress distribution over the height of the section located in the middle of the span. From which it can be seen that the value of the height of the tensile concrete above the crack is lower than in the experimental samples.

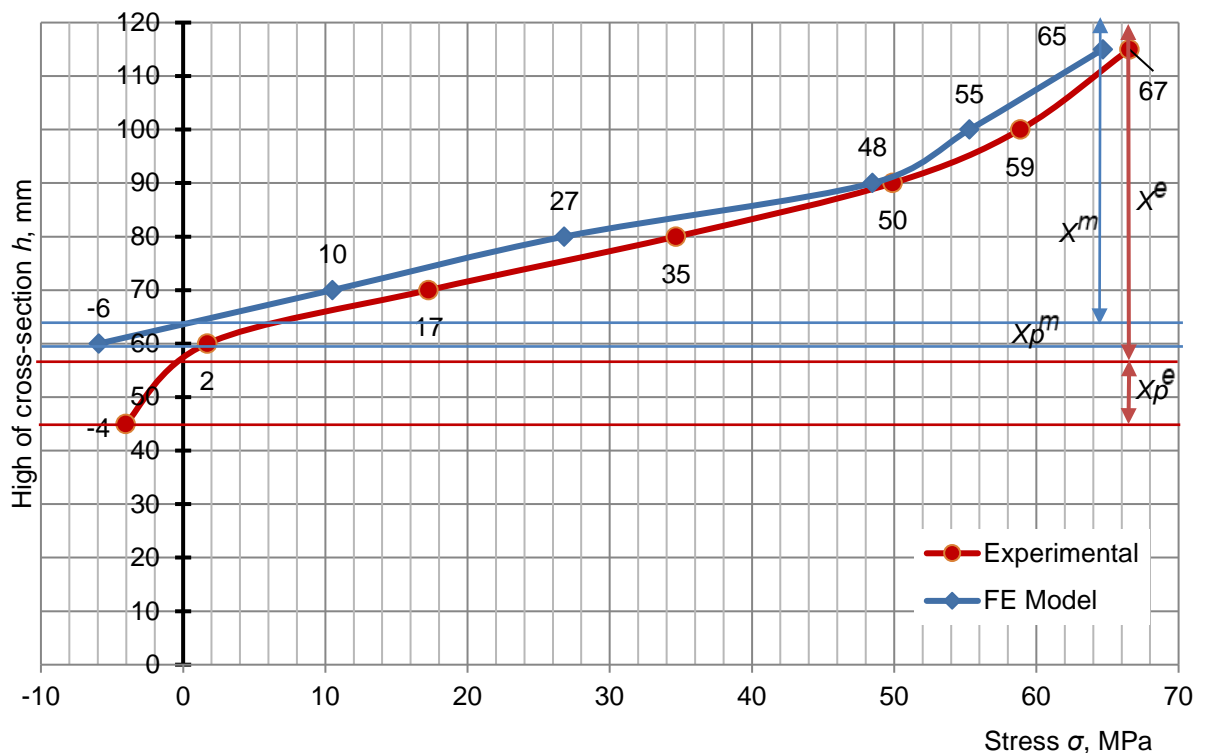


Figure 9. Normal stresses in cross-section of beam with $\mu = 3.6\%$ reinforcement at failure.

Figures 10-15 show a general view of the model of the beam and the reinforcement at failure.

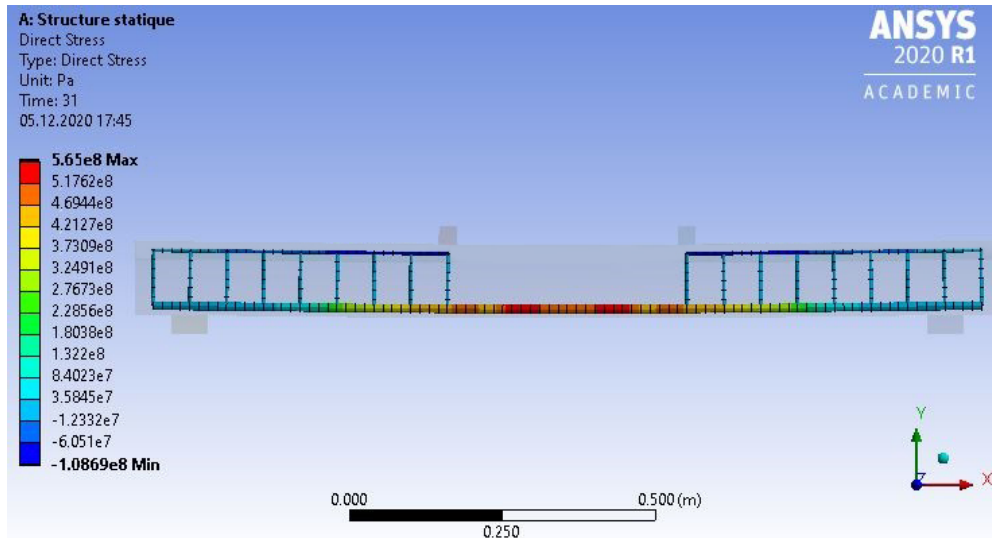


Figure 10. Normal stresses in reinforcement in the FE model of a beam with $\mu = 0.8\%$ reinforcement at failure.

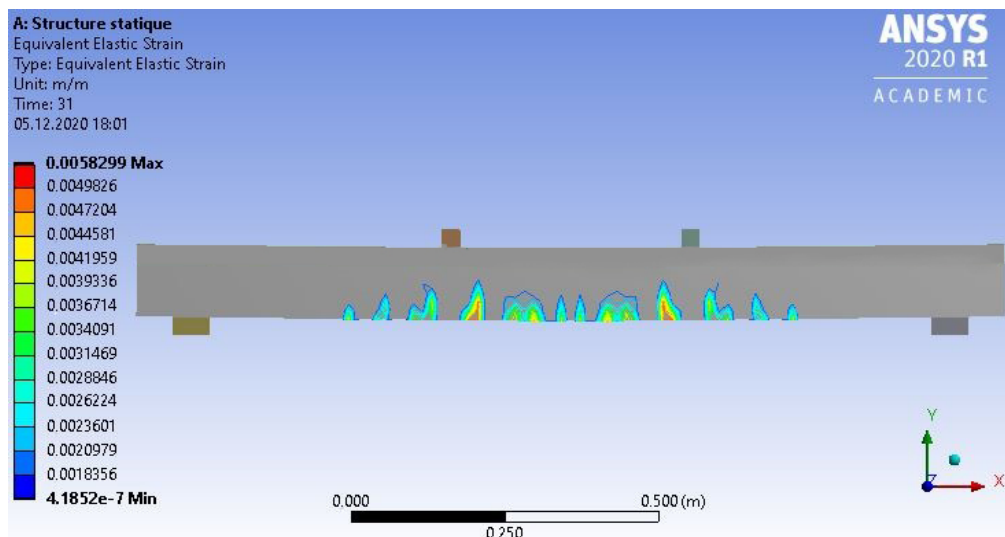


Figure 11. Development of elastic strain (cracks) in the FE model of a beam with $\mu = 0.8\%$ reinforcement at failure.

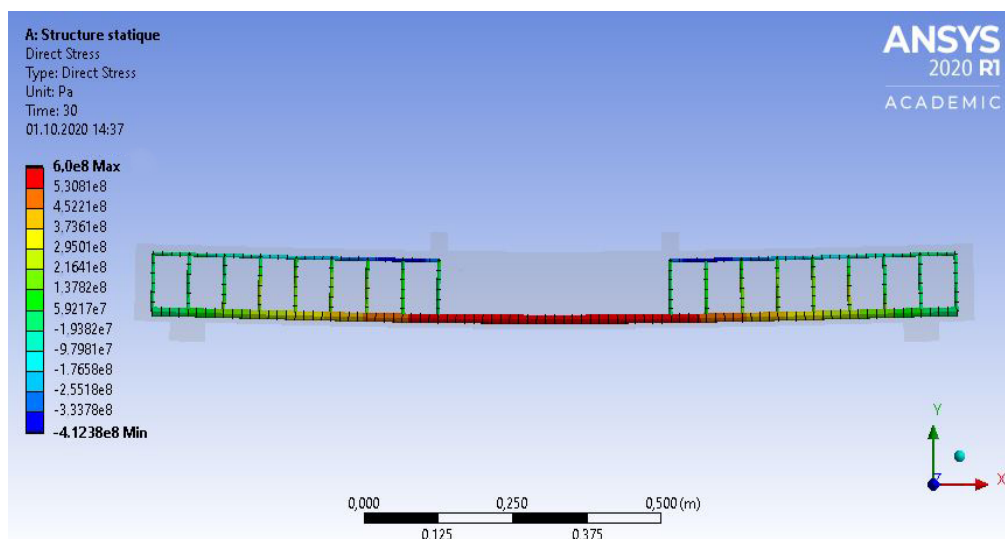


Figure 12. Normal stresses in reinforcement in the FE model of a beam with $\mu = 3.6\%$ reinforcement at failure.

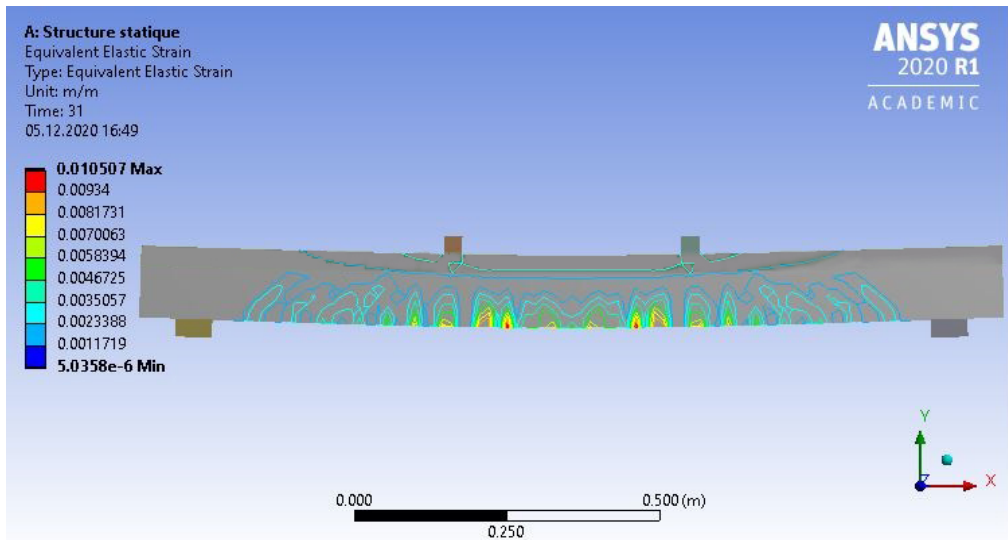


Figure 13. Development of elastic strain (cracks) in the FE model of a beam with $\mu = 3.6\%$ reinforcement at failure.

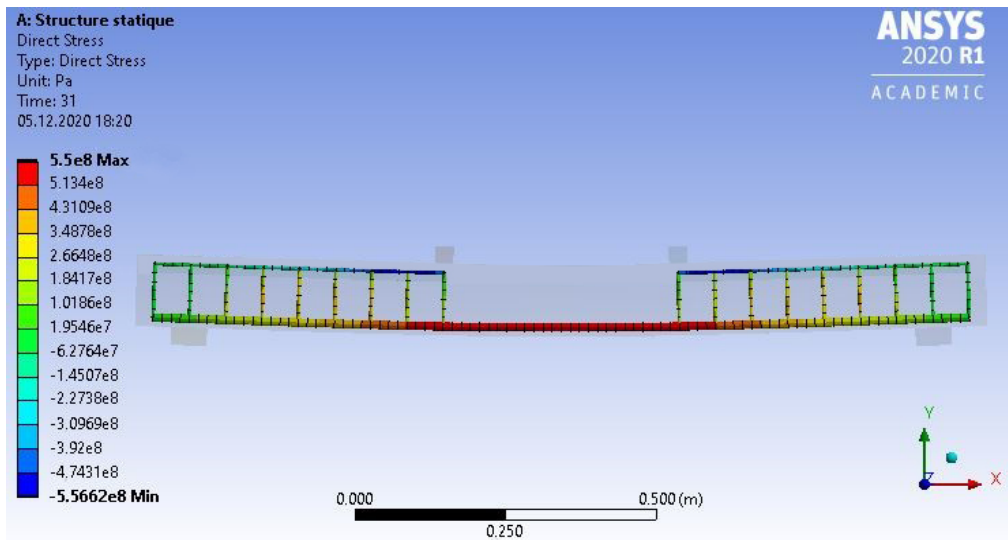


Figure 14. Normal stresses in reinforcement in the FE model of a beam with $\mu = 6.3\%$ reinforcement at failure.

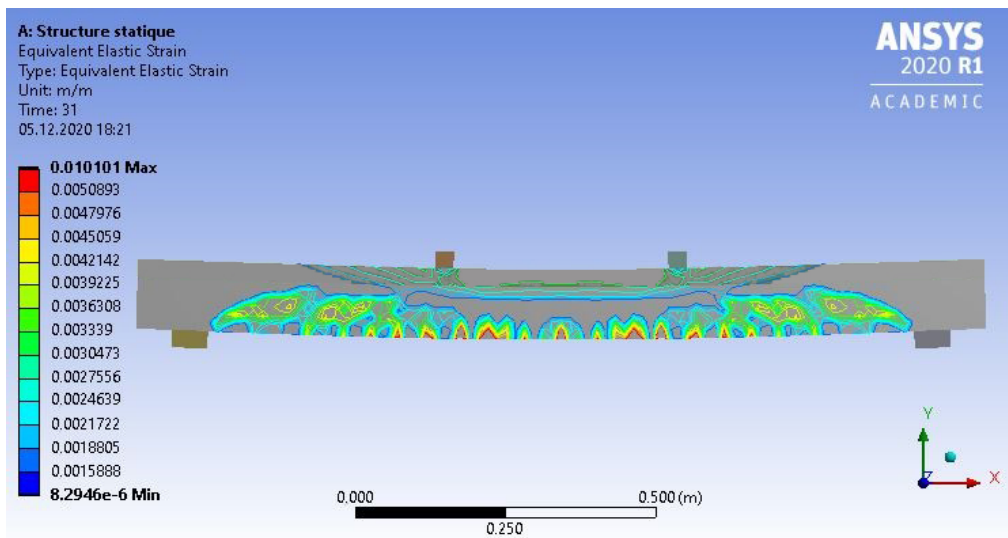


Figure 15. Development of elastic strain (cracks) in the FE model of a beam with $\mu = 6.3\%$ reinforcement at failure.

It is obvious that the general picture of the FE model of the beam before failure with an increase in the percentage of reinforcement corresponds to the logic of failure of bending elements, i.e. the model shows the appearance and development of a larger number of areas of development of elastic strains (cracks). Also, according to Figures 8 and 9, it can be argued about the adequacy and good convergence of the data obtained from the results of finite element analysis.

The results of the carried out theoretical, experimental and numerical studies of rubcon bending elements are summarized in Table 4.

Table 4. Research results.

Beam designation	Reinforcement percentage $\mu, \%$	M_u^t , kNm	M_u^m , kNm	M_u^e , kNm	ΔM_u^t , %	ΔM_u^m , %
BRR - 1x8	0.8	2.51	2.60	2.96	-18.0	-13.8
BRR - 1x10	1.25	4.02	4.20	4.28	-6.6	-1.9
BRR - 1x12	1.8	5.82	6.00	5.80	0.4	3.3
BRR - 2x10	2.5	7.92	8.00	7.82	1.3	2.3
BRR - 2x12	3.6	10.86	11.20	10.30	5.2	8.0
BRR - 2x14	4.95	14.47	15.20	14.00	3.3	7.9
BRR - 2x16	6.3	14.96	16.80	15.32	-2.4	8.8

Note: M_u^t is ultimate bending moment according to the design results according to the proposed method; M_u^m is ultimate bending moment according to the results of design in ANSYS®; ΔM_u^t is deviation of calculation results according to the proposed method from experimental values; ΔM_u^m is deviation of calculation results in ANSYS® from experimental values.

The relationship between the ultimate bending moment and the percentage of longitudinal reinforcement is shown in Figure 16.

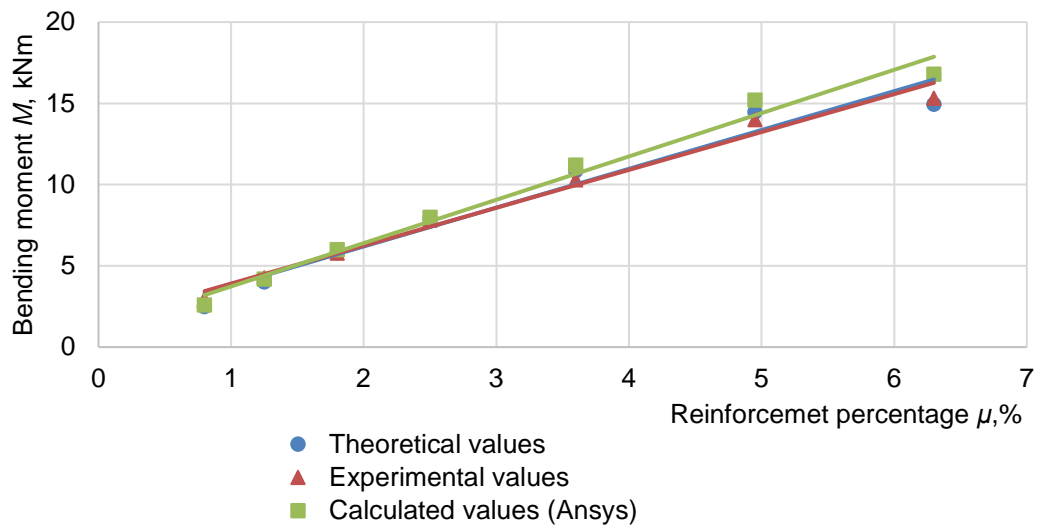


Figure 16. Relationship between the ultimate bending moment and reinforcement percentage.

Table 5 shows the values of the heights of the compressed and tensile zones of concrete above the crack, as well as the values of the height of the tensile zone calculated without taking into account the accepted prerequisite. Table 6 shows the deviations of the values of Table 5 from the experimental.

Table 5. Height of compressed and tensile zones.

Beam designation	x^t , mm	x_p^t , mm	x^e , mm	x_p^e , mm	x^m , mm	x_p^m , mm	x_p , mm
BRR - 1x8	39	22.5	32	22	32.5	17.5	14.2
BRR - 1x10	41	19.2	38	18	40	15	11.9
BRR - 1x12	45	16.6	46	16	42.5	15	10.1
BRR - 2x10	51	14.7	44	16	52.5	10	8.9
BRR - 2x12	57	12.3	61	15	55	7.5	7.4
BRR - 2x14	63	10.2	62	11	6,5	7.5	6.1
BRR - 2x16	67	9.8	60	10	72.5	7.5	6.4

Table 6. Value of deviation from experimental data.

Beam designation	$\Delta x^t, \%$	$\Delta x_p^t, \%$	$\Delta x^m, \%$	$\Delta x_p^m, \%$	$\Delta x_p, \%$
BRR - 1x8	-22.6	-2.1	-1.6	20.5	35,5
BRR - 1x10	-9.0	-6.2	-5.3	16.7	33,9
BRR - 1x12	1.4	-3.4	7.6	6.3	36,9
BRR - 2x10	-15.3	8.7	-19.3	37.5	44,4
BRR - 2x12	6.1	21.8	9.8	50.0	50,7
BRR - 2x14	-2.3	8.0	-4.8	31.8	44,5
BRR - 2x16	-12.0	2.4	-20.8	25.0	36,0

Note: x^t, x_p^t are height of compressed and tensile zones according to the design results according to the proposed method; x^m, x_p^m is height of compressed and tensile zones according the results of design in ANSYS®; $\Delta x^t, \Delta x_p^t$ are deviation of calculation results according to the proposed method from experimental values; $\Delta x^m, \Delta x_p^m$ are deviation of calculation results in ANSYS® from experimental values; Δx_p is deviation of calculation results without taking into account the pre-fracture zone from experimental values.

As can be seen from Table 6, the most correctly values of the height of the tensile concrete zone are determined according to the method developed by the author.

The above assumptions of the calculation are confirmed by the studies in the article [5], which indicate the need to take into account the pre-fracture zone when calculating reinforced concrete elements in the stage of exploitation, as well as studies of the stress-strain state of rubber concrete bending elements of rectangular section [3], and T-section [11]. In order to reduce the cost of manufacturing beams, the authors of [9] propose to use a "cage" made of rubber polymer concrete, however, this method will significantly increase the resistance of the structure to environmental influences and only slightly the bearing capacity and crack resistance. To increase the load-bearing capacity and reduce the cost of rubcon beams, in [10], studies of a two-layer bending element with a rubcon only in the tensile zone were carried out, but now these studies were carried out only in the experimental stage without implementation of software packages.

Approach implemented with FE modeling of rubcon beams, as described above, was tested in [25] for calculating the reinforced concrete elements and the calculating the concrete elements reinforced by CFRP lamellas [26] and showed excellent agreement with experimental data.

From the analysis of Figure 16, it can be said that the proposed method for calculating the strength of normal sections provides excellent convergence with the experimental values (the largest deviation is 18.0% in the series of beams BRR-8). Application of ANSYS® software allows to adequately perform a numerical strength analysis (the largest deviation is 13.8% towards the margin in the series of BRR-8 beams, the smallest deviation is 1.9% in the series of BRR-10 beams). Consequently, the strength calculation method proposed in this work provides sufficient convergence with experimental values and is confirmed by theoretical and numerical studies.

The accepted prerequisites in the calculation model allow to more correctly describe the deformation of polymer concrete in reinforced structures.

4. Conclusion

1. Rubber concrete beams are competitive in the construction industry in terms of their strength characteristics in combination with chemical resistance.
2. The proposed method for calculating the strength of normal sections provides excellent convergence with experimental values.
3. A comparison of the results of theoretical, numerical and experimental studies showed that the "Willam-Warnke" theory for composite materials, implemented in the ANSYS® software with the application of the established characteristics of materials, allows to calculate the strength of rubcon beams.
4. The conducted experimental studies can be replaced by numerical studies.

References

1. Figovsky, O. New polymeric matrix for durable concrete. Proceedings of the International Conference on Cement Combinations for Durable Concrete. 2005. DOI: 10.1680/ccfdc.34013.0029.
2. Figovsky, O., Beilin, D., Blank, N., Potapov, J., Chernyshev, V. Development of polymer concrete with polybutadiene matrix. Cement and Concrete Composites. 1996. 18(6). DOI: 10.1016/S0958-9465(96)00036-4.

3. Polikutin, A., Potapov, Y., Levchenko, A., Perekal'skiy, O. The Stress-Strain State of Normal Sections Rubcon Bending Elements with Mixed Reinforcement. *Advances in Intelligent Systems and Computing*. 2019. 983. DOI: 10.1007/978-3-030-19868-8_56.
4. Figovsky, O., Beilin, D. *Advanced polymer concretes and compounds*. 2013.
5. Iakovenko, I.A., Kolchunov, V.I. The development of fracture mechanics hypotheses applicable to the calculation of reinforced concrete structures for the second group of limit states. *Journal of Applied Engineering Science*. 2017. 15(3). DOI: 10.5937/jaes15-14662.
6. Potapov, Yu.B., Chmykhov, V.A., Borisov, Yu.M. Resistance of a polymer concrete based on polybutadiene binder to organic and inorganic acids. *Scientific Israel - Technological Advantages*. 2013. 15 (4). Pp. 7–10.
7. Potapov, Yu. B., Borisov, Yu. M. Wear-Resistant Coatings On The Basis Of Oligodienes. *Russian Journal Of Building Construction And Architecture*. 2010. No. 1. Pp. 38–44.
8. Bedi, R., Chandra, R., Singh, S.P. Reviewing some properties of polymer concrete. *Indian Concrete Journal*. 2014. 88(8).
9. Potapov, Y.B., Pinaev, S.A., Arakelyan, A.A., Barabash, A.D. Polymer-cement material for corrosion protection of reinforced concrete elements. *Solid State Phenomena*. 2016. 871. DOI:10.4028/www.scientific.net/MSF.871.104.
10. Borisov, Yu. M., Polikutin, A. E., Nguen Phan Duy. The Stress-strain state of normal sections of double-layered, rubcon-concrete bending elements of building structures. *Russian Journal Of Building Construction And Architecture*. 2011. No. 2. Pp. 6–13.
11. Potapov, Y. Polikutin, A. Panfilov, D. Okunev, M. Comparative analysis of strength and crack resistance of normal sections of bent elements of T-sections, made of rubber concrete, caout reinforcement and concrete. *MATEC Web of Conferences*. 2016. No. 73. DOI:10.1051/mateconf/20167304018.
12. Borisov, Y.M., Polikutin, A.E. Strength of inclined sections of bendable reinforcing elements. *Beton i Zhelezobeton*. 2004. (1).
13. Gorninski, J.P., Dal Molin, D.C., Kazmierczak, C.S. Comparative assessment of isophthalic and orthophthalic polyester polymer concrete: Different costs, similar mechanical properties and durability. *Construction and Building Materials*. 2007. 21(3). DOI: 10.1016/j.conbuildmat.2005.09.003.
14. Ahmed, H.Q., Jaf, D.K., Yaseen, S.A. Flexural Capacity and Behaviour of Geopolymer Concrete Beams Reinforced with Glass Fibre-Reinforced Polymer Bars. *International Journal of Concrete Structures and Materials*. 2020. 14(1). DOI: 10.1186/s40069-019-0389-1.
15. Kar, A., Ray, I., Halabe, U.B., Unnikrishnan, A., Dawson-Andoh, B. Characterizations and Quantitative Estimation of Alkali-Activated Binder Paste from Microstructures. *International Journal of Concrete Structures and Materials*. 2014. 8(3). DOI: 10.1007/s40069-014-0069-0.
16. Mehta, K. Reducing the Environmental Impact of Concrete. *Concrete international*. 2001.
17. Radhakrishna, Venu Madhava, T., Manjunath, G.S., Venugopal, K. Phenomenological Model to Re-proportion the Ambient Cured Geopolymer Compressed Blocks. *International Journal of Concrete Structures and Materials*. 2013. 7(3). DOI: 10.1007/s40069-013-0048-x.
18. Najafgholipour, M.A., Arabi, A.R. Finite-Element Study on the Behavior of Exterior Reinforced Concrete Beam-to-Column Connections with Transverse Reinforcement in the Joint Panel. *Practice Periodical on Structural Design and Construction*. 2021. 26(1). DOI: 10.1061/(asce)sc.1943-5576.0000537.
19. Mansour, W. Numerical analysis of the shear behavior of FRP-strengthened continuous RC beams having web openings. *Engineering Structures*. 2021. 227. Pp. 111451. DOI:10.1016/j.engstruct.2020.111451.
20. Lokuge, W., Aravinthan, T. Effect of fly ash on the behaviour of polymer concrete with different types of resin. *Materials and Design*. 2013. 51. DOI: 10.1016/j.matdes.2013.03.078.
21. Zhurtov, A. V., Khezhev, T.A., Mailyan, D.R. Analysis of the Stress-Strain State of Two-Layer Reinforced Cement Structures. *Proceedings of the 2018 International Conference "Quality Management, Transport and Information Security, Information Technologies", IT and QM and IS 2018*. 2018. DOI: 10.1109/ITMQIS.2018.8525119.
22. Irwin, G.R. Plastic zone near a crack and fracture toughness. *7th Sagamore Ardance Materials Research Conference*. 1960.
23. Peresypkin, E.N. Raschyot sterzhnevnyh zhelezobetonnyh elementov [Calculation of reinforced concrete core elements]. 1988. (rus)
24. Willam, K.J., Warnke, E.P. Constitutive Model for the Triaxial Behaviour of Concrete. *IABSE Proceedings, Vol 19*. 1975.
25. Mostofinejad, D., Talaeitaba, S.B. Nonlinear modeling of RC beams subjected to torsion using the smeared crack model. *Procedia Engineering*. 2011. 14. DOI:10.1016/j.proeng.2011.07.182.
26. Hii, A.K.Y., Al-Mahaidi, R. An experimental and numerical investigation on torsional strengthening of solid and box-section RC beams using CFRP laminates. *Composite Structures*. 2006. 75(1–4). DOI:10.1016/j.compstruct.2006.04.050.

Information about authors:

Artem Levchenko

ORCID: <https://orcid.org/0000-0002-6875-754X>

E-mail: Alevchenko@vgasu.vrn.ru

Aleksei Polikutin, PhD in Technical Science

ORCID: <https://orcid.org/0000-0001-7280-5746>

E-mail: a.pl@mail.ru

Received 06.03.2021. Approved after reviewing 19.11.2021. Accepted 24.11.2021.



Research article

UDC 697.133

DOI: 10.34910/MCE.113.2



Thermoeconomic model of a building's thermal protection envelope and heating system

D.A. Avsyukevich  , E.V. Shishkin , N.B. Litvinova , A.N. Mirgorodskiy 

Military Space Academy named after A.F. Mozhaysky, St. Petersburg, Russia

 avsdim@mail.ru

Keywords: buildings, building component, heating system, energy efficiency, cost effectiveness, thermoeconomic model, civil engineering

Abstract. The article is devoted to the determination of the patterns of joint influence exerted by the heating system and heat-protective envelope of a building on its energy consumption, taking into account the composition of the enclosing structures and the peculiarities of the course of thermodynamic processes in the enclosing structures and engineering equipment. The paper presents an overview of the literature on energy saving in the field of construction. It is concluded that it is necessary to form a new approach to optimizing the thermal insulation of buildings based on the method of thermoeconomics, which allows increasing the energy efficiency of buildings. A schematic diagram of the object under study is presented, for which a thermoeconomic model has been developed in the form of several zones connected in series. All cost components affecting the energy efficiency of buildings have been investigated, and the division of costs into energy and non-energy costs is substantiated. Dependences of the reduced costs on the variables to be optimized are given. The dependence of the reduced costs on the cost of the chosen enclosing structures (heat-shielding shell) of the building and engineering equipment is revealed. The analysis of the results obtained is carried out. It is concluded that it is possible to decrease the reduced costs by an average of 20–25 % in comparison with traditional approaches, and the energy consumption of the building by 30–34 %.

Citation: Avsyukevich, D.A., Shishkin, E.V., Litvinova, N.B., Mirgorodskiy, A.N. Thermoeconomic model of a building's thermal protection envelope and heating system. Magazine of Civil Engineering. 2022. 113(5). Article No. 11302. DOI: 10.34910/MCE.113.2

1. Introduction

In recent decades, the issues of energy saving in the field of construction are extremely relevant in all countries. According to various estimates, only in the field of housing and communal services, the potential resources of energy saving are at least 50 %. In the Russian Federation, resolutions of the Government of the Russian Federation have been adopted, which formulate a program for improving energy efficiency in the field of construction. In accordance with this program, the energy consumption of buildings should be systematically reduced. For example, in the period 2016–2020 by 30 %, and after 2021 by 40 %.

The decisive influence on the energy consumption of the building is exerted by the heat-protective envelope of the building, which is a set of enclosing structures that form a closed loop that limits the heated volume of the building.

Therefore, at present, it is necessary to develop existing and find new approaches to optimizing the heat-shielding envelope of buildings in order to increase the energy efficiency of buildings under construction and reconstruction. The relevance of these issues is confirmed by the regular scientific conferences and seminars on this topic.

One of the tasks in this direction is the optimization of interacting and interconnected heat fluxes in a complex architectural-constructive (thermodynamic) system with a variety of its constituent elements of the building envelope (heat shield) and engineering equipment, each of which is an energy carrier and an energy transmitter. A fundamental feature of this system is the fact that a building as a single energy system is not a simple summation of these elements, but a special combination of them, which gives the entire system as a whole new qualities that are absent in each of the elements.

The fundamentals of a systematic approach to a building as a single energy system, the theoretical foundations of the creation of energy efficiency buildings are set forth in the works of Yu.A. Tabunshchikova, for example [1]. The energy saving indicator is understood as a qualitative and / or quantitative characteristic of projected or implemented energy saving measures. Activities in the field of energy conservation of buildings under construction and renovation are characterized by indicators of actual energy savings, reduction of losses of energy resources, including by optimizing the operating parameters of energy consumption, carrying out energy-saving measures that do not require significant investments, etc.

There is a fairly large number of different works, approaches, methods for assessing the energy consumption of buildings, which allow taking into account all the main types of energy costs and their reduction through the use of almost any known energy-saving measures.

It should be noted the importance of having a well-developed regulatory framework in the field of thermal protection of buildings. The issues of regulation of energy efficiency in construction, measures to reduce energy consumption of buildings are considered in the work [2]. The work notes that it is most expedient to increase energy efficiency by combining various design and engineering measures, for example, simultaneously increasing the heat-shielding properties of enclosing structures and using modern engineering energy-saving methods. The development of the regulatory framework in the field of thermal protection of buildings is also influenced by the existing differences in Russian and international standards in determining the calculated values of thermal conductivity of building materials and products. In work [3], it is indicated that the calculated and actual values of the thermal conductivity of building materials used in the construction of external enclosing structures are inconsistent, which leads to an increase in heat loss through them and the loss of thermal energy for heating buildings. The article also notes that a significant revision of the standards on the basis of which building materials are manufactured is required, and their correct representation in the current regulatory documents.

The problem of measuring thermal performance during the acceptance of buildings into operation, as well as when performing work on the energy classification of buildings during operation is solved in work [4]. The authors propose a two-stage procedure for determining the specific consumption of heat energy for heating: The authors propose a two-stage procedure for determining the specific consumption of heat energy for heating:

The effectiveness of LEED certification in terms of reducing the energy consumption of buildings, the feasibility of using available energy performance indicators for buildings certified according to the LEED standard, are discussed in [5]. An archetype-based quantification of uncertainties in the thermal building model (energy consumption model) is carried out in the work [6].

The features of comparing the economic efficiency of various energy saving measures based on a mathematical model for assessing the discounted payback period of investments aimed at reducing the energy resources consumed in the building are considered in the work [7].

In work [8], on the basis of experimental data, two methods of facade insulation are analysed: a ventilated facade system and an external thermal insulation composite system, an assessment of the energy saving potential and the discounted payback period of investments for facade insulation is given.

A dynamic numerical model of thermal protection of enclosing structures based on heat balance equations is proposed by the authors of the article [9]. A simplified dynamic model was developed and implemented in Python 2.7, the authors compared the values of energy demand for heating and air conditioning with advanced software systems: EnergyPlus, BEPS and TRNSYS.

The effect of thermal insulation thickness in building envelope on carbon dioxide emissions is discussed in [10]. The work [11] considers the problem of calculating the optimal thermal protection of buildings using the theory of risk. The function of the density distribution of damage has been determined, which makes it possible to determine the acceptable damage and the corresponding thickness of thermal protection, minimizing the probability of damage release beyond a given level.

The problem of taking into account the influence of heat-conducting inclusions on the reduction of resistance to heat transfer during the thermal modernization of panel buildings is considered in work [12]. The studies took into account such heat-conducting inclusions as the design of panel joints, the slope of the window and the geometry of the outer wall (outer corner). Possible ways to improve the heat-shielding properties of wall panels are considered.

The study of thermal inertia in the heat-protective envelope of buildings was carried out in works [13, 14]. These works indicate that taking into account thermal inertia makes it possible to obtain optimal solutions for the heat-protective envelope of buildings, allowing to reduce the energy consumption of the building.

There is a fairly large number of scientific works in which, in order to increase energy efficiency, the features of the flow of heat and mass transfer processes in the enclosing structures, the features of the functioning of engineering systems are investigated [15–17].

Book [18] describes the optimal design and modernization of energy efficient buildings. The book contains energy statistics, building codes for energy efficiency, and standards from around the world. It also provides an overview of advanced building energy efficiency technologies, including dynamic insulation materials, phase change materials, LED lighting and daylight controls, and more. Applied solutions for energy efficient modernization of buildings with a description of materials, technologies are given in the book [19].

The integration (embedding) of photovoltaic cells into a building envelope, such as a façade or roof, to generate energy from sunlight to reduce the building's energy consumption is presented in the article in [20]. Also, an economic analysis was carried out and the advantages of introducing the proposed system over traditional facades and roofing building materials were shown.

The possibilities of using artificial intelligence in the design of energy efficient buildings, forecasting and minimizing energy consumption, and developing strategies to reduce environmental and climate impacts are discussed in [21]. This article provides an overview of recent AI applications in energy efficient buildings, with a focus on machine learning and large databases. Directions for future research are also indicated. It is emphasized that artificial intelligence can significantly improve the energy efficiency and economic efficiency of buildings that are designed to provide residents with a comfortable living environment.

In most of the above works, an economic calculation of the effectiveness of energy-saving measures is carried out, based on the minimization of the reduced costs for the creation and operation of the building envelope. The main differences in these works are in the methods and formulas for calculating the reduced costs.

Modern research shows that energy systems, which include a complex system consisting of elements of a building's heat-shielding envelope and engineering equipment, should be evaluated using thermodynamic analysis methods. Accordingly, the function of the reduced costs should take into account not only the complex composition of the enclosing structures, but also the peculiarities of the course of thermodynamic processes in the enclosing structures and engineering equipment.

From the methods of thermodynamic analysis, exergy analysis is increasingly used [22, 23]. An increase in the number of studies based on exergy analysis is evidenced by the fact that an International Conference on Exergoeconomics was planned in August 2020 [24]. Thermoeconomics as a mechanism for comparing technical systems is a unique combination of thermodynamic (exergy) and cost analyzes and is capable of providing a designer or operator with a wide range of information on the profitability of a system that cannot be obtained exclusively by traditional methods. So in work [25] a model of a building based on exergy is presented. The authors assess the potential of exergy use in increasing the efficiency of the construction sector. In work [26] it is indicated that the exergy model of the building allows to reduce the energy consumption of the building by 36 %. And in the work [27] examples of the implementation of technology for the construction of buildings with low energy consumption (LowEx) or, in other words, low-energy building systems are presented.

In work [28] the minimization of the total costs for the building and its operation: financial, energy and exergy is carried out, dependences of exergy on the thickness of the walls are obtained.

A thermoeconomic analysis of the energy modernization of buildings using VIP – vacuum insulation panels was performed in the work [29].

In the study [30], an exergoeconomic and ecological-economic analysis of the building heating system was carried out using the SPECO and Lowex methods. The heating system of a building is examined from the heat source (generating component) to the building envelope. This study uses the Lowex approach based on static calculation methods, which may not be very accurate compared to dynamic calculation methods.

There is a large number of works in which exergy, exergoeconomic, thermoeconomic analysis of various equipment and engineering systems is carried out, for example [31–37]. The articles [38, 39] consider the issues of energy saving in central air conditioning systems by optimizing the parameters of their functioning based on the method of thermoeconomics.

The “Average Cost Theory” approach to the analysis of an energy conversion system with gas recovery and intercooling is described in [40].

From the analysis of the above literature, it follows that exergy analysis was practically not used in order to jointly optimize the enclosing structures (heat-shielding shell) of the building and engineering equipment. It should be noted that buildings with a low level of exergy provide significant prospects for the design of buildings with high performance characteristics. Therefore, this article describes a new approach to optimizing the

thermal insulation of buildings based on the method of thermal economics, which improves the energy efficiency of buildings.

The purpose of the research in this article is to develop a thermoeconomic model of the thermal protective shell of buildings together with a heating system, taking into account the composition of the enclosing structures and the peculiarities of the course of thermodynamic processes in the enclosing structures and engineering equipment. To achieve this goal, the article solves a number of particular tasks: determining the main factors affecting the energy efficiency of buildings, formalizing energy consumption processes, analyzing the analytical relationships and results obtained.

2. Methods

When optimizing the thermal insulation of buildings together with the heating system, it is necessary to provide the required exergy of internal air in the premises of the building. The thermoeconomic analysis considers and takes into account the exergy losses that occur during the transmission and transformation of energy in the heat-protective envelope of the building and individual elements of the heating system, as well as the economic costs associated with the creation and operation of the building envelope and individual elements of the heating system.

At the substantive level, the optimization problem solved in this article is formulated as follows: *find the minimum of the reduced costs for the creation and operation of the building envelope together with the heating system while maintaining the required microclimate in the building.*

The object of research is a reconstructed building of a computing center with a total area of 1764 sq. M. and a height of 12 m, the existing enclosing structures – slag concrete panels without thermal insulation. During the research, options for reconstruction using several types of thermal insulation were considered. At the same time, for each type of thermal insulation and heating system equipment, individual service lives declared by manufacturers were considered. Heating system – two-pipe water with artificial circulation of the coolant. The requirements for heat energy for heating needs were taken into account. Modeling was carried out using climate data for the city of Moscow. In the course of modeling, the estimated price of consumed heat energy is 2000 rubles/Gcal, the price of consumed electrical energy is 4 rubles kW*hour.

The schematic diagram of the object under study, for which the thermoeconomic model is being created, is shown in Fig. 1. Fig. 1 indicates the following: zone I is the individual heating point (IHP); zone II is the heating devices in serviced premises; zone III is the building envelope; 11 is the heat exchanger; 12 is the circulation pump IHP; 21 are the heating devices; 31 is the thermal insulation of the building envelope (walls); 32 is the coating insulation; 33 are the windows; T1, T2 are the supply and return pipelines of the coolant.

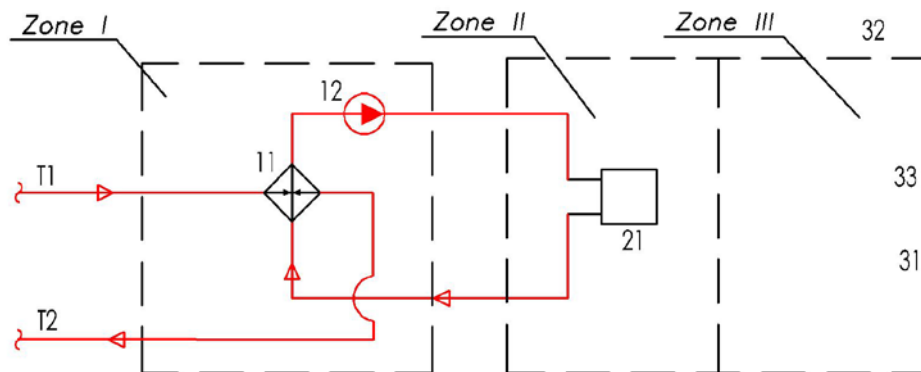


Figure 1. Schematic diagram of the object under consideration.

In the method of thermoeconomics, the main indicator of efficiency that ultimately determines "to be or not to be" of a technical system is the reduced costs Z , referred to a certain period of time [23, 41]:

$$Z = E_{hi} \cdot K_i + \Omega_i, \quad (1)$$

where Z is the annual reduced costs, rubles; E_{hi} is the discount coefficient (coefficient of efficiency of investments in the i^{th} element of the heating system, thermal insulation of enclosing structures, etc.); K_i is the investment in the i^{th} element of the heating system, thermal insulation of enclosing structures, etc., rub.; Ω_i is the operating costs for the i^{th} heating system, thermal insulation of enclosing structures, etc., rub.

The discount factor is calculated depending on the refinancing rate and the time during which it is expected to make a profit:

$$E_{hi} = \frac{1}{(1-r)^{n_i}}, \quad (2)$$

where r is the discount rate (refinancing rate, inflation, expected profitability, etc.); n_i is the estimated period of profit (project implementation period, service life of the i^{th} element, etc.), year.

Operating costs for the i^{th} element are determined by the formula:

$$\Omega_i = b_i K_i + \sum_{i=1}^m S_i^{en} + S_{0i}, \quad (3)$$

where b_i is the coefficient of deductions for depreciation and repair of the i^{th} element; $\sum_{i=1}^m S_i^{en}$ is the total annual energy costs for each i^{th} resource, rubles; S_{0i} is the costs of maintenance and current repair of i^{th} element, salary to personnel, etc., rub.

The decisive advantage of this indicator (reduced costs) is the ability to assess how effective the investment will be in various elements of the heating system and thermal insulation of the building envelope, as well as to assess the amount of subsequent operating costs while maintaining the required microclimate in the building.

In all processes subjected to thermoeconomic analysis, it is advisable to separate energy and non-energy costs, since the former are directly related to the thermodynamic characteristics of both the system as a whole and its zones and sections. Non-energy costs are also associated with thermodynamic parameters, but the nature of these relationships is much more complex; corresponding dependences in analytical or any other form can be obtained for each type of system.

According to [23], the annual reduced costs are determined by summing the product of the annual consumption of each type of resource by the cost of its unit of measurement (energy costs) and the amount of costs attributable to each unit of equipment in operation (its cost, upkeep, maintenance, staff salaries, regulatory deductions and etc.). Is the non-energy costs:

$$Z = \sum_{i=1}^m S_i^{en} + \sum_{i=1}^n S_i^{noten}, \quad (4)$$

where $\sum_{i=1}^m S_i^{en}$ is the total annual energy costs for each i^{th} consumed resource, rubles; $\sum_{i=1}^n S_i^{noten}$ is the total annual non-energy costs for each i^{th} element (equipment) of the optimized system; m is the number of types of resources (energy) used during the operation of the engineering equipment of the building in question; n is the number of units of elements (equipment) of the system under consideration.

The division of costs into energy and non-energy costs is possible by combining equations (1) and (3). Then the total energy costs directly related to the thermodynamic characteristics of the system, including the cost of all energy flows entering the system, will be

$$\sum_{i=1}^m S_i^{en} = \sum_{i=1}^m e_i \cdot c_i \cdot t_{hp}, \quad (5)$$

where e_i is the applied exergy of the i^{th} type, J/s; c_i is the price of exergy of the i^{th} type, rubles/J; t_{hp} is the estimated operating time of the heating system per year (for the heating period), s.

The total non-energy costs take into account capital investments in the creation (modernization) of heating system elements and thermal insulation of enclosing structures, as well as labor costs for operating the system (costs for maintenance, maintenance, disposal, salary for personnel, etc.):

$$\sum_{i=1}^n S_i^{noten} = \sum_{i=1}^n ((E_{hi} + b_i) \cdot K_i + S_{0i}), \quad (6)$$

Expression (6) allows one to obtain particular mathematical models of the formation of non-energy costs for the i^{th} element during the heating period:

$$z_i = \frac{S_i^{noten}}{t_{hp}} = \frac{(E_{hi} + b_i) \cdot K_i + S_{0i}}{t_{hp}}. \quad (7)$$

To solve the optimization problem solved in the article, a thermoeconomic model of the heat-protective shell of a building is developed, which is presented in the form of several separate zones connected in series. Each zone includes either the thermal insulation of the enclosing structures, or a group of heating system elements that have relative independence within the system. Such a linearized representation of the object of research greatly simplifies further calculations by excluding from consideration individual technological connections that do not affect the energy consumption of the object. When constructing a thermoeconomic model of the heat-protective shell of a building envelope, a number of restrictions and assumptions are used. For example, the effect of heat engineering non-uniform sections of enclosing structures (heat-conducting inclusions) on heat losses through the shell of buildings is not taken into account. In the calculations, it is assumed that the enclosing structures are thermally homogeneous. Reducing heat loss by taking into account inhomogeneous sections of enclosing structures is discussed in detail in [42]. The assumption is also used that the thermophysical properties of materials and the thermotechnical characteristics of the enclosing structures remain unchanged over time.

Fig. 2 shows a thermoeconomic model of the research object, which includes a heating system and thermal insulation of enclosing structures. Such a model is applicable for buildings in which there is no central ventilation and air conditioning systems.

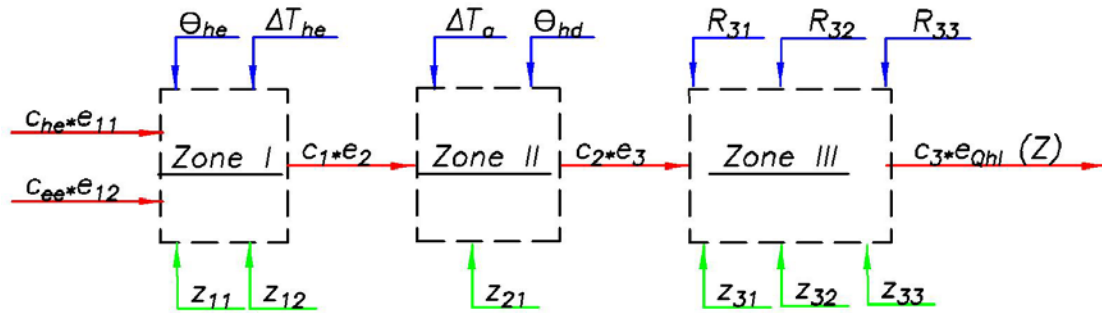


Figure 2. Thermoeconomic model of the heating system and thermal insulation of enclosing structures, presented in the form of the series of connected zones.

Through the control surface of the model from an external source to the first zone, the exergy e_{11} is supplied – the exergy of the coolant coming from the boiler room and e_{12} is the exergy to the drive of the electric motor of the circulation pump. The price of exergy supplied from an external source is known and is equal to: c_{he} is the price of consumed heat energy, c_{ee} is the price of consumed electrical energy. Also, through the control surface of the model, non-energy costs for each i^{th} element (equipment) of the optimized system are brought to different zones: z_{11} is the specific fixed costs for IHP equipment; z_{12} is the unit fixed costs for pumping equipment; z_{21} is the specific fixed costs for heating devices; z_{31} is the specific fixed costs for wall insulation; z_{32} is the specific fixed costs for thermal insulation of the coating; z_{33} is the specific fixed costs for windows. In each zone of the thermoeconomic model, energy dissipation and an increase in equipment costs occur, which leads to an increase in the specific cost of exergy: c_1, c_2, c_3 are the specific cost of exergy after the I, II, and III zones, respectively.

During the operation of the research object, thermal processes are the most important, therefore, variables are used as the optimized variables that allow the development of a thermoeconomic model and it is relatively easy to determine the temperature conditions of the processes in the research object. These variables are as follows: Θ_{he} is the temperature difference in the ITP heat exchanger; ΔT_{he} is the change in the temperature of the circulating heat carrier in the heat exchanger; Θ_{hd} is the temperature head in the heating device; ΔT_a is the change in the temperature of the air heated in the heater; R_{31} is the reduced total thermal resistance of enclosing structures (walls); R_{32} is the reduced total thermal resistance of the coating; R_{33} is the reduced total thermal resistance of the windows.

Taking into account the accepted designations, equation (1) can be represented as:

$$Z = (e_{11} \cdot c_{he} + e_{12} \cdot c_{ee} + z_{11} + z_{12} + z_{21} + z_{31} + z_{32} + z_{33}) \cdot t_{hp}. \quad (8)$$

Moreover, $Z \rightarrow \min$.

The presentation of the thermoeconomic model of the research object in the form of a series of sequentially connected zones allows expressing the exergy and non-energy costs supplied to each of the zones in the form of functional dependences on the exergy flow leaving the considered zone and the optimized variables affecting this zone.

Then the amount of exergy supplied to various elements of the heating system from an external source e_i (Fig. 2), and non-energy costs for elements of the heating system and thermal insulation of the enclosing structures z_j are generally described as follows:

$$\left. \begin{aligned} e_{11} &= E_{11}(e_2, \Delta T_{he}, \Theta_{he}) \\ z_{11} &= Z_{11}(e_2, \Delta T_{he}, \Theta_{he}) \\ e_{12} &= E_{12}(e_2, \Delta T_{he}, \Theta_{he}) \\ z_{12} &= Z_{12}(e_2, \Delta T_{he}, \Theta_{he}) \\ z_{21} &= Z_{21}(e_3, \Delta T_a, \Theta_{hd}) \\ z_{31} &= Z_{31}(e_{Qhl}, R_{31}, R_{32}, R_{33}) \\ z_{32} &= Z_{32}(e_{Qhl}, R_{31}, R_{32}, R_{33}) \\ z_{33} &= Z_{33}(e_{Qhl}, R_{31}, R_{32}, R_{33}) \end{aligned} \right\}, \quad (9)$$

where e_i is the amount of exergy, E_i is a function that describes the change in exergy, z_j is the amount of non-energy costs, Z_j is a function that describes the change in non-energy costs.

Separate zones of the thermoeconomic model are interconnected. This connection can be represented in the form of a functional dependence on the exergy flow leaving the zone and the optimized variables affecting the zone under consideration:

$$e_2 = E_2(e_3, \Delta T_a, \Theta_{hd}); \quad e_3 = E_3(e_{Qhl}, R_{31}, R_{32}, R_{33}). \quad (10)$$

There are connections between the variables being optimized, which requires considering the problem of minimizing the value of reduced costs as a problem of optimizing a function of several variables in the presence of constraints such as equalities (communication equations), i.e. as the problem of finding a conditional extremum. Such problems are successfully solved by one of the methods of conditional optimization, for example, the method of undefined Lagrange multipliers [41].

The minimum of the reduced costs Z of the object under study is determined by the thermodynamic perfection of the processes of heat transfer and energy consumption, which depend on the temperature head Θ and changes in the coolant temperatures ΔT in heat exchangers, thermal resistances of the enclosing structures R , which, in their turn affect the cost of equipment and thermal insulation of enclosing structures. And, the more thermodynamically perfect the system, the higher its cost (Fig. 3).

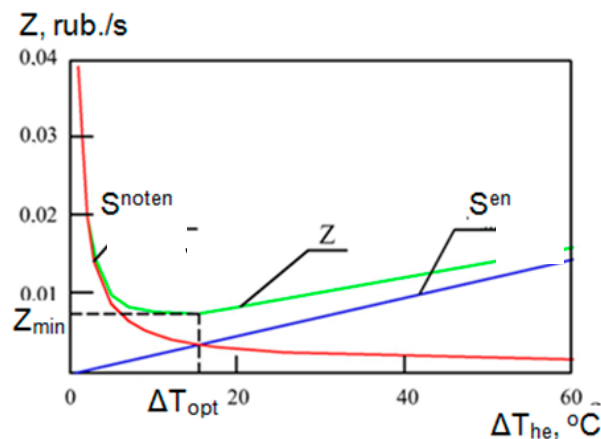


Figure 3. Dependence of reduced costs Z from the change in the temperature of the coolant in the heat exchanger ΔT_{he} .

The selected optimized variables affect the investment in the heating system equipment and the thermal insulation of the enclosing structures, and during subsequent operation, these variables determine the operating modes of the research object, which affect the operating costs. Therefore, in order to find the optimal value of the reduced costs Z , it is necessary to obtain analytical dependences of the cost indicators on the data of the optimized variables. The range of variation of the optimized variables is due to the physics of thermal processes in the corresponding structures and equipment.

The resulting dependences of investments in equipment and materials are presented below.

Investment in heat exchange equipment of the ITP will be:

$$K_{11i} \left(Q_{hl}, \Theta_{he}, k_i^{he} \right) = \frac{N_{11i} + M_{11i} \cdot Q_{hl}}{k_i^{he} \cdot \Theta_{he}}, \quad (11)$$

where K_{11i} is the investment in the i -type heat exchanger, rubles; Q_{hl} is the heat loss of the building through the enclosing structures (heating system performance), J/s; k_i^{he} is the heat transfer coefficient of the i -type heat exchanger, W/m²·K; N_{11i} , M_{11i} is the numerical coefficients determined for heat exchangers of the i th type.

The investment in the circulation pump will be:

$$K_{12i} \left(\Delta T_{he}, Q_{hl} \right) = \frac{N_{12i} + M_{12i} \cdot Q_{hl}}{c_{hc} \cdot \rho_{hc} \cdot \Delta T_{he}}, \quad (12)$$

where K_{12i} is the investment in the circulation pump of the i th type, rubles; ρ_T is the density of the heat carrier kg/m³; c_{hc} is the heat capacity of the coolant, Jm³·K; N_{12i} , M_{12i} is the numerical coefficients determined for circulation pumps of the i th type.

The investment in heating devices will be:

$$K_{21i} \left(Q_r, \Theta_{hd}, k_i^{hd} \right) = \frac{N_{21i} + M_{21i} \cdot Q_{hl}}{k_i^{hd} \cdot \Theta_{hd}}, \quad (13)$$

where K_{21i} is the investment in heating devices of the i th type, rubles; k_i^{hd} is the heat transfer coefficient of the i th type heater, W/m²·K; N_{21i} , M_{21i} is the numerical coefficients determined for type i heaters.

The investment in wall insulation will be:

$$K_{31i} \left(R_{31i} \right) = F_w \cdot \left(N_{31i} + M_{31i} \cdot R_{31i} \right), \quad (14)$$

where K_{31i} is the investment in wall insulation with type i thermal insulation, rubles; R_{31i} is the heat transmission resistance of thermal insulation of the i th type, m²·K/W; F_w is the the area of the enclosing structures (walls) of the building, m²; N_{31i} , M_{31i} is the numerical coefficients determined for type i thermal insulation.

Investment in coatings insulation will be:

$$K_{32i} \left(R_{32i} \right) = F_{cov} \cdot \left(N_{32i} + M_{32i} \cdot R_{32i} \right), \quad (15)$$

where K_{32i} is the investment in the insulation of coatings with thermal insulation of the i th type, rubles; R_{32i} is the heat transmission resistance of thermal insulation of the i th type, m²·K/W; F_{cov} is the area of coverage of the building, m²; N_{32i} , M_{32i} is the numerical coefficients determined for thermal insulation of the i th type.

Investment in insulation (replacement) of windows will be:

$$K_{33i} \left(R_{33i} \right) = F_{ws} \cdot \left(N_{33i} + M_{33i} \cdot R_{33i} \right), \quad (16)$$

where K_{33i} is the investment in insulation (replacement) of windows of the i^{th} type, rubles; R_{33i} is the reduced total thermal resistance of windows of the i^{th} type, $\text{m}^2\cdot\text{K}/\text{W}$, F_{ws} is the area of the building windows, m^2 ; N_{33i} , M_{33i} is the numerical coefficients determined for windows of the i^{th} type.

3. Results and Discussion

The solution of the problem of minimizing the value of the reduced costs, taking into account the obtained dependences of capital investments, as well as analytical expressions describing the processes occurring in individual elements of the heating system, makes it possible to determine the preferred option d_{po} of the enclosing structures (heat-shielding shell) of the building and engineering equipment in order to increase the energy efficiency of buildings under construction and renovation.

In the course of the research, it was revealed that the optimized variables to varying degrees affect the value of the reduced costs (Table 1). The reduced total thermal resistance of enclosing structures (walls, coatings, windows) have the greatest influence on the value of the reduced costs. A change in the temperature of the air heated in heating devices ΔT_a has practically no effect on the value of the reduced costs.

Table 1. Ranking Optimized Variables

Variable	Parameter weight
R_{31}	0.312
R_{32}	0.262
R_{33}	0.206
Θ_{he}	0.102
Θ_{hd}	0.089
ΔT_{he}	0.023
ΔT_a	0.006

Examples of the dependence of the function of reduced costs on R_{32} and Θ_{he} are shown in Fig. 4. Fig. 4 shows that the reduced costs have clearly expressed minima for the corresponding values of the optimized variables. These minima, through the reduced resistances to heat transfer of the enclosing structures, determine the optimal thickness of the additional layer of thermal insulation used in the reconstruction of the building under study, and also determine the optimal temperature head or temperature changes of the coolant during the operation of the heating system.

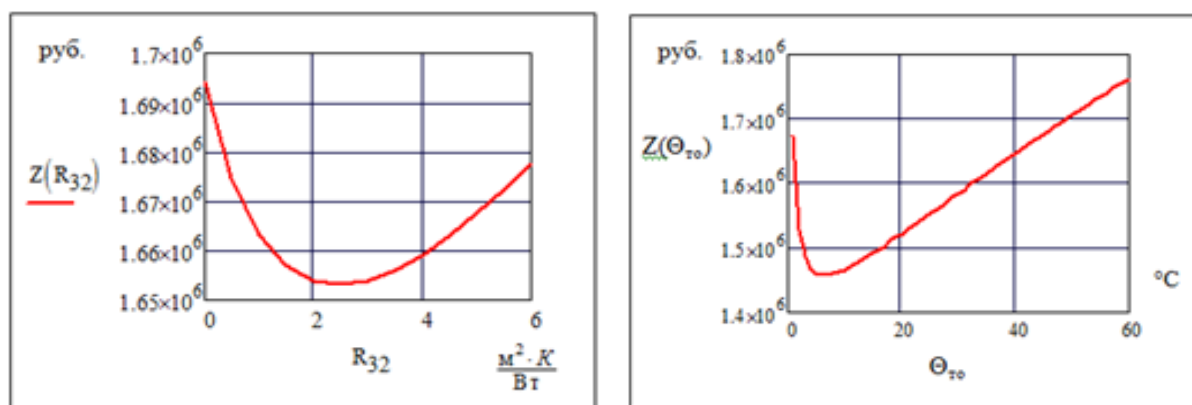


Figure 4. Dependences of the reduced cost function on R_{32} and Θ_{he} .

In the course of the research, possible options for insulating enclosing structures (heat-shielding shell) of the building d_i and the selected engineering equipment for the investigated building were also formed. Each option is a set of measures for the insulation of enclosing structures and the modernization of heating equipment in various combinations (Table 2).

Table 2. Developed options for insulation of enclosing structures and modernization of heating equipment

No	List of options d_i	Option implementation cost, C_i , million rubles	Reduced costs, Z_i , million rubles	Change in reduced costs, ΔZ_i , million rubles	$\Delta Z_i / C_i$
1	Project option	–	2.019	–	
2	Replacement of the pump and heat exchanger IHP	0.283	1.653	0.365	1.292
3	Insulation of the coating	0.365	1.616	0.402	1.102
4	Replacement of windows	0.604	1.605	0.414	0.685
5	Replacement of the pump and heat exchanger IHP + insulation of the coating	0.643	1.677	0.342	0.532
6	Replacement of the pump and heat exchanger IHP + replacement of windows	0.879	1.665	0.354	0.402
7	Insulation of the coating + replacement of windows	0.97	1.596	0.423	0.436
8	Replacement of the pump and heat exchanger IHP + insulation of the coating + replacement of windows	1.239	1.656	0.363	0.189
9	Wall insulation	1.345	1.292	0.727	0.54
10	Replacement of the pump and heat exchanger IHP + wall insulation	1.569	1.345	0.670	0.427
11	Insulation of the coating + wall insulation	1.716	1.277	0.742	0.434
12	Replacement of the pump and heat exchanger IHP + wall insulation + coating insulation	1.93	1.339	0.680	0.352
13	Wall insulation + replacement of windows	1.949	1.255	0.764	0.392
14	Replacement of heating devices	2.047	1.371	0.648	0.316
15	Replacement of the pump and heat exchanger IHP + wall insulation + replacement of windows	2.165	1.327	0.692	0.319
16	Wall insulation + insulation of the coating + window replacement	2.314	1.227	0.792	0.342
17	Replacement of the pump and heat exchanger IHP + replacement of heating devices	2.33	1.432	0.587	0.252
18	Insulation of the coating + replacement of heating devices	2.365	1.365	0.654	0.277
19	Replacement of the pump and heat exchanger IHP + wall insulation + insulation of the coating + replacement of windows	2.525	1.171	0.848	0.336
20	Replacement of windows + replacement of heating devices	2.565	1.356	0.663	0.259
21	Wall insulation + replacement of heating devices	2.805	1.073	0.946	0.337
22	Insulation of the coating + replacement of windows + replacement of heating devices	2.882	1.349	0.669	0.232
23	Insulation of the coating + wall insulation + replacement of heating devices	3.123	1.067	0.952	0.305
24	Thermal insulation of walls + replacement of windows + replacement of heating devices	3.323	1.058	0.961	0.289
25	Wall insulation + insulation of the coating + replacement of windows + replacement of heating devices	3.64	1.052	0.967	0.266
26	Replacement of the pump and heat exchanger IHP + wall insulation + insulation of the coating + replacement of windows + replacement of heating devices	3.851	1.026	0.992	0.258

Each reconstruction option involves investment in its implementation, which in turn determines the reduced costs corresponding to this option. Options in which the cost of implementation increases, but the reduced costs do not decrease, are excluded from further consideration. The remaining options allow you to build a graph of reducing the reduced costs during the operation of the computing center building, depending on the increase in the cost of implementing a particular reconstruction option C_{di} . From the graph, you can determine the most rational reconstruction option, depending on the amount of funds available (Fig. 5).

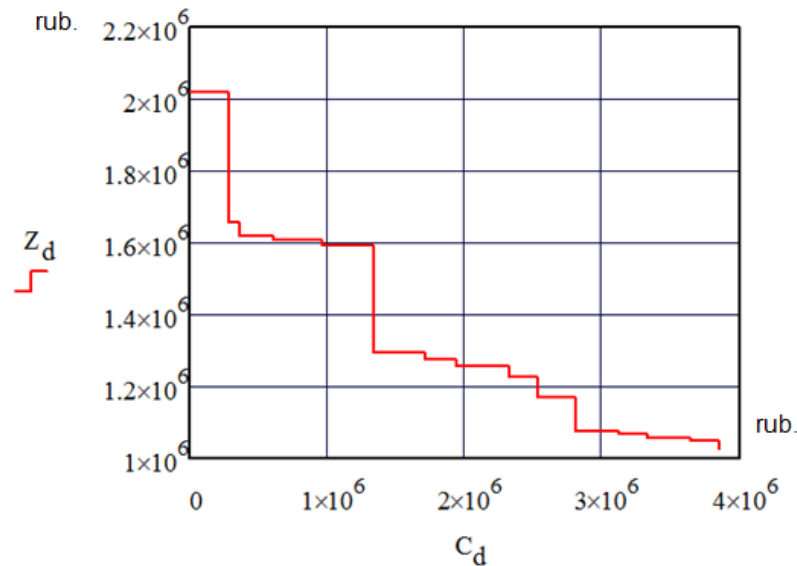


Figure 5. Dependence of the reduced cost function on the cost of the option of insulating enclosing structures (heat-shielding shell) of the building and the selected engineering equipment.

The approach proposed in the article to the thermoeconomic analysis and optimization of the enclosing structures (heat-shielding shell) of a building and engineering equipment (heating system) makes it possible to reduce the reduced costs of their creation and operation by an average of 20–25 % in comparison with traditional approaches, and reduce the energy consumption by 30–34 % (Fig. 6). Fig. 6 shows the dependence of the energy consumption of a building at different ambient temperatures. It can also be seen that the percentage reduction in energy consumption of a building is obviously greater than the possible error arising from the introduction of restrictions and assumptions in the development of a thermoeconomic model.

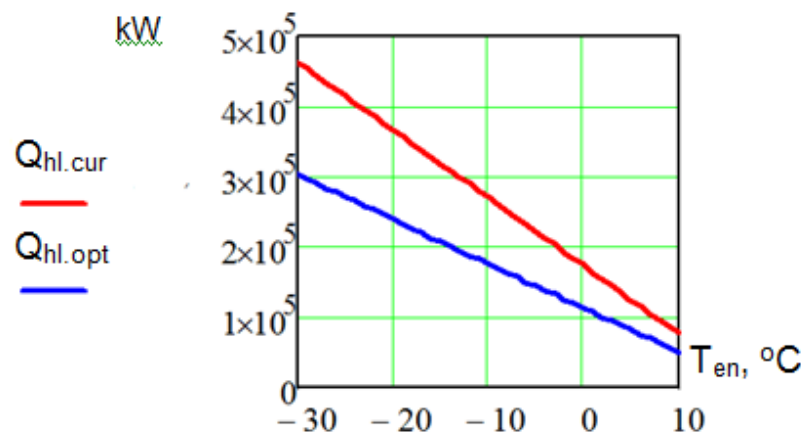


Figure 6. Reducing building energy consumption at different ambient temperatures.

Analysis of the results obtained shows their convergence with the results of similar studies, for example [28], but the results obtained take into account not only the complex composition of the enclosing structures, their cost, but also the peculiarities of the course of thermodynamic processes in the enclosing structures and engineering equipment. Analysis of the results obtained shows their convergence with the results of similar studies, but the results obtained take into account not only the complex composition of the enclosing structures, their cost, but also the peculiarities of the course of thermodynamic processes in the enclosing structures and engineering equipment. For example, in [28], graphs of financial costs for the creation and power supply of a brick building are given, which are similar in terms of the dependences of the reduced cost function in Fig. 4. At the same time, the decrease in financial costs for the creation and power supply of the building with the optimal thickness of thermal protection amounted to an average of 25–28 %, and the reduction in energy consumption for the creation and energy supply of the building was 30–40 %, which is comparable to the results obtained in this article. The new results obtained show the possibility of their application in practice in order to increase the energy efficiency of buildings under construction and reconstructed ones.

Thus, a thermoeconomic model of the heat-protective envelope of the building has been obtained together with the heating system, which allows optimizing the heat-protective envelope of the building in order to increase the energy efficiency of buildings under construction or reconstruction. The resulting model is quite simple and suitable for use not only in engineering practice, but also in the educational process.

4. Conclusions

1. The article reviews the literature on energy conservation, energy efficiency improvement of buildings under construction or reconstruction.
2. Applied exergy analysis to the heat-protective envelope of the building and engineering equipment, considered as a single energy system.
3. A thermoeconomic model of the thermal protective shell of buildings together with a heating system has been developed, taking into account the composition of the enclosing structures and the peculiarities of the course of thermodynamic processes in the enclosing structures and engineering equipment.
4. Expressions are given in general form that allow solving the problem of minimizing the reduced costs for the creation and operation of the enclosing structures (heat-shielding shell) of a building and engineering equipment.
5. Analytical dependences of investments in heating system equipment and thermal insulation of enclosing structures on the optimized variables have been obtained.
6. It was revealed that the reduced total thermal resistance of enclosing structures (walls, coatings, windows) has the greatest influence on the value of the reduced costs.
7. The graphs of the function of reduced costs from the optimized variables R_{32} and Θ_{he} and to are built. It is shown that when using the developed thermoeconomic model, the costs are reduced on average by 20–25 % compared to traditional approaches, and the energy consumption of the building is reduced by 30–34 %.
8. The analysis of the obtained analytical dependencies and results is carried out, their convergence with the results of similar studies is shown.
9. The results of the study can be used by investors, design and operating organizations to assess the energy efficiency of buildings under construction or reconstruction and to select the optimal option for the building envelope (heat shield) and engineering equipment.

References

1. Tabunshchikov, Yu.A., Brodach, M.M., Shilkin, N.V. *Energoeffektivnyye zdaniya* [Energy efficient buildings]. Moscow: AVOK - press, 2003. 198 p. (rus).
2. Gorshkov, A.S. Energoeffektivnost' v stroitel'stve: voprosy normirovaniya i mery po snizheniyu energopotrebleniya zdaniy [Energy efficiency in construction: regulation issues and measures to reduce energy consumption of buildings]. Magazine of Civil Engineering. 2010. No 1(11). Pp. 9-13. DOI: 10.18720/MCE.11.2 (rus)
3. Vatin, N., Korniyenko, S.V., Gorshkov, A.C., Pestryakov, I.I., Olshevskiy, V. Actual thermophysical characteristics of autoclaved aerated concrete. Magazine of Civil Engineering. 2020. No. 96 (4). Rr. 129–137. DOI: 10.18720/MSE.96.11
4. Danilevsky, L.N., Danilevsky, S.L. The algorithm and accuracy of definition of heattechnical indicators of buildings. Magazine of Civil Engineering. 2017. No 5(73). Pp. 49–61. DOI: 10.18720/MCE.73.5
5. Scofield, J.H. Efficacy of LEED-certification in reducing energy consumption and greenhouse gas emission for large New York City office buildings. Energy and Buildings. 2013. Vol. 67. Pp. 517–524. DOI: 10.1016/j.enbuild.2013.08.032
6. Brogger, M., Witthen, K. Quantifying Uncertainties in an Archetype-Based Building Stock Energy Model by Use of Individual Building Models. International Journal of Energy and Environmental Engineering. 2018. Vol. 12. No. 9. Pp. 611–618. DOI: 10.5281/zenodo.1474571
7. Gorshkov, A.S. Vatin, N.I., Rymkevich, P.P., Kydrevich, O.O. Payback period of investments in energy saving. Magazine of Civil Engineering. 2018. No 2(78). Pp. 65–75. doi: 10.18720/MCE.78.5
8. Kostenko, V., Gafiyatullina, N., Zulkarneev, G., Gorshkov, A., Petrichenko, M., Movafagh, S. Solutions to Improve the Thermal Protection of the Administrative Building. MATEC Web of Conferences. 2016. Vol. 73. 02011.. TPACEE-2016. DOI: 10.1051/mateconf/20167302011
9. Perminov, R.E., Alekhin, V.N., Noskov, A.S., Khait, A.V., Popova, M.N., Bianco V. Numerical model of thermal protection of building envelope. Akademicheskii vestnik UralNIIProyekt RAASN. 2016. No. 1(28). Pp. 87–92.
10. Çomaklı, K., Yüksel, B. Environmental impact of thermal insulation thickness in buildings. Applied Thermal Engineering. 2004. 24(5). Pp. 933–940. DOI: 10.1016/j.applthermaleng.2003.10.020
11. Uzdin, A.M., Belash, T.A., Iglina, A.A. Primenenie teorii riska k podboru teplozashchity zdaniy [Application of the theory of risk to the selection of thermal protection of buildings]. Promyshlennoe i grazhdanskoe stroitel'stvo. 2017. No 12. Pp. 97–100. (rus).
12. Filonenko, O., Yurin, O., Kodak, O. Thermal Modernization of the Panel Buildings External Walls. International Journal of Engineering & Technology. 2018. No. 7 (3.2). Pp. 116–122.
13. Gracia, A., Cabeza, L.F. Phase change materials and thermal energy storage for buildings. Energy and Buildings. 2015. Vol. 202. Pp. 414–419. DOI: 10.1016/j.enbuild.2015.06.007
14. Podnebesny, S.V., Bogatikova, N.P., Zaitsev, O.N. Vliyanie na teplovoj rezhim pomeshcheniya inercionnosti ograzhdayushchih konstrukcij i otopitel'nyh priborov [Influence of the inertia of the enclosing structures and heating devices on the thermal regime of the room]. Stroitel'stvo i tekhnogennaya bezopasnost'. 2016. No 3(55). Pp. 87–91. (rus).
15. Petrichenko, M.R., Nemova, D.V., Kotov, E.V., Tarasova, D.S., Sergeev, V.V. Ventilated facade integrated with the HVAC system for cold climate. Magazine of Civil Engineering. 2017. No 1(77). Pp. 47–58. doi: 10.18720/MCE.77.5
16. Bayburin, A.Kh., Rybakov, M.M., Vatin, N.I. Heat loss through the window frames of buildings. Magazine of Civil Engineering. 2019. No 1(85). Pp. 3–14. DOI: 10.18720/MCE.85.1
17. Tarasova, D.S., Petrichenko, M.R. Buildings quasi-stationary thermal behavior. Magazine of Civil Engineering. 2017. No 4(72). Pp. 28–35. doi: 10.18720/MCE.72.4

18. Krarti, M. Optimal Design and Retrofit of Energy Efficient Buildings, Communities, and Urban Centers. Butterworth-Heinemann, 2018. 646 p.
19. Pacheco-Torgal, F., Granqvist, C., Jelle, B., Vanoli, G., Bianco, N., Kurnitski, J. Cost-Effective Energy Efficient Building Retrofitting. 1st Edition. Materials, Technologies, Optimization and Case Studies. Butterworth-Heinemann, 2017. 632 p.
20. Gholami, H., Rostvik, H.N., Müller-Eie, D. Holistic economic analysis of building integrated photovoltaics (BIPV) system: Case studies evaluation. Energy & Buildings. 2019. Vol. 203. DOI: 10.1016/j.enbuild.2019.109461
21. Mehmood, M.U., Chun, D., Zeeshan, Z., Han, H., Jeon, G., Chend, K. A Review of the Applications of Artificial Intelligence and Big Data to Buildings for Energy-Efficiency and a Comfortable Indoor Living Environment. Energy and Buildings. 2019. Vol. 202, 1. DOI: 10.1016/j.enbuild.2019.109383
22. Tsatsaronis, J. Vzaimodejstvie termodinamiki i ekonomiki dlya minimizacii stoimosti energopreobrazuyushchej sistemy [The interaction of thermodynamics and economics to minimize the cost of an energy conversion system]. Odessa: Studio "Negotiant", 2002. 152 p. (rus).
23. Brodjanskij, V.M., Fratsher, V., Mihalek, K. Jeksergeticheskij metod i ego prilozhenija [Exergy method and its application]. Pod. red. V.M.Brodjanskogo. Moscow: Jenergoatomizdat, 1988. 288 p. (rus).
24. Konferentsiya Exergoeconomics, Exergoeconomic i Exergoenvironmental Analysis [Online]. URL: <https://waset.org/exergoeconomics-exergoenvironmental-and-exergoeconomic-analysis-conference-in-august-2020-in-paris> (Da-ta obrashcheniya 10.09.20).
25. Kerdan, I.G., Raslan, R., Ruyssevelt, P., Morillon, D. The role of an exergy-based building stock model for exploration of future decarbonisation scenarios and policy making. Energy and Buildings. 2019. Vol. 202, 1. DOI: 10.1016/j.enbuild.2019.109383
26. Razmara, M., Maasoumy, M., Shahbakhti, M., Robinett, R.D. Exergy-based model predictive control for building HVAC systems. American Control Conference (ACC), 2015. DOI: 10.1109/ACC.2015.7170974
27. Meggers, F., Ritter, V., Goffin, P., Baetschmann, M., Leibundgut, H. Low exergy building systems implementation. Energy. 2012. Vol. 41. Pp. 48–51. DOI: 10.1016/j.energy.2011.07.031
28. Shcheklein, S.E., Shastin, A.G. On the problem of the Thermodynamic optimization of thermal protection of buildings. Alternative Energy and Ecology (ISJAE). 2015. No. 08-09 (172-173). Pp. 63–69. DOI: 10.15518/isjaee.2015.08-09.008
29. Fantucci, S., Garbaccio, S., Lorenzati, A., Perino, M. Thermo-economic analysis of building energy retrofits using VIP – Vacuum Insulation Panels. Energy and Buildings. 2019. Vol. 196. DOI: 10.1016/j.enbuild.2019.05.019
30. Yucera, C.T., Hepbaslib, A. Exergoeconomic and enviroeconomic analyses of a building heating system using SPECO and Lowex methods. Energy and Buildings. 2014. Vol. 73. Pp. 1–6. DOI: 10.1016/J.ENBUILD.2014.01.023
31. Elhaj, M.A., Yassin, J.S. Exergy Analysis of a Solar Humidification-Dehumidification Desalination Unit. International Journal of Mechanical and Mechatronics Engineering. 2013. Vol. 7. No. 8. Pp. 1697–1701. DOI: doi.org/10.5281/zenodo.1335552
32. Sachdeva, G., Bilash, R. Thermodynamic Analysis of a Vapor Absorption System Using Modified Gouy-Stodola Equation. International Journal of Energy and Power Engineering. 2014. Vol. 8. No. 12. Pp. 2229–2234. DOI: 10.5281/zenodo.11-00478
33. Ozdil, N.F.T., Tanteekin, A. Exergoeconomic Analysis of a Fluidized Bed Coal Combustion Steam Power Plant. Thermal Science. 2017. Vol. 21. No. 5. Pp. 1975–1984. DOI: 10.2298/TSCI151210056T
34. Akbari, R., Ehyaei, M.A., Shavvon, R.S. Optimization of Solar Rankine Cycle by Exergy Analysis and Genetic Algorithm. International Journal of Energy and Power Engineering. 2019. Vol. 13. No. 9. Pp. 630–637. DOI: 10.5281/zenodo.3461974
35. Jayasuriya, W.J.A., Athukorala, A.U.C.D., Ragulageethan, S., Perera, A.T.D., Sirimanna, M.P.G. Thermo-economic analysis of a hybrid photovoltaic/thermal (PV/T) system for different configuration settings. CISBAT 2015 – September 9-11, 2015. No. 7. Pp. 687–692. DOI: 10.5075/epfl-cisbat2015-687-692
36. Teodoros, L.C., Andresen, B. Thermoeconomic Optimization of a Combined Heating and Humidification Coil for HVAC Systems. Journal of Non-Equilibrium Thermodynamics. 2016. Vol. 41. No. 3. Pp. 237–247. DOI: 10.1515/jnet-2015-0057
37. Sangi, R., Martin, P.M., Mueller, D. Thermoeconomic analysis of a building heating system. Energy. 2016. Vol. 111. Pp. 351–363. DOI: 10.1016/j.energy.2016.05.112
38. Avsyukevich, D.A. Exergoeconomic model of a central air conditioning system. Magazine of Civil Engineering. 2016. No. 7. Pp. 22–30. DOI: 10.5862/MCE.67.3
39. Zhykharieva, N., Khmelniuk, M. Thermoeconomic Model of Air Conditioning System. Energy Engineering and Control Systems. 2019. Vol. 5. No. 2. Pp. 66–74. DOI: 10.23939/jeecs2019.02.066
40. Sahu, M., Choudhary, T., Sanjay. Thermoeconomic Modelling and Analysis of Energy Conversion System: Intercooled Recuperated Gas Turbine. Proceedings of ICEMIT. 2017. Vol. 1. Pp. 69–88. DOI: 10.1007/978-981-13-2116-0_7
41. Avsyukevich, D.A. Buyakov, S.N., Litvinyuk, A.V., Mirgorodsky, A.N. Optimizaciya parametrov funkcionirovaniya sistemy otopleniya i teplozashchity zdaniy i sooruzhenij na osnove termoekonomicheskogo metoda [Optimization of the functioning parameters of the heating system and thermal protection of buildings and structures on the basis of the thermoeconomic method]. *Trudy Voenno-kosmicheskoy akademii imeni A. F. Mozhajskogo*. Vyp. 651. Saint-Petersburg: Izd-vo VKA imeni A. F. Mozhajskogo, 2016. Pp. 7-13. (rus).
42. Korniyenko, S. Complex analysis of energy efficiency in operated high-rise residential building: Case study. E3S Web of Conferences. 2018. 33, 02005. DOI: 10.1051/e3sconf/20183302005

Information about authors:

Dmitriy Avsyukevich,

Doctor of Technical Science

ORCID: <https://orcid.org/0000-0001-6885-9258>

E-mail: avsdim@mail.ru

Evgeniy Shishkin,

PhD of Technical Science

ORCID: <https://orcid.org/0000-0002-1872-0861>

E-mail: shishkin78@ya.ru

Natalia Litvinova,

Doctor of Education

ORCID: <https://orcid.org/0000-0002-6950-3138>

E-mail: skarlet27@list.ru

Aleksandr Mirgorodskiy,

PhD of Technical Science

ORCID: <https://orcid.org/0000-0001-5647-502X>

E-mail: a89112455906@yandex.ru

Received 28.01.2021. Approved after reviewing 23.11.2021. Accepted 03.12.2021.



Research article

UDC 699.86

DOI: 10.34910/MCE.113.3



Energy performance of buildings made of textile-reinforced concrete (TRC) sandwich panels

N. Vatin ^a , S.V. Korniyenko ^b  

^a Peter the Great St. Petersburg Polytechnic University, St. Petersburg, Russia

^b Volgograd State Technical University, Volgograd, Russia

✉ svkorn2009@yandex.ru

Keywords: building, façade system, sandwich panel, textile-reinforced concrete, building component, thermal conductivity, heat absorption, water vapour permeability, thermal resistance, thermal transmittance, energy saving

Abstract. This research aimed to investigate the energy properties of buildings made of textile-reinforced concrete (TRC) sandwich panels in various humidity-climatic zones. Two configurations of sandwich panel are considered: conventional and advanced. The conventional sandwich panel consists of inner and outer 75 mm thick reinforced concrete layers with separated by a layer of insulation made of extruded 50 mm thick foam polystyrene (XPS) slabs. In the advanced design, due to the use of TRC, the thickness of interior and exterior structural layers is reduced to 40 mm (while maintaining strength), and the thickness of the heat-insulating layer increased to 120 mm. Glass plastic connectors of 10 mm diameter located in nodes of a square grid connect the structural layers. The authors applied an analytical method of research to buildings' energy performance made of TRC sandwich panels based on the investigation of heat and moisture transfer processes in continuous heterogeneous media and analysis of energy indicators of buildings. For the purposes of this research, the element-by-element and complex assessment of building thermal protection was performed. Based on the results of this research, the main thermal advantages of these facade systems are identified. Building component thermal resistance is increased in multiple humidity-climatic zones, providing a high thermal protection level in winter compared to conventional facade systems. Building component heat absorption is increased by 34.4% (compared to conventional facade systems), excluding the risk of overheating of premises in summer. The risks of moisture condensation and deterioration of hydrothermal-protective properties of building components are minimized. The use of TRC sandwich panels allows reducing total heat loss through the building envelope by 26.5%. Simultaneously, the building's specific thermal characteristic is decreased by 16.7%, and the energy-saving class increases to high levels. Construction with advanced facade systems, when the precast sandwich panels with structural layers from textile-reinforced concrete are used, extends the creative boundaries of architecture and allows you to solve the current problem of improving the architectural environment's quality and conserve energy for future generations.

Citation: Vatin, N., Korniyenko, S.V. Energy performance of buildings made of textile-reinforced concrete (TRC) sandwich panels. Magazine of Civil Engineering. 2022. 113(5). Article No. 11303. DOI: 10.34910/MCE.113.3

1. Introduction

Nowadays, there is escalating concern on the sustainable building development around the world [1–3]. One of the major aspects is energy saving in buildings [4]. A significant portion of the energy is consumed by today's buildings in developed and developing countries. For example, about 40% of the total primary energy in Europe is consumed by buildings today, and more than 50% of that energy going toward

heating in winter and cooling in summer of the indoor environment [5]. This fact emphasizes on the imperative need for energy conservation in buildings [6, 7].

Building energy efficiency can be improved by implementing either active or passive energy efficient strategies [8]. Improvements to heating, ventilation and air conditioning (HVAC) systems, electrical lighting, etc. can be categorized as active strategies, whereas, improvements to building envelope elements can be classified under passive strategies. Recent years have seen a renewed interest in environmental-friendly passive building energy efficiency strategies. This idea of sustainable buildings encompasses various issues regarding energy, water, land and material conservation, together with environmental pollution and the quality of indoor and outdoor environments [9].

A building envelope is contour that separated the indoor and outdoor environments of a building. It is the key factor that determines the quality and controls the indoor conditions irrespective of transient outdoor conditions [10]. Building experts desire to create a durable and esthetic building envelope, adapted to environmental changes with all its potentials [11–13]. Research for new building materials, technological advancement, and structural development are the key targets for achieving this goal. There is a growing trend to use biofibers as fillers and reinforces in composites [14, 15]. Technological advancements in the production of building, structural, and infrastructural components, suggests advanced manufacturing techniques will allow these components to address issues including construction speed, structural performance, combinatorial material efficiencies, and economics of production [16]. A major building element able to benefit from these technological advancements and meet the demands of current urban growth is the development of a more intelligent and responsible building envelope [17–19].

The performance criteria of an effective building envelope is to be the protective layer around a building possessing the qualities of a thermal and moisture break, structural stability, wind and impact resistance, locally acclimated to environmental conditions, and provide the aesthetic expression of the building [21–23]. It is one of the most direct methods to develop a more efficient, sustainable, and economically feasible means to address the pressing needs of rapid urbanization and the performance criteria associated with more intelligent and responsible design. A key component toward developing a more advanced building envelope is the utilization of a precast concrete cladding system, particularly the further advancement of precast concrete sandwich panels. The development of Ultra-High-Performance Fiber-Reinforced-Concrete (UHP-FRC) has made it possible to investigate the extent of a stronger, lighter, and more durable precast concrete sandwich panel [24–26].

Textile-Reinforced Concrete (TRC) is a new composite material made of fine-grained concrete and textile reinforcements with high load-bearing capacities [27]. Due to its material properties, textile reinforced concrete offers a considerable application potential for thin-walled and lightweight facade constructions [20]. For example, sandwich panels, made of two thin TRC facings and a core of polymeric rigid foam present an attractive choice for modern building envelopes. These combine low weight with a high structural capacity, while simultaneously fulfilling structural and physical demands. However, the applicable slenderness is limited because of demands on the load-bearing capacity, deformation, and safety against cracking. Thus, monolithic or metallic bracings are required for large curtain panels. The use of 3D additive technologies is a perspective trend of TRC utilization in modern design [28]. The development of sandwich panels made of TRC has been the subject of several research projects at the Institute for Structural Concrete of RWTH Aachen University in Germany.

It is well known that sandwich panels with facings made of thin metal sheets (less than 1 mm) or reinforced concrete wythes (70–140 mm) have been successfully used in industrial and multistory buildings for decades [29, 30]. Their design principles and structural models are significantly different from each other. Sandwich panels made of TRC with facing thicknesses of 30–70 mm combine the advantages of the aforementioned constructions in terms of weight reduction, great potential for reduction of carbon footprint, and safety against corrosion [20].

Replacing traditional reinforced concrete layers in sandwich panels with thinner TRC structural layers makes it possible to increase the heat insulation layer's thickness at the same thickness of the structure and, therefore, increase the thermal performance of exterior walls. However, the thermal characteristics of TRC type façade are not well researched. There is no data on thermal performance under various humidity-climatic impacts. TRC sandwich sections' thermal stability is practically not studied, which makes it difficult to heat estimate structures in summer, with intense exposure to solar radiation. The processes of heat and moisture transfer in such structures and the influence of these processes on building components' moisture-protective properties are not fully studied. The absence of TRC sandwich panels' thermal characteristics makes it difficult to assess the buildings thermal performance and slows down the implementation of TRC in energy-saving construction. Therefore, it required comprehensive research of the energy performance of buildings made of TRC sandwich panels.

This research aimed to investigate the energy performance of buildings made of TRC sandwich panels in various humidity-climatic zones.

2. Materials and Methods

2.1. Building energy performance calculation concept

The authors applied an analytical method of research on buildings' energy performance made of TRC sandwich panels based on the investigation of heat and moisture transfer processes in continuous heterogeneous media and analysis of energy indicators of buildings.

For this research, the element-by-element and complex assessment of building thermal protection was performed (Fig. 1).

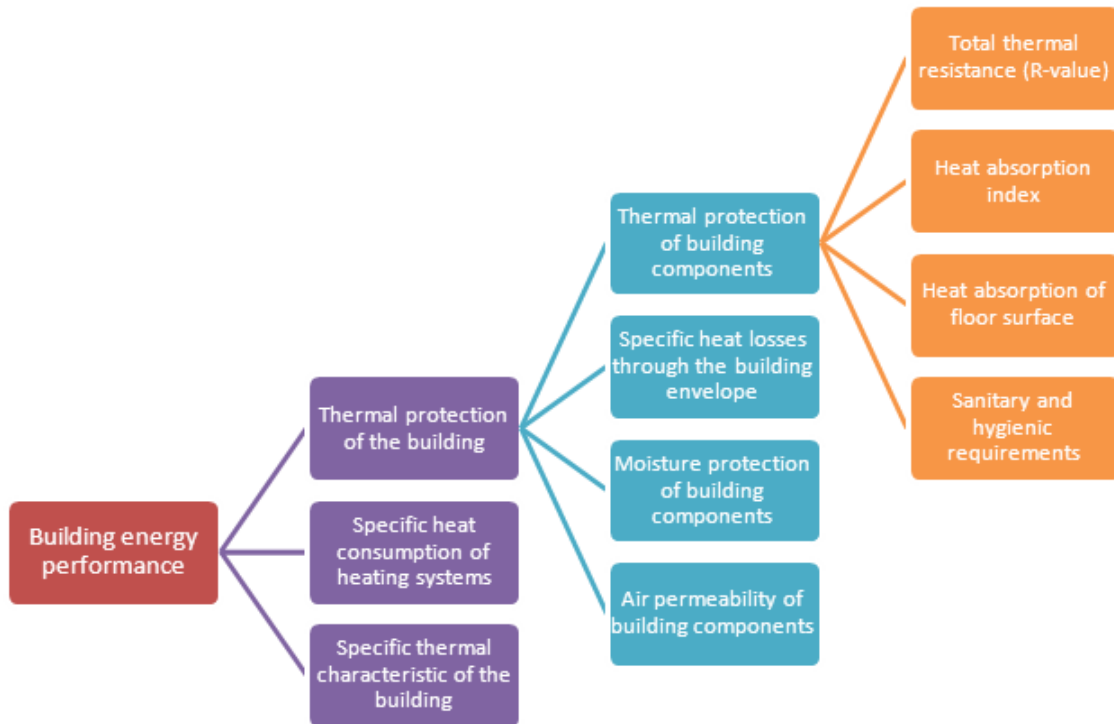


Figure 1. Building energy performance calculation concept according to Russian State Standard GOST 31427–2020 "Residential and public buildings. Composition of energy efficiency indicators."

For element-by-element thermal evaluation, the building envelope should be divided into separate homogeneous building components. The thermal quantities shall be calculated for each building component. The requirements on a building's thermal protection are considered fulfilled if each building component meets the thermal requirements.

A complex assessment of building thermal protection is based on a calculation of energy indicators for the entire building. The advantage of such a method is consideration of not only structural but also space-planning, climatological, engineering, and technical characteristics of building. Results of complex assessment of building thermal protection are the basis for determining the energy-saving class of building.

Generally, the thermal quantities of building components are thermal resistance, heat absorption index, resistance to air permeation, moisture-protective properties. These quantities are calculated as a function of thermal properties, composition, and geometry of element and boundary conditions. The sandwich panel's outer and inner structural layers are made of dense low-porous materials, which practically eliminate through air filtration. Therefore, the calculation of this structure's air permeability in the case that joints of panels are well-sealed is not required.

Building energy characteristics calculation is necessary to evaluate it from the point of energy efficiency. Building energy characteristics includes specific heat losses through the building envelope (SHL), specific thermal characteristic of the building (STC) and specific heat consumption of heating systems (SHC).

There are two methods for calculating the thermal quantities of a building component. The detailed calculation method is a numerical simulation carried out on the whole building component or a

representative part. The method is valid for any building component. However, the complexity of this method makes it difficult to apply it widely in practice. The simplified calculation method is valid for components consisting of thermally homogenous or inhomogeneous layers. Obviously, this method is less accurate than the detailed calculation method, but it is much simpler and more accessible. Therefore, for the purpose of this research, we use simplified calculation methods.

2.2. Building components

Typical precast concrete sandwich panel consists of two precast reinforced concrete layers (called *wythes*) separated by insulation and joined with connectors penetrate through insulation. Two sandwich panel configurations are considered: conventional (Fig. 2, a) and advanced (Fig. 2, b). The conventional sandwich panel consists of inner and outer reinforced concrete layers with a thickness of 75 mm separated by a layer of insulation made of extruded foam polystyrene (XPS) 50 mm thick slabs. In advanced design, due to the use of TRC, the thickness of interior and exterior structural layers is reduced to 40 mm (while maintaining strength), and the thickness of the heat-insulating layer increased to 120 mm. 10 mm diameter glass plastic connectors located in nodes of a square grid connect structural layers. Grid spacing is 185 mm; the number of connectors is 19 pcs per 1 m² of section.

Compared to the conventional product, the use of thinner TRC structural layers allows reducing the mass of the precast sandwich panel by almost half, which contributes to a significant reduction in the entire building's material consumption.

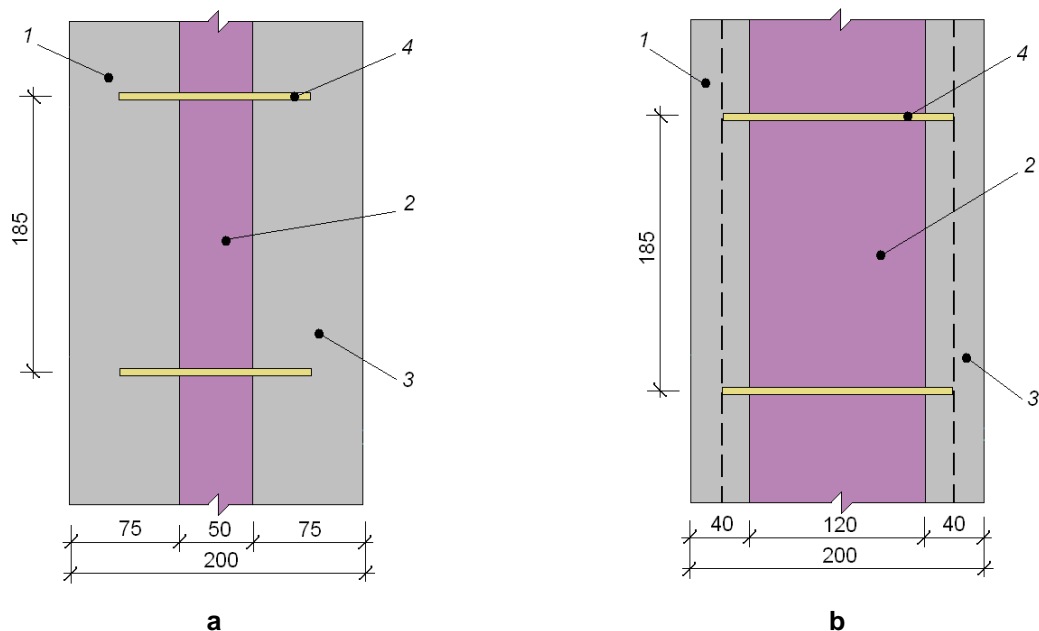


Figure 2. Conventional (a) and advanced (b) sandwich panel configuration: 1 — interior structural layer; 2 — thermal insulation; 3 — exterior structural layer; 4 — connector.

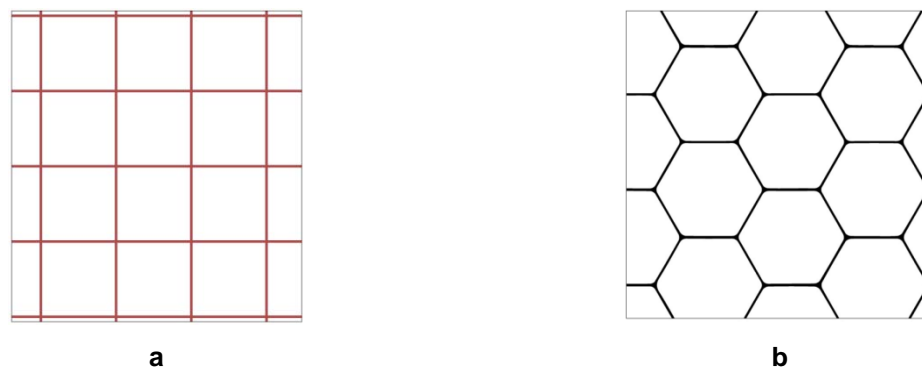


Figure 3. Location of the connectors in the square (a) and hexagonal (b) grid nodes.

In this research, we use the method of designing building components without thermal bridges. Placing low-thermal conductivity connectors in square or hexagonal grid nodes (Fig. 3) minimizes additional heat loss through the nodes. Sandwich panels in completed form is a continuous heat protection envelope, which practically eliminates additional heat losses through the horizontal and vertical joints of the panels. The use of window blocks with a wide box (frame thickness 80–120 mm), in combination with a relatively

small length of assemblies, also contributes to reducing additional heat losses and their insignificant effect on the thermal resistance of building components.

2.3. Environmental conditions

Thermal and hygrothermal performance analysis of outer walls in winter was carried out on the sample locations in various humidity-climatic zones of the European part of Russia: Volgograd (dry zone), Moscow (normal zone), and St. Petersburg (wet zone). Figure 4 shows the external environmental conditions of these locations.

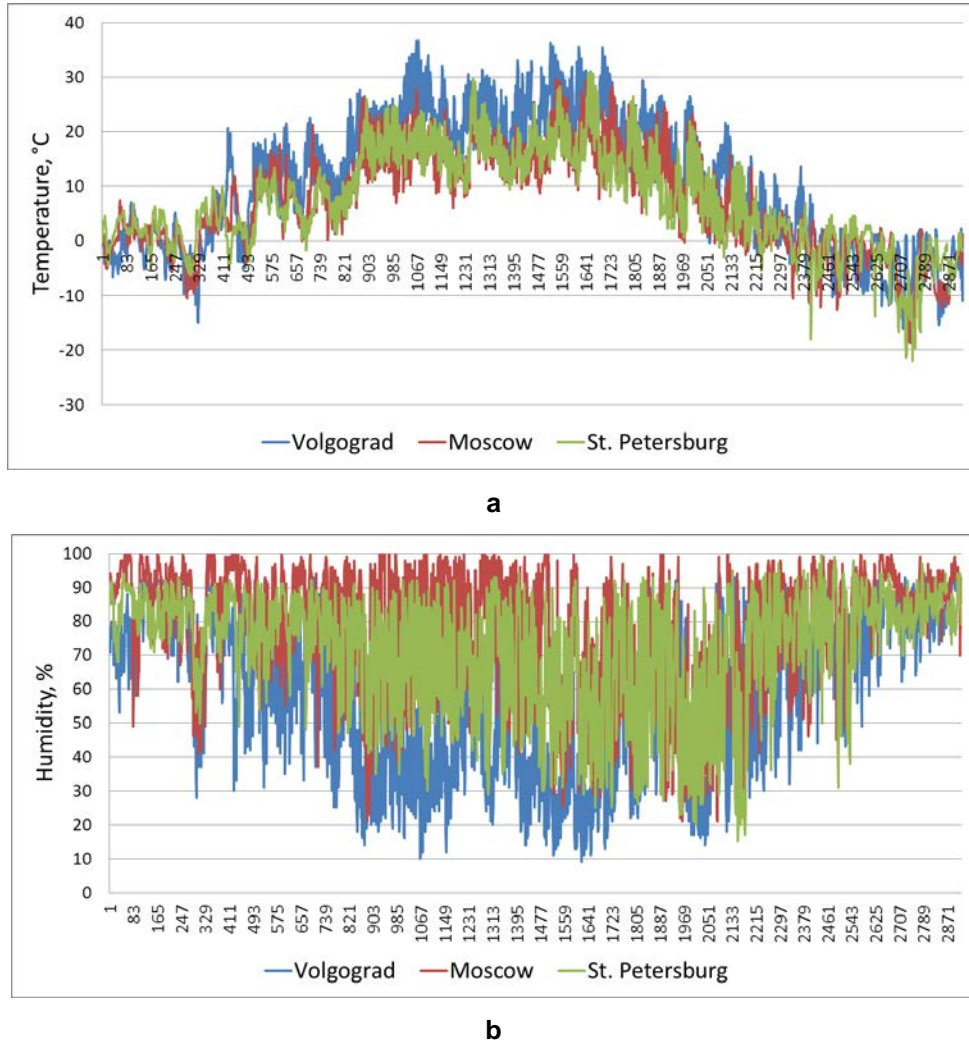


Figure 4. Temperature (a) and humidity (b) analyze at the locations under consideration.

Parameters of external climate for these points are shown in Table 1.

Table 1. Conditions of the outside air.

	Volgograd (48°42'N, 44°30'E)	Moscow (55°45'N, 37°37'E)	St. Petersburg (59°57'N, 30°19'E)
Heating period			
Duration of period, day/year	176	205	213
Outside temperature (average value), °C	-2.3	-2.2	-1.3
Humidity, %	75	82	77
Summer and transition periods			
Duration of period, day/year	189	160	152
Outside temperature (average value), °C	18.6	15.1	14.8
Humidity, %	46	70	64

Thermal stability analysis of outer walls was carried out in the summer period for Volgograd.

Building energy performance of buildings made of TRC sandwich panels was carried out for optimal air parameters (see Table 2).

Table 2. Optimal air parameters in offices (according to Russian State Standard GOST 30494-2011 "Residential and public buildings. Microclimate parameters for indoor enclosures").

Time of the year	Temperature, °C	Humidity, %	Speed, m/s
Cold period	19–21	30–45	0.2
Non-heating period	23–25	30–60	0.15

2.4. Thermal properties of building materials

Thermal properties for sandwich panel materials are adopted depending on the building component's operating conditions (Table 3).

Table 3. Material properties.

Building element	Quantity	Symbol, unit	Design values		
			Conventional configuration	Advanced configuration	
Wythe	Density	ρ_c , kg/m ³	2500	2400	
	Thermal conductivity at the moisture content of material is 2% mass by mass	λ_c , W/(m·K)	1.92	1.74	
			at the moisture content of material is 3% mass by mass	2.04	1.86
	Heat absorption at the moisture content of material is 2% mass by mass	s_c , W/(m ² ·K)	17.98	16.77	
			at the moisture content of material is 3% mass by mass	18.95	17.88
	Water vapour permeability	μ_c , kg/(m·s·Pa)	$8.33 \cdot 10^{-12}$	$9.72 \cdot 10^{-12}$	
	Insulation	Density	ρ_{ins} , kg/m ³	30	30
		Thermal conductivity at the moisture content of material is 1% mass by mass	λ_{ins}^{eq} , W/(m·K)	0.030	0.030
				at the moisture content of material is 2% by mass	0.031
		Heat absorption at the moisture content of material is 2% mass by mass	s_{ins} , W/(m ² ·K)	0.3	0.3
at the moisture content of material is 3% mass by mass				0.31	0.31
Water vapour permeability		μ_c , kg/(m·s·Pa)	$1.39 \cdot 10^{-12}$	$1.39 \cdot 10^{-12}$	
Connector	Density	ρ_{fg} , kg/m ³	1467	1467	
	Thermal conductivity	λ_{fg} , W/(m·K)	0.48	0.48	
	Heat absorption	s_{fg} , W/(m ² ·K)	6.57	6.57	
	Water vapour permeability	μ_{fg} , kg/(m·s·Pa)	~0	~0	

To take into account the effect of connectors on sandwich panels' thermal characteristics, we used the method of equivalent characteristics based on the addition of thermal transmittance. This method's advantage is the possibility of approximate assessment of impact efficiency of inhomogeneous thermal sections of building components without labor-intensive calculations of temperature fields [20]. Since the influence of connectors is most pronounced concerning the insulation layer, its equivalent characteristics (thermal conductivity and heat absorption) can be calculated by formulas:

$$\lambda_{\text{ins}}^{\text{eq}} = \lambda_{\text{XPS}} + d_{\text{con}} (\lambda_{\text{fg}} - \lambda_{\text{XPS}}),$$

$$s_{\text{ins}}^{\text{eq}} = s_{\text{XPS}} + d_{\text{con}} (s_{\text{fg}} - s_{\text{XPS}}),$$

where λ_{XPS} , λ_{fg} are the thermal conductivity, in W/(m·K), of XPS and fiberglass, respectively;

s_{XPS} , s_{fg} are the heat absorption, in W/(m²·K), of XPS and fiberglass, respectively;

d_{con} is the fraction occupied by connectors, calculated by the formula:

$$d_{\text{con}} = \frac{\pi}{4} D_{\text{con}}^2 n_{\text{con}},$$

where D_{con} is connector diameter, in m;

n_{con} is a number of connectors per 1 m² of panel.

2.5. Thermal properties of building components

Total thermal resistance of building components (from environment to environment) characterizes the heat-protecting properties under steady-state conditions. This thermal quantity is equal to the ratio of temperature difference on different sides of the building component to the density of heat flow rate averaged by area through the building component. In the case of simplified calculation method, the total thermal resistance of a plane building component consisting of thermally homogeneous layers perpendicular to heat flow shall be calculated by the following formula:

$$R_o = \frac{1}{\alpha_{\text{si}}} + \frac{2\delta_c}{\lambda_c} + \frac{\delta_{\text{ins}}}{\lambda_{\text{ins}}^{\text{eq}}} + \frac{1}{\alpha_{\text{se}}},$$

where R_o is the total thermal resistance, in m²·K/W;

α_{si} is the inside surface heat-transfer coefficient, in W/(m²·K);

δ_c is the thickness of the structural layer, in m;

λ_c is the thermal conductivity of the structural layer, in W/(m·K);

δ_{ins} is the thickness of insulation, in m;

$\lambda_{\text{ins}}^{\text{eq}}$ is the equivalent thermal conductivity of insulation, in W/(m·K);

α_{se} is the outside surface heat-transfer coefficient, in W/(m²·K).

Heat absorption index is the property of a building component to maintain relative temperature constancy when thermal effects from external and internal environments of space periodically change. The heat absorption index may be calculated through the well-known heat absorption theory. This theory is characterized by the following main thermal indicators: decrement factor (DF) and time lag (TL).

Building component decrement factor shall be calculated by the formula:

$$v = v_1 v_2 v_3 v_{se},$$

where v is the decrement factor of a component;

v_1, v_2, v_3, v_{se} are the decrement factors in the first, second, third layer and at the outer surface of the wall, calculated by the formulae:

$$v_1 = 0.95 \exp\left(\frac{D_1}{\sqrt{2}}\right) \frac{s_1 + \alpha_{si}}{s_1 + Y_1};$$

$$v_2 = \exp\left(\frac{D_2}{\sqrt{2}}\right) \frac{s_2 + Y_1}{s_2 + Y_2};$$

$$v_3 = 0.95 \exp\left(\frac{D_3}{\sqrt{2}}\right) \frac{s_3 + Y_2}{s_3 + Y_3};$$

$$v_{se} = 1 + \frac{Y_3}{\alpha_{se}},$$

where D_i is the thermal inertia of the i -th layer ($D_i = R_i s_i$);

R_i is the thermal resistance of the i -th layer, in $\text{m}^2 \cdot \text{K}/\text{W}$;

s_i is the design heat absorption of the i -th layer, in $\text{W}/(\text{m}^2 \cdot \text{K})$;

Y_i is the heat absorption at the outer surface of the i -th layer, in $\text{W}/(\text{m}^2 \cdot \text{K})$.

The procedure for calculating the values of Y_i is well known; therefore, it is not considered here.

It is known that the time lag of a building component is given by:

$$\varepsilon = \frac{1}{15} \left(40.5D - \arctg\left(\frac{\alpha_{si}}{\alpha_{si} + Y_{si}\sqrt{2}}\right) + \arctg\left(\frac{Y_{se}}{Y_{se} + \alpha_{se}\sqrt{2}}\right) \right),$$

where ε is the time lag, in hours and minutes;

D is the thermal inertia;

Y_{si} is the heat absorption at the inner surface of the component in the direction of the heat wave movement from the inside to the outside, in $\text{W}/(\text{m}^2 \cdot \text{K})$;

Y_{se} is the heat absorption at the inner surface of the component in the opposite direction of the heat wave motion, in $\text{W}/(\text{m}^2 \cdot \text{K})$.

Moisture performance assessment of building components was carried out according to the maximum permissible state of humidification during the annual cycle using the simplified calculation method [23], harmonized with International Standard ISO 13788. Unlike the method for calculating moisture-protective properties adopted in Russian standards, this method allows to analyze the dynamics of moisture accumulation in building components during the year. Compared to International Standard ISO 13788, this method gives a more accurate assessment of humidity conditions of multilayer enclosing structures with a high level of thermal protection.

Thermal quantities calculated for office building. Input data listed in Table 4.

Table 4. Geometric and thermal data.

Name	Unit	Design values
Floors	Number	4
Design area of the building	m^2	2099
Heated volume of the building	m^3	9468
Factor of building compactness	m^{-1}	0,34
Coefficient of glazing	%	17
Share of enclosing structures (walls/windows/roof/basement) in the building envelope	%	44.8/10.6/19.1/25.5

Name	Unit	Design values
Thermal resistance of building components (walls/windows/roof/basement) using conventional sandwich panels	m ² ·K/W	1.85/0.76/3.11/4.57
using TRC sandwich panels		4.08/0.76/3.11/4.57
Ventilation rate in the building during the heating period (average)	h ⁻¹	0.712
Heating heat control efficiency factor	–	0.95

3. Results and Discussion

3.1. Thermal resistance of building components

The design values of the total thermal resistance of the walls are given in Fig. 5.

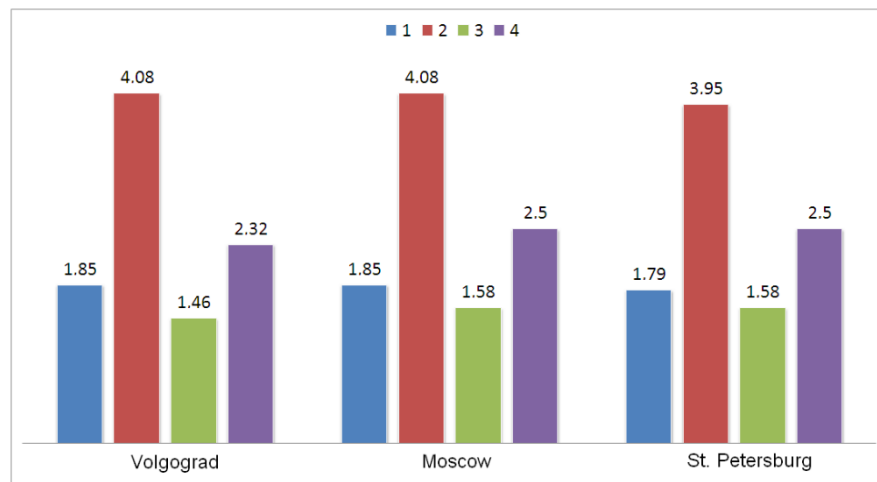


Figure 5. Total thermal resistance of outer walls (R_o , in m²·K/W): 1 — conventional configuration; 2 — advanced configuration (3 and 4 — respectively minimum and reference values of total thermal resistance according to Russian Standard SP 50.1330.2012).

Fig. 5 demonstrated that the thermal resistance of outer walls made of TRC sandwich panels higher (2.2 times) than the R-value of conventional structures in various humidity-climatic zones. Thus, these façade systems can provide a high level of thermal protection of buildings during the cold period.

3.2. Building components heat absorption

Heat absorption index calculation results for outer walls are given in Table 5.

Table 5. Heat absorption properties of outer wall (Volgograd).

Building element	Conventional sandwich panel			TRC sandwich panel		
	D	$Y, W/(m^2 \cdot K)$	ν	D	$Y, W/(m^2 \cdot K)$	ν
Interior structural layer	0.702	15.9	1.23	0.386	12.6	1.25
Insulation	0.5	0.602	25.3	1.16	0.30	48.8
Exterior structural layer	0.702	12.9	0.939	0.386	6.72	0.907
Outside surface of the wall			1.74			1.39
Building component	1.90		50.8	1.93		76.9

Calculation results analysis demonstrated that the maximum local value of DF is observed in the heat-insulating layer of the outer wall. The minimum value of local DF occurs in the outer structural layer, which can be explained not so much by the low thermal inertia of this layer as by the heat insulation layer located behind it with low heat absorption of the outer surface. In the inner structural layer, the value of DF is slightly greater than in the outer layer, which is due to the higher heat absorption value at the outer surface of the inner layer. Therefore, the decrement factor in the layer depends not only on the properties of its material but also on the layer following it. Therefore, it is possible to increase the heat absorption of these façade systems by different layer combinations.

Based on calculation results, we also established that the value of TL at the inner surface of the conventional structure is 5 hours 12 minutes, for advanced design is 4 hours 18 minutes. The use of structural layers made of TRC in sandwich panels increases external walls heat absorption by 34.4%, reducing the overheating risk of premises in summer.

3.3. Building components hygrothermal-protective properties

Humidity conditions calculation results in outer wall are given in Fig. 6, 7.

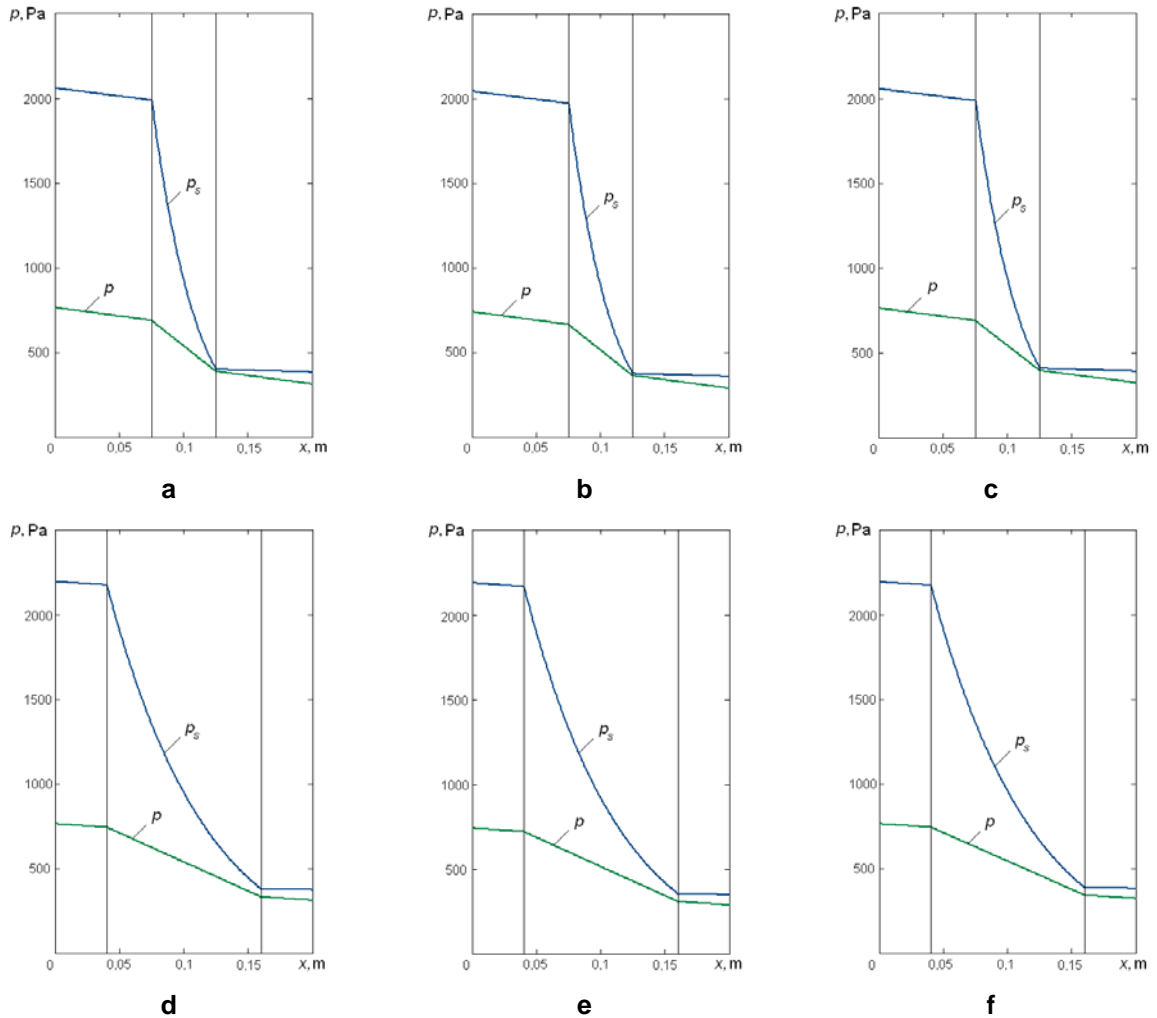


Figure 6. Water vapour diffusion in the multi-layer building components without any interstitial condensation in January (p is the water vapour pressure, in Pa; p_s is the value at saturation, in Pa): a — conventional configuration, Volgograd; b — conventional configuration, Moscow; c — conventional configuration, St. Petersburg; d — advanced configuration, Volgograd; e — advanced configuration, Moscow; f — advanced configuration, St. Petersburg.

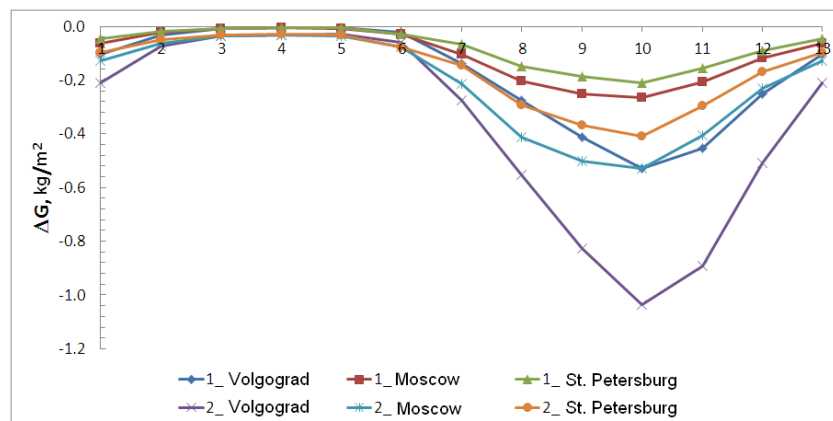


Figure 7. Moisture rate increment in building components during the annual cycle (1 — conventional configuration; 2 — advanced configuration).

In these cases, as shown in Figure 7, there is no condensation at the interface between insulation and exterior structural layer in the coldest month. The maximum convergence of water vapour pressure profile and the value at saturation is noted at the junction of heat insulation and exterior structural layer that increases the risk of moisture condensation, but this effect is characteristic of conventional design. The monthly condensation rate in the building components is negative, indicating no moisture accumulation during the year. Therefore, hygrothermal-protective properties of building components are provided. This conclusion is qualitatively correspondent to the results [29], according to which the risks of moisture condensation and hygrothermal-protective properties deterioration of outer wall made of sandwich panels are minimized.

3.4. Building energy performance

Specific heat losses through the building envelope are demonstrated in Fig. 8.

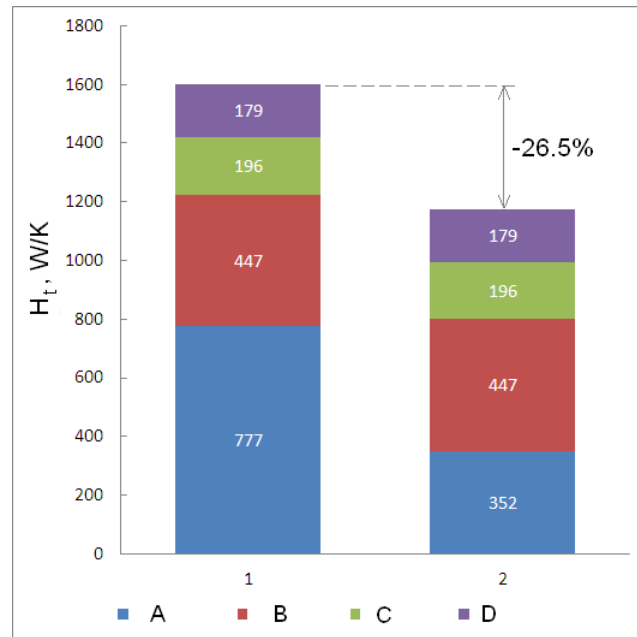


Figure 8. The specific heat losses through the building envelope when applied conventional (1) and advanced (2) sandwich panels: A — outer walls; B — windows; C — roof; D — floor on the ground.

Fig. 8 shows that when using the conventional sandwich panels, maximum heat loss is noted through outer walls (48.6%), minimum heat loss through the floor on the ground (11.2%). The use of advanced sandwich panels makes it possible to balance transmission heat losses, while total heat loss through the building envelope is reduced by 26.5%.

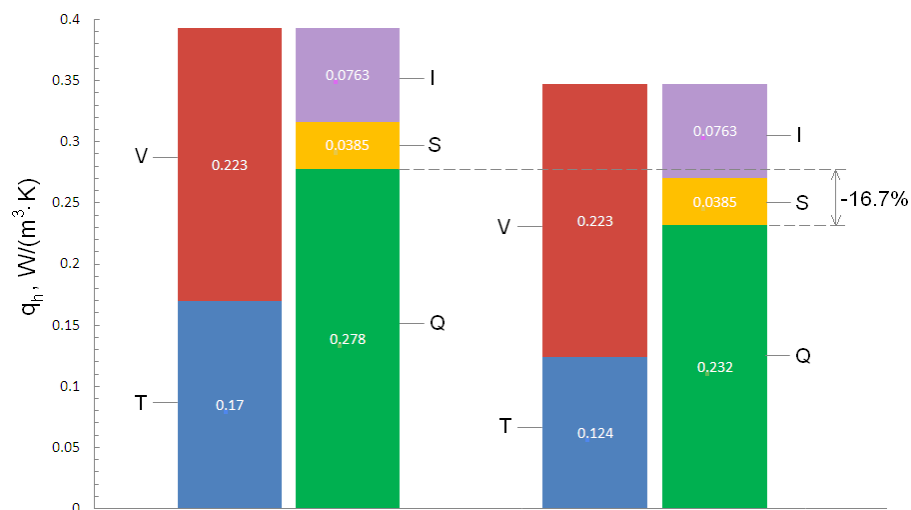


Figure 9. Building thermal balance when used conventional (left) and advanced (right) sandwich panels: T — transmission heat loss; V — ventilation heat loss; I — internal heat gain; S — solar heat gain; Q — heat energy demand for heating and ventilation.

As shown in Figure 9, the specific thermal characteristic of the building when used a conventional façade system is $0.278 \text{ W}/(\text{m}^3\cdot\text{K})$. The reference value of the specific thermal characteristic of the building is $0.313 \text{ W}/(\text{m}^3\cdot\text{K})$. The energy-saving class of building is C + (normal). The application of an advanced façade system reduces the specific thermal characteristic of buildings by 16.7%, while the energy-saving class of buildings increases to level B (high).

Based on received results, the values of specific heat consumption of heating systems of the building are given: $25 \text{ kWh}/(\text{m}^3\cdot\text{year})$ when used conventional façade system and $20.9 \text{ kWh}/(\text{m}^3\cdot\text{year})$ when used advanced façade system. Then, based on data [26], it is possible to receive values of the total specific consumption of thermal and electric energy for the operation of building during the year, 125 and 121 $\text{kWh}/(\text{m}^3\cdot\text{year})$, respectively. In this case, the reduction of energy consumption of buildings will be 3.2%, which is well consistent with the calculation data [26] obtained for small office buildings under similar climatic conditions (Fig. 10), and, therefore, confirms the validity of our calculations.

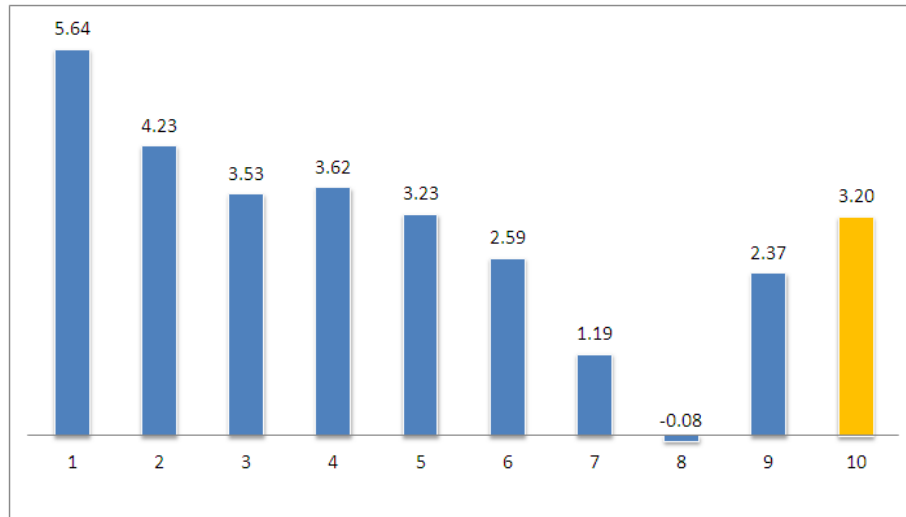


Figure 10. Buildings energy consumption reduction (%) [26]: 1 — Fairbanks; 2 — Duluth; 3 — Helena; 4 — Burlington; 5 — Chicago; 6 — Boise; 7 — Albuquerque; 8 — San Francisco; 9 — Salem McNary; 10 — Russia, Volgograd (our calculations).

Further tasks of research are to refine the actual thermal performance of façade system and analyze the results of the simulation of the thermal conditions of buildings based on detailed calculation methods.

4. Conclusions

This research aimed to investigate the energy properties of buildings made of textile-reinforced concrete (TRC) sandwich panels in various humidity-climatic zones. Two configurations of sandwich panel are considered: conventional and advanced. The conventional sandwich panel consists of inner and outer reinforced concrete layers with a thickness of 75 mm separated by a layer of insulation made of extruded foam polystyrene (XPS) 50 mm thick slabs. In advanced design, due to the use of TRC, the thickness of interior and exterior structural layers is reduced to 40 mm (while maintaining strength), and the thickness of the heat-insulating layer increased to 120 mm. 10 mm diameter glass plastic connectors located in nodes of a square grid connect structural layers. Grid spacing is 185 mm; the number of connectors is 19 pcs per 1 sq. m of section. The analytical method of research was applied to the energy performance of buildings made of TRC sandwich panels based on the investigation of heat and moisture transfer processes in continuous heterogeneous media and analysis of buildings' energy indicators. For this research, the element-by-element and complex assessment of building thermal protection was performed.

Based on the results of this research, the main thermal advantages of these façade systems are identified:

I. Building component thermal resistance is increased in multiple in various humidity-climatic zones, providing a high level of thermal protection in winter compared to conventional facade systems.

II. Building component heat absorption is increased by 34.4 % (compared to conventional facade systems), excluding the risk of overheating of premises in summer.

III. The risks of moisture condensation and deterioration of hygrothermal-protective properties of building components are minimized.

IV. The use of TRC sandwich panels allows reducing total heat loss through the building envelope by 26.5 %. At the same time, specific thermal characteristic of the building is decreased by 16.7 %, and the energy-saving class increases to high levels.

Construction with advanced façade systems, when used the precast sandwich panels with structural layers from textile-reinforced concrete, extends the creative boundaries of architecture and allows you to solve the current problem of improving the quality of the architectural environment and conserve energy for future generations.

References

- Kalamees, T., Jylhä, K., Tietäväinen, H., Jokisalo, J., Ilomets, S., Hyvönen, R., Saku, S. Development of weighting factors for climate variables for selecting the energy reference year according to the en ISO 15927-4 standard. *Energy and Buildings*. 2012. 47. Pp. 53–60. DOI: 10.1016/j.enbuild.2011.11.031.
- Grazulevičiute-Vileniske, I., Seduikyte, L., Teixeira-Gomes, A., Mendes, A., Borodinecs, A., Buzinskaite, D. Aging, living environment, and sustainability: What should be taken into account? *Sustainability (Switzerland)*. 2020. 12(5). Pp. 1–12. DOI: 10.3390/su12051853.
- Barbosa, A.A.R., Vilnitis, M. Innovation and construction management in Brazil: Challenges of companies in times of quality and productivity. *IOP Conference Series: Materials Science and Engineering*. 2017. 251(1). DOI: 10.1088/1757-899X/251/1/012040.
- Chan, A.L.S., Chow, T.T., Fong, K.F., Lin, Z. Investigation on energy performance of double skin façade in Hong Kong. *Energy and Buildings*. 2009. 41(11). Pp. 1135–1142. DOI: 10.1016/j.enbuild.2009.05.012.
- Vatin, N., Korniyenko, S. V., Gorshkov, A.S., Pestryakov, I.I., Olshevskiy, V. Actual thermophysical characteristics of autoclaved aerated concrete. *Magazine of Civil Engineering*. 2020. 96(4). Pp. 129–137. DOI: 10.18720/MCE.96.11.
- Hallik, J., Kalamees, T. The effect of flanking element length in thermal bridge calculation and possible simplifications to account for combined thermal bridges in well insulated building envelopes. *Energy and Buildings*. 2021. 252. DOI: 10.1016/j.enbuild.2021.111397.
- Vilnitis, M., Lapsa, V.A., Veinbergs, A. Sustainable construction success indicators. *IOP Conference Series: Materials Science and Engineering*. 2019. 660(1). DOI: 10.1088/1757-899X/660/1/012041.
- Sadinieni, S.B., Madala, S., Boehm, R.F. Passive building energy savings: A review of building envelope components. *Renewable and Sustainable Energy Reviews*. 2011. 15(8). Pp. 3617–3631. DOI: 10.1016/j.rser.2011.07.014.
- Bhandari, M., Shrestha, S., New, J. Evaluation of weather datasets for building energy simulation. *Energy and Buildings*. 2012. 49. Pp. 109–118. DOI: 10.1016/j.enbuild.2012.01.033.
- Hamburg, A., Kalamees, T. How well are energy performance objectives being achieved in renovated apartment buildings in Estonia? *Energy and Buildings*. 2019. 199. Pp. 332–341. DOI: 10.1016/j.enbuild.2019.07.006.
- Zemitis, J., Borodinecs, A., Frolova, M. Measurements of moisture production caused by various sources. *Energy and Buildings*. 2016. 127. Pp. 884–891. DOI: 10.1016/j.enbuild.2016.06.045.
- Faruk, O., Bledzki, A.K., Fink, H., Sain, M. Progress in Polymer Science Biocomposites reinforced with natural fibers : 2000 – 2010. *Progress in Polymer Science*. 2012. 37(11). Pp. 1552–1596. DOI: 10.1016/j.progpolymsci.2012.04.003.
- Korniyenko, S. V. Renovation of Residential Buildings of the First Mass Series. *IOP Conference Series: Materials Science and Engineering*. 2018. 463(2). DOI: 10.1088/1757-899X/463/2/022060.
- Bazhenov, Y.M., Bataev, D.K.S., Murtazaev, S.A.U., Alarkhanova, Z.Z., Goitmirov, R.U., Mazhiev, K.N., Khasbulatova, Z.S., Bataeva, P.D. Ways to improve properties of high-strength building polymer composites. *IOP Conference Series: Materials Science and Engineering*. 2020. 905(1). DOI: 10.1088/1757-899X/905/1/012006.
- Gaujena, B., Agapovs, V., Borodinecs, A., Strelets, K. Analysis of thermal parameters of hemp fiber insulation. *Energies*. 2020. 13(23). Pp. 1–14. DOI: 10.3390/en13236385.
- Sanjay, M.R., Siengchin, S., Parameswaranpillai, J., Jawaid, M., Pruncu, C.I., Khan, A. A comprehensive review of techniques for natural fibers as reinforcement in composites: Preparation, processing and characterization. *Carbohydrate Polymers*. 2019. 207(November 2018). Pp. 108–121. DOI: 10.1016/j.carbpol.2018.11.083.
- Coakley, D., Raftery, P., Keane, M. A review of methods to match building energy simulation models to measured data. *Renewable and Sustainable Energy Reviews*. 2014. 37. Pp. 123–141. DOI: 10.1016/j.rser.2014.05.007.
- Park, B., Srubar, W. V., Krarti, M. Energy performance analysis of variable thermal resistance envelopes in residential buildings. *Energy and Buildings*. 2015. 103. Pp. 317–325. DOI: 10.1016/j.enbuild.2015.06.061.
- Korniyenko, S. V., Astafurova, T.N., Kozlova, O.P. Energy Efficient Major Overhaul in Residential Buildings of the First Mass Series. *IOP Conference Series: Materials Science and Engineering*. 2020. 753(4). DOI: 10.1088/1757-899X/753/4/042039.
- Shams, A., Horstmann, M., Hegger, J. Experimental investigations on textile-reinforced concrete (TRC) sandwich sections. *Composite Structures*. 2014. 118(1). Pp. 643–653. DOI: 10.1016/j.compstruct.2014.07.056.
- Ficco, G., Iannetta, F., Ianniello, E., D'Ambrosio Alfano, F.R., Dell'Isola, M. U-value in situ measurement for energy diagnosis of existing buildings. *Energy and Buildings*. 2015. 104. Pp. 108–121. DOI: 10.1016/j.enbuild.2015.06.071.
- Rubene, S., Vilnitis, M. Impact of moisture content in AAC on its heat insulation properties. *IOP Conference Series: Materials Science and Engineering*. 2017. 251(1). DOI: 10.1088/1757-899X/251/1/012070.
- Korniyenko, S. Advanced Hygrothermal Performance of Building Component at Reconstruction of S. Radonezhskiy Temple in Volgograd. *MATEC Web of Conferences*. 2016. 53. Pp. 2–7. DOI: 10.1051/mateconf/20165301003.
- Aghdasi, P., Heid, A.E., Chao, S.H. Developing ultra-high-performance fiber-reinforced concrete for large-scale structural applications. *ACI Materials Journal*. 2016. 113(5). Pp. 559–569. DOI: 10.14359/51689103.
- Ahlborn, T.M., Harris, D.K., Misson, D.L., Peuse, E.J. Characterization of strength and durability of ultra-high-performance concrete under variable curing conditions. *Transportation Research Record*. 2011. (2251). Pp. 68–75. DOI: 10.3141/2251-07.
- Abediniangerabi, B., Shahandashti, S.M., Bell, B., Chao, S.H., Makhmalbaf, A. Building energy performance analysis of ultra-high-performance fiber-reinforced concrete (UHP-FRC) façade systems. *Energy and Buildings*. 2018. 174. Pp. 262–275. DOI: 10.1016/j.enbuild.2018.06.027.

27. Shams, A., Hegger, J., Horstmann, M. An analytical model for sandwich panels made of textile-reinforced concrete. *Construction and Building Materials*. 2014. 64. Pp. 451–459. DOI: 10.1016/j.conbuildmat.2014.04.025.
28. Khan, M.S., Sanchez, F., Zhou, H. 3-D printing of concrete: Beyond horizons. *Cement and Concrete Research*. 2020. 133(April). DOI: 10.1016/j.cemconres.2020.106070.
29. Abdou, O.A., Murali, K., Morsi, A. Thermal performance evaluation of a prefabricated fiber-reinforced plastic building envelope system. *Energy and Buildings*. 1996. 24(1). Pp. 77–83. DOI: 10.1016/0378-7788(95)00967-1.
30. Korniyenko, S. V., Astafurova, T.N., Kozlova, O.P. Thermal Renovation of Facade Systems in Block Buildings. *IOP Conference Series: Materials Science and Engineering*. 2020. 753(2). DOI: 10.1088/1757-899X/753/2/022026.

Information about authors:

Nikolai Vatin

Doctor of Technical Science

ORCID: <https://orcid.org/0000-0002-1196-8004>

E-mail: vatin@mail.ru

Sergey Korniyenko

Doctor of Technical Science

ORCID: <https://orcid.org/0000-0002-5156-7352>

E-mail: svkorn2009@yandex.ru

Received 01.04.2021. Approved after reviewing 17.11.2021. Accepted 29.11.2021.



Research article

UDC 693.557

DOI: 10.34910/MCE.113.4



Thermal stresses at the early stage of the hardening of steel-fiber reinforced concrete

G.A. Pikus , A.R. Lebed , A.A. Bondar 

South Ural State University, Chelyabinsk, Russia

✉ pikusga@susu.ru

Keywords: steel fiber, thermal stresses, temperature control, thermal expansion, deformation, viscosity, fiber reinforced concrete

Abstract. The article studies the influence of steel fiber on the change in temperature stresses in concrete at an early hardening stage. When hardening concrete is exposed to heat treatment, its volume and, consequently, density change. Under certain circumstances, this can lead to its structural damage and, ultimately, to a decrease in its physical and mechanical properties at the design age. Such structural damage of concrete can appear even at the earliest hardening stage, before the formation of the elastic properties of the material. When testing concretes subjected to heating, we recorded the development of temperature deformations and assessed their plastic viscosity. To determine the temperature stresses, we proposed a method based on the Kelvin-Voigt rheological model. Studies have shown that the presence of steel fibers in concrete leads to a decrease in the deformations of concrete during heat treatment. To assess the thermal stresses arising at the early stage of hardening, we derived an analytical dependence, taking into account the viscosity of the hardening concrete. During the experiments, we obtained values for the viscosity of steel-fiber reinforced concrete depending on its fiber content. The results showed that, without changing its density, steel-fiber reinforced concrete can take significantly higher thermal stresses than unreinforced concrete at the early hardening stages. With an increase in the temperature, the change in the thermal stresses, depending on the fiber content, begins to have a more pronounced non-linear nature. We also showed that before a certain structural strength is reached, there are no thermal stresses in steel-fiber reinforced concrete due to the steel-fiber induced redistribution of temperature forces throughout the volume of concrete.

Citation: Pikus, G.A., Lebed, A.R., Bondar, A.A. Thermal stresses at the early stage of the hardening of steel-fiber reinforced concrete. Magazine of Civil Engineering. 2022. 113(5). Article No. 11304. DOI: 10.34910/MCE.113.4

1. Introduction

The formation of a favorable thermally stressed state of concrete during hardening is the basis for ensuring the quality of monolithic structures.

The problem of the thermo-stressed state of concrete structures has been most fully explored for dams, since such massive structures may have large temperature differences over the cross-section [1–3]. The temperature differences between the core and the peripheral zones of structures are caused by the exothermic hydration reaction given the relatively low thermal conductivity of concrete. Heat treatment of concrete is not used in such structures, since a large amount of heat is already released during the hydration process. On the contrary, the technologies limiting the temperature of concrete are used in massive structures.

Non-massive concrete structures are heated in low air temperature conditions or to accelerate hardening. When concrete is exposed to heat treatment, its volume constantly changes. Such deformations

indicate a change in the density of the material, and, consequently, a degree of structural damage during its heat treatment [4]. Such structural damage negatively affect its physical and mechanical properties at the age of 28 days.

It is possible to create conditions to minimize $\text{grad}t$ over the cross-section of concrete [5–7], but it is impossible to influence the continuity of the temperature change function when concrete is heated. With the largest construction size of 2 m and a permissible $\text{grad}t$ of 0.1 °C/cm, there will be a temperature drop over the cross-section of concrete of up to 20 °C, while heating this structure from 10 to 50 °C will ultimately lead to a temperature difference at the same point already at 40 °C [8] show that the maximum increase in the deformations of concrete occurs when it is heated and directly depends on the temperature elevation rate. Taking into account that the structure of concrete is formed in its initial hardening period, the effect of such deformations on the properties of concrete at the design age is fundamental.

Most studies assess thermal stresses through Hooke's law, considering the deformation of concrete at the elastic stage, when it already has a certain value of the elastic modulus [9–11]. The minimum time before concrete can be considered as an elastic material is 6 hours [12]. Data on the formation of elastic properties in 12 hours [13], and some works mention not the holding time, but about the concrete strength of 22–30 % [4, 10, 14]. By this time, concrete is already able to take some stress values without changing its structure (volume). Even at early hardening stages, the physical and mechanical properties of steel-fiber reinforced concrete are higher than for standard concrete [15], therefore, it can take higher thermal stresses.

To get an idea of the order of magnitudes of the thermal stresses when standard concrete is heated at the elastic stage, [4] gives an example, which demonstrates stresses of about 2942 kPa. A similar value (3138 kPa) was obtained in [16].

The physical and mechanical properties of concrete directly depend on its density, which is formed during the compaction of concrete mixtures. Starting from the time when the concrete mixture was compacted and until the beginning of the elastic stage (as mentioned, at least 6 hours), temperature effects can lead to irreversible plastic deformations which reduce the density of the material and lead to a worsening of its design characteristics. However, in severe climatic conditions, it is impossible to keep concrete in the formwork for 6 hours without temperature variation and it may freeze over this time period with negative consequences [17].

During the heat treatment of concrete, thermal stresses may occur, however, they are almost unlikely [18]. This is primarily explained by the low structural strength of fresh concrete and the zero elasticity modulus. Nevertheless, according to such models as Kelvin-Voigt or Maxwell, stresses arise in elastic and viscoelastic materials. Steel-fiber concrete mixtures have a significantly higher structural strength than standard concretes due to the formation of a spatial frame using steel fiber [19]. When the geometric characteristics of the fiber change, such a frame can pass from a free-flowing to a bound state.

A fundamentally important task is to identify the possible participation of reinforcement in absorbing thermal stresses and ensuring crack resistance of structures [20]. The solution to this problem resulted in the amendment in 1987 of SNIP III-15-76 in terms of clarifying the maximum permissible temperature differences between the concrete surface and the environment during stripping. Notably, steel fiber fully or partially plays the role of reinforcement in steel-fiber concrete structures.

We consider below the distribution of thermal stresses over time in heated steel-fiber reinforced concrete at its early hardening stage. These studies are of important scientific interest since they cover the initial period of the formation of the steel fiber reinforced concrete structure.

The main purpose of the study is to determine the influence of steel fiber on the change in temperature stresses in concrete at its early hardening stage.

To achieve this purpose, the authors carried out several tests of concretes subjected to heating, as a result of which they recorded the development of temperature deformations and assessed their plastic viscosity. To determine the temperature stresses, they proposed a method based on the Kelvin-Voigt rheological model.

2. Methods

The experiments were carried out on concrete prisms of 300×100×100 mm. The concrete used in the experiments (per 1 m³ of concrete) had the following composition: cement – 450 kg, sand – 890 kg, crushed stone – 800 kg, water-cement ratio – 0.4, superplasticizer – 0.25 % of the cement mass. We used fibers cut from a Fibrex steel sheet with a nominal diameter of 0.67 mm and a length of 40 mm.

We determined the rheological characteristics of the concrete mixtures using a technical viscometer [21] installed on a vibrating platform.

To assess temperature deformations, we used two ICh-0.01 dial gauges located at a distance of 75 mm from the ends of the prism (Fig. 1). Plastic washers with a diameter of 20 mm and a thickness of 2 mm were placed under the indicator feet. The averaged values of the readings of the two indicators were taken as the calculated temperature deformations.

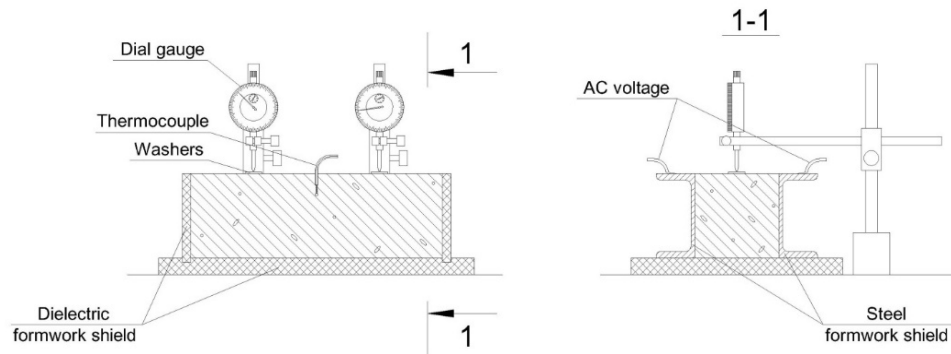


Figure 1. The experimental setup.

The concrete was heated by the AC passing through the concrete sample from two electrodes (from the channel steel), which are also the longitudinal elements of the formwork. The temperature was determined using a chromel-alumel thermocouple located at a depth of 25 mm from the surface of the prism in the middle of the indicators. All the formwork elements are rigid (with a thickness of at least 10 mm for the vertical elements and 20 mm for the horizontal base), so that their shape does not change during the temperature deformations of the concrete.

The initial concrete temperature was 18 °C. The heating rate was 5 °C/min and was regulated by a laboratory transformer by changing the voltage of the electric current. For convenience, the time when the concrete temperature was 20 °C was taken as the zero reading. Such a high heating rate forms the shock nature of the temperature influence on the hardening concrete and allows us to simulate the most negative consequences of its structural changes. Due to the small mass of the sample (the modulus of the sample surface is 47 m⁻¹) and the close arrangement of the electrodes (100 mm), there is almost no significant temperature gradient over the cross-section of concrete at such a heating rate. This allows us to assume that concrete deformations in the experiment are mainly caused by the temperature changes in time but not in space.

3. Results and Discussion

The results of the experiments for the assessment of temperature deformations are summarized in Table 1 and shown in Fig. 2.

Table 1. Values of sample deformations during heating

Heating time, min	Concrete temperature, °C	Relative concrete deformations (*10 ⁻³) at the fiber content, %			
		0	0.5	1	1.5
0	20	0	0	0	0
1	25	0.2	0	0	0
2	30	1.4	0.6	0	0
3	35	3.4	2.4	0.8	0.2
4	40	5.9	4.5	2.4	1.2
5	45	8.9	7.3	4.4	2.2
6	50	12.8	11.0	7.4	3.7
7	55	17.4	15.1	11.1	5.2
8	60	23.4	20.2	16.6	7.2
9	65	32.1	28.0	22.6	9.9
10	70	44.1	37.9	31.1	12.7

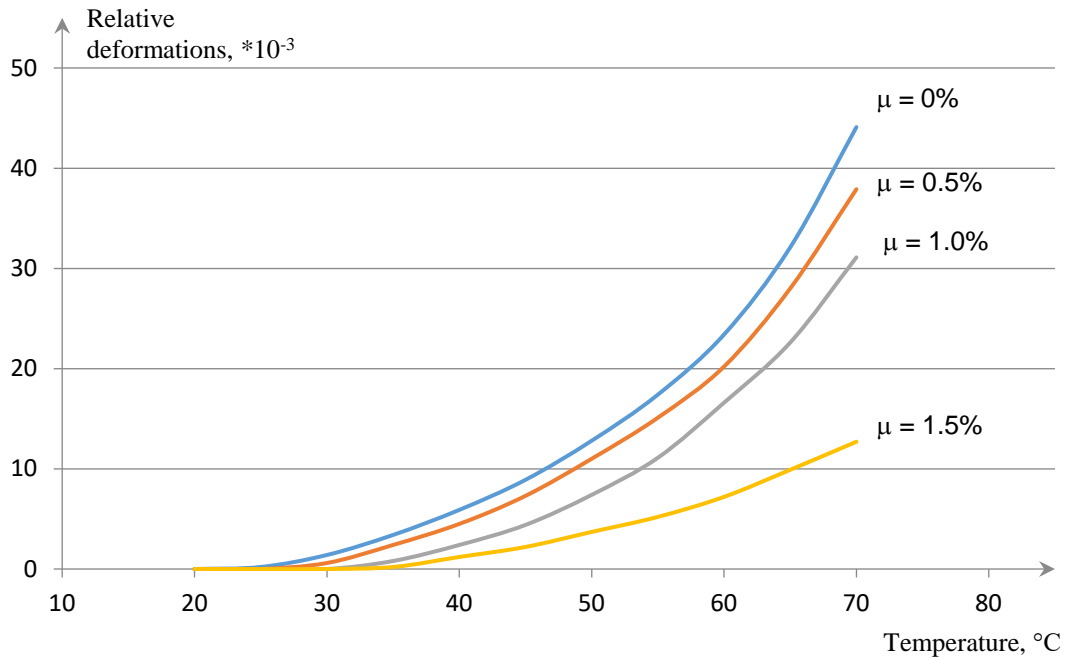


Figure 2. Growing deformations of the samples with a change in their temperature.

Table 1 and Fig. 2 show that the risk of developing unacceptable concrete deformations can be reduced by regulating the content of steel fiber, limiting the heating rate and the maximum concrete temperature.

To assess thermal stresses during heating, we consider fresh concrete according to the Kelvin-Voigt model, as a viscoelastic material. The stresses in such material are

$$\sigma = \sigma_{elas} + \sigma_{vis} = E\varepsilon + \eta\dot{\varepsilon}, \quad (1)$$

where η is plastic viscosity; E is concrete elasticity modulus; ε , $\dot{\varepsilon}$ are relative concrete deformations and rate of relative concrete deformations, respectively.

Taking into account that at the initial moment of concrete hardening its elasticity modulus is 0, we can write formula (1) in differential form:

$$\sigma = \eta \frac{d\varepsilon}{d\tau}. \quad (2)$$

By analogy with the known formula for calculating temperature deformations in an elastic body [4]:

$$\sigma_t = \frac{\alpha E \Delta t}{1 - \nu},$$

where α is the coefficient of linear thermal expansion of concrete; ν is Poisson's ratio of concrete (at an early stage of curing it can be taken to be 0.15), formula (2) can be written as follows:

$$\sigma_t = \sum \frac{\alpha \frac{\eta}{\tau_i} \Delta t_i}{1 - \nu}. \quad (3)$$

Here, Δt_i is the change in the concrete temperature (°C) over time τ_i (seconds).

The plastic viscosity for a technical viscometer can be determined by [22]:

$$\eta = 91.79k\tau_a = [\text{kPa} \cdot \text{sec}], \quad (4)$$

where k is the constant of the device (for the technical viscometer used in the research $k = 0.45$); τ_a is the time for leveling the concrete mixtures in the inner and outer cylinders of the technical viscometer, sec.

Taking into account formula (4) and considering that $\varepsilon = \alpha \Delta t$, formula (3) can be written as follows

$$\sigma_t = \sum \Delta \varepsilon_i \frac{91.97k\tau_a}{\Delta \tau_i (1-\nu)} \quad (5)$$

Formula (5) replaces the integration with the summation of the values of the deformation rates at separate time intervals.

The coefficient of the linear thermal expansion of concrete (α) changes depending on the percentage of steel-fiber reinforcement [23].

In formula (5), the plastic viscosity of concrete (the numerator) is assumed constant over time since the tests showed that it changes insignificantly during 10 minute heating, which is in line with [24]. The obtained values of time τ_a are:

- for the fiber-free concrete mixture = 2 seconds,
- for the concrete mixture with 0.5 % fiber = 7 seconds,
- for the concrete mixture with 1.0 % fiber = 18 seconds,
- for the concrete mixture with 1.5 % fiber = 32 seconds.

The results using formula (5) with the data from Table 1 are shown in Table 2.

Table 2. Changes of the thermal stresses in concrete during heating

Heating time, min	Thermal stresses (kPa) at the following percentage of fiber reinforcement			
	0	0.5	1.0	1.5
1	0.324	–	–	–
2	2.265	3.403	–	–
3	5.502	13.602	11.660	5.188
4	9.552	25.517	34.990	31.097
5	14.416	41.384	64.145	57.016
6	20.731	62.360	107.883	95.889
7	28.184	85.612	161.820	134.773
8	37.903	114.522	241.999	186.601
9	51.995	158.740	329.474	256.581
10	71.432	214.874	453.391	329.150

An increase in the mechanical stresses in structures is proportional to the increase in the rigidity of the material. This is attributable to the elasticity modulus in elastic structures, and plastic viscosity in viscous materials. That is, with an increase in viscosity (the content of fiber), the thermal stresses arising in concrete increase, which is confirmed by the data in Table 2. We can see that the stress values at the same temperature increase with an increase in the percentage of fiber reinforcement from 0 to 1 %.

This can be explained by the fact that the heating process is accompanied by the appearance of excess pressure in the vapor-air medium of concrete, which leads to the separation of solid concrete particles and a decrease in its density. During the heat and mass transfer process, moisture moves from more stressed capillaries to less stressed ones. That is, during such moisture migration, the latter acts as a damper, reducing and leveling the thermal stresses in concrete due to their redistribution. Due to friction and mechanical linkage, the fiber additionally restrains the separation of the concrete mixture components, thereby maintaining the density and strength of the material. This fiber behavior is observed in hardened and fresh concrete [25]. This contributes to an increase in the thermal stresses taken without significant deformations.

The reverse trend appears in concrete with a steel-fiber reinforcement of over 1 %: the thermal stresses begin to decrease. This can be explained by the fact that while the viscosity growth rate slows with an increase in the content of fiber [26], due to the larger number of fibers per unit volume, it better restrains concrete deformations. With an increase in the concrete temperature, the change in the thermal stresses depending on the fiber content begins to have a more pronounced nonlinear nature (Fig. 3). At a temperature of 40 °C, the changes in the thermal stresses with an increase in the fiber reinforcement percentage can be described with a second-degree polynomial, while at temperatures of 55 and 70 °C they are described by a third-degree polynomial. Such nonlinearity is caused by the low growth rate of the relative deformations in concrete with a 1.5 % fiber reinforcement compared to the consistently high growth rate of

such deformations with fiber content of up to 1 %. This phenomenon is clearly observed in the temperature range from 40 to 70 °C.

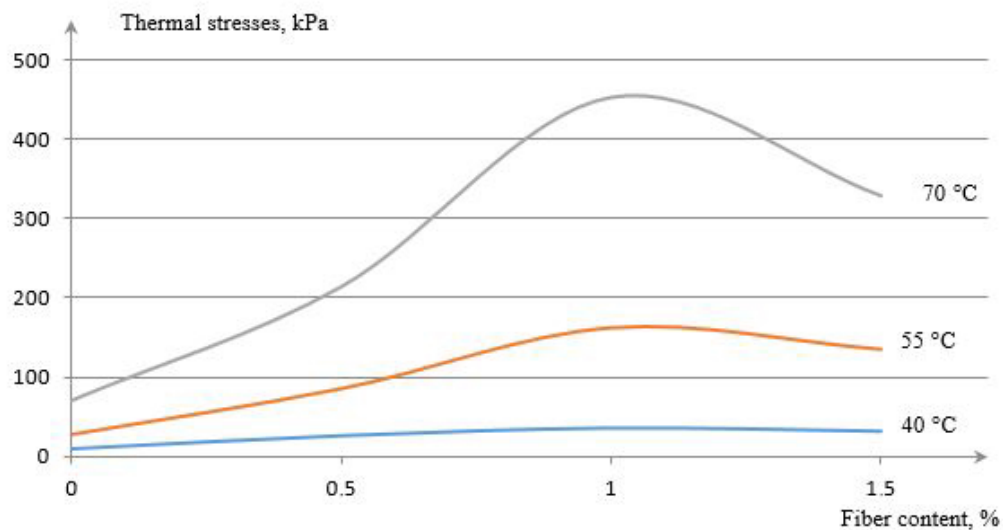


Figure 3. The change in the thermal stresses with an increase in the fiber reinforcement percentage.

This allows us to understand why zero deformations in standard concrete are retained only when it is heated from 18 to 20 °C, while in steel fiber reinforced concretes with a fiber content of 1–1.5 %, they are retained when it is heated to 30 °C. In fact, the temperature of 20 °C is the limit of the viscous capabilities of fresh concrete to move moisture from stressed capillaries to less stressed ones without the appearance of thermal stresses. 30 °C is the structural strength limit of viscoelastic concrete when thermal stresses do not arise due to the redistribution of temperature forces throughout the volume of concrete because of the use of steel fiber. Thus, at this heating rate, stresses will arise in steel fiber reinforced concrete with 1 % and 1.5 % reinforcement when it is heated by 12 °C, and in ordinary concrete by 2 °C.

4. Conclusion

1. In the viscous state of hardening concrete, thermal stresses are an order of magnitude less than in the elastic state. While at the elastic stage they can be about 2942 kPa, in the viscous state they are 71.4–453.4 kPa. Nevertheless, even such low stresses should not be ignored, since they arise during the most crucial period of the formation of a concrete structure.

2. Even during the early hardening stage, steel-fiber reinforced concrete can take 3–6 times higher thermal stresses than standard concrete of the same age. This is connected with the preservation of the concrete density during heating because the fiber restrains the separation of the components of concrete.

3. With an increase in the temperature of concrete, the change in the thermal stresses depending on the fiber content begins to have a more pronounced nonlinear nature which is preconditioned by the low growth rate of the relative deformations of steel-fiber reinforced concrete with a high reinforcement percentage at the concrete temperatures above 40 °C.

4. At the early hardening stage, thermal stresses in standard concrete arise when it is heated by 2 °C, and they arise in steel-fiber reinforced concrete with a reinforcement 1 % or more only when it is heated by 12 °C (from 18 to 30 °C), which is connected with the redistribution of temperature forces throughout the volume of concrete because of the use of fiber.

References

1. Aniskin, N.A., Nguyen, T.C. The thermal stress of roller-compacted concrete dams during construction. MATEC Web of Conferences. 2018. Vol. 196 (04059). DOI: 10.1051/mateconf/201819604059
2. Bingqi, L., Zhenhong, W., Yunhui, J., Zhenyang, Z. Temperature control and crack prevention during construction in steep slope dams and stilling basins in high-altitude areas. Advances in Mechanical Engineering. 2018. Vol. 10. Pp. 1–15. DOI: 10.1177/1687814017752480
3. Kuzmanovic, V., Savic, Lj., Mladenovic, N. Thermal-Stress Behaviour of RCC Gravity Dams. FME Transactions. 2015. 43, Pp. 30–34. DOI: 10.5937/fmet1501030K
4. Krasnovskiy, B.M. Inzhenerno-fizicheskiye osnovy metodov zimnego betonirovaniya [Engineering and physical foundations of winter concreting methods]. Moscow: Izdatel'stvo GASIS, 2004. 470 p.

5. Pikus, G.A., Lebed, A.R. Warming of Monolithic Structures in Winter. IOP Conference Series: Materials Science and Engineering. 2017. 262. Pp. 012064. DOI: 10.1088/1757-899X/262/1/012064
6. Nikonorov, V.V., Nikonorova, D.O., Pikus, G.A. Thermophysical properties of the soil massif. Magazine of Civil Engineering. 2019. 92 (8). Pp. 27–35. DOI: 10.18720/MCE.92.2
7. Utepov, Ye.B., Aniskin, A., Ibrashov, A.P., Tulebekova, A. Maturity sensors placement based on the temperature transitional boundaries. Magazine of Civil Engineering. 2019. 90 (6). Pp. 93–103. DOI: 10.18720/MCE.90.9
8. Van Lam, T., Nguyen, C.C., Bulgakov, B.I., Anh, P.N. Composition calculation and cracking estimation of concrete at early ages. Magazine of Civil Engineering. 2018. 82 (6). Pp. 136–148. DOI: 10.18720/MCE.82.13
9. Ayman El-Zohairy, Hunter Hammontree, Eddie Oh, Perry Moler. Temperature Effect on the Compressive Behavior and Constitutive Model of Plain Hardened Concrete. Materials. 2020. 13. 2801. DOI: 10.3390/ma13122801
10. Kuchin, V.N., Shilonosova, N.V. Features of peripheral heating of monolithic reinforced concrete structures. IOP Conference Series: Materials Science and Engineering. 2018. 451. Pp. 012088. DOI: 10.1088/1742-6596/451/1/012088
11. Bushmanova, A.V., Kharchenko, D.K., Semenov, K.S., Barabanshchikov, Yu.G., Korovina, V.K., Demakova, A.V. Thermal cracking resistance in massive steel-reinforced concrete structures. Magazine of Civil Engineering. 2018. No. 3. Pp. 45–53. DOI: 10.18720/MCE.79.5
12. Harrison, T.A. Formwork striking times – criteria, prediction and methods of assessment. CIRIA Report 136. 1995. pp. 71.
13. Klausen, A.E., Kanstad, T., Bjøntegaard, Ø. Hardening concrete exposed to realistic curing temperature regimes and restraint conditions: Advanced testing and design methodology. Hindawi Advances in Materials Science and Engineering. 2019. 9071034. DOI: org/10.1155/2019/9071034
14. Leshchinskiy, M.Yu. Ispytaniye betona: spravochnoye posobiye [Testing Concrete: A Reference Guide]. Moscow: Stroyizdat, 1980. 360 p. [Online]. System requirements: DjVu Reader. URL: <http://www.zimbeton.ru/info/124.djvu> (reference date: 05.03.2021).
15. Chuan-Qing, Fu, Qin-yong, Ma, Xian-yu, Jin, A.A. Shah, Ye-Tian. Fracture property of steel fiber reinforced concrete at early age. Computers and Concrete. 2014. Vol. 13, No. 1. Pp. 31–47. DOI: 10.12989/cac.2014.13.1.031
16. Nguyen, C.T., Aniskin, N.A. Temperature regime during the construction massive concrete with pipe cooling. Magazine of Civil Engineering. 2019. 89 (5). Pp. 156–166. DOI: 10.18720/MCE.89.13
17. Golovnev, S.G. Tekhnologiya zimnego betonirovaniya. Optimizatsiya parametrov i vybor metodov [The winter concreting technology. The parameters optimization and choice of ways]. Chelyabinsk: SUSU, 1999. 156 p.
18. Malinina, L.A. Teplovlazhnostnaya obrabotka tyazhlogo betona [Heat and humidity treatment of heavy concrete]. Moscow: Stroyizdat, 1977. 159 p. [Online]. System requirements: Adobe Acrobat Reader. URL: <http://www.zimbeton.ru/info/122.pdf> (reference date: 05.03.2021).
19. Pikus, G.A. Steel fiber concrete mixture workability. Procedia Engineering. 2016. 150. Pp. 2119–2123. DOI: 10.1016/j.proeng.2016.07.250
20. Krasnovskiy, B.M. Dinamika termonapryazhennogo sostoyaniya konstruktsiy pri zimnem betonirovanii [Dynamics of the thermally stressed state of structures during winter concreting] Beton i zhelezobeton. 1986. 12. Pp. 18–20. [Online]. System requirements: AdobeAcrobatReader. URL: https://www.booksite.ru/beton/1986/1986_12.pdf (reference date: 05.03.2021).
21. Russian State Standard GOST 10181.1-81. Concrete mixtures. Test methods for determination of workability. Moscow. 1982. 16 p. [Online]. System requirements: Adobe Acrobat Reader. URL: <http://www.zimbeton.ru/info/126.pdf> (reference date: 05.03.2021).
22. Kunnos, G.Ya. Vibratsionnaya tekhnologiya betona [Vibration concrete technology]. Leningrad: Stroyizdat, 1967. 168 p. [Online]. System requirements: Adobe Acrobat Reader. URL: <http://www.zimbeton.ru/info/123.pdf> (reference date: 05.03.2021).
23. SP 52-104-2006*. Steel fiber reinforced concrete structures. Moscow. 2010. 62 p.
24. Figmig, R., Kovac, M. The influence of aggregate gradation on the fresh and hardened concrete properties. IOP Conf. Ser.: Mater. Sci. Eng. 2019. 566 012007. DOI: 10.1088/1757-899X/566/1/012007
25. Pikus, G.A., Manzhosov, I.V. Pressure of Fiber Reinforced Concrete Mixtures on Vertical Formwork Panels. Procedia Engineering. 2017. 206. Pp. 836–841. DOI: 10.1016/j.proeng.2017.10.560
26. Evseev, B.A., Platunov, B.I. Reologicheskiye svoystva stalefibrobetona [Rheological properties of SFRC]. Effektivnaya tekhnologiya betonnykh rabot v usloviyakh vozdeystviya okruzhayushchey sredy: Tematicheskiy sbornik nauchnykh trudov [An effective technology of concreting in the environmental impact conditions: A subject collection of research papers]. Chelyabinsk: ChPI, 1986. Pp. 39–41. [Online]. System requirements: AdobeAcrobatReader. URL: <http://www.zimbeton.ru/info/125.pdf> (reference date: 05.03.2021).

Information about authors:

Grigorii Pikus,

PhD of Technical Science

ORCID: <https://orcid.org/0000-0002-4148-2515>

E-mail: pikusga@susu.ru

Anna Lebed,

ORCID: <https://orcid.org/0000-0003-1936-8238>

E-mail: lebedar@susu.ru

Anastasia Bondar,

ORCID: <https://orcid.org/0000-0002-4942-0829>

E-mail: bondaraa@susu.ru



Research article

UDC 624

DOI: 10.34910/MCE.113.5



Impact of pond ash as fine aggregate on mechanical and microstructural properties of geopolymer concrete

V. Vidyadhara^a , B. Saurabh^b, R.V. Ranganath^a 

^a BMS College of Engineering, Bangaluru, Karnataka, India

^b KRIDL, Gulbarga, Karnataka, India

✉ vidyadharav@bmsce.ac.in

Keywords: concrete, geopolymer, pond ash, aggregate, microstructure, mechanical properties

Abstract. In this research, geopolymer concrete (GPC) was produced using pond ash (PA) as a fine aggregate replacement to river sand (RS). The focus of the study is to investigate the effect of PA as fine aggregate on the mechanical and microstructural properties of GPC. The present study detailed characterization of PA which includes particle size distribution, X-ray diffraction (XRD) analysis, scanning electron microscopy (SEM) analysis, energy dispersive X-ray (EDAX) studies, and chemical analysis including reactive silica (R-SiO₂). PA replaced RS at percentages of 0, 20, 40, 60, 80 and 100% in GPC. Properties like compressive strength, flexural strength, split tensile strength and water permeability of GPC were studied. It was found that compressive strength, flexural strength and split tensile strength of GPC with 80% PA as fine aggregate are, respectively, 26%, 29% and 31% greater compared to concrete with RS as aggregate. The inclusion of reactive sand-like PA increased the R-SiO₂/Na₂O ratio from 3.2 to 5.4 in GPC mixes with up to 80% replacement and contributed to higher compressive strength. SEM studies, R-SiO₂, EDAX and Fourier-transform infrared spectroscopy (FTIR) analysis of GPC confirmed the participation of PA particles in polymerization thereby contributing to higher strength. Utilization of pond ash as fine aggregate provides a valuable addition to GPC in aspects of strength and economics as well as alleviates the environmental problems caused by coal ash ponding.

Citation: Vidyadhara, V., Saurabh, B., Ranganath, R.V. Impact of pond ash as fine aggregate on mechanical and microstructural properties of geopolymer concrete. Magazine of Civil Engineering. 2022. 113(5). Article No. 11305. DOI: 10.34910/MCE.113.5

1. Introduction

Coal ash (CA) is a by-product from thermal power plant, which includes fly ash (FA) collected through electrostatic precipitator and bottom ash (BA) collected from bottom of the boiler furnace [1]. In most of the thermal power plants, the unused FA and BA are conveyed to landfills by means of water and is termed as pond ash (PA) [2]. Disposal of CA into the ash pond results in environmental problems like pollution of air, soil and water [3]. Hence, it is inevitable to find ways to utilize the ponded ash especially in construction sector to alleviate the previously mentioned environmental problems.

PA encompasses finer reactive particles of FA and coarser less reactive or non-reactive particles of BA [4]. Burnt clay bricks produced by replacing clay with PA have been studied earlier [5]. Sintered aggregates with high water absorption feature can be manufactured by using PA [6]. Presence of coarser non-reactive particles in PA, prompted researchers to use it as replacement to aggregates in cement concrete and higher water demand to achieve required workability was observed in such concretes [7]. PA has been tried as replacement to cement in cement mortar [2] and as raw material in the manufacture of cement by black meal process [8].

Geopolymer technology is emerging as one of the alternative binder to cement when it comes to sustainability and durability aspects [9]. In geopolymer concrete (GPC); an aluminosilicates material is activated by alkaline solution forming a paste which binds coarse and fine aggregate with other unreacted material. The fresh and hardened properties of GPC depend on proportioning and properties of alkaline solution and base material [10]. In earlier studies, coal ashes are used as precursor [11, 12] and as aggregates [13, 14] in making geopolymer composites. In production of geopolymer mortar, PA is used as base material along with ultra-fine slag and the resultant mortar exhibited good durability characteristics [3]. Earlier researchers have tried using PA as fine aggregate and replacement to cement in cement concrete and as base material in geopolymer mortar. PA as fine aggregate in GPC needs to be explored.

During the year, 2018-19, in India 217 million tons (MT) of CA has been generated from 195 thermal power plants. In which 22 % of CA has been disposed as PA [15]. Disposal of CA into the ash ponds results in degrading the fertility of soil and quality of water [3]. Further aggregates which contributes 70 % of the volume of concrete are derived from natural queries and river sand [16]. Increase in the demand of concrete in future, is likely to exploit the non-renewable sources by taking raw materials for cement manufacturing and aggregate production. Geopolymer composites made up of using industrial by-products as both base material and as aggregates is one of the alternative solutions for previously mentioned problems. Hence, the present study focusses on making of geopolymer concrete using FA and ground granulated blast furnace slag (GGBS) as base material and PA as replacement to river sand (RS) at 0,20,40,60 and 100 percentages.

The objective of the present study is to assess the influence of PA as fine aggregate replacement to RS on mechanical properties of GPC. In addition, using scanning electron microscope (SEM) studies, energy dispersive X- ray analysis (EDAX) and Fourier transform infrared spectroscopy (FTIR) analysis microstructure of GPC made up of PA is evaluated.

2. Methods

2.1. Materials

The raw materials used in this study were FA, GGBS, PA, coarse aggregate and RS. GGBS was purchased from local manufacturers, Coarse aggregate and RS from local suppliers. FA and PA were procured from Udipi thermal power plant, Karnataka, India. Physical properties of materials are shown in Table 1, Specific surface area of GGBS is 400 m²/Kg and is higher than cement and FA [17], further PA has exhibited greater moisture absorption compared to RS and coarse aggregate. In PA, percentage of particles finer than 600 μ are exceeding the limit prescribed in IS 383-2016 for zone II sand [18] which can be noticed from Fig. 1. Particle size distribution curves in Fig. 2 reveal that FA and GGBS exhibit wide range of particle sizes compared to PA. Chemical composition and Reactive silica (R-SiO₂) of FA, PA and GGBS were determined using gravimetric analysis and is presented in Table 2. It confirms that FA comes under Class F Pozzolan as per ASTM C618 [19] and PA has abundant silica and aluminium oxide. Even though GGBS has less Total silica (T-SiO₂) compared to FA and PA, R-SiO₂ is more in GGBS than other two. Ponding action and presence of BA yielded less R-SiO₂ values for PA than FA as observed from Table 2. X-ray diffraction (XRD) curves shown in Fig. 3 supports R-SiO₂ values, absence of crystalline peaks in GGBS confirms presence of greater reactive or amorphous phases. Hump formation in XRD curve between 20° and 30°, is indication of presence of amorphous phase and is better for FA than PA. Elemental composition of PA (Fig. 4) obtained by EDAX revealed that PA is rich in silica and alumina, same result was observed in the earlier studies [20].

SEM images of cement, GGBS, FA and PA are shown in Fig. 5. Cement particles are angular in shape, while particles of GGBS are in anomalous shape with clear edges and angles [21]. FA particles are spherical [22] and PA composed of both spherical FA particles and agglomerated porous coarser BA particles same is depicted in Fig. 5.

Sodium silicate (Na₂SiO₃) and sodium hydroxide (NaOH) were procured from local supplier. Pellets of NaOH with 98 % purity were used in this research. Chemical composition of silicate was 11 % of Na₂O, 31.25 % of SiO₂, 13.08 % of R-SiO₂ and 56.5 % of H₂O.

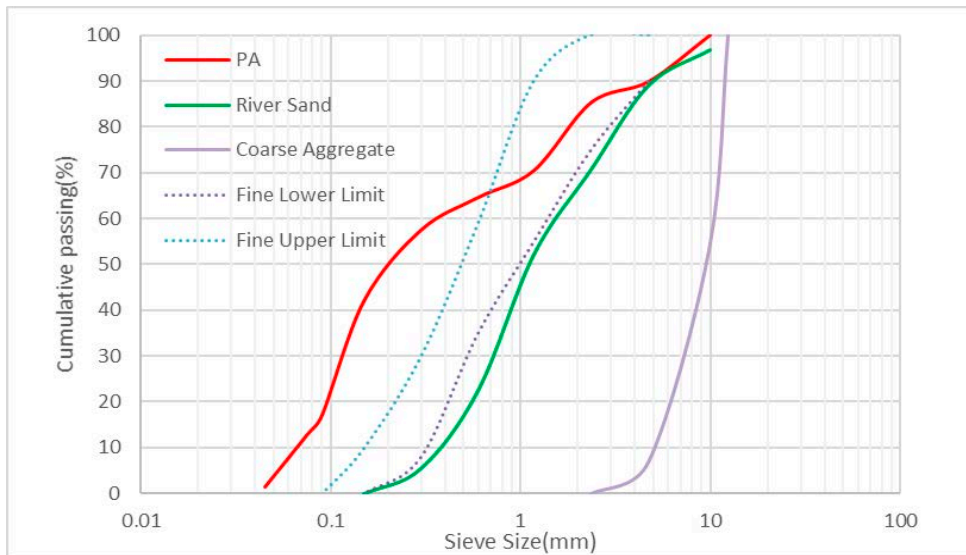


Figure 1. Grain size distributions of aggregates.

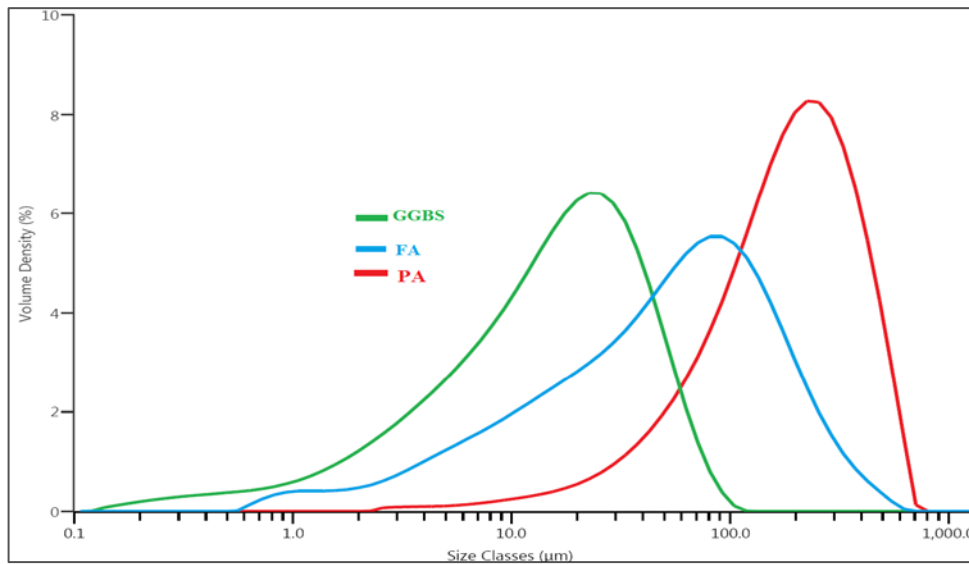


Figure 2. Particle size distribution curves.

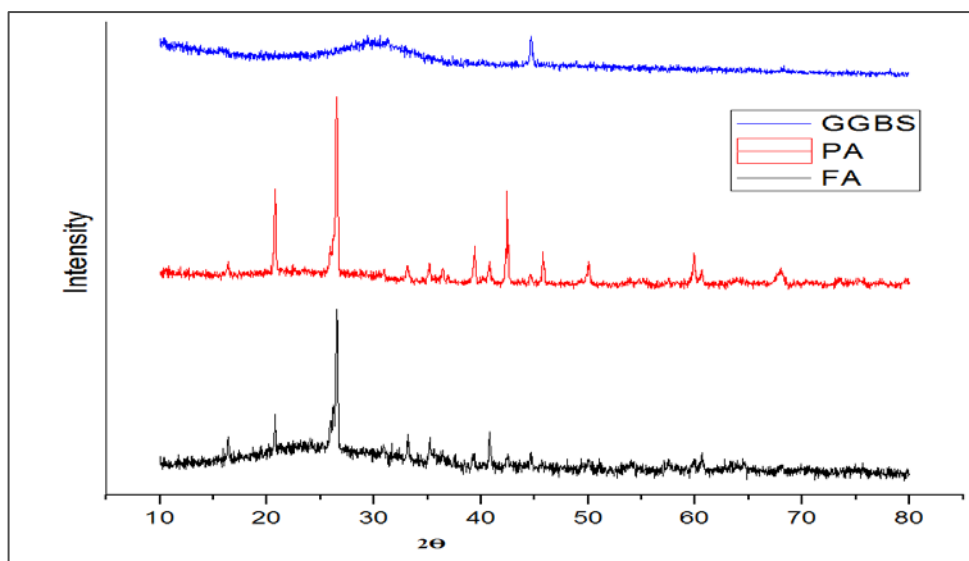


Figure 3. XRD curves of GGBS, PA and FA.

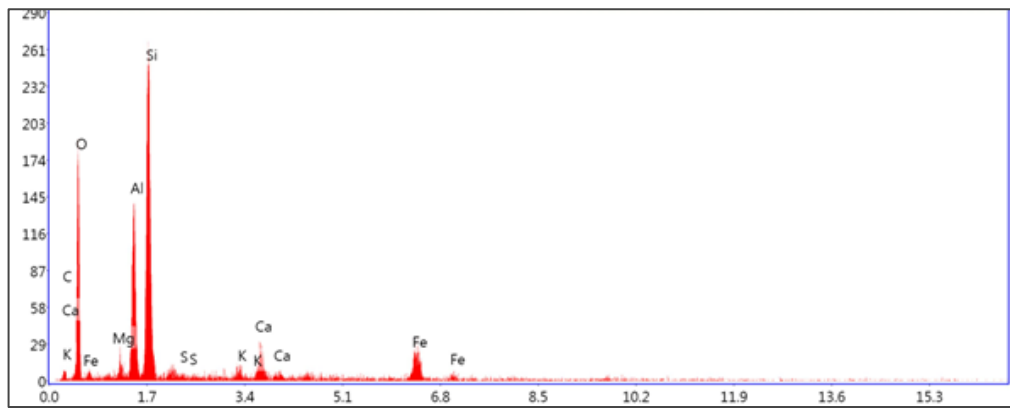


Figure 4. Micrograph of Pond Ash obtained by EDAX analysis.

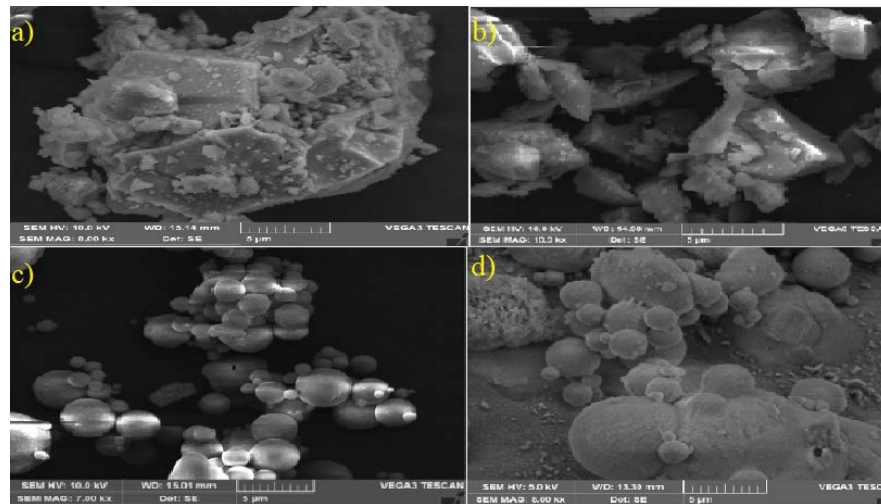


Figure 5. SEM images of a) Cement b) GGBS c) FA d) PA.

Table 1. Physical properties of materials

Properties	PA	River sand	Coarse Aggregate	FA	GGBS
Residue on 45 μ (%)	–	–	–	32	10
Blaine surface area (m ² /Kg)	–	–	–	386	400
Specific gravity	2.45	2.50	2.65	2.10	2.90
Fineness modulus	4.75	2.80	7.80	–	–
Moisture absorption (%)	5.2	1.5	0.1	–	–

Table 2. Chemical composition of GGBS, FA and PA

Oxides (%)	GGBS	FA	PA
LOI	1.41	0.57	5.30
T-SiO ₂	33.80	56.16	58.38
R-SiO ₂	32.80	29.71	20.60
Al ₂ O ₃	17.36	20.16	25.34
Fe ₂ O ₃	1.36	10.34	5.68
CaO	38.30	7.20	2.69
MgO	4.90	2.26	0.98
SO ₃	0.02	0.41	0.06
Others	2.85	2.90	1.57

2.2. Mix Proportions

Geopolymer concrete mix proportioning was carried out by fixing total water content and density of concrete to 202 Kg/m³ and 2400 Kg/m³ respectively. Here, total water content includes water present in sodium silicate and sodium hydroxide solution. Mix proportions for pond ash geopolymer concrete represented in Table 3. RS, PA and coarse aggregates were mixed with FA and GGBS for four minutes in dry state. Later, alkaline solution was added and mixing was continued for five more minutes. Concrete was poured in moulds for testing with proper compaction carried out using vibrating table. All the test samples were cured in ambient temperature at 27 °C till the day of testing.

For concrete casting, alkaline solution was prepared one day prior to casting by mixing 10M sodium hydroxide and sodium silicate solution in the ratio 1: 2.5 respectively.

Table 3. Mix proportions per m³ of geopolymer concrete

Mixes	Replacement of River Sand	Fly ash (Kg)	GGBS (Kg)	River Sand (Kg)	Pond ash (Kg)	Coarse aggregate (Kg)	NaOH (Kg)	Na ₂ SiO ₃ (Kg)
PA0	0			660	0			
PA20	20%			528	132			
PA40	40%			396	264			
PA60	60%	330	83	264	396	990	96	241
PA80	80%			132	528			
PA100	100%			0	660			

2.3. Testing

Workability of GPC was measured using slump cone test as per IS : 1199 – 1959 [23]. Compressive and flexural strength of GPC were tested following the guidelines of IS : 516 – 1959 [24]. IS 5816:1989 [25] specifications were followed in finding the splitting tensile strength of GPC. Cylinder of size 200 mm height and diameter of 100 mm were casted and tensile strength was found out by splitting cylinder at loading rate of 1.2–2.4 MPa/min.

Water permeability of GPC was found out by measuring the water ingress into the cylinder specimens under 5 bar pressure applied for a period of 3 days as mentioned in DIN 1048 [26]. After 3 days, penetration of water is measured by splitting the cylinder along long side using compression machine. Test set up for water permeability shown in Fig. 6.



Figure 6. Test setup for Water permeability.

3. Results and Discussion

3.1. Fresh property

Increase in PA replacement to RS, resulted in decreasing of workability of GPC which can be noticed from Table 4. Since PA contains porous bottom ash particles, these porous bottom ash particles absorb water and cause water deficiency for lubrication of particles [27–29]. In addition, as depicted in Fig. 1

particles finer than 600 μ in PA are considerably greater in quantity than in RS. Presence of these finer particles in PA demands extra water for wetting their outer surface. Thus, increase in PA content in GPC drops the workability. Further, handling of GPC became difficult at 80 % and 100 % replacement as it turns into more cohesive. In order to restore the workability, naphthalene based superplasticizer (SP) i.e. Conplast SP 30 was used in PA 80 and PA 100 mixes. As a result of this slump increased from 200 to 250 mm and 50 to 185 mm in 80 % and 100 % replacement mixes respectively (Fig. 7).

3.2. Compressive strength of GPC

Compressive strength results of GPC at 3, 7 and 28 day curing for different PA content are depicted in Fig. 8. It can be noticed that as the RS replacement by PA increases, the compressive strength increases till 80 % replacement. Meanwhile, 4 to 5 MPa reduction in strength was noticed for 100 % replacement when compared with 80 % replacement. However, at all curing periods compressive strength of pond ash GPC has shown greater strength irrespective of replacement level compared to control mix i.e. 100 % RS geopolymer concrete. 80 % replacement of river sand by PA contributed for 26 % increase in strength compared to control mix. In addition to FA and GGBS, it appears that PA aggregates also participated in polymerization by leaching out silica and alumina from it. Y. Zaetang et al., have reported similar phenomena while using bottom ash as aggregate in geopolymers [13].

3.3. Flexural strength, splitting tensile strength and water permeability of GPC

Flexural strength, splitting tensile strength and water permeability tests were carried out for control and 100 % PA mixes, respective results are shown in Table 5. 100 % PA mixes exhibited greater flexural and splitting tensile strength at 28-day curing period compared to control mix. PA particles participation in polymerization reaction contributed for 29 % and 31 % improvement in flexural and splitting tensile strength respectively.

Water penetration depth in 100 % PA mix specimen was 12 mm, whereas in control mix it was observed as 20 mm. Water permeability test clearly indicates 100 % PA mix exhibited greater resistance to water penetration than control mix.



Figure 7. Slump in 100 % pond ash replacement a) without SP and b) with SP.

Table 4. Flow / slump of geopolymer concrete

Pond ash content	Slump/Flow values (mm)	T ₅₀₀ (Second)
0 %	690	3
20 %	650	4
40 %	590	49
60 %	545	62
80 %	200	-
80 % with SP	250	-
100 %	50	-
100 % with SP	185	-

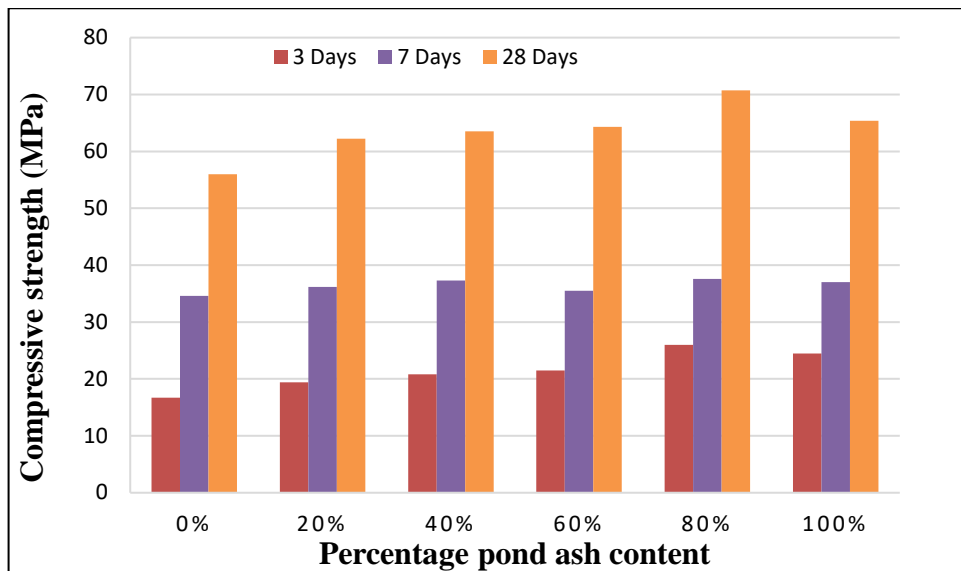


Figure 8. Compressive strength of GPC.

Table 5. Results of flexural strength, splitting tensile strength and water permeability

Pond Ash Content	28 days Flexural strength (MPa)	28 days Tensile strength (MPa)	Maximum water depth (mm)
0%	3.1	2.6	20
100%	4.0	3.4	12

3.4. Effect of R-SiO₂ on strength of GPC

R-SiO₂ in an aluminosilicates material is the non-crystalline, a fraction of total silica which have the ability to react with lime yielding increased contents of C-S-H gel [30]. R-SiO₂ in fly ash is the critical factor in strength contribution [31, 32]. R-SiO₂ values of GPC mixes used in this study are shown in Table 6. As RS which is inert when replaced by PA, the total R-SiO₂ content in GPC increases due to the contribution from PA as it contains about 20 % of R-SiO₂. Table 6 also shows ratio of R-SiO₂/Na₂O for different mixes used in the study. As can be seen increase in the ratio increases compressive strength of concrete and same can be noticed from Fig. 9. It is further observed that increase of ratio from 3.2 to 4.3 and then from 4.3 to 5.4 can yield an increase in strength of about total 14 MPa which is significant. Such an increase in strength can also be obtained by increasing either FA or GGBS in the binder. However, such an attempt would have cost implications. Earlier study on geopolymerization revealed, availability of more R-SiO₂ improves the geopolymerization reaction [33] and same results are observed in present study.

Table 6. R-SiO₂ values of GPC mixes

Mixes	R-SiO ₂ in Kg				Total R-SiO ₂ (Kg)	R-SiO ₂ /Na ₂ O	Compressive strength 28 days
	Fly ash	GGBS	Pond ash	Na ₂ SiO ₃			
PA0			0		157	3.2	56.0
PA20			27		184	3.8	62.2
PA40	98	27	54	32	211	4.3	63.5
PA60			82		239	4.9	64.3
PA80			109		266	5.4	70.7
PA100			133		290	5.9	65.4

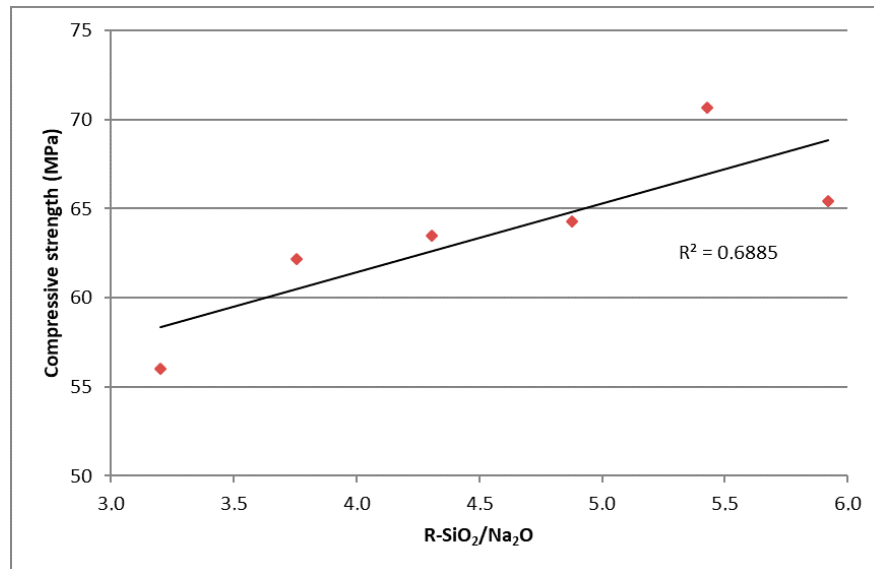


Figure 9. Effect of reactive silica on compressive strength of GPC.

3.5. Microstructure analysis of GPC

Earlier studies on microstructure analysis of fly ash based geopolymers revealed that, polymerization involves three stages a) chemical attack on fly ash surfaces and gradual development to form holes b) bi-directional alkaline attack in case of larger ash particles as sometimes their holes are filled with smaller particles c) product formation both inside and outside the spherical surface till particle of ash is completely consumed [34]. SEM images shown in Fig. 10 indicates that both FA and some portion of PA involved in polymerization and product formation both inside and outside the spherical surfaces as observed in studies done by Hassan. A et al. [34]. It is also observed that dense matrix in case of PA80 and PA100 samples along with PA and FA particles embedded in it.

Oxide compositions of GPC tested samples obtained through EDAX analysis are presented in Table 7. In geopolymerization $\text{SiO}_2/\text{Na}_2\text{O}$ and $\text{Na}_2\text{O}/\text{Al}_2\text{O}_3$ ratio indicates the availability of sodium ions for activation and dissolution of aluminosilicates [35]. In present study maximum strength is achieved for $\text{SiO}_2/\text{Na}_2\text{O}$ value 5.85 and $\text{Na}_2\text{O}/\text{Al}_2\text{O}_3$ value 0.78 which is corresponding to 80 % PA GPC. It is also noticed that $\text{SiO}_2/\text{Na}_2\text{O}$ value increased with introduction of PA in concrete indicating the dissolution of more aluminosilicates.

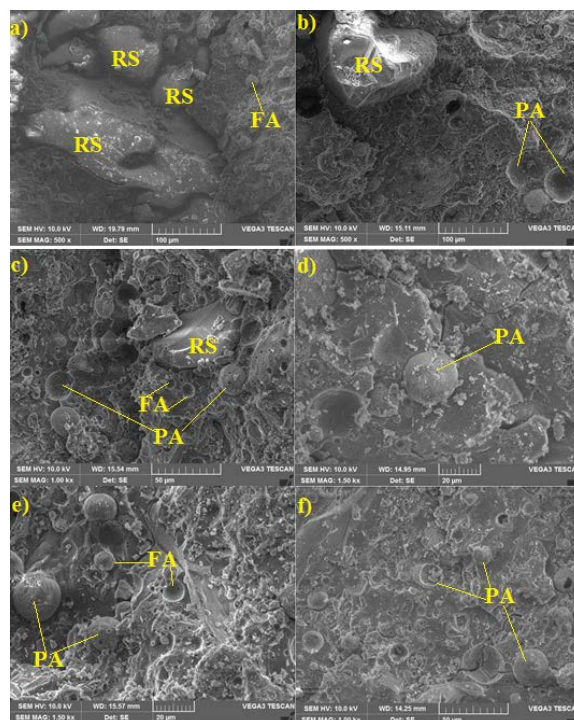
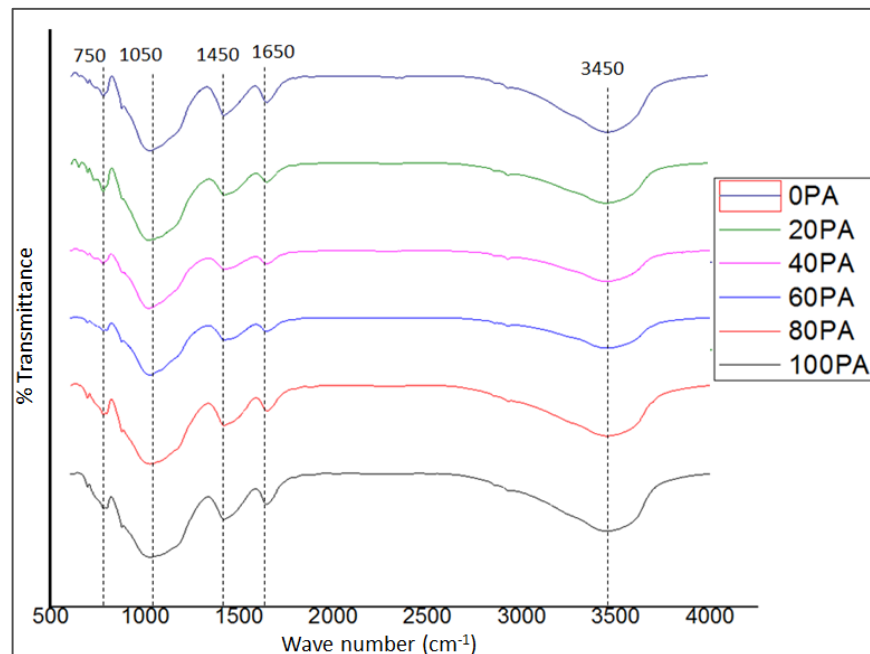


Figure 10: SEM images of 28 days tested samples
a) PA0 b) PA20 c) PA40 d) PA60 e) PA80 f) PA100.

Table 7. Oxide composition of GPC tested samples obtained by EDAX

Compound	PA0	PA20	PA40	PA60	PA80	PA100
Na ₂ O	12.64	11.65	11.07	10.68	9.55	10.03
MgO	3.55	3.33	3.81	3.83	3.20	3.20
Al ₂ O ₃	10.79	10.78	12.96	11.36	12.13	13.65
SiO ₂	58.82	59.26	57.9	58.17	55.96	59.47
K ₂ O	1.46	0.92	1.51	1.09	1.35	0.85
CaO	10.3	11.36	9.80	12.07	14.65	9.91
TiO ₂	1.38	1.07	1.40	1.58	1.53	1.24
Fe ₂ O ₃	1.07	1.62	1.55	1.23	1.63	1.66
SiO ₂ /Na ₂ O	4.65	5.08	5.23	5.44	5.85	5.92
Na ₂ O/Al ₂ O ₃	1.17	1.08	0.85	0.94	0.78	0.73
CaO/SiO ₂	0.17	0.19	0.16	0.2	0.26	0.16
SiO ₂ /Al ₂ O ₃	5.45	5.49	4.46	5.12	4.61	4.35

**Figure 11. FTIR graphs of GPC.**

FTIR analysis on GPC was conducted and respective graphs are presented in Fig. 11. The absorption bands corresponding to wave numbers 3450 cm⁻¹ and 1650 cm⁻¹ are indicative of vibrations of O-H and H-O-H bonds in water molecules [36]. The C-O asymmetric stretching is denoted by vibration bands located roughly around 1450 cm⁻¹ [37]. Spectra bands situated approximately around wavenumber 750 cm⁻¹ represents crystalline phases of quartz [36]. The Si-O-T (T is Si or Al) asymmetric vibration is indicated by bands of FTIR spectrum with wave numbers ranging around 1050 cm⁻¹ and degree of geopolymerization is determined from this bond [38]. Higher absorption at 1050 cm⁻¹ records high rate of geopolymerization [36] and in Fig. 11 it can be noticed that GPC mixes with PA have shown greater absorption at 1050 cm⁻¹ than GPC with RS. The absorption is significant beyond 60% replacement indicating the contribution of PA in polymerisation reaction.

3.6. Cost analysis of pond ash geopolymer concrete

Cost analysis of concrete clearly indicates; apart from alkaline solution fine aggregate play a major role in fixing the cost of concrete. Keeping quantity of solution constant, thereby replacing the RS with PA reduces cost of concrete per cubic metre to greater extent. As observed from Table 8, the cost of control mix made up of RS was around rupees (Rs) 9000/- and it got reduced to Rs 7000/- as PA replaces RS totally. It is conclusive that PA as fine aggregate in GPC can outperform RS in both cost and strength aspects.

Table 8. Cost of Pond Ash geopolymer blocks and concrete

Material	Unit cost (Rs/Kg)	0% PA		100% PA	
		Kg/m ³	Total Cost (Rs)	Kg/m ³	Total Cost (Rs)
Fly ash	2.5	330	825	330	825
GGBFS	2.5	83	206	83	206
Pond ash	1.0	–	–	660	660
River Sand	4.0	660	2640	–	–
Coarse Aggregate	1.0	990	990	990	990
Alkaline Solution (NaOH + Na ₂ SiO ₃)	15.0	268	4022	268	4022
Water	1.0	165	165	165	165
Total			8,848/-		6,868/-

4. Conclusion

PA was replaced to RS at different percentages in making geopolymer concrete and its mechanical properties were assessed. Based on the aforementioned studies following conclusions are made

1. Replacement of river sand by pond ash resulted in stiffening of concrete, especially at 80 and 100 % replacement. However, it can be restored by using suitable super plasticizers.

2. In addition to Fly Ash and GGBS, finer reactive pond ash particles also actively participated in geopolymerization process by leaching out silica and alumina. Thus compressive strength, flexural strength and split tensile strength of GPC with 80 % pond ash as fine aggregate are 26 %, 29 % and 31 % greater compared to concrete with river sand as aggregate. Pond Ash GPC unveiled greater resistance to water permeability than GPC made up of river sand.

3. Inclusion of reactive sand such as PA increases the ratio R-SiO₂/Na₂O from 3.2 to 5.4 in GPC mixes with up to 80 % replacement and contributes for higher compressive strength up to 14 MPa. SEM studies on GPC revealed that both FA and PA involved in reaction product formation resulting in dense matrix. Ratio SiO₂/Na₂O which is indicative of dissolution of aluminosilicates in GPC is higher i.e. 5.85 for GPC with 80 % PA as evidenced from EDAX results. FTIR curves confirmed participation of reactive silica of PA in geopolymerization by showing significant absorption rates.

Utilization of pond ash as fine aggregate provides value addition to GPC in aspects of strength and economics. In addition, environmental problems caused due to the land filling of pond ash will be alleviated. Keeping pond ash participation in polymerization process, research on GPC with pond ash as precursor needs to be explored.

References

- Singh, N., Bhardwaj, A. Reviewing the role of coal bottom ash as an alternative of cement. *Construction and Building Materials*. 2020. 233. Pp. 117276. DOI: 10.1016/j.conbuildmat.2019.117276.
- Sofi, A., Phanikumar, B.R. An experimental investigation on flexural behaviour of fibre-reinforced pond ash-modified concrete. *Ain Shams Engineering Journal*. 2015. 6 (4). Pp. 1133–1142. DOI: 10.1016/j.asej.2015.03.008
- Saxena, S.K., Kumar, M., Singh, N.B., Kumar, M., Singh, N.B. Effect of Alccofine powder on the properties of Pond fly ash based geopolymer mortar under different conditions. *Environmental Technology & Innovation*. 2018.
- Ranganath, R.V., Bhattacharjee, B., Krishnamoorthy, S. Influence of size fraction of ponded ash on its pozzolanic activity. *Cement and Concrete Research*. 1998. 28 (5). Pp. 749–761. DOI: 10.1016/S0008-8846(98)00036-2
- Sonawane, P.G., Dwivedi, A.K., Ash, P. Technical Properties of Pond Ash – Clay Fired Bricks – An Experimental Study. *American Journal of Engineering Research (AJER)*. 2013. 2(9). Pp. 110–117.
- Vasugi, V., Ramamurthy, K. Identification of admixture for pelletization and strength enhancement of sintered coal pond ash aggregate through statistically designed experiments. *Materials and Design*. 2014. 60. Pp. 563–575. DOI: 10.1016/j.matdes.2014.04.023.
- Ganesh, B., Bai, H.S., Nagendra, R., Narendra, B.K. Characterization of Pond Ash as Fine Aggregate in Concrete. *International Conference on Advances in Architecture and Civil Engineering*. 2012. 1 (June). Pp. 119–125.
- Singh, N.B., Bhattacharjee, K.N., Shukla, A.K. Pond ash – a potential reactive raw material in the black meal process of cement manufactijre by vertical shaft kiln (VSK) technology. *Cement and Concrete Research*. 1995. 25(3).
- Rangan, B.V. Fly Ash-Based Geopolymer Concrete. *International Workshop on Geopolymer Cement and Concrete*, Allied Publishers Private Limited, Mumbai, India, December 2010. 2014. (December 2010).

10. Lloyd, N.A., Rangan, B.V. Geopolymer Concrete with Fly Ash. Second International Conference on Sustainable Construction Materials and Technologies. 2010. 7.
11. Ul-Haq, E., Kunjalukkal Padmanabhan, S., Licciulli, A. Synthesis and characteristics of fly ash and bottom ash based geopolymers-A comparative study. *Ceramics International*. 2014. 40 (2). Pp. 2965–2971. DOI: 10.1016/j.ceramint.2013.10.012.
12. Chindaprasirt, P., Jaturapitakkul, C., Chalee, W., Rattanasak, U. Comparative study on the characteristics of fly ash and bottom ash geopolymers. *Waste Management*. 2009. 29 (2). Pp. 539–543. DOI: 10.1016/j.wasman.2008.06.023
13. Zaetang, Y., Wongsas, A., Sata, V., Chindaprasirt, P. Use of coal ash as geopolymer binder and coarse aggregate in pervious concrete. *Construction and Building Materials*. 2015. 96. Pp. 289–295. DOI: 10.1016/j.conbuildmat.2015.08.076.
14. Wongsas, A., Zaetang, Y., Sata, V., Chindaprasirt, P. Properties of lightweight fly ash geopolymer concrete containing bottom ash as aggregates FA. *Construction and Building Materials*. 2016. 111. Pp. 637–643. DOI: 10.1016/j.conbuildmat.2016.02.135
15. CEA (Central Electricity Authority) India. Report on fly ash generation at coal/lignite based thermal power stations and its utilization in the country for the year 2018-19.
16. Vardhan, K., Siddique, R., Goyal, S. Influence of marble waste as partial replacement of fine aggregates on strength and drying shrinkage of concrete. *Construction and Building Materials*. 2019. 228. Pp. 116730. DOI: 10.1016/j.conbuildmat.2019.116730
17. Yang, K.H., Hwang, Y.H., Lee, Y., Mun, J.H. Feasibility test and evaluation models to develop sustainable insulation concrete using foam and bottom ash aggregates. *Construction and Building Materials*. 2019. 225. Pp. 620–632. DOI: 10.1016/j.conbuildmat.2019.07.130.
18. IS383-2016. Coarse and fine aggregate for concrete. Indian Standard Code. 2016. Third edit (January). Pp. 21.
19. ASTM C618-17a. Standard specification for coal fly ash and raw or calcined natural pozzolan for use in concrete. Annual Book of ASTM Standards. 2017.
20. Vidyadhara, V., Gowda, T.S., Ranganath, R. V. An Investigation on Pozzolanicity of Mechanically Activated Pond Ash. IOP Conference Series: Materials Science and Engineering. 2020. 936 (1). DOI: 10.1088/1757-899X/936/1/012004
21. Wan, H., Shui, Z., Lin, Z. Analysis of geometric characteristics of GGBS particles and their influences on cement properties. *Cement and Concrete Research*. 2004. 34 (1). Pp. 133–137. DOI: 10.1016/S0008-8846(03)00252-7
22. Rajib Kumar Majhi, A.N. Properties of Concrete Incorporating Coal Fly Ash and Coal. *Journal of The Institution of Engineers (India): Series A*. 2019. DOI: 10.1007/s40030-019-00374-y
23. BIS:1199. Indian Standard Methods of sampling and analysis of concrete. Bureau of Indian Standards, New Delhi. 2004. DOI: 10.2174/187221013804484881
24. BUREAU OF INDIAN STANDARDS. IS 516 -1959: Method of Tests for Strength of Concrete. IS 516 -1959: Method of Tests for Strength of Concrete. 2004.
25. BIS:5816. Indian Standard Splitting tensile strength of concrete- method of test. 1999.
26. DIN-1048. German Standard for determination of Permeability of Concrete.-DIN-1048.PDF2016.
27. Jaturapitakkul, C., Cheerarat, R. Development of bottom ash as pozzolanic material. *Journal of Materials in Civil Engineering*. 2003. 15(1). Pp. 48–53. DOI: 10.1061/(ASCE)0899-1561(2003)15:1(48)
28. Jun Ng, H., Bakri Abdullah, M.M. Al, Tan, S.J., Sandu, A.V., Hussin, K. Characterisation and understanding of Portland cement mortar with different sizes of bottom ash. *Advances in Cement Research*. 2018. 30 (2). Pp. 66–74. DOI: 10.1680/jadcr.17.00076
29. Sathonsaowaphak, A., Chindaprasirt, P., Pimraksa, K. Workability and strength of lignite bottom ash geopolymer mortar. *Journal of Hazardous Materials*. 2009. 168 (1). Pp. 44–50. DOI: 10.1016/j.jhazmat.2009.01.120
30. Antiohos, S.K., Tsimas, S. Reactive Silica of Fly Ash As an Indicator for the Mechanical Performance of Blended Cements. *Measuring, Monitoring and Modeling Concrete Properties*. 2007. Pp. 403–409. DOI: 10.1007/978-1-4020-5104-3_49
31. Antiohos, S., Tsimas, S. Investigating the role of reactive silica in the hydration mechanisms of high-calcium fly ash/cement systems. *Cement and Concrete Composites*. 2005. 27 (2). Pp. 171–181. DOI: 10.1016/j.cemconcomp.2004.02.004
32. Sivapullaiah, P.V., Prashanth, J.P., Sridharan, A., Narayana, B.V. Reactive silica and strength of fly ashes. *Geotechnical and Geological Engineering*. 1998. 16 (3). Pp. 239–250. DOI: 10.1023/A:1008889326269
33. Dinesh, H.T., Shivakumar, M., Dharmaprakash, M.S., Ranganath, R.V. Influence of reactive SiO₂ and Al₂O₃ on mechanical and durability properties of geopolymers. *Asian Journal of Civil Engineering*. 2019. 20 (8). Pp. 1203–1215. DOI: 10.1007/s42107-019-00167-5
34. Hassan, A., Arif, M., Shariq, M. Use of geopolymer concrete for a cleaner and sustainable environment – A review of mechanical properties and microstructure. *Journal of Cleaner Production*. 2019. 223. Pp. 704–728. DOI: 10.1016/j.jclepro.2019.03.051
35. Singh, S., Aswath, M.U., Ranganath, R.V. Effect of mechanical activation of red mud on the strength of geopolymer binder. 2018. 177. Pp. 91–101.
36. Ng, C., Alengaram, U.J., Sing, L., Hung, K., Zamin, M., Ramesh, S. A review on microstructural study and compressive strength of geopolymer mortar, paste and concrete. *Construction and Building Materials*. 2018. 186. Pp. 550–576. DOI: 10.1016/j.conbuildmat.2018.07.075
37. Bocullo, V., Vitola, L., Vaiciukyniene, D., Kantautas, A., Bajare, D. The influence of the SiO₂/Na₂O ratio on the low calcium alkali activated binder based on fly ash. *Materials Chemistry and Physics*. 2021. 258 (September 2020). Pp. 123846. DOI: 10.1016/j.matchemphys.2020.123846
38. Gao, K., Lin, K.L., Wang, D., Hwang, C.L., Shiu, H.S., Chang, Y.M., Cheng, T.W. Effects SiO₂/Na₂O molar ratio on mechanical properties and the microstructure of nano-SiO₂ metakaolin-based geopolymers. *Construction and Building Materials*. 2014. 53. Pp. 503–510. DOI: 10.1016/j.conbuildmat.2013.12.003

Information about author:

Veerakyatharaya Vidyadhara,

ORCID: <https://orcid.org/0000-0001-9837-5449>

E-mail: vidyadharav@bmsce.ac.in

Bhiman Saurabh,

E-mail: saurabhbihan@yahoo.com

Ramappa Venkataswamy Ranganath, PhD

ORCID: <https://orcid.org/0000-0002-3766-5079>

E-mail: ranganath.civ@bmsce.ac.in

Received 05.06.2021. Approved after reviewing 08.10.2021. Accepted 08.10.2021.



Research article

UDC 666.97

DOI: 10.34910/MCE.113.6



Blended binder based on Portland cement and recycled concrete powder

O. Larsen  , S. Samchenko , V. Naruts 

National Research Moscow State Civil Engineering University, Moscow, Russia

 larsen.oksana@mail.ru

Keywords: construction and demolition waste, recycled concrete, recycled concrete powder, recycled screening waste, mechanochemical activation, blended binder

Abstract. The article investigates the properties of recycled concrete powder obtained by mechanochemical activation of recycled screening waste with organic plasticizer in vibrating mill. The waste concrete powder was considered as a part of blended binder based on Portland cement. The optimal powder ratio in blended binder was 30% by weight of cement with the maintenance of the strength properties. The laser diffraction method, X-ray analysis and IR spectroscopy, as well as standard methods were used to estimate the properties of activated powder. The activation of recycled screening waste in 150 min with 0.5% plasticizer allowed us to achieve the specific surface area of the powder at the range of 457.5 cm²/g with content of fine-grained particles in the size of 0–10 μm (26.6%) and 0–20 μm (31.2%). It was estimated that the increase of powder ratio in blended binder reduces the standard consistency of the paste and extends the setting time of the binder. The optimal content of the powder was 30% by weight of cement with standard consistency of 24.6%. The compressive strength at the age of 2, 7 and 28 days was 24.3, 37.4 and 50.5 MPa respectively. The structure change of recycled screening waste particles by mechanical destruction and surface amorphization of initial crystalline phases was confirmed by XRD method and IR spectroscopy.

Citation: Larsen, O., Samchenko, S., Naruts, V. Blended binder based on Portland cement and recycled concrete powder. Magazine of Civil Engineering. 2022. 113(5). Article No. 11306. DOI: 10.34910/MCE.113.6

1. Introduction

The growth of energy and resource-saving technologies has become one of the main goals of sustainable development. The construction industry accounts about 50% of the total use of natural raw materials, 40% of energy consumption and almost half of generated worldwide industrial waste. At the present time the increase of world population and the improvement of life quality have led the development of increased construction activity, which further entails certain negative environmental impact.

Concrete is the most widely used building material. Concrete production is considered to have high negative environmental and social costs. According to the data [1], it is about 75.7 million m² residential buildings were built in 2018. At the same time, in 2018 global cement production amounted 53.7 million tons, and at the end of 2019, this value increased up to 57.8 million tons. Currently, all industries, including the construction sector, are trying to reduce their impact on the environment.

Construction and demolition waste reuse stay relevant not only for foreign countries, but also for Russia. The growth of concrete production causes the increase of waste of volume from old buildings. In European Union it is annually generated about 850 million tons of industrial waste [2], but only some of it obtained from concrete and demolition waste [3] are used as recycled concrete powder.

Large volume of concrete and demolition waste accumulates in large areas and represents a serious environmental problem [4]. Earlier dismantled concrete elements have not been widely used, they were dumped in landfills or used as sub-base material in road construction [5]. Several countries in Europe have accepted the mix of recycled concrete aggregate into concrete [6]. In recent decades many studies have shown their application as coarse and fine recycled concrete aggregates not only in ordinary concrete, but also in self-compacting concrete mixtures [7-10]. This approach aims to conserve natural resources, reduce construction cost related to aggregates supply and transport, decrease the consumption of non-renewable natural resources, minimize waste and associated emissions.

Recycled concrete aggregates have poor quality due to the presence of mortar in relation to natural aggregates. As a result, their use in load bearing concrete is limited [11].

The process of crashing and screening of demolished concrete forms a significant amount of waste. The maximum content of adhered mortar fraction 5-10 mm is up to 75% of the total mass of recycled concrete aggregate [12, 13].

The production of recycled aggregates is associated with generation of recycled screening waste, its content depends on the crushing method and can be from 30% to 70% of the crushed material [14, 15]. The use of recycled screening waste can be considered as supplementary cementitious materials in preparation of waste powder concrete [3, 16, 17], that can be considered as a part of blended binder based on Portland cement.

Various industrial waste is used as powder in concretes [18, 19]. Industrial waste should be activated due to their diverse chemical composition and properties. The activation increases the reactivity and uniformity of waste. It accelerates chemical reactions, both between solid-phase components and between solid and liquid. It changes the composition and structure of the crushed substance.

The pre-treatment of recycled screening waste is necessary for the preparation of recycled concrete powder with stable properties. Various grinding equipment can be used for preparing recycled screening waste, and the type of the mill significantly affect recycled concrete powder properties [20, 21].

It is known that recycled concrete powder can exhibit cementitious properties due to the content of unreacted particles of clinker minerals. The activation gives the ability to exhibit cementitious properties. It can be assumed that the use of such waste can be a valuable resource in production of the SCC mixture and it is aimed to reduce the consumption of cement.

Mechanochemical activation is considered as a joint grinding of recycled screening waste with a dry superplasticizer Melflux 5581F in vibrating mill. This is necessary to create an adsorptive layer on the surface of recycled screening waste particles, to reduce their strength, deformation and destruction due to the decrease in surface energy, as well as for the subsequent partial dispersion of the composite system [22]. Mechanochemical activation is effective resource- and time-saving method of obtaining binders with low water to binder ratio and active powder for concretes. The method consists in joint grinding of cement or other disperse materials with dry superplasticizer in the mill to accelerate the process of activation. Mechanochemical activation of binders and powders with superplasticizers promotes the formation of polymer shell on the surface of grains, provides faster grinding due to the Rebinder effect. The specific surface area of the material while mechanical activation increases and its chemical reactivity enhances [23].

It is advisable to apply recycled screening waste in self-compacting concrete in order to expand the range of supplementary cementitious materials (microsilica, ground blast furnace slag, fly ash). Therefore, the aim of this study is to obtain the high-fineness recycled concrete powder by the mechanochemical activation and evaluate its properties for use in self-compacting concrete. Thus, the efficiency of activating recycled screening waste can be evaluated by specific surface area on the recycled powder and its particle size distribution. It is necessary to establish the required amount of superplasticizer and activation time, to obtain the recycled powder with specified properties to measure the effect of recycled powder on properties of composite binder.

2. Materials and Methods

2.1. Materials

The cement used in this study was Ordinary Portland Cement type CEM I 42.5 R Mordovcement in accordance with Russian standard 31108-2016. The mineralogical composition of the clinker is presented in Table 1. The specific surface area of cement was 344.5 m²/kg. The main physical properties and chemical composition of cement are presented in Table 2 and Table 3.

The choice of cement was due to the low content of C_3A and its granulometric composition. The low content of C_3A contributes the reduction of heat release of the concrete. Furthermore, the effect of superplasticizers is most evident in low-alumina Portland cement. The granulometric composition of the selected Portland cement contributes the uniform particle size distribution, which allows to get the structure of blended binder with dense packing of the particles when the powder is added.

Table 1. Mineralogical composition of the clinker.

Mineral content (%)			
C_3S	C_2S	C_3A	C_4AF
62.40	17.56	5.49	14.55

Table 2. Main physical properties of cement.

Standard water requirement (%)	Setting time (min)		Compressive strength (MPa)		Expansion (mm)
	initial	final	2 days	28 days	
26.5	185	245	23.3	54.4	0

Table 3. Chemical composition of the clinker.

Components (%)									
Loss ignition	SiO_2	Al_2O_3	Fe_2O_3	CaO	SO_3	MgO	K_2O	Na_2O	R_2O
0.21	21.65	4.73	4.36	65.47	0.40	1.27	0.84	0.26	0.81

Superplasticizer Melflux 5581F as grinding aid for recycled concrete powder was used. The recommended dosage of superplasticizer is 0.1–0.5 % by mass of cement. At the same time, it was taken into account that the subsequent overdose of the plasticizer leads to segregation, retardation and lack of concrete mixture setting with reduction the mechanical characteristics of the concrete.

The recycled concrete powder was produced from the internal wall panel of a residential building in Moscow (Table 4). The chemical and phase composition of recycled screening waste are presented in Table 5 and Table 6.

Table 4. Particle size distribution of recycled screening waste.

Fractions (mm)	2.5	1.25	0.63	0.315	0.16	pallet
Partial sieve residue (%)	25.1	15.5	19.1	21.5	13.3	5.7
Total sieve residue (%)	25.1	40.5	59.6	81.1	94.3	100

Table 5. Chemical composition of recycled screening waste.

Oxide	Content (%)
CaO	49.02
SiO_2	39.45
Al_2O_3	3.74
Fe_2O_3	2.50
MgO	1.76
K_2O	1.12
SO_3	1.05
Na_2O	0.587
TiO_2	0.222
P_2O_5	0.153
ZnO	0.0917
MnO	0.0851

Oxide	Content (%)
SrO	0.0742
BaO	0.0631
CuO	0.0222
Cl	0.0190
ZrO ₂	0.0152
Cr ₂ O ₃	0.0139
Co ₃ O ₄	0.0072
V ₂ O ₅	0.0064
Loss ignition	0.0139

Table 6. Phase composition of recycled screening waste.

Phase	Content (%)
Quartz	53.5
Foshagite	11.0
Microcline	8.6
Muscovite	2.4
Chlorite	0.7
Calcite	11.2
Dolomite	3.3
Alite	0.6
Belite	1.3
Brownmillerite	1.0
portlandite	0.6
Ettringite	0.8
Amorphous phase	5.0

2.2. Methods

The main properties of the binder were determined in accordance with Russian standard 310. The laser diffraction analysis was used to determine the particle size distribution of Portland cement and recycled concrete powder. The X-ray diffractometer ARL X'tra was used to determine the phase composition of recycled screening waste. The ARL Optim'X X-ray fluorescence spectrometer was used to determine the chemical composition of the samples. The Vertex 70 Fourier spectrometer was used in IR spectroscopy.

3. Results and Discussion

The demolished internal wall panel was broken mechanically and cleaned from reinforcement. Recycled screening waste with fraction 0–2.5 mm was activated in a laboratory vibration mill during 150 min with dry superplasticizer Melflux 5581F content of 0.1–0.5 % by mass of recycled screening waste. The mode of activation was experimentally established with optimal operation of the equipment. The purpose of activation was to obtain the activated powder with specific surface area at the range of 450 m²/kg. The optimal dosage of Melflux 5581F was 0.5%. The specific surface area increases from 395.6 to 457.5 m²/kg (Table 6).

The influence of activated recycled concrete powder on properties of blended binder was estimated by the maximum change of main properties: standard consistency of the binder, setting time and compressive strength. It was found that the optimal content of the powder in blended binder is 30%. It was determined that standard consistency of blended binder has reduced from 26.5% up to 24.6%.

The Melflux 5581F superplasticizer acts as an activation intensifier to obtain the grain composition of the powder with increased number of fine particle fractions, which creates an adsorbed layer of polycarboxylate molecules on the grains of the powder.

The chemical reactions and initial hydration activity of the powder are accelerated due to application of mechanochemical activation. The mechanochemical activation is considered as a process of activation

of recycled concrete particles and dry polycarboxylate superplasticizer Melflux 5581F in vibrating mill. The formation, movement, and multiplication of various structural defects under high-intensity destructive action on solid state is theoretical background of activation [24]. The penetration of polycarboxylate molecules into microcracks occurs simultaneously and is accompanied by the Rebinder effect. The destruction of the material is facilitated and the newly formed surface is modified with a polymer modifier. Mechanochemical activation brings an increase of chemical activity of substance due to the accumulation of energy in structural defects [25]. When the mechanical action stops, it causes the stabilization of the solid body structure. The period of relaxation processes occurs, the activity of the substance decreases. In this case, the inculcation of polycarboxylate fragments on activated powder contributes to the consolidation of defects in its structure [26].

The results of mechanochemical activation of the powder are estimated by the change in particle size distribution and the specific surface area (Table 7).

Table 7. Particle size distribution of 150 min activation.

Dosage of Melflux 5581F in % by mass of recycled screening waste	Specific surface area, m ² /kg	Fraction content (%)					
		0–5 μm	5–10 μm	10–20 μm	0–10 μm	0–20 μm	>80 μm
0	395.6	3.3	21.0	14.9	17.6	40.3	2.9
0.1	415.6	4.4	18.7	16.7	18.2	40.1	1.9
0.2	432.6	5.5	15.4	17.8	20.9	38.8	1.5
0.3	441.0	6.1	15.9	18.3	23.6	34.9	1.2
0.4	448.5	6.3	16.3	15.8	27.0	33.6	1.0
0.5	457.5	7.2	14.9	19.3	26.6	31.2	0.8

The use of the Melflux5581F has positive effect on fineness of activated powder which is directly proportional to its content. The specific surface area increases by 15.65% compared to the plain powder (from 395.6 to 457.5 m²/kg) with 0.5 % of Melflux 5581F in recycled screening waste and significantly reduces the energy consumption of activation (Figure 1).

In Fig. 1 the curve is linear within 60 min of activation in vibrating mill with different content of superplasticizer, and it corresponds with Rittinger law [26, 27]. The specific surface area of the powder increases with growth of Melflux 5581F dosage. Further activation does not lead to a significant specific surface area growth of the powder due to particles agglomeration, that observes in plain composition.

The superplasticizer as grinding intensifier provides less agglomeration of the particles due to the disjoining and electrostatic repulsion of the particles containing superplasticizer on their surface. The activation efficiency evaluated by degree of dispersion and size change of the powder particles. It depends on time of exposure in vibrating mill and dosage of Melflux 5581F. The granulometric composition of the powder and Portland cement showed in Figure 2.

The main properties of blended binder consisted of Portland cement and activated powder with content from 10 up to 70% was studied. The properties were compared with the properties of Portland cement in accordance with Russian standards. The results are shown in Table 8. It was found that the optimal content of the powder was 30% with uniform distribution of the powder by volume of cement matrix. The necessary properties were achieved with minimum change in setting time and compressive strength.

The obtained data corresponds with the data of other authors. Previous studies have shown [28] the effect of recycled concrete powder on properties of concrete at the age of 28 days with 0.35 water-cement ratio. It was determined that compressive strength with content of the powder 10, 20, 30, and 40% was 60.69, 59.19, 56.18, and 45.64 MPa respectively. It has been shown [29] that the strength of cement paste with water-cement ratio of 0.4 and mechanoactivated recycled screening waste in the amount of 0.1% at the age of 3, 28 days was 21.2 and 47.6 MPa; with content of 0.2% - 18.8 and 43.3 MPa respectively. In research [16] it was determined that adding of 5, 10, and 15% increases the strength of concrete by 167, 228 and 333 % in comparison with plain composition. Previous studies reported [28] that the initial setting time of cementitious materials containing 0, 15, 30 and 45% recycled concrete powder was approximately 273, 288, 298 and 309 min respectively, and the results for the final setting time were 469, 520, 539 and 590 min.

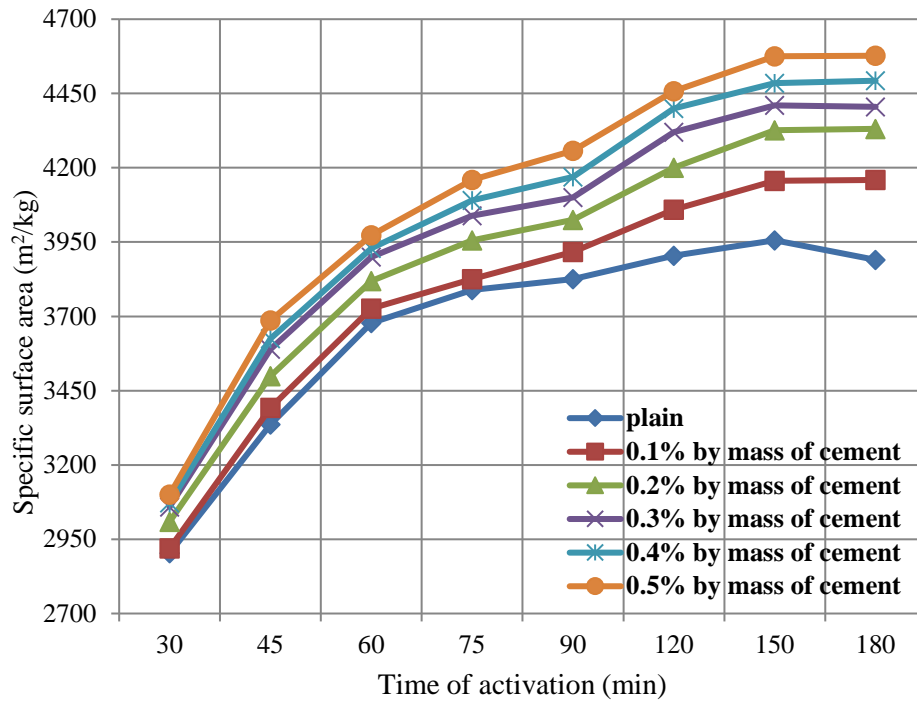


Figure 1. Effect of activation time on specific surface of recycled concrete powder.

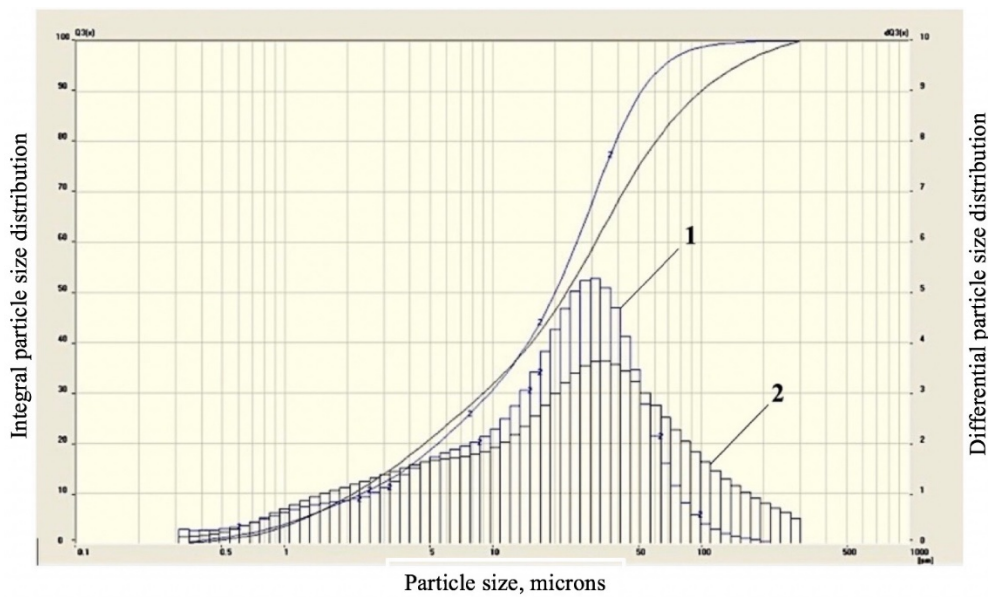


Figure 2. Particle size distribution of recycled concrete powder (1) and Portland cement CEM I 42.5 R (2).

Table 8. Properties of blended binder based on recycled concrete powder and Portland cement.

Powder content in mixture (%)	Standard water requirement (%)	Setting time (min)		Compressive strength (MPa)		
		initial	final	2 days	7 days	28 days
0	26.5	185	245	23.3	38.3	51.4
10	25.5	217	255	23.5	38.0	54.5
20	25.0	226	275	24.1	37.9	54.2
30	24.6	233	305	24.3	37.4	50.5
40	24.0	265	345	18.6	30.2	42.5
50	23.5	275	365	16.5	26.5	39.5
60	23.5	300	380	14.5	25.2	35.6
70	23.0	315	415	13.8	24.9	34.2

The results of X-ray analysis of recycle concrete powder before and after activation are presented in Figure 3 and Figure 4. It was determined that the activation changes the structure of recycle concrete powder particles by mechanical destruction and amorphization of the initial constituent phase of calcium silicate hydrates. It is confirmed the XRD diffraction of unactivated recycle concrete powder (Figure 3) shows the presence of peaks: calcium silicate hydrates of foshagite type $\text{Ca}_4\text{Si}_3\text{O}_9(\text{OH})_2$ ($d = 0.4914$; 0.2894 ; 0.2196), calcium carbonate CaCO_3 ($d = 0.3858$; 0.3033) and silica SiO_2 ($d = 0.4260$; 0.3345 ; 0.1821 ; 0.1604). During the life cycle, calcium silicate hydrate undergoes transformation. In the initial stage of concrete hardening, calcium silicate hydrates as foshagite contain a large amount of crystal and adsorbed water. In the late stage of hardening, when the concrete dries the adsorbed water disappears, and calcium silicate hydrates become dehydrated. The crystal water of calcium silicate hydrates as foshagite undergo their changes along with the structure. In long-term hardening concretes they are formed with a minimum amount of water $(1.5\text{--}2)\text{H}_2\text{O}$. In hardened concrete foshagite is identified as $\text{Ca}_4\text{Si}_3\text{O}_9(\text{OH})_2$ according to the international classification. Such calcium silicate hydrate is formed in lime-sand mixtures during synthesis in laboratory hydrothermal treatment.

The intensive mechanical impact on recycle concrete powder shows the absence of peaks of calcium silicate hydrates and the presence of intense lines of quartz and calcium carbonate at the X-ray diffraction diagram. It causes the surface amorphization with deep phase material change (Fig. 4) and transition to an amorphous state.

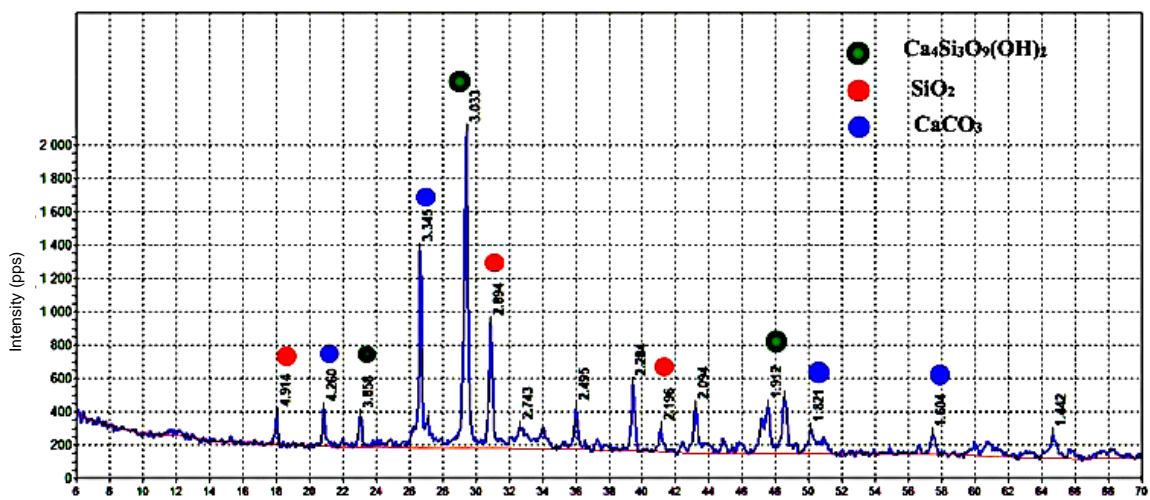


Figure 3. X-ray diffraction diagram of recycle concrete powder before activation.

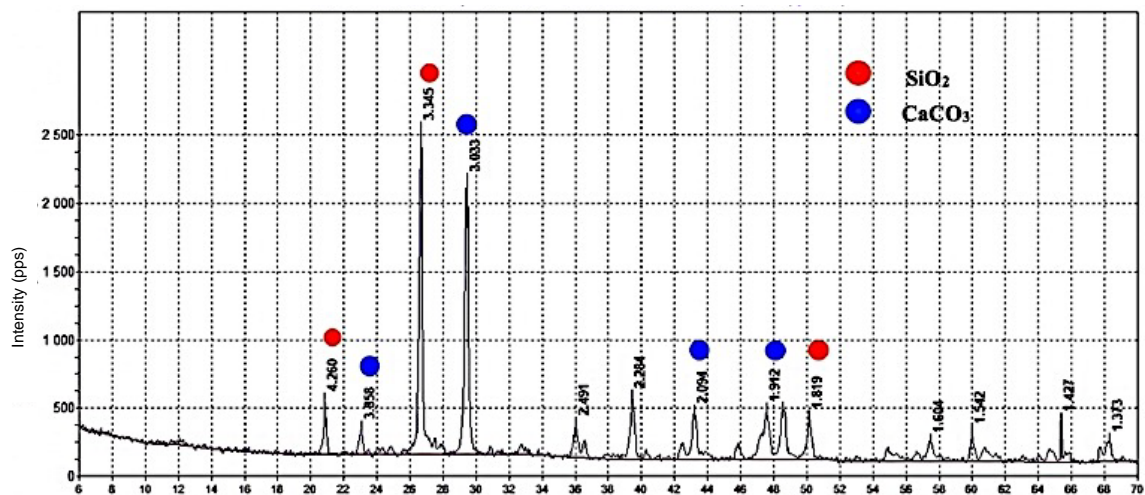


Figure 4. X-ray diffraction diagram of recycle concrete powder after 150 min activation with 0,5 % Meliflux 5581F.

The IR spectroscopy results of recycle concrete powder before and after activation are presented in Fig. 5, 6. They show the change in structure of the material before and after mechanochemical activation. IR reflectance spectrums have differences, which are expressed in changes in the intensity of absorption bands in the range of $3500\text{--}2500\text{ cm}^{-1}$, $1100\text{--}1000\text{ cm}^{-1}$ and $900\text{--}750\text{ cm}^{-1}$. The change in high-frequency absorption band at the range of $3000\text{--}2800\text{ cm}^{-1}$ after activation indicates the presence of carbonyl groups of superplasticizers that confirms its chemisorption by the surface of the powder. The appearance of organic

compound shows the increase of the peak at the range of $1100\text{--}1000\text{ cm}^{-1}$. The transformation of silicon component indicates the presence of an absorption line contour in frequency range of $900\text{--}750\text{ cm}^{-1}$ that explains the amorphization of the surface during mechanochemical activation.

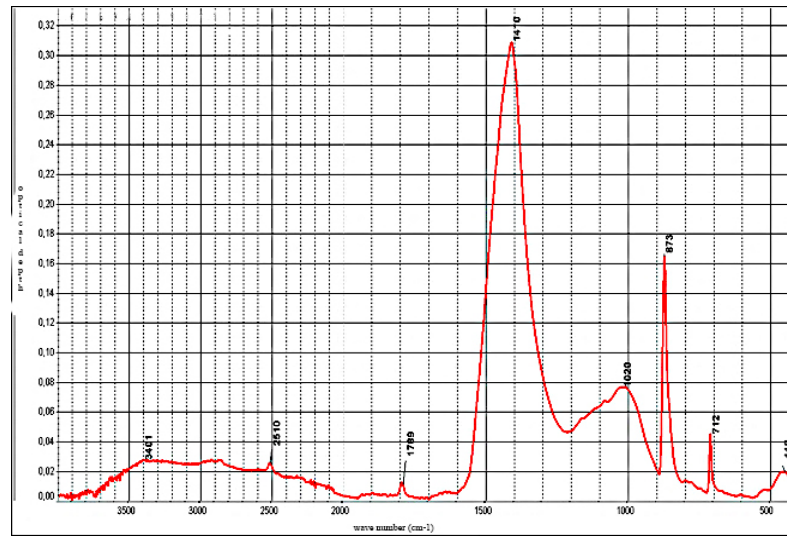


Figure 5. IR reflectance spectrum of recycle concrete powder before activation.

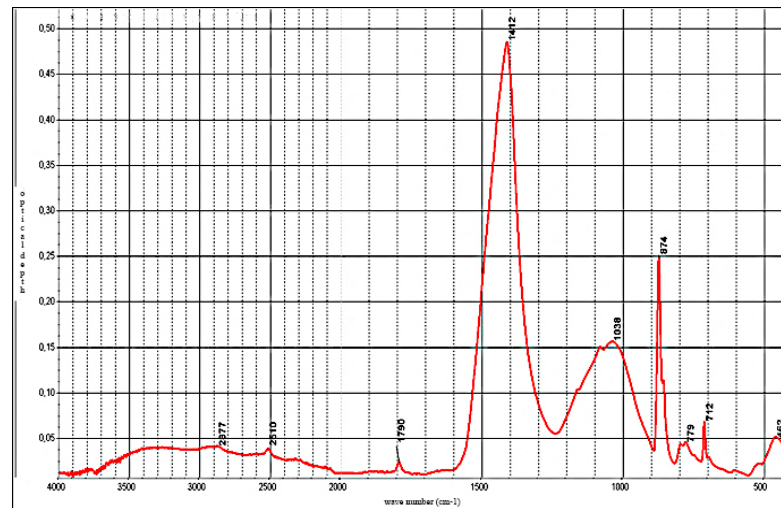


Figure 6. IR reflectance spectrum of recycle concrete powder after 150 min activation with 0.5 % Melflux 5581F.

4. Conclusion

1. The results of experimental investigation showed the potential of recycled concrete powder that can be used as an alternative supplementary material with residual cementitious properties.
2. The obtained blended binder consisted of Portland cement and recycled concrete powder. The optimal content of recycled concrete powder in blended binder was 30%. The powder was obtained while activation of recycled screening waste in vibration mill during 150 min with 0.5 % of Melflux 5581F.
3. It was determined that the obtained recycled concrete powder while activation consisted of fine particles with size $0\text{--}10\text{ }\mu\text{m}$ and $0\text{--}20\text{ }\mu\text{m}$ in the range of 26.6% and 31.2% respectively.
4. The efficiency of mechanochemical activation was confirmed by XRD and IR spectroscopy. It was determined that activation of recycled screening waste and polycarboxylate superplasticizer Melflux 5581F in vibration mill leads to production the powder with hydraulic properties.
5. It was established that the standard consistency of blended binder was 24.6%. The recycled concrete powder in the amount of 30% provides the appropriate setting time (initial – 233 min; final – 305) and compressive strength of 50.5 MPa.

References

1. Evans, L., Mutter, M. Ekologicheskij rejting cementa [Ecological rating of cement]. Cement and its application. 2019. 4. Pp. 24–27.
2. EEA, European Environment Agency. EU as a recycling society: present recycling levels of Municipal Waste and Construction & Demolition Waste in the EU. ETC/SCP working paper, Denmark. 2009. 73 p.
3. Ma, Zh., Liu, M., Duan, Zh., Liang, Ch., Wu, H. Effects of active waste powder obtained from C&D waste on the microproperties and water permeability of concrete. Journal of Cleaner Production. 2020. 257. P. 120518. DOI: 10.1016/j.jclepro.2020.120518
4. Cantero, B., Bravo, M., de Brito, J., Saez del Bosque, I.F., Medina, C. Mechanical behaviour of structural concrete with ground recycled concrete cement and mixed recycled aggregate. Journal of Cleaner Production. 2020. 275. P. 122913. DOI: 10.1016/j.jclepro.2020.122913
5. Engelsens, Ch. J., Van der Sloot, H. A., Petkovic, G. Long-term leaching from recycled concrete aggregates applied as sub-base material in road construction. Science of the Total Environment. 2017. 587/588. Pp. 94–101. DOI: 10.1016/j.scitotenv.2017.02.052
6. Nedeljkovic, M., Visser, J., Savija, B., Valcke, S., Schlangen, E. Use of fine recycled concrete aggregates in concrete: A critical review. Journal of Building Engineering. 2021. 38. P. 102196. DOI: 10.1016/j.job.2021.102196
7. Naruts, V. V., Larsen, O. A. Optimizaciya sostava samouplotnyayushchegosya betona na osnove betonogo loma dlya polov promyshlennykh zdaniy [Optimization of composition of self-compacting concrete based on recycled concrete for the floors of industrial buildings]. BST-Bulletin of construction Equipment. 2020. 3(1027). Pp. 56–59.
8. Larsen, O. A., Naruts, V. V., Voronin, V. V. Tekhnologiya pererabotki betonogo loma s cel'yu polucheniya samouplotnyayushchegosya betona [Technology of processing of concrete scrap for the purpose of obtaining self-compacting concrete]. Construction and reconstruction. 2020. 2(88). Pp. 61–66. doi: 10.33979/2073-7416-2020-88-2-61-66.
9. Naruts, V. V., Larsen, O. A., Samchenko, S. V., Alexandrova, O. V., Bulgakov, B. I. Razrabotka sostavov samouplotnyayushchegosya betona na osnove betonogo loma s ispol'zovaniem strukturnykh harakteristik [Development of compositions of self-compacting concrete on the basis of recycled concrete with the use of structural characteristics]. Vestnik BSTU. 2020. 4. Pp. 8–16. doi: 10.34031/2071-7318-2020-5-4-8-16.
10. Sun, C., Chen, Q., Xiao, J., Liu, W. Utilization of waste concrete recycling materials in self-compacting concrete. Resources, Conservation and Recycling. 2020. 161. P. 104930 DOI: 10.1016/j.resconrec.2020.104930
11. Santos, S., da Silva, P.R., de Brito, J. Self-compacting concrete with recycled aggregates – A literature review. Journal of Building Engineering. 2019. 22. Pp. 349–371. DOI: 10.1016/j.job.2019.01.001
12. Pacheco-torgal, F., Ding, Y., Miraldo, S., Abdollahnejad, Z., Jabrincha, A. L. The suitability of concrete using recycled aggregates for high-performance concrete. Handbook of recycled concrete and demolition waste. Woodhead Publishing Limited. Sawston, Cambridge, 2013. 17. Pp. 424–438.
13. Golovin, N. G., Alimov, L. A., Voronin, V. V. Problema utilizacii zhelezobetona i poisk effektivnykh putej ee resheniya [The problem of utilization of reinforced concrete and the search for effective ways to solve it]. Vestnik MGSU. 2011. 2. Pp. 65–71.
14. Tam, V.W.Y., Soomro, M., Evangelista, A.C.J. A review of recycled aggregate in concrete applications. Construction and Building Materials. 2018. 172. Pp. 272–292. DOI: 10.1016/j.conbuildmat.2018.03.240
15. Mourtazayev, A.Yu., Ismailova, Z.K., Khasiyev, A.A., Nakhaev, M.R. Utilizaciya otseva drobleniya betonogo loma [Recycling of Concrete screening waste]. Ecology and Industry of Russia. 2012. 8. Pp. 26–28. DOI: 10.18412/1816-0395-2012-8-26-28
16. Krasnikova, N.M., Kyrillova, E.V., Khozin, V.G. Vtorichnoe ispol'zovanie betonogo loma v kachestve syr'evykh komponentov cementnykh betonov [Reuse of concrete waste as input products for cement concretes]. Construction materials. 2020. 1/2. Pp. 56–65. DOI: 10.31659/0585-430X-2020-778-1-2-56-65
17. Tang, Q., Ma, Z., Wu, H., Wang, W. The utilization of eco-friendly recycled powder from concrete and brick waste in new concrete: A critical review. Cement and Concrete Composites. 2020. 114. P. 103807 DOI: 10.1016/j.cemconcomp.2020.103807
18. Okamura, H., Ouchi, M. Self-Compacting Concrete. Journal of Advanced Concrete Technology. 2003. 1(1). Pp. 5–15.
19. Grdic, Z. J., Toplicic-Curcic, G. A., Despotovic, I. M., Ristic, N. S. Properties of self-compacting concrete prepared with coarse recycled concrete aggregate. Construction and Building Materials. 2010. 24(7). Pp. 1129-1133. DOI: 10.1016/j.conbuildmat.2009.12.029
20. Babaev, Sh. T., Bashlykov, N. F., Goldina, I. Ya. Povyshenie prochnosti cementnogo kamnya [Increasing the strength of cement stone]. Cement. 1990. 9. Pp. 13-15.
21. Higerovich, M. I. Gidrofobnyj cement i gidrofobno-plastificiruyushchie dobavki [Hydrophobic cement and hydrophobic-plasticizing additives]. Moscow: Promstroyizdat, 1957. 208 p.
22. Bazhenov, Y.M., Alimov, L.A., Voronin, V.V. Structure and properties of concrete with nanomodifiers based on technogenic waste [Struktura i svojstva betonov s nanomodifikatorami na osnove tekhnogennykh othodov]. ASV: Moscow, 2013. 204 p.
23. Gusev, B., Samchenko, S., Krivoborodov, Y. The temperature effect on the properties of the binder recovered from waste concrete (Wplyw temperatury na wlasnosc spoiwa odzyskanego z odpadow betonowych). Cement, Wapno, Beton. 2019. 5. Pp. 407–412. doi: 10.32047/CWB.2019.24.5.7
24. Bazhenov, Y. M., Demyanova, V. S., Kalashnikov, V. I. Modificirovannye vysokokachestvennye betony [Modified high performance concrete]. Moscow: ASV, 2006. 368 p.
25. Yarlushkina, S. Kh. Fiziko-himicheskie processy i ih rol' v formirovanii prochnosti cementnogo kamnya s zapolnitelyami [Physico-chemical processes and their role in the formation of the strength of cement stone with aggregates]. Sbornik trudov NIIZHB "Structure formation of concrete and physico-chemical methods of its research". Moscow. Stroyizdat, 1980. Pp. 60–69.
26. Trautvain, A. I., Yadykina, V. V., Gridchin, A.M. Povyshenie reakcionnoj sposobnosti napolnitelej v rezul'tate pomola [Increasing the reactivity of fillers as a result of grinding]. Vestnik BSTU. 2010. 12. Pp. 82–85.
27. Meloni, P., Carcangiu, G., Delogu, F. Specific surface area and chemical reactivity of quartz powders during mechanical processing. Materials Research Bulletin. 2012. 47. Pp.146–151. DOI: 10.1016/j.materresbull.2011.09.014
28. Kim, Y.J., Choi, Y.W. Utilization of waste concrete powder as a substitution material for cement. Construction and Building Materials. 2012. 30. Pp. 500–504. DOI: 10.1016/j.conbuildmat.2011.11.042.
29. Murtazaev, S-A. Yu., Saidumov, M. S., Abdullaev, M. A-V., Khasiev, A. A. Ispol'zovanie mekhanoaktivirovannykh otsevo drobleniya betonogo loma v proizvodstve betonokompozitov [The use of mechanoactivated screenings of recycled concrete in

production of concrete composites]. Vestnik Dagestanskogo gosudarstvennogo tekhnicheskogo universiteta. Technical sciences. 2011. 22. Pp. 136–140.

Information about author:

Oksana Larsen

PhD in Technical Science

ORCID: <https://orcid.org/0000-0002-9612-7190>

E-mail: larsen.oksana@mail.ru

Svetlana Samchenko

Doctor of Technical Science

ORCID: <https://orcid.org/0000-0002-3523-593X>

E-mail: samchenko@list.ru

Vitali Naruts

ORCID: <https://orcid.org/0000-0001-6280-2541>

E-mail: insolent88@mail.ru

Received 25.01.2021. Approved after reviewing 20.12.2021. Accepted 21.12.2021.



Research article

UDC 551.341

DOI: 10.34910/MCE.113.7



Long-term strength of frozen saline soils

P.I. Kotov¹  , J.V. Stanilovskaya² 

¹ Lomonosov Moscow State University, Moscow, Russia

² Total Energies, Paris, France

✉ kotovpi@mail.ru

Keywords: mechanical properties, strength, temperature, testing, forecasting, frozen saline soil, spherical template indenter test, time analogy method, equivalent cohesion

Abstract. There are many experimental methods for determining the strength of frozen soils. However, the experimental period is always much shorter than the period of infrastructure facilities operation on permafrost. Hence, one of the main tasks of the frozen soils mechanics is the development of methods for prediction of long-term strength. The aim of the research is selection of equations for long-term strength prediction of frozen saline soils. The selection is carried out based on spherical template indenter test (STI) using artificial samples of two soil types (fine sand, loam) with different salinity (from 0.07% to 1.42%), water content and temperature (-2°C, -4°C, -6°C). There were 200 experimental tests. Two approaches with 10 empirical equations and time analogy method were used for long-term strength prediction. As a result, only four equations satisfied the selection criteria and can be used for the long-term strength calculations. Our studies have shown the possibility of using the time analogy method for saline frozen soils. Calculated values of equivalent cohesion for a saline-time analogy as well as for a temperature-time analogy were within confidence interval: 90% and 80% of values respectively.

Citation: Kotov, P.I., Stanilovskaya, J.V. Long-term strength of frozen saline soils. Magazine of Civil Engineering. 2022. 113(5). Article No. 11307. DOI: 10.34910/MCE.113.7

1. Introduction

Long-term strength is one of the most important and poorly understood issues of soil mechanics. Freezing of water cements ground particles and increases the strength of frozen soil in comparison with thawed one. However, ice (as an ideal rheological body) causes rheological processes in frozen soils, such as creep, a decrease in strength and relaxation of stresses in time. Therefore, an important practical task is to develop reliable methods to predict long-term strength (for the 50–100 years' service life of infrastructure) using experimental data (obtained over a short period from several hours to several days).

Studies of frozen soil strength began in the 1950s under the leadership of S.S. Vyalov [1–2]. Many researchers pursued research of how various factors influence strength [1–16]. The results of those experimental and theoretical studies made it possible to get several equations of long-term strength prediction. Long-term strength depends on many factors: grain size, mineral composition, cryogenic structure, temperature, time, salinity, confining stress, load, dynamic load, relative content of organic matter, unfrozen water content, ice content. This explains the large number of solutions suggested by many authors to predict the long-term strength of frozen soils (Table 1).

Table 1. Equations for long-term strength prediction

No	Equation	Author
1	$\sigma_t = \frac{\beta}{\ln \frac{t+t^*}{B}}$	Vyalov [1]
2	$\sigma_t = \left(\frac{t+1}{T} \right)^{-\alpha}$	Vyalov [17]
3	$\sigma_t = \sigma_0 - \frac{(\sigma_0 - \sigma_\infty) \cdot t_t}{t_t + B_t}$	Zaretsky [18]
4	$\sigma_t = \sigma_\infty + \frac{\delta (\sigma_0 - \sigma_t) \cdot t}{T (t - t_0)}$	Fish [19]
5	$\sigma_t = \frac{\sigma_m}{\left(\frac{t}{t_m} \right)^\beta}$	Roman [20]
6	$\sigma_t = \frac{\sigma_0}{\left(\frac{t}{t_0} \right)^\beta}$	Wu [21]
7	$\sigma_t = \sigma_0 \left(\frac{t}{t_0} \right)^J$	Konovalov [22]
8	$\sigma_t = \sigma_0 \left(\frac{t_0}{t} \right)^{1/\alpha}$	Fish [19]
9	$\sigma_t = \frac{1}{\beta} \ln \left(\frac{B}{t} \right)$	Zhurkov [23]
10	$\sigma_t = \sigma_i - \frac{T_r}{t} (\sigma_0 - \sigma_i)$	Grechishchev [24]

Notes: σ_t is strength at moment t ; σ_i is strength at moment i ; σ_0 is initial strength; σ_∞ is long-term strength; σ_m is strength equal to the abscissa of the pole $\ln t_m$; t is time; t_0 is initial time; t^* is the unit time; T_r is relaxation time; t_m is time equal to 10^{-12} s; T is absolute temperature; β , B , α , T , J , δ , B_t are experimental parameters.

Almost all equations were obtained for non-saline soils. Saline permafrost is widespread in sub-sea and coastal areas of the Arctic, where NaCl salts originate from marine deposits and/or seawater incursions [25–27]. Salinity affects strength [28–32]; therefore, an important task is to select the equations for predicting long-term strength of frozen saline soils.

Another way to predict long-term strength is the method of time analogies [20, 33–34]. The prediction of long-term strength is based on a regular relationship between the influence of time on the process of frozen soils destruction and the factors that determine the intensity of this process (temperature, some physical properties: salinity, ice content, organic content, etc.).

Long-term strength characteristics of frozen soil have been obtained from uniaxial and triaxial creep tests, spherical template indenter tests (STI). However, methodology may be different, even for the same test. For example, the uniaxial creep tests carry out different methods to determine the long-term strength of frozen soils: a series of samples of the same type under a constant but different load for each sample [17, 35]; under stepwise increasing loads [17; 36]; constant-stress creep [31]; the regime of relaxation [17, 37]. Another important issue in the processing of experimental data is the choice of the long-term strength criterion [16]. Spherical template indenter test has no such uncertainties. It has found wide application in the practice of research and engineering because of its simplicity and informativeness [15, 20]. STI test also allows determine the deformation modulus and viscosity [20, 38–41].

The aim of the research is to select equations for long-term strength prediction of frozen saline soils using spherical template indenter test.

2. Methods

2.1. Sample preparation

Two soil types were used to measure mechanical properties of saline frozen soils, each having a different grain size distribution: (Y) fine sand and (Z) loam. The individual soil grain size distribution curves are shown in Fig. 1.

The main parameter of saline frozen soils is salinity (i.e. salt content). Salinity is defined as the ratio of the mass of salt to the mass of absolutely dry soil and is expressed as a percentage (D_{sal} , %). The determination and classification of saline frozen soils are described in the Russian standard [42]. The basic method for salinity measurement is titration. We apply this approach to calculate salinity.

Initial (0.18 % – loam and 0.08 % – fine sand) and three additional salinities were studied throughout the test program. This range of salinities was selected to represent natural salinities found in the Arctic [25]. A salinity of 0.08 % represents a low salinity soil, whereas 1.42 % represents a high salinity soil. Temperatures for the tests varied between $-2\text{ }^{\circ}\text{C}$ and $-6\text{ }^{\circ}\text{C}$, which reflects the range of ground temperatures on the Arctic coasts [25].

There are two water content values: saturated frozen (19 % – fine sand; 36 % – loam) and unsaturated frozen soils (9 % – fine sand; 20 % (plastic limit) – loam).

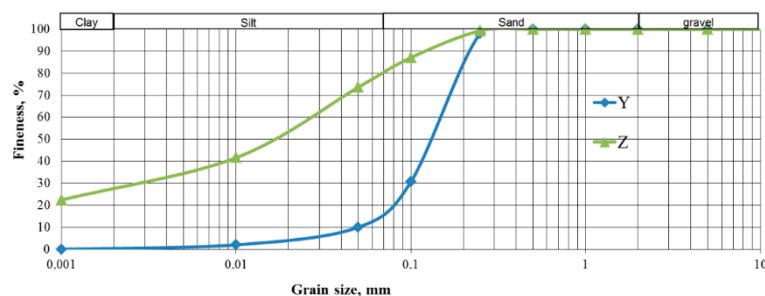


Figure 1. Grain size distribution of tested soils.

The soil was air dried prior to being mixed with water. Sand (sample Y) was sieved to eliminate any particles $> 2\text{ mm}$, and then submerged in a NaCl solution of the desired salinity and vibrated for 10 minutes to remove any trapped air. Soils Z were prepared by mixing each with a NaCl solution of the desired salinity until a fluid paste was obtained. Then soils were kept in the respective NaCl solution for 24 hours.

The density was set by compaction metal ring with a 7 cm diameter and 3.5 cm height. The density of each sample was determined prior to test. Salinity measurements were carried out by titration using the pore fluid extracted from the thawed samples. Water content, soil density, salinity, freezing point were determined for each test (Table 3).

Samples were subsequently frozen in a cold room at $-15\text{ }^{\circ}\text{C}$ for 24 hours to create massive cryogenic textures, to exclude the influence of the cryogenic structure on the mechanical properties. Then samples were placed in a cold room at experimental temperature for 24 hours before testing.

2.2. Spherical template indenter test

A spherical template indenter test was carried out according to Russian standard [36]. The Test program consisted of three eight-hour tests and one long-term test (prior to stabilization deformation 144–240 hours). The criteria for stabilization deformation was 0.01 mm in 24 hours.

The equivalent cohesion of frozen soil (C_{eq}) MPa is determined:

$$C_{eq} = 0.6K \frac{F}{dS_t} \quad (11)$$

where F is vertical load of spherical template indenter, d is diameter of spherical indenter, S_t is depth pressed into a sample, K is coefficient equal to 1 for long-term test.

Statistical processing of the test data was carried out according to the following algorithm. Average value C_{eqn} of the equivalent cohesion was assumed to be equal to the arithmetic mean value and was calculated from the formula

$$C_{eqn} = \frac{1}{n} \sum_{i=1}^n C_i, \quad (12)$$

where n is the test number; C_i are the values obtained from the results of eight-hour tests.

S is a standard deviation of the characteristic, calculated by the formula

$$S = \sqrt{\frac{1}{n-1} \sum_{i=1}^n (C_n - C_i)^2}. \quad (13)$$

The coefficient of variation V of the characteristic was calculated by the formula:

$$V = \frac{S}{C_{eqn}} 100. \quad (14)$$

2.3. Algorithm of calculation

The algorithm to evaluate the applicability of the long-term strength equation was as follows:

1. Data processing of eight-hour tests to obtain the parameters of the equations showed in Table 1.
2. Calculation of the long-term strength for the maximum time in the experiment and obtaining the calculated value of equivalent cohesion.
3. Calculation of confidence intervals for equivalent cohesion (based on statistical processing of eight-hour test data).
4. Comparison of the calculated values and an experimental one considering a confidence interval. The confidence interval was calculated as 3 standard deviations because the probability of deviation from the average value by more than $3S$ is very small.
5. Based on comparison, choosing the equations where the calculated values belong to the confidence interval.
6. Analysis of the relative error of equations and choosing equations with the least one.
7. Relative error between the calculated and experimental values was calculated using the formula:

$$\sigma = \frac{(C_{eqn} - C_{eqc})}{C_{eqn}}, \quad (15)$$

where σ is the relative error, C_{eqn} is the experimental value of equivalent cohesion; C_{eqc} is the calculated value of equivalent cohesion.

Analysis of dependency on water content, soil type and salinity.

2.4. Data processing by time analogy method

Another method to predict the long-term strength is time analogy method. STI test results were processed by saline-time and temperature-time analogies.

The experimental data on the dependence of the equivalent cohesion on time for different salinity are shown in Fig. 2a.

According to the eight-hour tests data, a curve $C_{eq} - \ln(t)$ is drawn (time in seconds). All curves are similar. Therefore, the construction of the generalized "base" curve is conducted graphically, same as for thermoreologically simple bodies. The time shifts between each pair of neighboring $C_{eq} - \ln(t)$ curves are determined and their mean value is found. Then the experimental points are transferred to the adjacent graph (Fig. 2b). Values with minimal salinity are transferred to the graph without changing the coordinates. The experimental points are shifted by $\Delta 1-2$; the points of the third curve are shifted by the sum of the time shifts between curves 1-2 and 2-3: etc. As a result of this construction, we obtain a generalized curve for a long-term equivalent cohesion for the conditions of the highest salinity Fig. 2b.

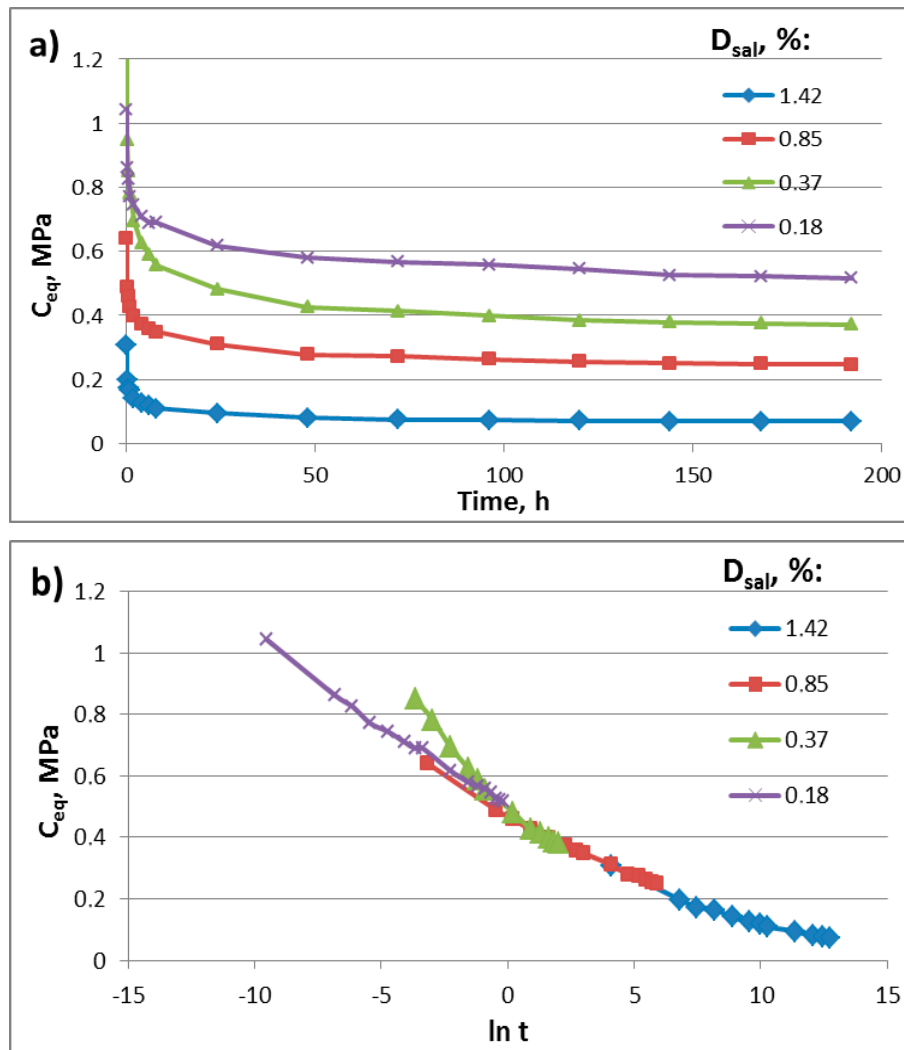


Figure 2. Test results (loam, water content = 20 %, $T = -6$ °C) (a) equivalent cohesion versus time for different salinity and (b) generalized curve for a long-term equivalent cohesion.

Next, we determine the dependence $\ln(\Delta)$ versus $D_{sal(n)} - D_{sal(n-1)}$ and the equation, which allow to calculate the shift value for any salinity. The experimental data processing showed that the generalized curves are well approximated by equation:

$$C_{eqc} = Ae^{B \ln(t)}, \quad (16)$$

where C_{eqc} is the calculated value of equivalent cohesion; A and B are parameters that depend on the type of soil, temperature, loading mode; t is time in seconds. The values of parameters A and B are determined based on computer-analyses.

Comparison of experimental and calculated values showed good convergence of results for loam (Table 2). The same approach was used for the method of temperature-time analogy. But instead of salinity, the dependence of the equivalent cohesion on temperature was considered.

Table 2. Experimental and calculated values equivalent cohesion for loam ($W = 20\%$, $T = -6\text{ }^{\circ}\text{C}$).

D_{sal}	Experimental values		Calculated values		
	t , h	C_{eqn} , MPa	A	B	C_{eqc} , MPa
0.18	192	0.52	2.6	-0.127	0.47
0.37	192	0.37	1.9	-0.127	0.34
0.85	192	0.25	1.16	-0.127	0.21
1.42	192	0.07	0.46	-0.127	0.08

3. Results and Discussion

The results of the experiments showed that an increase in salinity led to a decrease in equivalent cohesion for all tested soils. As a result, it was found that the coefficient of variation does not exceed 15%, and its average value is 7–9% (Table 3).

Table 3. Results of experimental research.

Soil	Test No.	W , %	ρ , g/sm ³	T_{bf} , $^{\circ}\text{C}$	D_{sal} , %	$T = -2\text{ }^{\circ}\text{C}$		$T = -4\text{ }^{\circ}\text{C}$		$T = -6\text{ }^{\circ}\text{C}$	
						C_{eqn} , MPa	V , %	C_{eqn} , MPa	V , %	C_{eqn} , MPa	V , %
Y	1	9	1.88	-0.34	0.08	0.36	5	0.59	13	0.70	13
	2	9	1.89	-0.64	0.16	0.20	6	0.27	9	0.39	12
	3	9	1.88	-1.28	0.38	0.02	9	0.07	2	0.18	9
	4	9	1.87	-3.90	0.76	–	–	0.04	6	0.11	5
	5	19	1.86	-0.35	0.08	0.38	8	0.80	11	0.85	9
	6	19	1.87	-0.56	0.16	0.22	12	0.53	14	0.65	15
	7	19	1.86	-1.05	0.30	0.09	14	0.17	9	0.31	6
	8	19	1.86	-3.71	0.66	–	–	0.07	13	0.15	8
	9	20	1.88	-0.45	0.18	0.33	9	0.42	12	0.63	11
Z	10	20	1.89	-0.98	0.37	0.23	6	0.39	14	0.51	13
	11	20	1.87	-1.96	0.85	0.07	11	0.24	6	0.34	12
	12	20	1.88	-3.69	1.42	–	–	0.04	12	0.12	12
	13	36	1.67	-0.39	0.18	0.47	8	0.53	13	0.61	10
	14	36	1.67	-0.88	0.35	0.43	10	0.50	13	0.58	14
	15	36	1.66	-1.85	0.78	0.19	11	0.26	13	0.48	12
	16	36	1.67	-3.44	1.33	–	–	0.08	13	0.17	10

Initially, all the data were processed and the parameters of the 10 equations (Table 1) were obtained. As a result, only four equations (1), (2), (5), (7) were selected, where calculated values of the equivalent cohesion were in the confidence interval (95 % of the calculated values). 80 % of the deviations in the calculated values of saline frozen soils strength were obtained for other formulas at a temperature of $-2\text{ }^{\circ}\text{C}$. Frozen soils are multicomponent systems and salinity affects the content of ice, unfrozen water and mechanical properties, especially in an area of intense phase transitions.

Relative error distribution for different temperatures was calculated for the four selected formulas (Fig. 3). Test number in the Fig. 3 and 4 corresponds to "Test No." in Table 3.

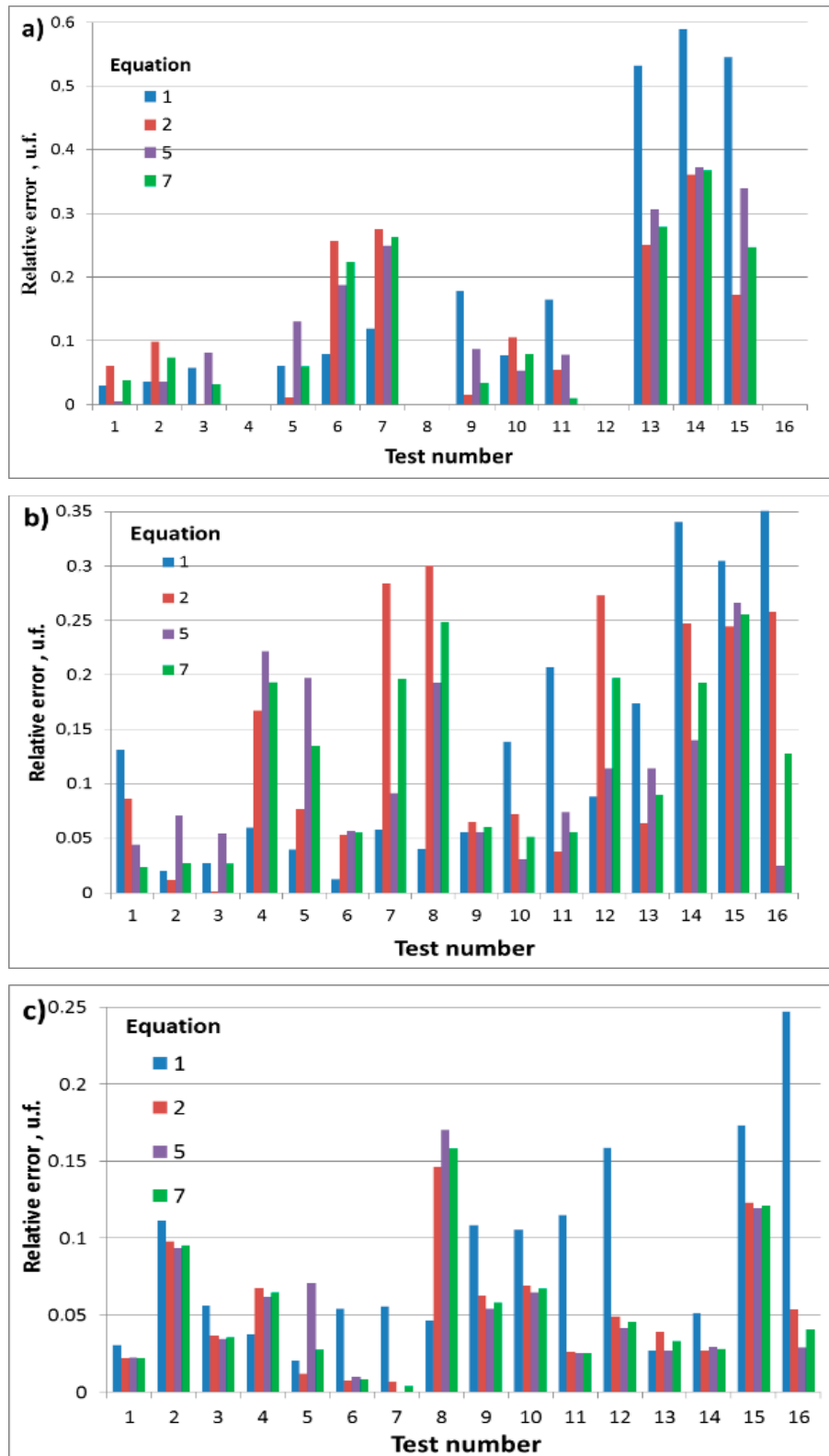


Figure 3. Histograms of distribution of relative errors for different soil types at different temperatures: a) $-2\text{ }^{\circ}\text{C}$, b) $-4\text{ }^{\circ}\text{C}$, c) $-6\text{ }^{\circ}\text{C}$.

The next step was to select the minimum value of the relative error and the most accurate equation. As a result, for fine sand, the data are best approximated by equation (1). For loam, at a temperature of $-2\text{ }^{\circ}\text{C}$, the best is the equation (2), and at temperatures $-4\text{ }^{\circ}\text{C}$ and $-6\text{ }^{\circ}\text{C}$ – the equation (5). For sandy soils, the relative error is less than in loam, which is associated with a different content of unfrozen water that significantly affects the strength properties.

The analysis of the equations applicability showed a high dependence on the temperature of the tests. Thus, the maximum values of the relative error are observed (up to 40 %) at a temperature of $-2\text{ }^{\circ}\text{C}$, and at a temperature of $-6\text{ }^{\circ}\text{C}$ the relative error does not exceed 15 %. As the temperature decreases, the strength increases. This is caused by the reduction in the layer's thickness of unfrozen water and the increase in the ice cementations of soil particles. In addition, we can note an increase in the relative error with increasing salinity at temperatures $-2\text{ }^{\circ}\text{C}$ and $-4\text{ }^{\circ}\text{C}$. The unfrozen water content, the thickness of the water films, and, probably, the number of the initial structural defects depend on salinity. This leads to large variations in strength values with increasing salinity.

An increase in the relative error is also obtained with increasing water content, especially at a temperature of $-2\text{ }^{\circ}\text{C}$. Probably, the increase of water content may lead to redistribution of stresses on weak saline pore ice [10].

The long-term equivalent cohesion was calculated according to the time analogies method. As a result, 90 % of the calculated values of the equivalent cohesion for the saline time analogy and 80 % for the temperature time analogy are within the confidence interval. Fig. 4 shows the relative error values for different soil types. The distribution of errors is quite chaotic in this case.

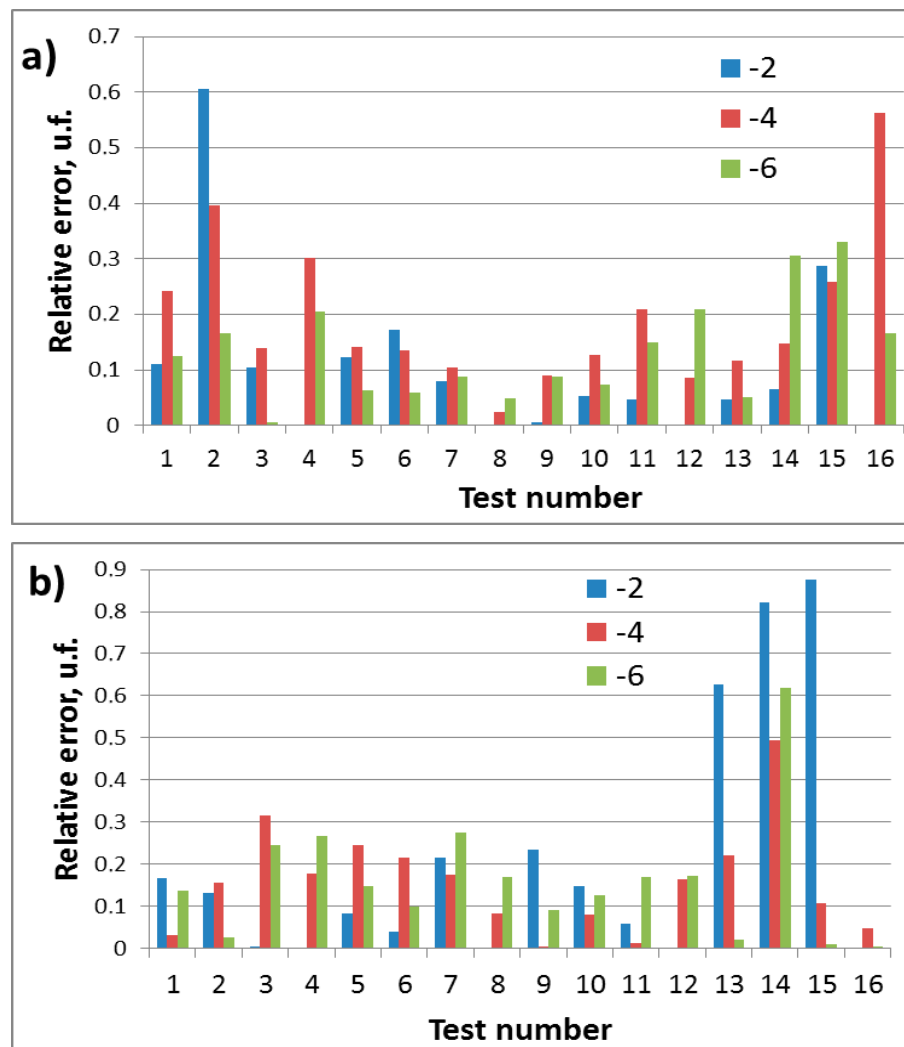


Figure 4. Histograms of distribution of relative errors for different soil types at different temperatures ($^{\circ}\text{C}$) with: a) saline time analogy b) temperature time analogy.

Basically, the researchers performed long-term strength calculations for only one equation. Many equations were developed in the 60s and 80s for non-saline soils. Comparison of several equations was practically not carried out. The article Zhang [15] describes the comparison of three equations (1, 5, 6) for non-saline soil (Shaanxi-Fuping loess) based on the data spherical template indenter test. The calculation

results of equation (1) were larger, than the other equations (5, 6). Therefore, the author suggested using equations (5, 6). The prediction of long-term strength for frozen non-saline and saline soils was carried out for Bolshezemel'naya tundra determined by uniaxial compression and spherical template indenter test [13]. Only four equations (1, 2, 3 and 5 Table 1) were used to predict long-term strength. Based on a comparison of the experimental and calculated values of long-term strength and an assessment of the reliability of the predictive equations, the following conclusions were obtained:

- Logarithmic equation (1) and Exponential equation (5) are acceptable for all types of soils.
- Exponential equation (2) yields good results for non-saline and slightly saline soils.
- Fractional-linear equation (3) yields satisfactory results for non-saline soils.

The same results were obtained for our saline frozen soil, the equations (1) and (5) showed better convergence. There are two hypotheses about long-term strength. According to the first one, long-term strength decreases indefinitely, and long-term strength tends to zero. According to the second one, long-term strength decreases to a limited extent and the long-term strength takes on a finite value. Equations (1) and (5) refer to the first case, which was developed based on the kinetic theory of body destruction [43].

The possibility of predicting long-term strength by the time analogy method was confirmed for other types of soils under various test methods [20, 33]. The methods of time-based analogies are very prospective to predict the long-term strength of frozen soils. These methods allow to obtain values of long-term strength for the entire range of factors that reduce strength (temperature, salinity, stress). The same series of experiments makes it possible to not only obtains the values of the long-term strength for a period comparable to the service life of structures, but also to determine the regularities of temperature, salinity influence on the strength of frozen soils. Our studies have shown the possibility of using time analogy method for saline frozen soils.

Sayles [3] carried out a complex research of the long-term strength of frozen soils. The strength decreased for 1000 hours from 25 % to 5 % compared with the instantaneous value. The general character of the dependence how the strength of frozen soils depends on time is the same [44]. There are many methods for determining the strength of frozen soils: shear, triaxial and uniaxial creep test, tension test, spherical template indenter test. Curves of long-term strength in different tests are identical, as shown by Vyalov [44]. They are similar for all types of tests and differ only in numerical values. If the absolute values of strength for different types of loading are different, their relative values, equal to the ratio of strength at a given instant of time to instantaneous strength, are practically the same. This testifies of the unified physical nature of the destruction process and independence of this process from the type of stress state. Thus, the obtained regularities and equations for predicting the long-term strength of frozen saline soils can also be used in other types of tests.

4. Conclusions

The analysis of all the considered equations of long-term strength (1-10 Table 1) allows us to draw following conclusions. Only four equations (1), (2), (5), (7) were selected, where calculated values of the equivalent cohesion were in the confidence interval (95 % of the calculated values). The data are best approximated by equation (1) for fine sand, equation (2) at a temperature of -2°C and equation (5) at temperatures -4 and -6°C for loam.

Time analogy method is very promising for the prediction of long-term strength of frozen soils. This method helps to predict the strength with temperature and salinity change. Using of equations does not allow this. 90 % of the calculated values of equivalent cohesion for a saline-time analogy and 80 % for a temperature-time analogy were within the confidence interval when calculating the long-term strength.

Thus, geotechnics can use the proposed formulas to predict long-term strength of frozen saline soils, which will increase the accuracy of calculations. Neglecting changes in strength with time may lead to accidents of infrastructure.

References

1. Vyalov, S.S. Rheological properties and bearing capacity of frozen soils. Transl. 74 (Tech Ed F J Sanger), U.S. ACRREL, USA, 1965. 105 p.
2. Vyalov, S.S. 1966. Methods of determining creep, long-term strength and compressibility characteristics of frozen soils. No.1364. NRC. Ottawa, 1965. 89 p.
3. Sayles, F.H. Low temperature soil mechanics. U.S. Army Cold Reg. Res. Eng. Lab. Tech. Note, Sept. USA, 1966. 67 p.
4. Tsytoich, N.A. The mechanics of frozen ground. McGraw-Hill. New York, 1975. 448 p.
5. Haynes, F.D. Strength and deformation of frozen silt. Proc. 3rd Int. Conf. on Permafrost, Edmonton, Alberta, Canada. Ottawa: National Research Council of Canada, Vol. I, 1978. Pp. 656–661.
6. Ting, J.M., Martin, R.T., Ladd, C.C. Mechanisms of strength for frozen sand. Geotech. Eng. ASCE. 1983. 109(10). Pp. 1286–1302. DOI: 10.1061/(ASCE)0733-9410(1983)109:10(1286)

7. Ting, J.M. Tertiary creep model for frozen sands. *Journal of Geotechnical Engineering*. 1983. 109(7). Pp. 932–945.
8. Nixon, J.F., Lem, G. Creep and strength testing of frozen saline fine-grained soils. *Canadian Geotechnical Journal*. 1984. 21(4). Pp. 518–29. DOI: 10.1139/t84-054
9. Zhu, Y., Carbee, D.L., Tensile strength of frozen silt. US Army Cold Regions Research and Engineering Laboratory, CRREL Report 87-15. USA, 1987. 23 p.
10. Hivon, E.G., Sego, D.C. Strength of frozen saline soils: *Canadian Geotechnical Journal*. 1995. 32(2). Pp. 336–354. DOI: 10.1139/t95-034
11. Aksenov, V.I., Kal'bergenov, R.G., Leonov, A.R. Strength characteristics of frozen saline soils. *Soil Mechanics and Foundation Engineering*. 2003. Vol. 40(2). Pp. 16–19. DOI: 10.1023/A:1024436118466
12. Arenson, L.U., Springman, S.M. Triaxial constant stress and constant strain rate test on ice-rich permafrost samples. *Canadian Geotechnical Journal*. 2005. 42. Pp. 412–430. DOI: 10.1139/t04-111
13. Roman, L.T., Krivov, D.N. Prediction of long-term strength for frozen soils of the Bolshezemel'naya Tundra. *Soil Mechanics and Foundation Engineering*. 2009. 46(5). Pp. 180–185. DOI: 10.1007/s11204-009-9068-6
14. Kutergin, V.N., Kalbergenov, R.G., Karpenko, F.S., Leonov, A.R., Merzlyakov, V.P. Influence of salinity on rheologic and strength properties of frozen soils in Yamal. *Soil Mechanics and Foundation Engineering*. 2012. 49. Pp. 105–110. DOI: 10.1007/s11204-012-9175-7
15. Zhang, Z., Zhou, H., Feng, W., Zhang, Z., Xiao, D. A spherical template indenter for a frozen soil long-term shear strength test. *Cold Regions Science and Technology*. 2016. 131. Pp. 10–15. DOI: 10.1016/j.coldregions.2016.07.011
16. Chen, D., Ma, W., Li, G., Zhou, Z., Mu, Y. A long-term strength criterion for frozen clay under complex stress states. *Cold Regions Science and Technology*. 2020. 176, 103089. DOI: 10.1016/j.coldregions.2020.103089
17. Vyalov, S.S. *Rheological fundamentals of soil mechanics*. Elsevier Science Ltd., 1986. 576 p.
18. Zaretskii, Y.K. Rheological properties of plastic frozen soils and determination of settlement of a test plate with time. *Soil Mechanics and Foundation Engineering*. 1972. 9. Pp. 81–85. DOI: 10.1007/BF01702891
19. Fish, A.M. Strength of frozen soil under a combined stress state. *Proceedings of the 6th International Symposium on Ground Freezing*. Beijing, 1991. Pp. 135–145.
20. Roman, L.T. *Mekhanika merzlykh gruntov [Mechanics of frozen soils]*. Moscow: Nauka / Interperiodika, 2002. 426 p.
21. Wu, Z., Zhang, J., Zhu, Y. Field experiments creep of ground ice on Qianghai-xizang plateau. *Professional Papers on Permafrost Studies of Qianghai-Xizang Plateau*. Academia Sinica. Chine, Lanzhou, 1983. Pp. 120–123.
22. Konovalov, A.A. Phase transition and longevity of frozen ground. *Cryosphere of the Earth*. 2014. v. XVIII, No. 1: Pp. 31–38.
23. Grechishchev, S.E. Nekotoryye problemy termoreologii merzlykh gruntov [Some problems of thermoregology of frozen soils]. Moscow: Nauka. 1976. Pp. 122–142.
24. Zhurkov, S.N. Reologiya gruntov [Rheology soil]. Moscow: Bulletin of Academy of Sciences of the USSR. 1957. T. KhIII. 78 p.
25. Brouchkov, A., Nature and distribution of frozen saline sediments on the Russian Arctic coast. *Permafrost and Periglacial Processes*. 2002. 13(2). Pp. 83–90. DOI: 10.1002/ppp.411
26. Hivon, E.G., Sego, D.C. Distribution of saline permafrost in the Northwest Territories, Canada: *Canadian Geotechnical Journal*. 1993. 30 (3). Pp. 506–514. DOI: 10.1139/t93-043
27. Ingeman-Nielsen, T., Foged, N.N., Jørgensen, A.S. Geophysical investigation of saline permafrost at Ilulissat, Greenland. *Proceedings of 9th International Conference on Permafrost*. Alaska, 2008. Pp. 773–778.
28. Pharr, G.M., Merwin, J.E. Effects of brine content on the strength of frozen Ottawa sand. *Cold Regions Science and Technology*. 1985. 11. Pp. 205–212. DOI: 10.1016/0165-232X(85)90044-8
29. Brouchkov, A. Frozen saline soils of the Arctic coast: their distribution and engineering properties. *8th International Conference on Permafrost*. Zürich, 2003. Pp. 95–100.
30. Hass, H., Jagow-Klaff, R., Wernecke, R. Influence of Salinity on the Strength of Various Frozen Soils. *Proceedings of 13th International Conference on Cold Regions Engineering*. Maine, 2007. Pp. 1–12. DOI: 10.1061/40836(210)40
31. Nguyen, A.D., Arenson, L.U., Sego, D.C., Biggar, W.K. The dependence of strength and modulus of frozen saline sand on temperature, strain rate and salinity. *Proceedings of the 63rd Canadian Geotechnical Conference*. Calgary, 2010. Pp. 467–475.
32. Hu, K., Chen, X. Laboratory investigation of deformation and strength characteristics of saline frozen silty sand. *Soil Mechanics and Foundation Engineering*. 2017. 54. Pp. 102–109. DOI: 10.1007/s11204-017-9441-9
33. Roman, L.T. Potential for use of time-analogy methods in mechanics of frozen soils. *Soil Mechanics and Foundation Engineering*. 2003. 40 (4). Pp. 146–151. DOI: 10.1023/A:1026265214082
34. Zhang, Z., Roman, L.T., Wei, M., Wenjie, F., Zhao, S. The freeze-thaw cycles-time analogy method for forecasting long-term frozen soil strength. *Measurement*. 2016. (92), Pp. 483–488. DOI: 10.1016/j.measurement.2016.06.044
35. ASTM D5520-94. *Standart Test Method for Laboratory Determination of Creep Properties of Frozen Soil Samples by Uniaxial Compression*. Philadelphia: ASTM International Publisher, 2006. 9 p.
36. Russian Standard GOST 12248.7-2020. Grunty. Opredeleniye kharakteristik prochnosti i deformiruyemosti merzlykh gruntov metodom ispytaniya sharikovym shtampom. [Soils. Determination of the strength and deformability characteristics of frozen soils by spherical template indenter test]. Moscow: Standartinform, 2020. 8 p.
37. Karpenko, F.S., Kalbergenov, R.G., Kutergin, V.N. Determination of Rheological Properties of Frozen Soils by Relaxation Method. *Soil Mech Found Eng*. 2020. 57. Pp. 364–369. DOI: 10.1007/s11204-020-09679-8
38. Roman, L.T., Veretkhina, E.G. Determination of deformation characteristics of permafrost from impression of a spherical plate. *Soil Mechanics and Foundation Engineering*. 2004. 41 (2): Pp. 60–64. DOI: 10.1023/B:SMAF.0000030895.72084.ac
39. Roman, L.T., Kotov, P.I., Determination of frozen ground viscosity by Sphere Punch. *Earth's Cryosphere*. 2013. No. 4. Pp. 30–35.
40. Roman, L.T., Kotov, P.I. Viscosity of frozen and thawed soil. *Soil Mechanics and Foundation Engineering*. 2016. 53(1). Pp. 19–23. DOI: 10.1007/s11204-016-9358-8
41. Huang, C.J., Zhang, Z., Jin, H.J., Li, X.Y., Chen, X., Feng, W.J. Comparison of modulus equations of frozen soil based on spherical template indenter. *Cold Regions Science and Technology*. 2020. Vol. 170, Pp. 102911. DOI: 10.1016/j.coldregions.2019.102911

42. Russian State Standard GOST 25100-2011. Grunty. Klassifikatsiya [Soils. Classification]. Moscow: Standartinform, 2012. 63 p.
43. Vyalov, S.S. Reologiya merzlykh gruntov [Rheology of frozen soils]. Moscow: Stroyizdat, 2000. 464 p.
44. Vyalov, S.S., Zaretsky, Yu. K., Gorodetsky, S.E. Raschety na prochnost' i polzuchest' pri iskusstvennom zamorazhivanii gruntov [Calculations on strength and creep during artificial freezing of soils]. Leningrad: Stroyizdat, 1981. 200 p.

Information about authors

Pavel Kotov,
PhD of Geological and Mineralogical Sciences
ORCID: <https://orcid.org/0000-0002-5945-3405>
E-mail: kotovpi@mail.ru

Julia Stanilovskaya
ORCID: <https://orcid.org/0000-0002-9856-2604>
E-mail: yulia.stanilovskay@totalenergies.com

Received 04.12.2020. Approved after reviewing 16.09.2021. Accepted 23.09.2021.



Research article

UDC 624.69-033

DOI: 10.34910/MCE.113.8



Metamorphic rocks for manufactured sand and coarse aggregate for concrete and mortar

B. Arulmoly^a , K.M.C. Konthesingha^a, S.M.A. Nanayakkara^b , H.M.R. Premasiri^c

^a Department of Civil Engineering, University of Sri Jayawardenepura, Ratmalana, Western Province, Sri Lanka

^b Department of Civil Engineering, University of Moratuwa, Moratuwa, Western Province, Sri Lanka

^c Department of Earth Resources Engineering, University of Moratuwa, Moratuwa, Western Province, Sri Lanka

✉ branavanarulmoly@sjp.ac.lk

Keywords: aggregates, concrete, mortar, construction industry, porosity, water absorption, compressive strength, tensile strength, mechanical properties, durability

Abstract. The present study determined the most applicable high-grade metamorphic rocks as the sources for manufactured sand and coarse aggregates production to apply in the construction industry. As the first stage of this study, representative samples of the most common ten types of metamorphic rock were collected and tested for mineralogical and chemical compositions to select the favorable rock types in concrete and mortar production. XRD diffraction patterns and quantitative analysis results of XRF were referred for identifying the mineral and chemical contents respectively. Secondly, among the favorable rock types, based on the geology, the area contribution by each rock was calculated and few abundantly available rocks were considered for further investigation. Finally, the compatibility of rocks was checked by analyzing the physical, mechanical, and durability characteristics. As the physical parameters, the specific gravity, water absorption, loose and packing density, and water content were checked. Mechanical properties of rocks were determined by investigating compressive and tensile strength, impact resistance, abrasion resistance, and crushing value. The durability of rocks against weather fluctuations was probed through the slake durability indexes. Results from the first stage revealed that Charnockite, Hornblende-Gneiss, Intrusive Charnockite, and Granitic-Gneiss were favorable rocks rich with concrete and mortar friendly minerals such as albite, k-feldspar, and quartz. Among the above four rocks, Charnockite contributed around 40% and Hornblende-Gneiss covered approximately 9.5% of the area, which were then considered for the next stage of the investigation. Charnockite and Hornblende-Gneiss showed similar porosities and water absorption in the range of 0.25–0.26%. Each mechanical property of both rocks complied with the requirements provided by the standards; moreover, they manifested excellent durability performance against cyclic wetting and drying as well.

Acknowledgment: The authors are grateful to the INSEE Cement, Sri Lanka for providing supports to conduct the Chemical and Mineralogical analysis of rocks.

Citation: Arulmoly, B., Konthesingha, K.M.C., Nanayakkara, S.M.A., Premasiri, H.M.R. Metamorphic rocks for manufactured sand and coarse aggregate for concrete and mortar. Magazine of Civil Engineering. 2022. 113(5). Article No. 11308. DOI: 10.34910/MCE.113.8

1. Introduction

The implementation of a proper alternative for river sand and natural coarse aggregate is the major problem that has risen now among the construction industries in most of the developing countries including

Sri Lanka. River sand is currently being used as the main fine aggregate in most construction activities [1]. Many restrictions have been imposed on river sand mining due to the adverse impact on the environment and ecological systems. Excessive excavations near the riverbanks caused serious environmental threats not only in Sri Lanka but also in many countries that are still extracting river sand for infrastructure developments [2]. The most identified impacts on the environment are riverbank collapses, loss of vegetation on the bank of rivers, saline water intrusion, river buffer zone encroachment, erosion of riverbank land areas, and deterioration of river water quality and groundwater quality [2–5]. Presently, the construction companies are trying to introduce manufactured sand as an alternative to river sand for the construction activities to immediately mitigate the issues with river sand mining [1, 6–8]. This leads to an increased number of quarries that are operated to supply the coarse aggregates as well as manufactured sand for both concrete and mortar works [9]. The source to produce manufactured sand is 'high-grade parent rock', which is a solid material with the collection of one or more mineralogical and chemical compositions [10–12]. Therefore, the quality of aggregates produced directly depends on the compositions of parent rocks, which may give positive and negative impacts on the performance of concrete and mortar [7, 8, 13].

Deliberation to manufactured sand production is crucial, as the implications of finely crushed minerals in concrete and mortar are higher than coarse aggregates. It was identified that still, the question remains among the local construction industries, mining industries, and quarries on selecting appropriate rock types for manufactured sand production due to the inclusions of different minerals and chemicals present in the rocks as well as the performance of the rocks [14]. This problem is serious because the potentially deleterious mineralogical and chemical compositions in parent rocks may affect the long and short-term durability of concrete and mortar. Also, when the rock-derived materials used in concrete and mortar are not capable to resist higher stresses or withstand the climatic changes, may fail the structural elements. Therefore, it is a must to investigate the chemical, physical, mechanical, and durability properties of high-grade metamorphic rocks before utilizing them as the sources for aggregate production in the construction work.

This study is focused on determining suitable metamorphic rock types in Sri Lanka and their characteristics for use as the raw materials for producing manufactured sand. Therefore, the outcomes of this research are expected as the guide for selecting appropriate high-grade parent rocks for producing manufactured sand to enhance a durable and sustainable built environment.

Earth's crust is mainly composed of three major rock classes such as igneous rocks, sedimentary rocks, and metamorphic rocks [10, 11]. Based on the simplified geology of Sri Lanka represented by Fig. 1, the crust part (nine-tenths) is mainly underlain by 'Precambrian' age rocks which are subdivided into three major groups based on tectonic setting and the age of rocks: Wannai Complex (WC), Vijayan Complex (VC) and Highland Complex (HC) [12, 15, 16]. The age of each above rock complex is also given in the figure as 'Ma', which defines the mega annum or millions of years. Sedimentary limestone with Miocene age (22.5 to 5 million years ago) can be identified in the North-Western area (coastal belt from Madurankuli to Killinochi). Northern province areas contain limestone facies and the North-Eastern area (coastal belt from Paranthan to Mullaithivu) is underlain by sandstone [17]. Small clusters of mudstone and sandstone of Jurassic age (201 million years) rocks were identified in Tabbowa, Andigama, and Pallama areas having hard sandstone and clay interbedded with limestone and mudstone [18]. Precambrian rocks such as quartzite, charnockite, granulite grade pelitic gneisses, limestone, biotite gneisses are found in HC. Similarly, granitic-gneiss, biotite gneiss, and calc-gneiss rocks are identified in VC while WC is with prominent rock types [15–17]. It is identified that mainly high-grade metamorphic rocks are distributed within this island, which is very strong and hard shows the possibility for manufacturing good quality concrete and mortar aggregates. Some parts of this country are covered with weathered rocks which are not deemed for aggregate production [19].

Some studies proved the linkage between Sri Lankan geology with the global geology, which leads to the depth of this research work to an extent. Prame [20] has explained the lithological similarity of HC with the Trivandrum block of the South Indian granulite belt. Kroner [21] and Pinna et al. [22] proposed that HC geology highly coincides Madagascar-Tanzania and Mozambique while VC rocks have similarities with East and West Gondwana. Sandiford (1986, cited in [20]) compared the lithological affinity with the Rayner Complex of Enderby Land, Antarctica. Yoshida et al. (1992, cited in [20]) correlated Ongul/Skallen groups, Yamato-Belgica Complex, and Prince Olav Complex of Antarctica with HC, VC, and WC respectively.

Limited studies have been carried out so far on the effect of mineral and chemical compositions on the quality of fine aggregates for concrete and mortar production and some of them are included in this section. Dahanayake and Jayasena [23] carried out a study on some of the mineral compounds, texture, and grain direction of gneiss, amphibolite, and some intrusive rocks in VC. A microscopical mineralogical backscattered electron analysis was done by Malaviarachchi and Takasu [24] on some pelitic and intermediate to mafic granulites from HC to check the metamorphic grade based on the mineral

assemblages. A key investigation was carried out by Jayawardena & Dissanayake [25] on the selection of suitable rock types for quarry dust production where the sample collections were done only in the Central and Northwestern provinces of Sri Lanka.

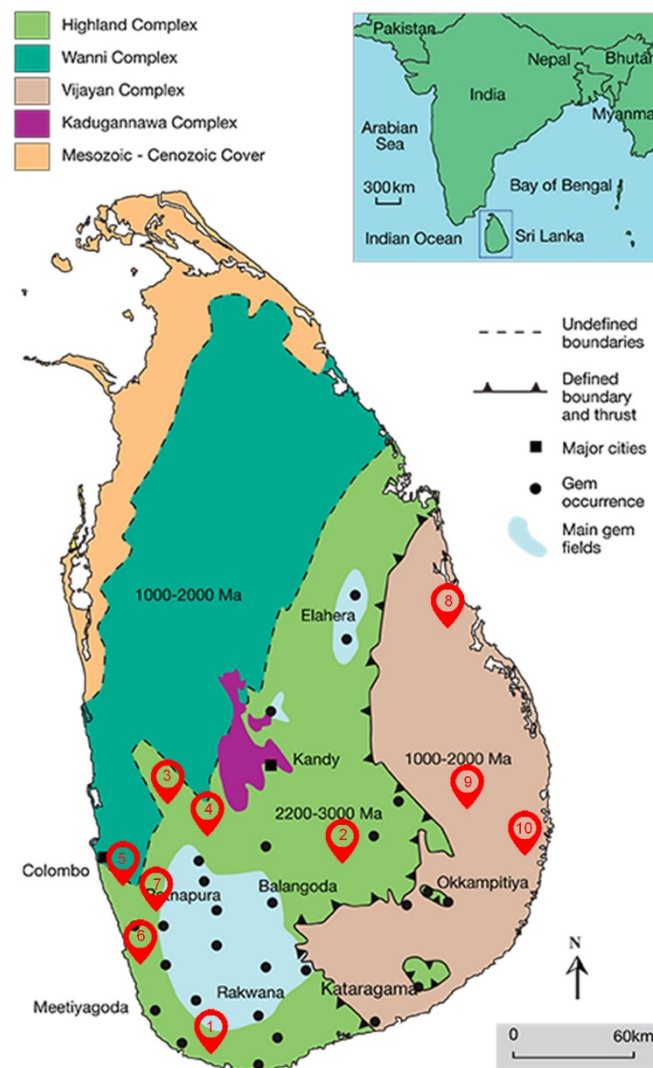


Figure 1. Simplified geological map of Sri Lanka [17].

Petrographic studies were followed for the collected samples and some important conclusions were derived: quartz, feldspar, hornblende, hypersthene, and a few biotite mica contents were identified in charnockite, hornblende-gneiss, and granitic-gneiss rocks from the collection areas which were mainly used for quarry dust production in the country. A recommendation of using quartzite for manufacturing quarry dust was also suggested by the authors as it is usually free from mica content. Mica and clay are considered the most harmful minerals in the rocks. Mica drastically lowers the workability of mixes due to flaky particles and clay significantly reduces the strength of concrete and mortar due to its fine form. Tugrul et al. [26] investigated the effects of feldspar, mica, and clay minerals on compressive strength of mortar where replacement of river sand with 20 % of mica and 4 % of clay minerals such as illite and montmorillonite reduced 50–60 % compressive strength at 28 days. A detailed study was accomplished by Leemann and Holzer [27] on various grain size inclusions of mica minerals such as muscovite, biotite, and chlorite in the mortar and muscovite in concrete. Diminished workability, compressive and flexural strengths, and increased void content were observed with higher larger grain-sized mica inclusions in mortar and concrete. From the investigation executed by Norvell et al. [28], greater water demand and drying shrinkage and dwindled compressive strength of concrete was noticed when the aggregates had higher contents of montmorillonite than illite and kaolinite.

Coarse aggregate is also a manufactured primary aggregate that is obtained from several industrial processes. The quality of rock-derived coarse aggregates mainly depends on the properties of the original rock which are used for manufacturing [29]. Therefore, coarse aggregates should have high strength, better particle shape and gradation, good wear resistance and resistance to climatic changes, etc. [30]. van Wyk and Croucamp [13] checked the suitability of quartzite, tillite, sandstone, and shale rocks for concrete based

on strength and durability parameters. Authors found that required concrete compressive strength was achieved with each rock aggregates but tillite and shale showed unsatisfactory performance with durability. Quartzite revealed the best durability among the selected rocks from slake durability test. Loorents and Johansson [31] studied the quality of granitoid rock aggregate based on free mica grains. Authors identified that the finer particles were abundant with free mica at each fraction while medium and coarse rocks showed high mica content at the fraction of 125–250 μm . Ugolini et al. [32] analyzed mineralogical, physical, and chemical properties of sandstone and siltstone fragments in the soil. The authors noticed that there was a distinct mineralogical difference between sandstone and siltstone while the physical and chemical properties were marginally similar. Scott and Rollinson [33] investigated the mineralogy and surface textures of granite, granodiorite, lava, pyroclastic, gabbro, dolerite, limestone, dolostone, gritstone, greywackes, anorthosite rocks. Johansson et al. [34] researched the quality of mica-schist rock by conducting the micro-Deval test, Los-Angeles abrasion test, and Nordic test on drilled samples. Because the results were within the required limits, the authors suggested the selected rock to produce good quality aggregate.

To achieve the aim of this study, a number of tasks were solved:

- a) investigation on identifying the high-grade metamorphic rocks available based on the geology and linkage with global geology based on the literature review;
- b) research of the mineralogical and chemical compositions of high-grade metamorphic rocks and identifying the most suitable rock types for concrete and mortar;
- c) study of the availability of selected rock types based on the geology;
- d) analyzation of the most determining physical, mechanical, and durability properties of the suitable and abundantly available rocks and compliance with standards.

2. Methods

2.1. Materials

Concerning the geology of Sri Lanka [17], for the preliminary investigation on chemical and mineralogical composition identifications, ten rock types were selected considering the metamorphic class. Fig. 1 shows the locations of sample collection for the first stage of this research. Here the weathered rocks such as alluvial, fluvial, and residual deposits which are covering the Northern and North-Western parts of the country were not selected as those are not usually suitable for aggregate. 'ExpertGPS 7.03 Map' software was used to locate the quarries with the global North (N)-East (E) coordinate system as mentioned in Table 1.

Table 1. Locations of sample collection for Stage 1.

Location code	Rock type	Complex	Quarry	Province	Coordinates	
					North (N)	East (E)
1	Charnockite	HC	Unawatuna	Southern	6.01913°	80.25134°
2	Calc-Gneiss	HC	Walapane	Central	7.09548°	80.85943°
3	Hornblende-Gneiss	HC	Pahala-Bomiriya	Western	6.93210°	80.00483°
4	Cordierite-Garnet-Gneiss	HC	Batawala	Western	6.88119°	80.05676°
5	Quartzite	HC	Mabima	Western	6.96388°	79.97711°
6	Schist	HC	Magala	Western	6.29783°	80.12590°
7	Marble	HC	Kosgoda	Western	6.33665°	80.03380°
8	Intrusive Charnockite	VC	Unnichai	Eastern	7.63300°	81.53725°
9	Granitic-Gneiss	VC	Damana	Eastern	7.20869°	81.61647°
10	Biotite-Gneiss	VC	Komari	Eastern	6.99742°	81.86762°

Approximately 12" \times 12" rubble sample was collected from each quarry as a representative of the corresponding rock type. Sample collection was done in two complexes as represented by Fig. 1: Highland Complex (HC) (covering the Central, Sabaragamuwa, and Western provinces and some parts of Eastern province) and Vijayan Complex (VC) (covering Eastern, Uva, and Southern provinces). Fig. 2 illustrates the digital images of the collected ten rock rubble samples for the identification of the mineralogical and chemical composition.

To investigate the physical parameters of the rock types which were filtered from the first and second stages of this research, various sizes of rock samples were collected from the corresponding quarries as mentioned here. For the determination of relative density (specific gravity) of rocks, a nominal maximum size of 19 mm rock samples was used. A nominal maximum size of 12.5 mm rock samples was utilized for identifying the loose and packing densities of rocks. The absorbed water and surface moisture of rocks were tested using the maximum size of 9.5 mm samples. Uniaxial compressive strength and tensile strength were determined based on the representative rock samples within the range of 55 mm to 70 mm. The aggregate impact value test was conducted using the rock specimens passing 12.5 mm sieve and retained on 9.5 mm sieve according to gradation criteria provided in ASTM C136. The same quantities of rock specimens retained on 9.5 mm and 6.3 mm sieves were collected for investigating the abrasion. For testing the crushing strength, rock specimens passing 12.5 mm sieve and retained on 9.5 mm sieve were utilized. The response of rocks to wetting and drying conditions was checked using representative rock specimens within the range of 50 mm to 65 mm.

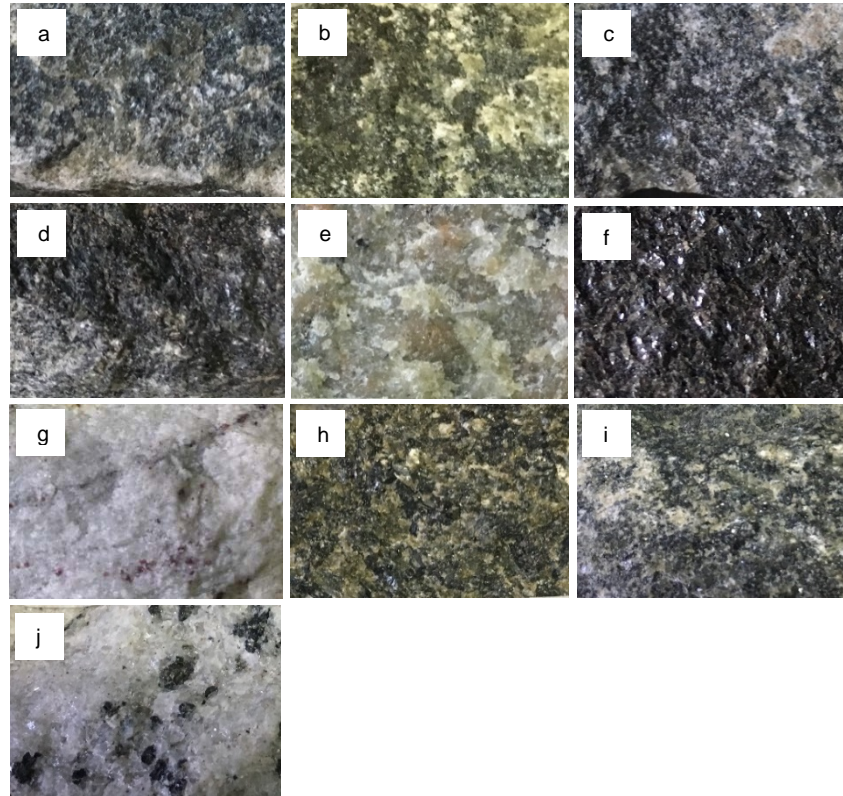


Figure 2. Digital images of rocks listed in Table 1 (a – Charnockite; b – Calc-Gneiss; c – Hornblende-Gneiss; d – Cordierite-Garnet-Gneiss; e – Quartzite; f – Schist; g – Marble; h – Intrusive-Charnockite; i – Granitic-Gneiss; j – Biotite-Gneiss).

2.2. Experiments and test methods

This study was carried out to suggest the most applicable metamorphic rock types for producing construction aggregates under three stages: Stage 1 (filtering the selected ten rock types based on the constitution of potentially harmful minerals), Stage 2 (determining the most suitable rock types among the filtered rocks from Stage 1, according to the availability) and finally Stage 3 (checking the physical, mechanical and durability characteristics of the selected rocks from Stage 2). Fig. 3 illustrates a flowchart for the methodology of this study and Table 2 lists down the experiments, standards referred to, the number of trials used for the experiments, and equations used for calculating the parameters in this study.

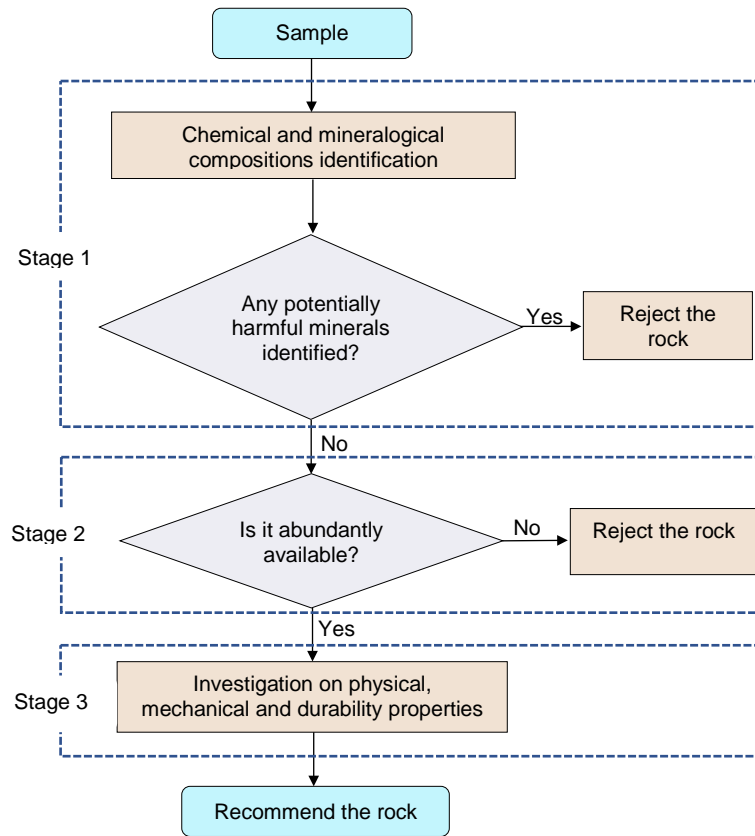


Figure 3. Methodology flowchart.

Table 2. Experiments, standards referred and equations used in this study.

Property (Stage No)	Experiment	Standard referred	Trials	Equations for determining numerical values
Chemical (1)	X-Ray diffraction (XRD)	-	1	-
	X-Ray fluorescence (XRF)	-	1	-
Physical (3)	Bulk SSD specific gravity (G_{SSD})		2	$G_{SSD} = M_{SSD} / (M_{SSD} - M_{SSD,W})$ [i]
	Apparent specific gravity (G_{AP})	ASTM C127	2	$G_{AP} = M_D / (M_D - M_{SSD,W})$ [ii]
	Water absorption ($W\%$)		2	$W = (M_{SSD} - M_D) / M_D \times 100$ [iii]
	Loose (ρ_l) & packing density (ρ_k)	ASTM C29	2	$\rho_k, \rho_l = M_{SSD} / V$ [iv]
	Water content ($w\%$)	ASTM D2216	3	$w = (M_w / M_D) \times 100$ [v]
Mechanica I (3)	Uniaxial compressive strength (f_c)		10	$f_c = I_s(50) \times factorC$ [vi]
	Tensile strength (f_t)	ASTM D5731	10	$f_t = 80\% \times I_s(50)$ [vii]
	Aggregate impact value (AIV)	EN 1097-2	2	$AIV\% = (M_D / M_{2.36}) \times 100$ [viii]
	Los-Angeles abrasion (LAA)	ASTM C131	2	$LAA\% = (M_{2.36} / M_D) \times 100$ [ix]
	Aggregate Crushing Value (ACV)	EN 1097-2	2	$ACV\% = (M_D / M_{2.36}) \times 100$ [x]
Durability (3)	Slake durability index ($I_d(2)$)	ASTM D4644	2	$I_d(2)\% = (M_{D,2} / M_{D,1}) \times 100$ [xi]
Note:	M_{SSD} is mass of SSD sample	M_w is mass of moist sample (soaked in water for 24 hours)		
	M_D is mass of oven-dried sample	$M_{2.36}$ is mass of sample passing 2.36 mm sieve after the test		
	$M_{SSD,W}$ is mass of SSD sample in water	$M_{D,1}$ is mass of oven-dried sample after 1 st cycle of rotation		
	V is volume of measure	$M_{D,2}$ is mass of oven-dried sample after 2 nd cycle of rotation		

2.2.1 Chemical properties

Firstly, a quantitative analysis was carried out to determine the chemical properties of the selected ten rock types. Initially, each collected rubble sample was crushed using a laboratory-scale 'Barmac' crusher to get a powdered form (particle size $< 30 \mu\text{m}$) and oven-dried at $105 \pm 5 \text{ }^\circ\text{C}$ for 48 h. XRD test was executed for investigating the mineralogical compositions of rocks using 'Rigaku Ultima IV X-ray Diffractometer'. Crushed powdered granular samples were tested from 2-theta (2θ) as small as 2° to 90° diffraction angle. XRF test was conducted to analyze the chemical compositions of the collected rock types. 'Spectro – XEPOS XRF Spectrometer' was used for this analysis using the pellet samples prepared from the rubble specimens. Output results such as spectral data and intensity of minerals present in the rocks and quantitative contents of chemical compositions were received.

2.2.2 Physical properties

Surface characteristics were visually observed using 10X magnification digital image process. The composed behavior of various minerals and chemicals in rocks influence the surface textures and porosity. The uniform composition of rocks (made up of uniform-sized minerals) enables higher porosity than rocks with different-sized minerals. The total porosity of a rock (n) was calculated theoretically using Equation 1 suggested by the studies [35, 36] based on bulk density (P_b) and particle density (P_d).

$$n = (1 - P_b/P_d) \times 100. \quad (1)$$

Bulk saturated surface dry (SSD) specific gravity (G_{SSD}), apparent specific gravity (G_{AP}) and water absorption ($W\%$) of rocks were analyzed using buoyancy balance with wire mesh basket conforming to ASTM C127. The corresponding equations for calculating the above parameters are mentioned in Table 2 [i-iii]. For the above tests, rock specimens were soaked in water for 24 hours to essentially fill the pores before the testing. Rock usually contains permeable and impermeable voids which determine the rate of water absorption. This influences the quality of rocks for construction works or is suitable for aggregate production. The density of rocks was determined in both loose and compacted form, which are also some of the important properties of rocks, determine the degree of compaction and self-weight of the structures that resulted from it. After the required calibration of measure, the loose density (ρ_l) and compacted or packing density (ρ_k) were investigated using 'shoveling' and 'rodding' procedures respectively as described in ASTM C29. Both absorbed water and surface moisture in rock-derived aggregates influence the drying shrinkage of concrete and mortar. Here, the water content of rocks ($w\%$) was determined by mass using 'Method B' as stated in ASTM D2216 and based on the equation provided in Table 2 [v].

2.2.3 Mechanical properties

Determination of uniaxial compressive strength (f_c), tensile strength (f_t) and failure patterns of rocks were investigated using the 'Point Load Index' test method according to ASTM D5731. Strengths were obtained by performing an irregular lump test to identify the point load strength index ($I_s(50)$) of the irregular rock samples. Ten rock specimens were selected from each rock type and initially, the preliminary specimen size requirements were checked as per the above standard. The load was applied to the specimens using platen-to-platen end condition attached to the point load tester and the strengths were calculated using the standard charts and the equations provided in Table 2 [vi-vii]. Additionally, the common failure patterns were also observed with the fractured rock specimens, and finally, the water content of the fractured specimens was determined individually. Fig. 4 shows the point load tester used for this analysis with the support conditions.



Figure 4. Point load tester.

Rock-derived aggregates should have enough toughness to withstand sudden shocks or impacts. Therefore, the rock sources for aggregates must have sufficient toughness to resist the impacts. The rock impact resistance capacity (AIV) was tested using an aggregate impact tester conforming to EN 1097-2. After enough impacts, mass losses were calculated using the weight of the specimen retained on a 2.36 mm sieve. The equation provided in Table 2 [viii] was used to calculate the AIV of each selected rock in percentage.

When rock aggregates are used in heavy-duty structures, there is a possibility of failure of particles due to the higher abrasion. Therefore, investigating the abrasion resistance of parent rocks may also give additional support to the selection of materials. Los Angeles abrasion (LAA) test was performed here for investigating the abrasion resistance of rocks according to ASTM C131. After the test, mass losses were determined based on the number of fines passing 2.36 mm sieve, and LAA % was determined according to the equation mentioned in Table 2 [ix]. Under the standardized conditions as per EN 1097-2, the crushing test was performed on rock specimens by applying a gradual compressive load using a universal testing machine. The crushing strength of aggregates (ACV) also partially determines the strength of constructions when the aggregates are only exposed to higher stresses. Once the test was carried out, the ACV was calculated in percentage using the weight of crushed particles passing through a 2.36 mm sieve based on the formulae given in Table 2 [x].

2.2.4 Durability properties

The durability of rock is affected mainly due to climatic changes. The cyclic process of wetting and drying can develop permanent strain in rocks, which may result in a volume increase. Due to the changes in temperature and moisture content, the expansion and contraction coefficients of rocks are varied. In this study, the durability of rocks was investigated quantitatively using slake durability test according to ASTM D4644. Rock specimens were undergone for two cycles of wetting and drying, and the mass losses were obtained after the specimens were oven-dried at 105 ± 5 °C for 48 hours. The equation given in Table 2 [xi] was used for determining the slake durability index ($I_d(2)$) after the two complete cycles of wetting and drying.

3. Results and Discussion

3.1. Stage 1: Identification of chemical and mineralogical compositions

Initially, complete mineralogical testing was carried out for each collected ten rock types. Table 3 represents the quantities (%) of the most common minerals present in the rock types. Based on the results, it was identified that except Calc-Gneiss, Intrusive Charnockite, and Granitic-Gneiss rocks, all others were abundant with quartz. Also, considerable intensities of feldspar minerals such as albite (plagioclase feldspar – $\text{NaAlSi}_3\text{O}_8$), anorthite (plagioclase feldspar – $\text{CaAlSi}_3\text{O}_8$, k-feldspar (orthoclase feldspar – KAlSi_3O_8) were noticed in the collected samples. The constitutions of calcite (CaCO_3), dolomite ($\text{CaMg}(\text{CO}_3)_2$), pyrite (FeS_2), and biotite minerals were very low compared to other available minerals. Here, special attention should be given to illite and biotite minerals, which are from non-expanding clay and mica mineral groups respectively may significantly give adverse effects on the performance of concrete and mortar.

Table 3. Mineral constituents of rocks (%).

Rock type	Calcite	Dolomite	Quartz *	Illite *	Pyrite *	Albite *	K-feldspar *	Anorthite	Biotite *
Charnockite *	1.97	0.23	27.95	1.66	0.01	18.03	27.15	4.36	0.00
Calc-Gneiss	0.00	0.46	2.51	13.43	1.06	10.63	9.39	50.33	0.09
Hornblende-Gneiss *	0.62	0.22	49.48	4.23	0.11	10.44	10.68	20.30	0.00
Cordierite-Garnet-Gneiss	0.00	0.18	68.33	9.50	0.15	4.92	3.08	12.53	0.05
Quartzite	1.64	0.26	32.59	4.77	0.08	16.48	10.35	20.32	0.12
Schist	0.44	0.60	30.44	4.73	0.46	14.35	12.41	30.37	0.00
Marble	2.45	1.43	40.11	2.85	0.15	15.99	24.07	8.33	0.00
Intrusive Charnockite *	0.35	0.09	18.06	1.57	0.12	27.90	28.63	19.02	0.00
Granitic-Gneiss *	2.06	0.82	21.49	3.07	0.06	36.66	31.13	2.86	0.00
Biotite-Gneiss	0.76	1.11	31.67	3.39	0.06	34.77	12.03	9.27	0.35
1 st richest rock									
2 nd richest rock									
3 rd richest rock									

* Most harmful minerals identified
* Minerals give positive effects
* Filtered rocks for Stage 2

A quick chemical/elemental analysis was carried out on the ten rock types and the chemical constituents are listed in Table 4. Rocks selected for this study can be categorized as silicate rocks, which are mainly composed of SiO₂ (more than 50 % of total mineral content). Oxides of Al (Al₂O₃) and Fe (Fe₂O₃) were also identified as abundant compositions in the samples, where the maximum values were noticed in Quartzite, Calc-Gneiss, and Schist rocks. It was noted that the constituents of sulfur trioxide (SO₃) and chloride (Cl⁻) can be negligible in each sample which is the main source, give adverse effects to the function of concrete and mortar. Higher contents of SO₃ may affect the dimensional stability, where Zayed et al. [37] found that aggregates contained SO₃ beyond 3 %, significantly increased the drying shrinkage of cement. More Cl⁻ content in aggregates gives harmful effects to the corrosion of reinforcements.

Alkali metal oxides such as Na₂O and K₂O and alkaline-earth metal oxides like CaO and MgO were also identified in the rocks with smaller quantities. Fig. 5 exhibits the diffraction patterns of the ten rock types resulted from the XRD test. The graphs were plotted with the counts against diffracted angle 2-theta (2θ). The peak intensities mentioned in Table 3 are also marked with the abbreviations of minerals. Various minerals present in the rock-derived aggregates can influence the strength, workability, and durability properties of concrete and mortar. When parent rocks are extracted and crushed for manufactured sand and coarse aggregate production, it enables the reactive form of minerals present in the outputs.

Table 4. Chemical compositions of rocks (%)

Rock type	SiO ₂	Al ₂ O ₃	Fe ₂ O ₃	CaO	MgO	SO ₃	Na ₂ O	K ₂ O	Cl ⁻
Charnockite	72.01	7.83	2.09	3.95	0.25	0.00	2.08	2.54	0.00
Calc-Gneiss	54.17	12.10	12.38	8.75	2.76	0.00	1.51	0.67	0.02
Hornblende-Gneiss	73.59	7.59	4.83	3.07	1.02	0.00	1.75	1.33	0.00
Cordierite-Garnet-Gneiss	79.14	5.70	7.05	0.00	0.73	0.00	1.03	1.09	0.00
Quartzite	68.38	10.60	7.01	3.83	0.85	0.00	2.26	1.32	0.00
Schist	66.30	10.56	8.41	4.29	0.83	0.00	2.77	1.18	0.00
Marble	70.51	8.09	1.34	4.43	0.22	0.00	2.05	2.34	0.00
Intrusive Charnockite	70.55	9.23	5.42	3.20	0.24	0.00	2.81	2.43	0.00
Granitic-Gneiss	68.86	9.55	6.89	3.21	0.38	0.00	3.02	2.52	0.00
Biotite-Gneiss	69.61	8.12	2.56	5.49	0.35	0.00	2.28	2.32	0.00

As discussed above, most of the selected rocks revealed higher content of quartz which is a crucial mineral for aggregates as it is always inert. At normal conditions quartz is a less reactive and more controllable tool for concrete and mortar and even at high temperatures, it is more stable with a very strong Si-O bond. In some cases, there is a possibility of the formation of silica gels (which attract water, swells, and form cracks) in concrete as the result of the reaction between very fine crystalline quartz and alkaline substances (typically Ca(OH)₂) [38]. Feldspar minerals were the second richest minerals identified in the rocks. Albite can fuse and act as a cementing medium at high temperatures which helps to bind the

materials. K-feldspar mineral usually has a greater hardness, which results in higher strength of cement-based mixes [35]. Anorthite is the least stable feldspar mineral but can encourage less hydration rate during the acceleratory period of cement [40]. Therefore, considering the durability, rocks such as Calc-Gneiss, Quartzite, and Schist should be neglected as the sources for aggregate production.

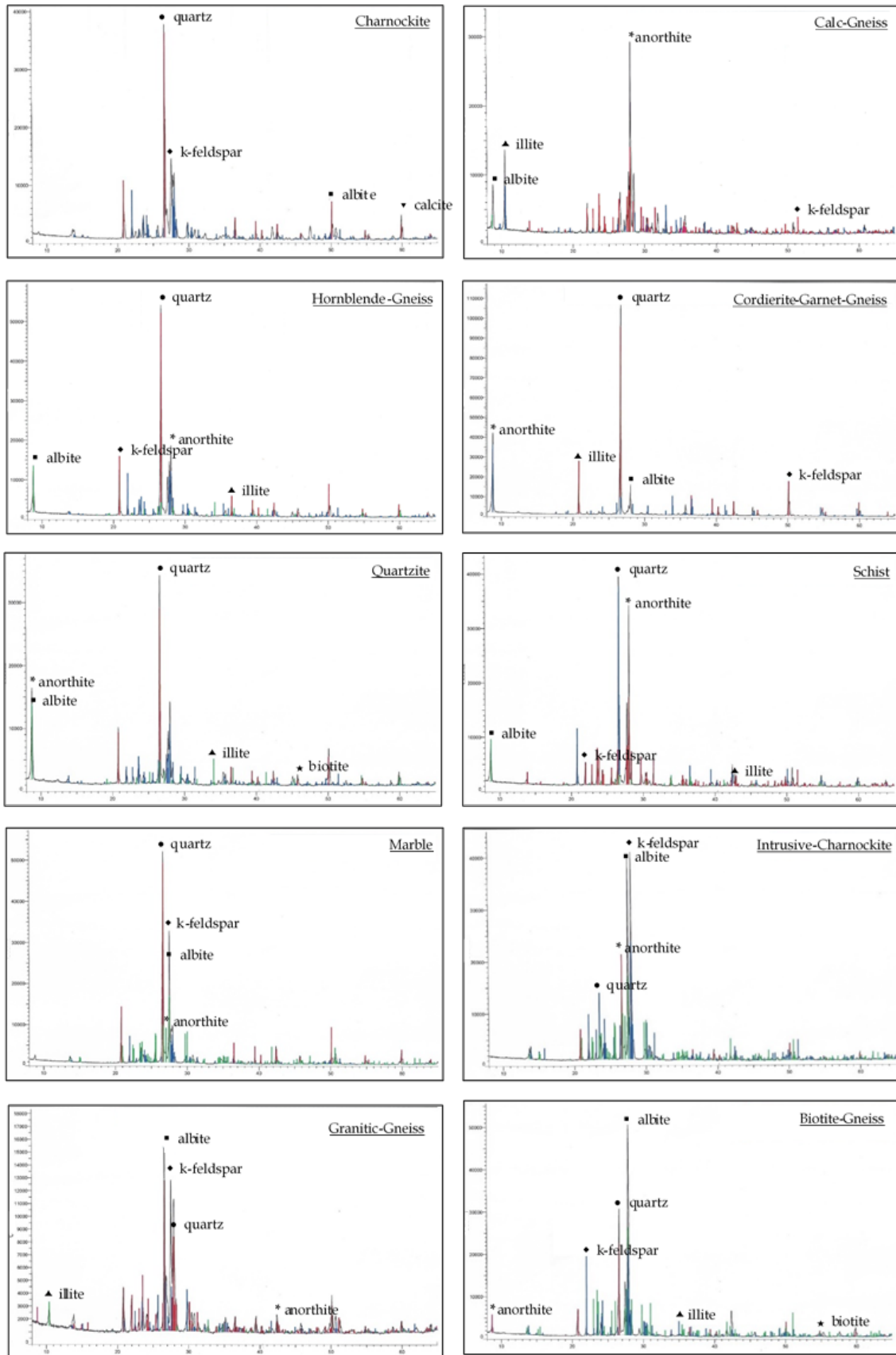


Figure 5. X-Ray diffraction patterns of rocks.

The availability of carbonate minerals is restricted in the collected samples. Two minerals of the carbonate mineral class were discerned: calcite and dolomite. Increased calcite demands the water requirement for the mixes and decreases free calcium hydroxide and bindings of aluminate phases, which help form stable hydration products [41, 42]. It is better to avoid marble for aggregate production as it showed a considerable percentage of calcite minerals. Dolomite mineral aggregates contribute high compressive strength and resistance against abrasion; however, dolomite contents are seemed identical in each rock type. Pyrite (FeS_2) is a sulfide mineral, gives harmful effects to concrete when manufactured sand or aggregates contained it. Pyrite starts to break down and forms sulfuric acid (from the oxidation process) when water and air get into the concrete through small cracks and pores. This enables the expansion of concrete by cracking and allowing more water and air into it [43, 44]. Based on Table 3, Calc-Gneiss rock revealed considerable pyrite content and should be avoided for aggregate production.

Calc-Gneiss and Cordierite-Garnet-Gneiss rocks were identified as the two main sources of illite, which is a clay toxic mineral that directly influences the compressive strength and workability of concrete and mortar. Illite is an intermediate level between smectite (clay mineral) and muscovite (mica mineral), which significantly increases the water requirement in the mixes. It also reduces the strength of concrete and mortar by diminishing the binding capacity between cement paste and aggregates when it acts as a coating [28].

Determination of mica minerals should be highlighted here as they are the most damaging minerals in the aggregates. According to ASTM C294, the mica class contains muscovite, biotite, and chlorite minerals, but based on the XRD patterns, biotite was the only mica mineral identified in the selected rocks. Increased mica minerals in the mixes lead to low workability and considerably lessen the strength and durability with the growth of voids. Among the ten rock types, Calc-Gneiss, Cordierite-Garnet-Gneiss, Quartzite, and Biotite-Gneiss rocks were sparsely detected with biotite; hence, the quarry operators should be vigilant in selecting these rocks for manufacturing aggregates.

Consequently, Charnockite, Hornblende-Gneiss, Intrusive Charnockite, and Granitic-Gneiss were deemed as the most suitable rock types for manufactured sand and coarse aggregate production as they were not highly detected with the potentially harmful minerals for concrete and mortar.

3.2. Stage 2: Filtering the rocks based on availability

Due to the rapid development of infrastructures, the construction activities have been escalated in most of the developing countries including Sri Lanka. It was also identified that; Sri Lanka is now running with the lack of availability of natural resources to fulfill the increased demand for aggregates in construction works. Therefore, proposing alternatives for natural aggregates should also comply with the possibility of continuous usage in the construction works.

As discussed in the previous section, Charnockite, Hornblende-Gneiss, Intrusive Charnockite, and Granitic-Gneiss were concluded as the acceptable rocks for producing aggregates among the ten rock types. To satisfy the persistent construction activities with rock-derived aggregates, this section focuses on the availability of the above four applicable rocks based on a detailed geological map of Sri Lanka. Fig. 6 elucidates the approximate area covered by each rock type mentioned in km^2 .

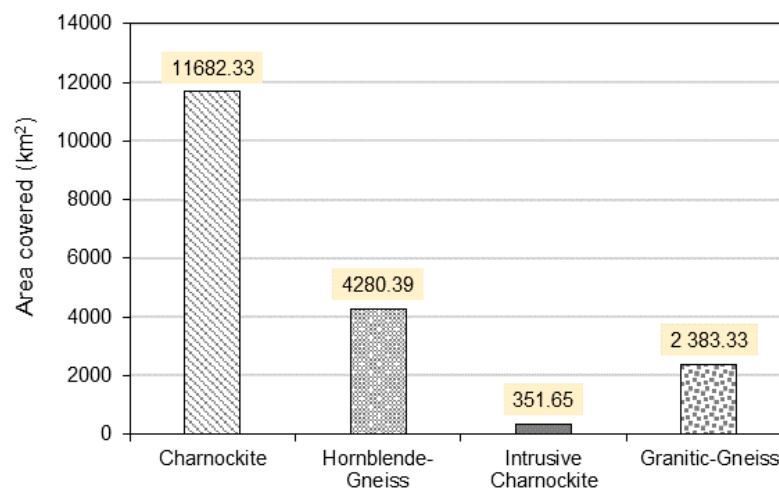


Figure 6. Area covered by the rocks selected from Stage 1.

Charnockite and Hornblende-Gneiss rocks are available in HC of the country. It was identified that Charnockite rock covers the most part, which is around more than 60 % of the total area of HC. This contributes around 40 % of the area of Sri Lanka. Around 15 % area of HC is contributed by Hornblende-

Gneiss rock which is around 9.5 % of the country. Intrusive Charnockite rock was observed in few areas of VC, wherefrom Fig. 6, it was noticed that the rock covers only 351.65 km². Granitic-Gneiss rock contributes around 25 % of the area of VC, which is around 6 % of the country's terra. Accordingly, Charnockite and Hornblende-Gneiss rocks were designated as the long-term available sources for construction aggregates production and selected for further investigation under Stage 3.

3.3. Stage 3: Checking the properties of most applicable and available rocks

Sections from here describe the analysis of physical, mechanical, and durability properties of the selected rocks from Stage 1 and Stage 2: Charnockite and Hornblende-Gneiss.

3.3.1 Surface texture, porosity, and other physical properties

Fig. 7(a) and 7(c) show the rubble samples of Hornblende-Gneiss and Charnockite collected to study the surface characteristics such as surface texture, crystallization, and surface pores which may influence the properties of concrete and mortar. Fig. 7(b) and 7(d) are the digital images of the representative surface of the above rock types used for this analysis. The surface texture of metamorphic rocks depends on the size, shape, and arrangement of the crystals, uniformity of composition, and degree of isotropy.

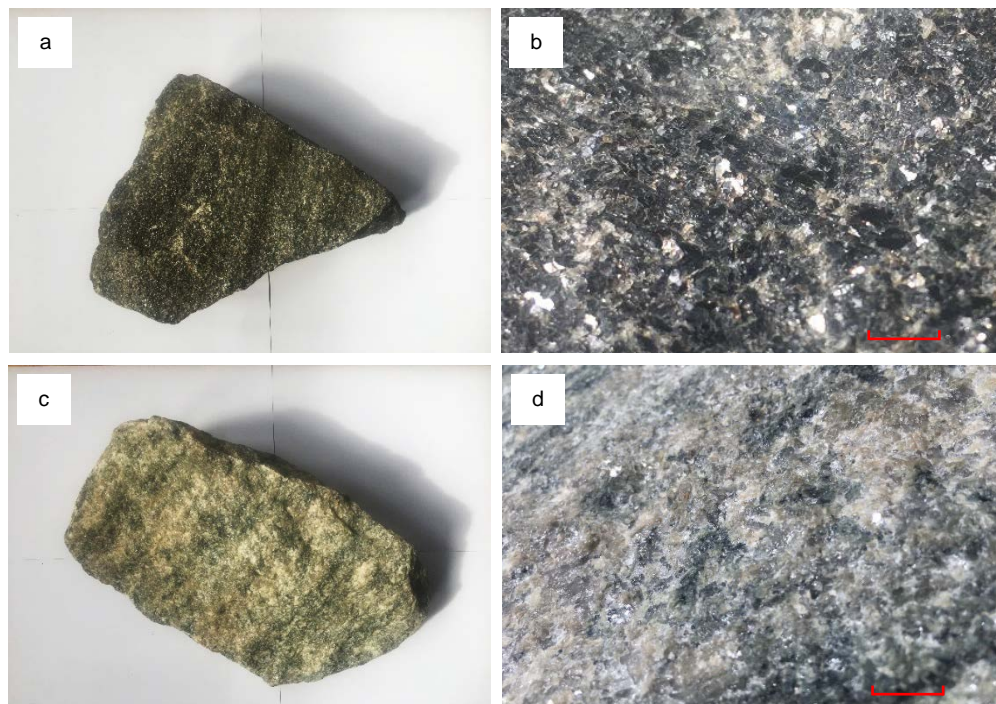


Figure 7. (a) Hornblende-Gneiss rubble sample; (b) digital surface image of Hornblende-Gneiss; (c) Charnockite rubble sample; (d) digital surface image of Charnockite.

From the observations, it was found that Hornblende-Gneiss was configured with medium-sized (0.75–1 mm) grains and 'isometric' crystals which are euhedral cube-shaped with sharp angles, edges, and smooth flat facets. Charnockite was deposited with very coarse-sized (> 2 mm) grains and 'enantiomorphic' shaped crystals which are having optical characteristics. Charnockite crystals, grains, and matrices showed the continuity and non-fabric (uniform arrangement of grains) behavior while Hornblende-Gneiss crystals were formed as fabric (non-uniform arrangement). Minerals were formed as layers (uniform distribution) in Charnockite, but a non-uniform (random) composition of minerals was observed with Hornblende-Gneiss. The above characteristics enhanced Hornblende-Gneiss with rougher surface texture than Charnockite.

The porosity of rocks also depends on the arrangement of grains, composition, and rock type. The calculated porosity values using Equation 1 were 0.25 % for Hornblende-Gneiss and 0.26 % for Charnockite. Both rocks were formed by metamorphism and the slight difference of porosity was due to the variation in grain size, shape, and composition of crystals. Fig. 8 can be referred to for a better understanding of the distribution of surface pores in the above rock types. It was observed that the pores are created at the intersections of grains of the rock. As described above, because of the larger grains in Charnockite, increased pore spaces were noticed than Hornblende-Gneiss.

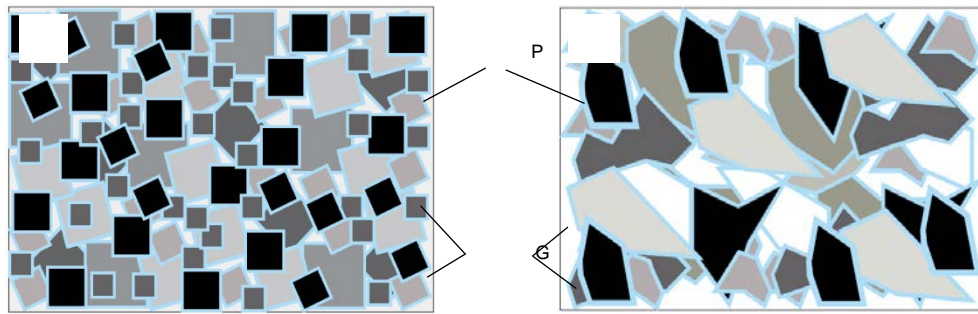


Figure 8. Surface pore space structure (a) Hornblende-Gneiss; (b) Charnockite.

Some basic physical properties of the above rock types were determined and the average values of the properties are listed in Table 5. It was identified that Hornblende-Gneiss was slightly denser than Charnockite. Specific gravity at saturated surface dry (SSD) condition, apparent specific gravity, and bulk specific gravity were noticed higher for Hornblende-Gneiss than Charnockite. This can be directly correlated with the porosity values mentioned above where Hornblende-Gneiss revealed lower porosity than Charnockite which resulted in higher specific gravity. Charnockite manifested greater water absorption than Hornblende-Gneiss which was due to the increased pores. Because of the higher unit weight and lower porosity of Hornblende-Gneiss, greater packing density was observed than Charnockite. Hornblende-Gneiss proved an inflated moisture content than Charnockite. Because of the rougher surface texture of Hornblende-Gneiss, there is always a possibility for trapping the moisture particles between the euhedral cube-shaped crystals.

Table 5. Average physical properties of rocks

Properties	Hornblende-Gneiss	Charnockite
P_d (kg/m ³)	2797	2697
G_{SSD}	2.804	2.704
G_{AP}	2.816	2.716
$W\%$	0.246	0.261
ρ_l (kg/m ³)	1359	1258
ρ_k (kg/m ³)	1553	1397
$w\%$	0.305	0.267

3.3.2 Strength and other mechanical properties

Strength properties of Hornblende-Gneiss and Charnockite were tested at SSD conditions. An irregular lump test was performed on the non-uniform sized rock specimens used for this investigation by calculating the equivalent core diameter (D_e) for all specimens to attain a common behavior against the applied point loads. Hornblende-Gneiss performed well against the applied point loads where increased uniaxial compressive strength (f_c) and tensile strength (f_t) were noticed than Charnockite. It was also noted that both rocks were weak against the tensile loads as they are brittle in nature. Table 6 tabulates the dimension, failure load, calculated equivalent core diameter, point load index, and the strengths of irregular rock specimens.

Table 6 mentions the failure type of all selected rock specimens where most of the Hornblende-Gneiss specimens manifested axial failure (AF) while a considerable number of Charnockite samples were fractured due to the shear failure (SF). Fig. 9 represents few samples from both rock types and their failure planes. In both cases at the start of load applying, cracks were propagated perpendicular to the stress applied, which ultimately left flat surfaces at the breakpoint. The failure behavior of rocks can be directly influenced by the grain direction and crystallization where layer arrangement of minerals in Charnockite gave the possibility of breaking along the weaker mineral layer, which formed a failure shear plane. However, the absence of the above feature in Hornblende-Gneiss ended up in axial failure. The rock specimens were considered at SSD condition for determining uniaxial compressive strength and tensile strength. Impermeable and permeable pores in rock specimens usually contain water when they are in SSD

condition. Therefore, the water content of rock specimens played a major role in the uniaxial compressive strength and tensile strength. To investigate this behavior, the relationship between water content and uniaxial compressive strength was analyzed and represented by Fig. 10(a). Linear relationships were observed between water content ($w\%$) and uniaxial compressive strength of both rock types (Hornblende-Gneiss: $R^2 = 0.9594$ and Charnockite: $R^2 = 0.9151$).

Table 6. Uniaxial compressive strength, tensile strength, and failure type of rocks

Rock type	w (mm)	d (mm)	P (N)	D_e (mm)	F	$l_s(50)$ (MPa)	f_c (MPa)	f_t (MPa)	Failure type	
Hornblende-Gneiss	1	37	17.5	13300	57.414	1.064	4.294	94.463	3.435	SF
	2	35.5	23	17800	64.473	1.121	4.801	105.627	3.841	AF
	3	36	25	18500	67.689	1.146	4.627	101.801	3.702	AF
	4	39	25	19600	70.453	1.167	4.608	101.367	3.686	SF
	5	37	17.5	14800	57.414	1.064	4.778	105.116	3.822	AF
	6	38	22.5	16700	62.406	1.105	4.738	104.231	3.790	AF
	7	45	27.5	18500	70.000	1.163	4.393	96.940	3.514	SF
	8	37.5	27.5	17700	42.457	1.182	4.389	96.560	3.511	AF
	9	42.5	26	19400	71.848	1.177	4.424	97.329	3.539	AF
	10	40	25	18500	66.742	1.139	4.729	104.048	3.784	AF
Charnockite	1	52	42	21300	105.445	1.399	2.680	64.323	2.144	SF
	2	44	36	22500	89.800	1.301	3.631	87.153	2.905	AF
	3	60	52.5	33400	126.635	1.519	3.164	75.939	2.531	SF
	4	62.5	53	39900	129.860	1.536	3.635	87.249	2.908	SF
	5	53	37	22500	99.916	1.366	3.078	73.862	2.462	SF
	6	45	32.5	25000	103.544	1.388	3.236	77.655	2.588	SF
	7	64	56.5	26500	135.679	1.567	2.256	54.141	1.805	AF
	8	55	51.5	26800	120.083	1.483	2.757	66.162	2.205	SF
	9	48	36	23500	93.793	1.327	3.545	85.090	2.836	SF
	10	57	32.5	21000	97.113	1.348	3.002	72.047	2.402	AF

w is sample width; d is sample depth; P is failure/fracture load

D_e is equivalent core diameter $[= 4(w \times d) / \pi]$

F is size correction factor $[= (D_e / 50)^{0.45}]$

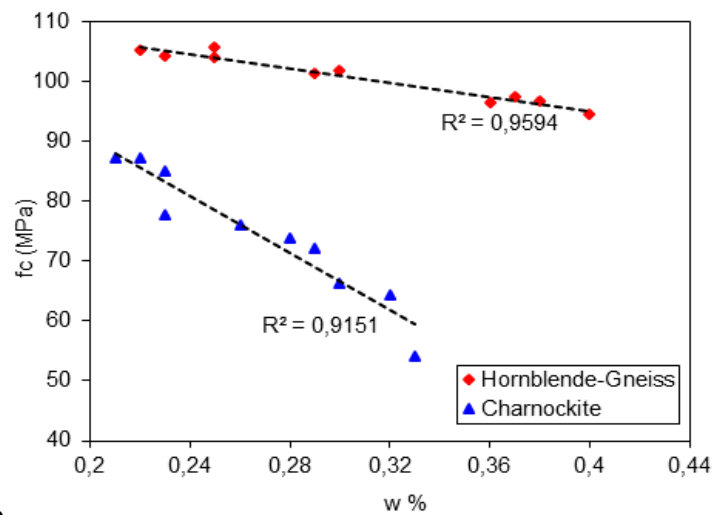
$l_s(50)$ is corrected point load strength index $[= F \times (P / D_e^2)]$

$f_c = l_s(50) \times \text{factor}C$ (for Hornblende-Gneiss = 22; Charnockite = 24)

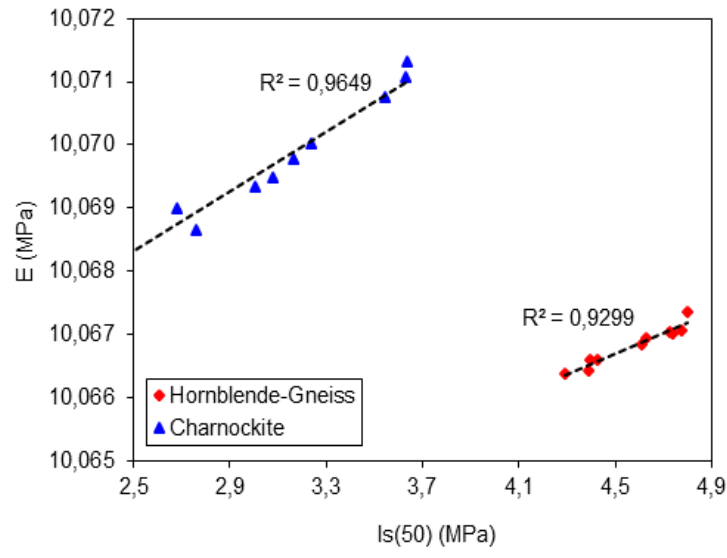
$f_t = 80\% \times l_s(50)$



Figure 9. Failure planes of typical rock specimens with respect to load applied (SF: Shear failure; AF: Axial failure).



a)



**Figure 10 (a): Effect of water content on uniaxial compressive strength;
(b): Young's modulus vs Corrected point load strength index.**

Both relationships showed a decreasing trend from which it can be concluded that uniaxial compressive strength was linearly and negatively affected by water content. Based on the regression equation derived by Leite and Ferland [45] as provided in Equation 2, Young's modulus (E) of rock specimens was calculated based on porosity (n) in this study.

$$E = 10.10 - 0.109 \times n. \quad (2)$$

Furthermore, the above regression was correlated with the corrected point load strength index ($I_s(50)$) which were calculated using equivalent core diameter, size correction factor, and failure load in this study as listed in Table 6. To achieve this, relationships between the E values determined using Equation 2 and $I_s(50)$ were plotted as shown in Fig. 10(b). Based on the results, it was observed that Equation 2 and the calculated values in this study were correlated with a high coefficient of determination values. Linear increasing relationships were noticed with E and $I_s(50)$ for Hornblende-Gneiss (with $R^2 = 0.9229$) and for Charnockite (with $R^2 = 0.9649$).

Multiple linear regression analysis was executed (at 95 % confidence interval) for uniaxial compressive strength of Hornblende-Gneiss ($f_{c, Hbl-Gn}$) (with adjusted $R^2 = 1.000$) and Charnockite ($f_{c, Chkt}$) (with adjusted $R^2 = 1.000$) as given in Equation 3(a) and 3(b) concerning porosity (n), water content (w), corrected point load strength index ($I_s(50)$) and density (ρ).

$$f_{c, Hbl-Gn} = -8.969 \times 10^{-13} + 2.084 \times 10^{-12} n - 3.268 \times 10^{-14} w + 22 I_s(50) + 5.142 \times 10^{-17} \rho; \quad (3a)$$

$$f_{c, Chkt} = 3.100 \times 10^{-13} - 1.100 \times 10^{-12} n - 1.900 \times 10^{-13} w + 24 I_s(50) + 6.000 \times 10^{-17} \rho. \quad (3b)$$

Simple regression was also done (at 95 % confidence interval) to determine the relationship between uniaxial compressive strength and young's modulus of rocks as represented by Equations 4(a) and 4(b). Hornblende-Gneiss ($R^2 = 0.9299$) and Charnockite ($R^2 = 0.9649$) revealed linear relationships.

$$E_{Hbl-Gn} = 7 \times 10^{-5} f_{c, Hbl-Gn} + 10.059; \quad (4a)$$

$$E_{Chkt} = 1 \times 10^{-4} f_{c, Chkt} + 10.062. \quad (4b)$$

The results of other mechanical properties such as 'Aggregate Impact Value' (AIV), 'Los Angeles abrasion value' (LAA), and 'Aggregate Crushing Value' (ACV) of Hornblende-Gneiss and Charnockite are reported here. AIV, LAA, and ACV are the determinations of toughness, abrasion resistance, and crushing resistance of the rock specimens. Table 7 mentions the average AIV, LAA, and ACV of Hornblende-Gneiss and Charnockite, and the recommended values suggested corresponding standards. Lower AIV indicates the rock specimens are tougher or more resistant to impact loads. Based on the provisions given in BS EN 12620:2002, it was concluded that the aggregates produced from Hornblende-Gneiss and Charnockite are safe to be used for heavy-duty concrete floor constructions.

Table 7. Average AIV, LAA, and ACV of rocks

Properties	Hornblende-Gneiss	Charnockite	Limiting values by standards
AIV (%)	22	23	< 25 % for heavy duty concrete floor finishes, BS EN 12620:2002
LAA (%)	60	61	< 30 % for stone matrix asphalt, AASHTO T96-02
ACV (%)	42	40	< 45 % for wearing surfaces, EN 1097-2

Rock abrasion characteristics are not very important in building constructions. However, in this study, LAA was determined to check the adequacy of rock specimens to degradation and disintegration when impact and abrasion loads are applied on the aggregates. It was found that the LAA of both rocks did not comply with the maximum limitations provided by AASHTO T96-02. ACV was determined under a gradually applied compressive load. Rock specimens with lower crushing values indicate the lower crushed fraction under the applied load and more economical performance. ACV of rocks acts a minor role in the constructions which are subjected to higher stresses. According to the test results, the ACV of the selected rocks satisfied the maximum limits and can be suggested for use in the construction of wearing surfaces.

3.3.3 Durability against wetting and drying

The durability of Hornblende-Gneiss and Charnockite rocks was estimated quantitatively after the two cycles of wetting and drying with abrasion. Slake durability index of both rocks were determined after the second cycle as abbreviated by ' $l_d(2)$ '. The higher $l_d(2)$ value defines the higher resistance to cyclic wetting and drying conditions. Results concluded that the corresponding average $l_d(2)$ values of Hornblende-Gneiss and Charnockite rocks were 99.285 % and 99.445 % respectively. Fig. 11 illustrates the observations made during and after the experiment.

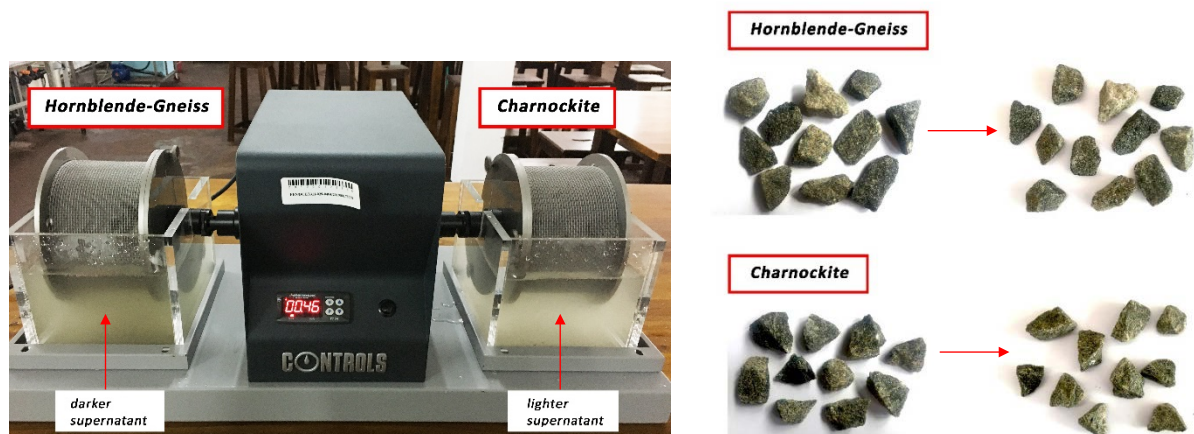


Figure 11. Slake durability test apparatus and transformation of rock specimens.

ASTM D4644 suggests three types of rock samples based on the visual observations after two complete cycles of wetting and drying: Type I (retained specimen remain virtually unchanged), Type II (retained specimen consist large and small fragments), and Type III (the retained specimen is exclusively small fragments). Because the retained Hornblende-Gneiss and Charnockite specimens remained virtually unchanged, it was concluded that they conformed to Type I. According to the classifications of $l_d(2)$ values provided by Franklin and Chandra [46], the rocks selected for this analysis were also termed as

'extremely high' durable rocks. Therefore, aggregates produced from Hornblende-Gneiss and Charnockite can be utilized for any building constructions without uncertainty.

According to the Franklin Rating System [47], Hornblende-Gneiss and Charnockite selected for this study were defined with a rating value (R) based on the average $l_d(2)$ and $I_s(50)$ values. The interpolated R -value for Hornblende-Gneiss was observed as 8.26 with $l_d(2)$ of 99.285 % and $I_s(50)$ of 4.578 MPa. The R -value for Charnockite was determined as 7.94 with $l_d(2)$ of 99.445 % and $I_s(50)$ of 3.098 MPa.

Various factors influence the durability of rocks, but the most dominant factors are the rock's mineral and chemical compositions. As observed in Section 4.1, Charnockite and Hornblende-Gneiss rocks are abundant with friendly minerals and chemicals. Anyhow, it was also noticed that there are few percentages of potentially harmful minerals present in those rocks. Therefore, the influence of those minerals on the durability of rocks was investigated and reported with the outcomes from multiple linear regression analysis and F -test. Here, the statistically significant effects of both friendly and harmful minerals on the slake durability indexes of rocks after the 1st cycle $l_d(1)$ and 2nd cycle $l_d(2)$ of wetting and drying were examined using F -test results and the relationships were derived with the multiple linear regression analysis as shown in Table 8.

Table 8. Summary of F -test and multiple linear regression analysis for $l_d(1)$ and $l_d(2)$ with durable and harmful minerals.

Predictor	F-test (at 95% confidence interval)			Multiple regression analysis (Linear model) (at 95% confidence interval)	
	df	f	* Statically significant?		
$l_d(1)$					
Quartz (Qz)	3	0.00015	Yes	$l_d(1) = 98.3 + 0.003 \text{ Qz} + 0.17 \text{ Ab} - 0.06 \text{ Kf}$	adj. $R^2 = 0.8745$
Albite (Ab)	3	0.00102	Yes		
K-feldspar (Kf)	3	0.00021	Yes		
Illite (Il)	3	0.00761	Yes	$l_d(1) = 100.0 - 0.11 \text{ Il} + 0.36 \text{ Py}$	adj. $R^2 = 0.9403$
Pyrite (Py)	3	1.49302	Yes		
$l_d(2)$					
Quartz (Qz)	3	0.00013	Yes	$l_d(2) = 92.1 + 0.01 \text{ Qz} + 1.17 \text{ Ab} - 0.51 \text{ Kf}$	adj. $R^2 = 0.8321$
Albite (Ab)	3	0.00093	Yes		
K-feldspar (Kf)	3	0.00019	Yes		
Illite (Il)	3	0.00694	Yes	$l_d(2) = 99.6 - 0.03 \text{ Il} - 0.81 \text{ Py}$	adj. $R^2 = 0.9911$
Pyrite (Py)	3	1.36055	Yes		

* Statistically significant result: "Yes": when f value < F critical value; "No": when f value > F critical value

df: Degree of freedom

As expected, from the F -test results, the durable and friendly minerals such as quartz, albite, and k-feldspar statistically and significantly affected both slake durability indexes. Also, the detected potentially harmful minerals such as illite and pyrite statistically and significantly affected the durability indexes after the 1st and 2nd cycle of wetting and drying. Here, biotite mineral was not considered as both Charnockite and Hornblende-Gneiss were not detected with considerable quantities. Therefore, based on the above statistical approaches, it was concluded the above five minerals revealed statistically significant effects on the durability of rocks. Consequently, analyzing the above minerals is mandatory when selecting the rock-derived aggregates for high durable applications.

4. Conclusions

This research was executed to implement the most appropriate high-grade metamorphic rocks available in Sri Lanka, for producing rock-derived outputs such as manufactured sand and coarse aggregate. All the rock types were selected from the high-grade metamorphic category having extreme

hardness and strength, which is expected as the ideal solution for construction aggregate manufacturing. It was identified that the demand for natural resources to fulfill the aggregate requirements in the construction activities has been escalated now. Therefore, the contractors are now trying to introduce both fine and coarse aggregates made from parent rocks in the construction works. The problem was noticed that the quarry operators who are producing manufactured sand and coarse aggregates are not paying much attention to selecting the suitable parent rocks. The investigation on analysis of the properties of high-grade rocks concludes the followings:

Initially, for sorting out the appropriate high-grade rocks, chemical and mineralogical tests were performed on the selected ten metamorphic rocks. Among the detected minerals, illite, pyrite, and biotite were considered as the most harmful constituents to the performance of concrete and mortar. Calc-Gneiss, Cordierite-Garnet-Gneiss, and Quartzite rocks showed a significant content of illite. Calc-Gneiss, Schist, and Marble rocks arrived with a considerable pyrite content. A noticeable content of biotite was observed in Calc-Gneiss, Quartzite, and Biotite-Gneiss rocks. Consequently, Charnockite, Hornblende-Gneiss, Intrusive Charnockite, and Granitic-Gneiss were concluded as the most suitable metamorphic rocks for producing aggregates for concrete and mortar.

To inspect the perpetuity of sources for aggregates to be used in constructions, the availability of the above selected four rock types was investigated using a detailed geological map of the country. Charnockite was identified as the most abundant rock type while, Hornblende-Gneiss revealed a considerable percentage of the total land area. Intrusive Charnockite and Granitic-Gneiss rocks underlie very small parts of the country's crust.

Physical, mechanical, and durability properties of the most applicable and plentifully available rocks such as Charnockite and Hornblende-Gneiss were examined. Hornblende-Gneiss manifested rougher surface texture than Charnockite. Other physical properties such as particle density, specific gravities, loose and packing densities, and water content were observed slightly higher with Hornblende-Gneiss than Charnockite. However, Charnockite showed higher water absorption than Hornblende-Gneiss due to the increased porosity.

Study on the strength properties resulted in good uniaxial compressive strength and tensile strength of Charnockite and Hornblende-Gneiss rocks. The *AIV*, *LAA*, and *ACV* of both rocks lied within the acceptable limits, which deduces the applicability of Charnockite and Hornblende-Gneiss derived aggregates in high-load bearing structures. Above both rocks manifested extreme performance against continuous wetting and drying cycles, which showed the pertinency of both rock-derived aggregates in high-durable applications.

As a consequence, high-grade metamorphic rocks such as Charnockite and Hornblende-Gneiss are deemed as the most appropriate and available rock types for producing manufactured sand and coarse aggregates to be used in concrete and mortar.

References

1. Branavan, A., Konthesingha, K.M.C. Fine Aggregate Usage in Concrete and Masonry Mortar by Local Construction Industries. Proceedings of 10th International Conference on Structural Engineering and Construction Management, Kandy. Sri Lanka, 2019. Pp. 106–113.
2. Pereira, K., Ratnayake, R. Water Integrity in Action: Curbing Illegal Sand Mining in Sri Lanka. Berlin, Germany. Water Integrity Network, 2013.
3. Padmalal, D., Maya, K. Sand Mining, Environmental Science and Engineering, 2014. Pp. 57–80.
4. Sing, M.C.P., Love, P.E.D., Tam, C.M. Review and exploration of river sand substitutes for concrete production in Asian countries, 2012. DOI: 10.1201/b13165-25
5. Gavriletea, M.D. Environmental Impacts of Sand Exploitation. Analysis of Sand Market. Sustainability. 2017. 9(1118). Pp. 1–26. DOI: 10.3390/su9071118
6. Branavan, A., Konthesingha, K.M.C., Nanayakkara, S.M.A., Premasiri, H.M.R. Optimizing Blending of Manufactured Sand with Offshore Sand Based on Physical and Virtue Characteristics. Journal of Materials Science Research and Reviews. 2020. 6 (3). Pp. 11–31. [Online]. URL: <https://www.journaljmsrr.com/index.php/JMSRR/article/view/30156> (date of application: 08.10.2021)
7. Branavan, A., Konthesingha, C., Nanayakkara, A. Performance evaluation of cement mortar produced with manufactured sand and offshore sand as alternatives for river sand. Construction and Building Materials. 2021. 297. DOI: 10.1016/j.conbuildmat.2021.123784
8. Branavan, A., Konthesingha, C., Nanayakkara, A. Influence of Blended Fine Aggregates on the Performance of Lime – Cement Mortar – A Statistical Approach. Proceedings of 7th International Multidisciplinary Engineering Research Conference (MERCon 2021), IEEE Xplore, Colombo, Sri Lanka. 2021. DOI: 10.1109/MERCon52712.2021.9525765
9. Jayawardena, U., Dissanayake, D. Identification of the most suitable rock types for manufacture of quarry dust in Sri Lanka. Journal of National Science Foundation Sri Lanka. 2008. 36 (3). Pp. 215–218. [Online]. URL: <https://jnfsf.sljol.info/articles/10.4038/jnfsr.v36i3.157/galley/298/download/> (date of application: 05.05.2020).
10. Jayatileke, S. Geology and Mineral Resources of Sri Lanka. Vidurava. 2015. 30 (1). Pp. 7–14.

11. Piyadasa, A. Prehistory of Sri Lanka: the geographical and geological background of Sri Lanka. 2017. [Online]. URL: <https://www.archaeology.lk/5186> (date of application: 14.04.2020).
12. Kroner, A., Cooray, P., Vitanaage, P. Lithotectonic Subdivision of the Precambrian Basement in Sri Lanka. In: Summary of Research of the German-Sri Lankan Consortium. Lefkosia, 1991. Pp. 5–21. [Online]. URL: [https://www.scrip.org/\(S\(351jmbnvtvnsjt1aadkposzje\)\)/reference/ReferencesPapers.aspx?ReferenceID=197417](https://www.scrip.org/(S(351jmbnvtvnsjt1aadkposzje))/reference/ReferencesPapers.aspx?ReferenceID=197417) (date of application: 15.08.2020).
13. van Wyk, P.R., Croucamp, L. Evaluation of rock types for concrete aggregate suitability for the construction of a gravimeter vault and access road at the Matjiesfontein Geodesy Observatory site near Matjiesfontein, South Africa. *Journal of the South African Institution of Civil Engineering*. 2014. 56 (2). Pp. 30–36. [Online]. URL: http://www.scielo.org.za/scielo.php?script=sci_arttext&pid=S1021-20192014000200004 (date of application: 16.08.2020).
14. Branavan, A., Konthesingha, C. Pertinence of Alternative Fine Aggregates for Concrete and Mortar: A Brief Review on River Sand Substitutions. *Australian Journal of Civil Engineering*. 2021. DOI: 10.1080/14488353.2021.1971596 [Article in Press].
15. Vitanaage, P. Tectonics and Mineralization in Sri Lanka. *Geol. Soc. Finl. Bull.* 1985. 57. Pp. 157–168. DOI: 10.17741/bgsf/57.1-2.013
16. Nawaratne, S.W. Feldspar and Vein Quartz Mineralization in Sri Lanka: A Possible Post Metamorphic Mid-Paleozoic Pegmatitic-Pneumatolytic Activity. *Journal of Geological Society of Sri Lanka*. 2009. 13. Pp. 83–96. [Online]. URL: http://www.investmentconsultantslk.com/industrial_reports_doc/feldspar%20&%20vein%20quartz%20in%20sri%20lanka.pdf (date of application: 13.04.2020).
17. Geological Map of Sri Lanka, Colombo: Geological Survey Department, Geological Survey and Mines Bureau, Sri Lanka. 1980.
18. Cooray, P. The Geology of Sri Lanka – problems and perspectives. *Journal of the Geological Society of Sri Lanka*. 1989. 3. Pp. 1–14. [Online]. URL: http://ifs.nsf.ac.lk/bitstream/handle/1/375/PRJ_11_ab.pdf?sequence=2&isAllowed=y (date of application: 05.04.2020).
19. McConnell, D., Steer, D. *The Good Earth: Introduction to Earth Science*. McGraw-Hill; McGraw-Hill Higher Education. 2nd edn. London, NY, 2010.
20. Prame, W. Crystalline Basement of Sri Lanka: An Overview based on Recent Advances. *Journal of the Geological Society of Sri Lanka*. 1995/96. 6. Pp. 37–49.
21. Kroner, A. African linkage of Precambrian Sri Lanka. *Geologische Rundschau*. 1991. 80 (2). Pp. 429–440. DOI: 10.1007/BF01829375
22. Pinna, P., Jourde, G., Calvez, J.Y., Mroz, J.M., Marques, J.M. The Mozambique Belt in northern Mozambique: Neo-proterozoic (1100-850 Ma) crustal growth and tectogenesis, and superimposed Pan-African (800-550 Ma) tectonism. *Precambrian Research*. 1993. 62(1-2). Pp. 1–59. DOI: 10.1016/0301-9268(93)90093-H
23. Dahanayake, K., Jayasena, H. General Geology and Petrology of some Precambrian Crystalline Rocks from the Vijayan Complex of Sri Lanka. *Precambrian Research*. 1983. 19 (3). Pp. 301–315. DOI: 10.1016/0301-9268(83)90018-9
24. Malaviarachchi, S.P., Takasu, A. Petrology of Metamorphic Rocks from the Highland and Kadugannawa Complexes, Sri Lanka. *Journal of the Geological Society of Sri Lanka*. 2011, 14, Pp. 103–122. DOI: 10.13140/2.1.5043.0401
25. Jayawardena, U., Dissanayake, D. Identification of the most suitable rock types for manufacture of quarry dust in Sri Lanka. *Journal of National Science Foundation Sri Lanka*. 2008. 36(3). Pp. 215–218. [Online]. URL: <https://jnsfsl.sjoi.info/articles/10.4038/jnsfsl.v36i3.157/galley/298/download/> (date of application: 04.08.2020).
26. Tugrul, A., Hasdemir, S., Yilmaz, M. The Effect of Feldspar, Mica and Clay Minerals on Compressive Strength of Mortar. *Engineering Geology for Society and Territory*. 2014. 5. Pp. 93–96. DOI: 10.1007/978-3-319-09048-1_18
27. Leemann, A., Holzer, L. Influence on mica on the properties of mortar and concrete. *Proceedings of 8th EMABM*. Athens, Greece, 2011, Pp. 199–204, [Online]. URL: https://www.researchgate.net/publication/304181219_Influence_of_mica_on_the_properties_of_mortar_and_concrete (date of application: 15.07.2020).
28. Norvell, J.K., Stewart, J.G., Juenger, M.C.G., Fowler, D.W. Influence of Clays and Clay-Sized Particles on Concrete Performance. *Journal of Materials in Civil Engineering*. 2007. 19 (12). Pp. 1053–1059. [Online]. URL: <https://ascelibrary.org/doi/10.1061/%28ASCE%290899-1561%282007%2919%3A12%281053%29> (date of application: 16.06.2020).
29. Grasso, J. Reasons for Choosing Quality Aggregate. *Monroe Recycling & Aggregates*. 2019. [Online]. URL: <https://www.monroeaggregate.com/2019/12/18/reasons-for-choosing-quality-aggregate/> (date of application: 05.02.2020).
30. Mitchell, C. Construction aggregates: evaluation and specification. *Proceedings of 3rd International Forum for Industrial Rocks and Mining*. Fujairah, UAE, 2015. [Online]. URL: <http://nora.nerc.ac.uk/id/eprint/510604/> (date of application: 16.05.2020).
31. Loorents, K.L., Johansson, E. Free mica grains in crushed rock aggregates. *Bull Eng Geol Environ*. 2007. 66. Pp. 441–447. DOI: 10.1007/s10064-007-0091-4
32. Ugolini, F.C., Corti, G., Agnelli, A., Piccardi, F. Mineralogical, Physical and Chemical Properties of Rock Fragments in Soil. *Soil Science*. 1996. 161 (8). Pp. 521–542. DOI: 10.1097/00010694-199608000-00007
33. Scott, P.W., Rollinson, G.K. Crushed Rock Aggregates: Their Mineralogy and Textures Using Automated Scanning Electron Microscopy. *Proceedings of the 18th Extractive Industry Geology Conference 2014 and technical meeting*, Oxford, UK, 2015. Pp. 49–68. [Online]. URL: https://www.researchgate.net/publication/307555555_CRUSHED_ROCK_AGGREGATES_THEIR_MINERALOGY_AND_TEXTURES_USING_AUTOMATED_SCANNING_ELECTRON_MICROSCOPY (date of application: 24.09.2020).
34. Johansson, E., Miskovsky, K., Loorents, K.J. Estimation of Rock Aggregates Quality Using Analyses of Drill Cuttings. *JMEPEG*. 2009. 18. Pp. 299–304. DOI: 10.1007/s11665-008-9284-7
35. Rahmouni, A., Boulanouar, A., Boukalouch, M., Samaouali, A., Geraud, Y., Sebbani, J. Porosity, Permeability and Bulk Density of Rocks and their Relationships based on Laboratory Measurements. *Romanian Journal of Materials*. 2014. 44 (2). Pp. 147–152. [Online].
36. Yu, Y. An Experimental Method to Measure the Porosity from Cuttings: Evaluation and Error Analysis. *Texas Tech University, Texas*, 2013. [Online]. URL: <https://ttu-ir.tdl.org/bitstream/handle/2346/48848/YU-THESIS.pdf?sequence=1> (date of application: 18.04.2020).
37. Zayed, A.M., Brown, K., Hanhan, A. Effects of Sulfur Trioxide Content on Concrete Structures Using Florida Materials. *University of Florida, Tampa*, 2014. [Online]. URL:

- <https://trid.trb.org/view/755078#:~:text=Concrete%20strength%20data%20indicate%20that,strength%20loss%20at%20180%20days.&text=For%20cements%20moderate%20in%20tricalcium,tolerant%20to%20higher%20SO3%20content> (date of application: 22.06.2020).
38. Bentz, D.P., Arnold, J., Boisclair, M.J., Jones, S.Z., Rothfeld, P., Stutzman, P.E., et al. Influence of Aggregate Characteristics on Concrete Performance. National Institute of Standards and Technology. Maryland, 2017. DOI: 10.6028/NIST.TN.1963
 39. University of Minnesota. Mineral Web Pages, 2010. [Online]. URL: https://www.esci.umn.edu/courses/1001/minerals/potassium_feldspar.shtml (date of application: 12.02.2020).
 40. Lagerblad, B., Kjellsen, K.O. Effect of Mineralogy of Fillers on the Cement Hydration. The Modelling of Microstructure and its Potential for Studying Transport Properties and Durability. 1996. 304. Pp. 157–165. [Online]. URL: https://link.springer.com/chapter/10.1007%2F978-94-015-8646-7_7 (date of application: 19.06.2020).
 41. Benachour, Y., Davy, C.A., Skoczylas, F., Houari, H. Effect of a high calcite filler addition upon microstructural, mechanical, shrinkage and transport properties of a mortar. Cement and Concrete Research. 2008. 38 (6). Pp. 727–736. DOI: 10.1016/j.cemconres.2008.02.007
 42. Borziak, O.S., Plugin, A.A., Chepurina, S.M., Zavalniy, O.V., Dudin, O.A. The effect of added finely dispersed calcite on the corrosion resistance of cement compositions. IOP Conf. Series: Materials Science and Engineering. 2019. 708. DOI: 10.1088/1757-899X/708/1/012080
 43. AGI, American Geosciences Institute, 2020, [Online]. URL: <https://www.americangeosciences.org/critical-issues/faq/how-dopyrite-and-pyrrhotite-damage-building-foundations> (date of application: 13.07.2020).
 44. Duchesne, J., Fournier, B. Deterioration of Concrete by the Oxidation of Sulphide Minerals in the Aggregate. Journal of Civil Engineering and Architecture. 2013. 7 (8). Pp. 922–931. DOI: 10.17265/1934-7359/2013.08.003
 45. Leite, M.H., Ferland, F. Determination of unconfined compressive strength and Young's modulus of porous materials by indentation tests. Engineering Geology. 2001. 59 (3). Pp. 267–280. DOI: 10.1016/S00137952(00)00081-8
 46. Franklin, J.R., Chandra, R. The Slake-Durability Test. Int. J. Rock Mech. Min. Sci. 1972. 9 (3). Pp. 325–341. DOI: 10.1016/0148-9062(72)90001-0
 47. Franklin Trow Associates. Field Evaluation of Shales for Construction Projects. Research and Development Project No. 1404, Ministry of Transportation and Communication, Research and Development Branch, Ontario, 1979.

Information about author:

Branavan Arulmoly

ORCID: <https://orcid.org/0000-0001-9058-6567>

E-mail: branavanarulmoly@sjp.ac.lk

Chaminda Konthesingha, PhD

E-mail: konthesingha@sjp.ac.lk

Anura Nanayakkara, PhD

ORCID: <https://orcid.org/0000-0003-4887-0526>

E-mail: smn@civil.mrt.ac.lk

Ranjith Premasiri, PhD

E-mail: ranjith@uom.lk

Received 02.01.2021. Approved after reviewing 08.10.2021. Accepted 09.10.2021.



Research article

UDC 625.85

DOI: 10.34910/MCE.113.9



Effect of temperature on permanent deformation of polymer-modified asphalt mixture

N. Lotfi Omran^a , K. Rajaei^b , S.M. Marandi^a 

^a Shahid Bahonar University of Kerman, Kerman, Iran

^b Graduate University of Advanced Technology, Kerman, Iran

✉ navid.lotfii.omran@gmail.com

Keywords: asphalt mixtures, polymers, temperature, dynamic creep test, permanent deformation

Abstract. This study aims to evaluate the permanent deformation of unmodified and styrene-butadiene-rubber (SBR) modified asphalt mixtures using dynamic creep test. The purpose was to assess the effect of SBR as one of the most plentiful and low-cost polymers in Iran on rutting resistance of asphalt mixtures in the regions with hot climate, such as the areas around the “Persian Gulf”, and the central deserts of the “Iran Plateau”. First, the critical gradation of aggregates with higher permanent deformation was determined. Then, the aggregates with critical gradation were mixed with the optimum amount of bitumen modified by different amounts of SBR, and tested to obtain an optimum SBR content with lower permanent deformation. Finally, the unmodified and SBR-modified asphalt mixtures with optimum SBR content (6%wt) were tested at 40 and 50 °C as the simulated ambient temperatures in order to evaluate the effect of SBR and rising temperature on rutting resistance of the asphalt mixtures. In addition, the flow number (FN) of asphalt mixtures is calculated according to Goh and You method. Results showed that with addition of 6% SBR, the permanent strains of asphalt mixtures decreased by 39 and 60%, and the creep modulus increased by 64 and 133% at 40 and 50 °C, respectively. Furthermore, with the temperature rising from 40 to 50 °C, the permanent strains of asphalt mixtures containing 0 and 6% SBR increased by 61 and 5%, and their creep modulus decreased by 34 and 6%, respectively. The FNs of unmodified samples were obtained 8416 and 9728 loading cycles at 40 and 50 °C, respectively. In contrast, up to the last loading cycle, the SBR-modified samples did not experience the tertiary flow at both ambient temperatures. These results let us conclude that the SBR-modified bitumen is able to significantly reduce the permanent deformations, and enhance the resilience and creep modulus of asphalt mixtures; moreover, it can minimize the negative effects of rising temperature on their engineering properties.

Citation: Lotfi Omran, N., Rajaei, K., Marandi, S.M. Effect of temperature on permanent deformation of polymer-modified asphalt mixture. Magazine of Civil Engineering. 2022. 113(5). Article No. 11309. DOI: 10.34910/MCE.113.9

1. Introduction

In recent decades, with progress in all fields of science, road construction was also included in this scientific development. The mixture of stone materials with bitumen provided a novel product called asphalt mixture. This material has a limited service life like other construction materials. However, two main factors, traffic loads and climate condition, cause more decrease in service life of asphalt mixtures than other construction materials. On the other hand, in recent years the costs of roads construction and their maintenance have increased. Thus, damages of asphalt layer of flexible pavements such as rutting, reflective cracking, fatigue cracking, etc., impose immense annual costs on the contractors and organizations responsible for road maintenance and operation. Rutting (permanent deformation) is one of the most common flexible pavements damages that occurs under heavy traffic loads particularly in hot climates [1, 2]. The pavement structure undergoes accumulated permanent deformations under repetitive

traffic loads [3]. Permanent deformation of pavements includes two different modes: first, the compactive deformation (consolidation of layers), and secondly, the plastic deformation (asphalt shear flow) [4, 5]. In the first mode, the deformed surface is lower than the initial pavement surface and is occurs in the wheel path; and in the second mode, the deformed surface is higher than the initial pavement surface and is occurs in form of "heave" between and outside of wheel paths due to shear flow of asphalt materials [5]. Presence of depressions and heaves on the pavement surface may cause serious hazards for vehicles. The resistance of different types of asphalt mixtures with the ordinary bitumen against high temperatures depends on the type and content of bitumen, shape and gradation of aggregates, as well as climate condition. Therefore, in view of high economical and time costs of annual repair of road surface, studying and introducing economically and technically optimized methods to improve the thermal stability and overcome the rutting of road surface is inevitable.

Binder modification using petrochemical products such as polymers is an effective method for improving the resistance of asphalt mixtures against the common damages [6] including fatigue cracking [7, 8], moisture susceptibility [7, 9], rutting in high temperature [5, 7, 8, 10–12], cracking in low temperature [10–13], etc. The styrene-butadiene rubber (SBR) is one of the polymers used for bituminous binder modification [13, 14] which is produced by copolymerization of styrene and butadiene [7]. SBR is a member of elastomers family which can improve the rheological properties, flexibility, thermal and fatigue cracking, and moisture susceptibility of asphalt mixtures [7]. The butadiene soft monomer makes the binder more flexible, while the styrene hardener monomer increases the binder softening point [7]. In addition, SBR has higher cracking resistance and lower cost in comparison to another binder modifier, styrene-butadiene-styrene (SBS) [11]. Several researchers investigated the performance of polymer-modified asphalt mixtures [5, 7, 8, 10, 13, 15–20] Khodaii and Mehrara [5] investigated the permanent deformation of unmodified and SBS-modified asphalt mixtures using dynamic creep test. They used 4, 5 and 6% of SBS as a binder modifier and concluded that the SBS-modified asphalt mixtures had lower permanent deformation and higher compactibility than unmodified asphalt mixture. Hao et al. [17] used the mixture of SBR and polyphosphoric acid (PPA) to improve different properties of asphalt and asphalt mixtures. They demonstrated that the combination of 0.75% PPA/2.5% SBR shows excellent anti-deformation property and cracking behavior. Zhai et al. [10] used the combination of SBR and nano-CaCO₃ to evaluating the performance of asphalt mixtures. Their results showed that 5% nano-CaCO₃/4% SBR significantly improved deformation resistance performance and provided superior rutting resistance of asphalt mixture compared to SBS-modified asphalt mixture. Vamegh et al. [7] assessed the moisture susceptibility and permanent deformation of modified asphalt mixtures by using the blends of SBR and polypropylene as inexpensive asphalt modifiers. Their experimental results indicated that the moisture resistance and retained Marshall stability of polymer blends-modified samples were approximately identical to SBS-modified samples. Moreover, with the increase in the SBR content, the indirect tensile strength, moisture resistance, ductility under repetitive loads and rutting resistance of asphalt mixtures increased as well. Ameri et al. [8] studied the fatigue life of asphalt mixture modified by styrene-butadiene rubber (SBR), poly butadiene rubber (PBR) and their residual wastes. They concluded that all used polymers and their residual wastes enhanced the fatigue resistance of asphalt mixtures, while the residual waste polymers with lower costs had an effect similar to that of the SBR and PBR. Liu and Liang [20] investigated the influence of SBR and SBS on properties of cement emulsified asphalt mortar (CEAM). Their results indicated that the flow time and air content of fresh CEAM decreased and increased with the SBR and SBS contents, respectively. In addition, the type and content of modifiers had less effect on compressive strength of CEAM at early age. Nevertheless, at later age, the compressive strength of SBS-modified CEAM reduced obviously, which was related to the non-uniformity and larger air content of this mixture. The flexural strength of modified CEAM had similar trend for both modifiers. The authors also said that after 100 freeze-thaw cycles, the quality of SBR-modified CEAM increased obviously.

There are technical and economical considerations of using appropriate binder modifiers and aggregate gradations for each special condition of the roads such as traffic loads and climate conditions. In addition, little attention is paid to the temperature effect on permanent deformation of SBR-modified asphalt mixtures as a common economical mixture in the literatures. Thus, this study aimed to investigate the permanent deformation of unmodified (dense and coarse graded asphalt mixtures) and SBR-modified asphalt mixtures under rising temperature using dynamic creep test. The flow number of the asphalt mixtures as a rutting indicator [21, 22] was determined using Goh and You method [23]. In the country of research, two main factors affected the selection of SBR as an asphalt modifier. First, very low price of SBR compared to SBS; and secondly, suitable performance of SBR-modified asphalt mixtures against many common damages of asphalt mixtures at both high [12, 24] and low temperatures [8, 10, 14, 25]. These properties are suitable for regions with hot summers and cold winters, such as central deserts of "Iran plateau", and the communication roads of commercial ports around the "Persian Gulf" with very hot climate and high volume traffic of heavy vehicles.

2. Materials

2.1. Stone materials

The siliceous filler and crushed aggregates were used as stone materials. To evaluation the effect of aggregate gradation on permanent deformation of asphalt mixtures, two gradations of aggregates known as coarse and dense grades were used. These gradations were in the permitted range (upper and lower limits) of aggregate gradations for asphalt mixtures according to the Journal No. 101 of Plan and Budget Organization of Iran, with the subject of "General Technical Specifications of the Road". The particle size distributions and some engineering properties of the used stone materials (dense and coarse graded) are shown in Figure 1 and Table 1, respectively.

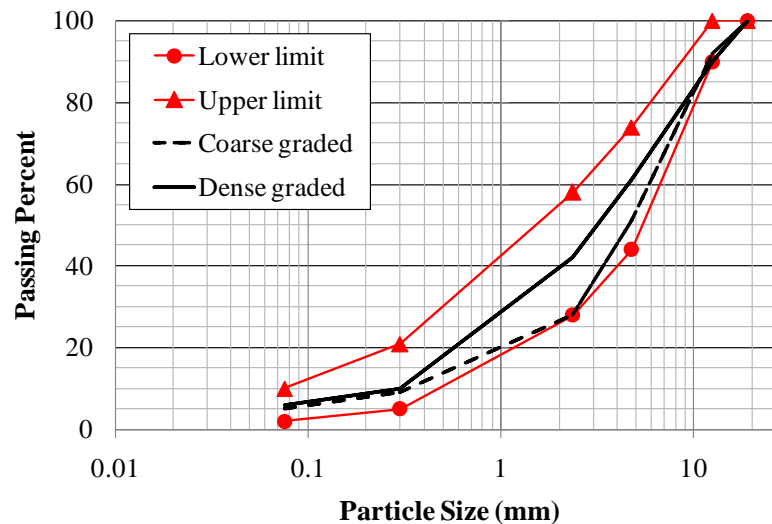


Figure 1. Particle size distribution of used stone materials (dense and coarse graded).

Table 1. Engineering properties of stone materials.

Property	Test method	Value	Standard value
Los Angeles abrasion loss (%)	AASHTO T96	29	$\leq 25^a$
Two fractured faces (%)	ASTM D5821	100	100^a
Flakiness index (%)	BS 812-105.1	10	$\leq 10^b$
Elongation index (%)	BS 812-105.2	10	$\leq 10^b$
Bulk specific gravity of coarse aggregates	AASHTO T85	2.659	
Absorption of coarse aggregates (%)	AASHTO T85	0.7	$\leq 2.5^a$
Bulk specific gravity of fine aggregates	AASHTO T84	2.592	
Absorption of fine aggregates (%)	AASHTO T84	1.7	$\leq 2.5^a$
Bulk specific gravity of mineral filler	AASHTO T84	2.721	

^a According to Journal No. 101 of Plan and Budget Organization of Iran, with the subject of "General Technical Specifications of the Road".

^b According to MS-2.

2.2. Binder

The used bitumen as a binder with penetration grade of 60–70 was produced in Isfahan oil refinery. Some engineering properties of bitumen are presented in Table 2.

Table 2. Engineering properties of bitumen.

Property	Test method	Value	
		Value	Standard value ^a
Specific gravity at 25 °C	AASHTO T228 (ASTM D70)	1.018	
Penetration at 25 °C (100g-5s) (0.1mm)	AASHTO T49 (ASTM D5)	66	60-70
Softening point (°C)	AASHTO T53 (ASTM D36)	50	49-56
Ductility at 25 °C (cm)	AASHTO T51 (ASTM D113)	>100	≥100
Solubility in trichloroethylene ^b	AASHTO T44 (ASTM D2042)	99.7	≥99
Flash point (°C)	AASHTO T48 (ASTM D92)	285	≥232
Kinematic viscosity at 120 °C (cSt)	AASHTO T201 (ASTM D2170)	565	
Kinematic viscosity at 135 °C (cSt)	AASHTO T201 (ASTM D2170)	321	
Kinematic viscosity at 160 °C (cSt)	AASHTO T201 (ASTM D2170)	133	
Thin-Film of bitumen (163 °C-5h)	AASHTO T179 (ASTM D1754)	+	≤0.8
Heating loss (%)	–	0.04	
Penetration index (PI)	–	-0.53	

^a According to the Journal No. 234 of Plan and Budget Organization of Iran, with the subject of "Iran Highway Asphalt Paving Code".

^b Conducted by CC4.

2.3. Binder modifier

Granular SBR-1712 with linear molecular structure was produced in Bandar-e-Imam Petrochemical Co., and used as a binder modifier with the amounts of 4, 6 and 8%wt of the bitumen. Some engineering properties of SBR-1712 are presented in Table 3.

Table 3. Engineering properties of SBR-1712 (reported by manufacturer).

Property	Test method	Value
Volatile materials (% wt)	ASTM D1416	<0.75
Ash content (% wt)	ASTM D1416	<1.5
Organic acids (% wt)	ASTM D1416	3.9–5.7
Soaps (% wt)	ASTM D1416	<0.5
Bounded styrene (% wt)	ASTM D1416	22.5–24.5
Raw viscosity	ASTM D1646	42–52
Compound viscosity	ASTM D1646	<62
Tensile strength (kg/cm ²)	ASTM D412	>200
Ultimate elongation (35 min cured) (%)	ASTM D412	>530
300% modulus (35 min cured) (kg/cm ²)	ASTM D412	79–109

2.4. Sample preparation

2.4.1. Obtaining the optimum bitumen contents (OBC)

To obtain the optimum bitumen contents (OBC) for unmodified coarse and dense graded mixtures, the Marshall method was used according to ASTM D1559 with 75 blows on two ends of each sample. Some of the base properties of unmodified coarse and dense graded asphalt mixtures are given in Table 4.

Table 4. Base properties of unmodified asphalt mixtures.

Property	Test method	Value		Standard value ^a
		Coarse graded	Dense graded	
Optimum bitumen content (OBC) (%)	ASTM D1559	5	5.5	
Marshall stability (kg)	ASTM D1559	640	610	≥800
Specific gravity	AASHTO T166	2.41	2.407	
Air void (%)	MS-2	1.9	1.5	3-5
Flow (mm)	ASTM D1559	2.7	3	2-3.5

^a According to AASHTO T245.

2.4.2. SBR-modified bitumen

To obtain a homogeneous SBR-modified bitumen, in premixing process, the bitumen was heated to 150 °C and SBR granules in desired percentages (4, 6 and 8% wt of bitumen) were added to the bitumen and mixed by a High-Shear mixer (Silverson 14RT) with the speed of 150 rpm for 5 min. After premixing process, the temperature and rotation speed of mixer were increased to 170°C and 1000 rpm respectively, until approximate homogeneity was achieved. Then, the mixing process was continued for 75–90 min with the speed of 2000 rpm.

2.4.3. Sample preparation for dynamic creep test

In order to prepare the samples for dynamic creep test, the Marshall method was used with 75 blows on two ends of each sample. The dimensions of cylindrical samples were 101.6 mm in diameter and 63.5±1 mm in height. It is worth noting that to determine the critical aggregate gradation in terms of permanent deformation value, the unmodified asphalt mixtures with coarse and dense graded aggregates were tested using dynamic creep test first. Then, the critical aggregate gradation with higher permanent deformation was selected to prepare the SBR-modified asphalt mixtures and continue the tests. The next section contains more explanations.

3. Results and Discussion

The dynamic creep tests were carried out on the samples using Universal Test Machine (UTM 14P) according to Australian code AS 2891.12.1. The used setup of UTM 14P and testing conditions are shown in Table 5.

Table 5. The used setup of UTM 14P and testing conditions.

Property	Value
Pre-loading stress (KPa)	10
Pre-loading time (s)	50
Confining pressure (KPa)	0
Contact stress (KPa)	2
Deviator stress (KPa)	200
Wave shape	Square pulse
Frequency (Hz)	0.5
Pulse width (ms)	500
Rest period (ms)	1500
One cycle time (ms)	2000
End of loading cycles	10000
Ambient temperatures (°C)	40 and 50

The repetitive axial stress pulse was applied to the samples and the vertical deformations were measured by the Linear Variable Displacement Transducer (LVDTs). Before the tests, the exact dimensions of each sample were measured and supplied to the device software. The UTM device was equipped with an environmental chamber to change the temperature of samples to desired ambient temperatures (40 and 50 °C). The main reason for selecting these ambient temperatures was to simulate the approximate normal range of maximum daily temperatures of the considered areas in the summer (the areas around the "Persian Gulf", and the central deserts of the "Iran Plateau"). These ambient temperatures were also applied by Khodaii and Mehrara [5] for dynamic creep test on polymer-modified asphalt mixtures. The samples were placed in the testing device 2 hours prior to loading start to achieve the temperature equilibrium. After that, the pre-load compressive stress (10 KPa) was applied onto the samples by loading shaft for 50 s to eliminate any probable roughness of samples surface. This causes a uniform load distribution on the cross section of the samples. Then, the stress was reduced to 2 KPa as contact stress and the deviator stress of 200 KPa was applied to the samples for 500 ms and lifted for 1500 ms as rest period. Each of these loading and lifting is known as one cycle. The dynamic creep tests were continued up to 10000 cycles and the contact stress was applied constantly throughout the tests, even in the rest periods.

In the first stage, the coarse and dense graded mixtures were prepared using unmodified bitumen to determine the critical mix design with more permanent deformation at the highest ambient temperature (50

°C). As shown in Figure 2, in the initial loading cycles (up to 1500 cycles), the permanent strain of coarse graded mixture was slightly higher than that for dense graded one. This can be due to more compactive deformation of coarse graded mixture because of more air voids. However, in cycles above 1500, there was a dramatic difference between the permanent strains of coarse and dense graded mixtures. So that at the end of 10000 cycles, the permanent strain of dense graded mixture (24623 μs) was about 96% higher than the coarse graded permanent strain. Like SMA mixtures, the skeleton of coarse graded mixture was built with the purpose of stress transition between the coarse aggregates, and the thin film of bitumen that covers the aggregates is more to prevent the aggregates segregation than for the load-bearing purpose. There is more bitumen content in the dense graded mixture than in the coarse graded one, and in consequence, the thermo-mechanical behavior of this mixture depends more on the properties of bitumen than that of the coarse graded mixture. Therefore, the dense graded mixture was selected as a critical mix design with high chance of the occurrence of rutting to be modified by SBR in further research.

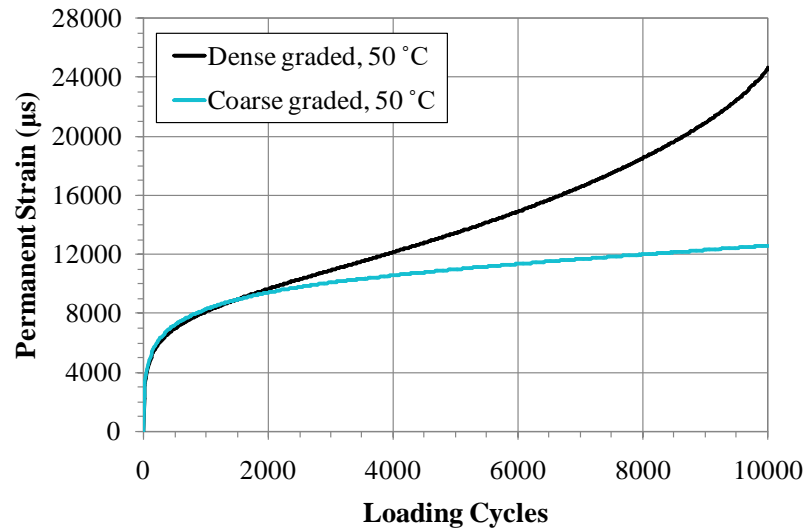


Figure 2. Permanent deformation curves of unmodified coarse and dense graded asphalt mixtures.

In the second stage, to determine the optimum SBR content, the dense graded aggregates as the critical gradation were mixed with modified bitumen by 4, 6 and 8%wt of SBR and tested by UTM device. These assumed SBR contents are close to the optimum polymer contents of some researches [5, 7, 26]. Figures 3 and 4 illustrated the permanent strains and creep modulus of unmodified and SBR-modified dense graded samples containing different SBR contents at ambient temperature of 40 °C, respectively. As can be seen in Figure 3, with addition of SBR into the samples, the permanent deformations were significantly decreased. This can be due to the good elastic properties of SBR and better adhesiveness of SBR-modified bitumen to the stone materials to create a stronger tensile connector between the aggregates. Moreover, as can be seen in Figure 4, with addition of SBR to the asphalt mixture, as well as with the increase of its content, the creep modulus of samples increased. The lowest permanent strain (9044 μs) and highest creep modulus (21.9 MPa) at the end loading cycle belonged to the sample containing 8% of SBR. However, the difference between the permanent strain and creep modulus of this sample and those of the 6% SBR sample (9355 μs and 21.3 MPa, respectively) was very slight. Therefore, since using as little polymeric materials as possible is more beneficial, 6% of SBR was considered an optimum content for consequent studies. The decrease in permanent deformation and increase in creep modulus of samples containing different amounts of SBR compared to unmodified sample are presented in Figure 5 (a and b). As can be seen in Figure 5a, with the increase of SBR content, the permanent deformation decreased more and more to the point the decrease in permanent deformations of samples containing 4, 6 and 8% of SBR, were 27, 39 and 41%, respectively. The decrease in permanent deformation value of the sample containing 4% of SBR has a considerable difference from that for the 6% SBR sample. On the other hand, the difference of the decrease of samples with 6 and 8% of SBR was only 2%. According to Figure 5b, the above mentioned relationships in terms of the increase in creep modulus of asphalt mixtures due to addition of SBR and increase in its content, are significant. So that in high SBR contents (6 and 8%), the creep modulus of modified asphalt mixtures increased 64 and 69%, respectively. Thus, as mentioned earlier, due to slight differences between the effectiveness of 6 and 8% of SBR on engineering properties of asphalt mixtures, 6% of SBR was chosen as the optimum content.

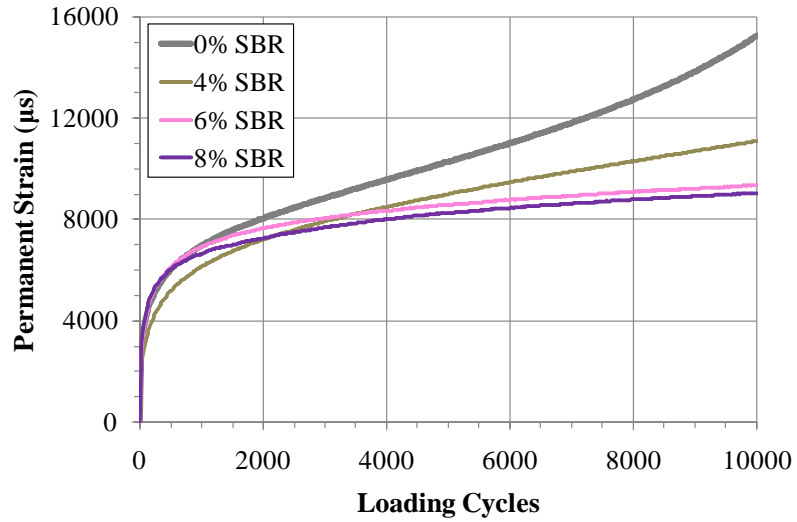


Figure 3. Permanent deformation curves asphalt mixtures containing different SBR contents at 40 °C.

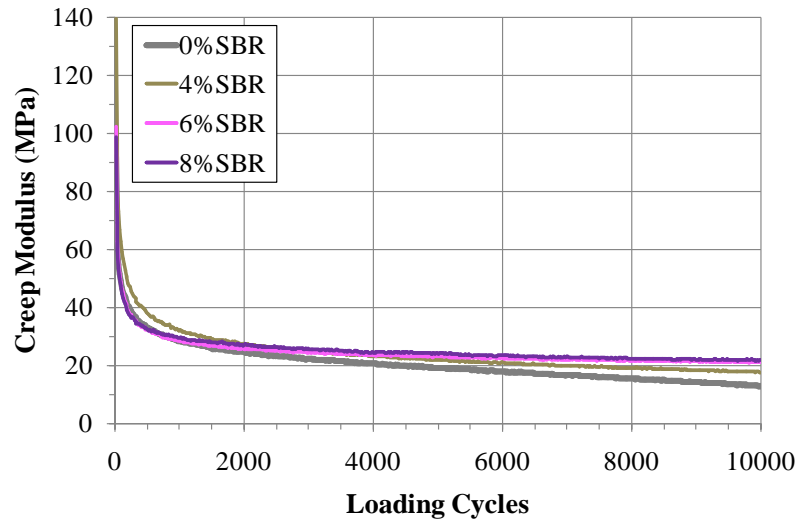


Figure 4. Creep modulus curves of asphalt mixtures containing different SBR contents at 40 °C.

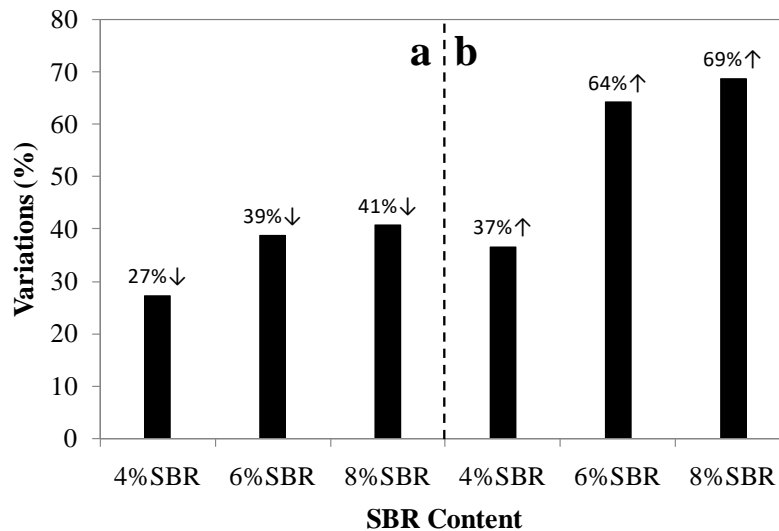


Figure 5. a) Decrease in permanent strain, and b) increase in creep modulus (Mc) of asphalt mixtures with addition of different amounts of SBR at 40 °C at the end of 10000 loading cycles.

In the third stage, the unmodified and modified dense graded samples with 6%wt of SBR were tested at 40 and 50 °C as ambient temperatures to evaluate the effect of SBR on permanent deformation of asphalt mixtures at high temperatures and in condition of rising temperature. As illustrated in Figure 6, at the last load cycle, the permanent strains of SBR-modified samples (9355 μs at 40 °C, and 9825 μs at 50 °C) were significantly lower than that for unmodified ones (15264 μs at 40 °C, and 24623 μs at 50 °C). Figure 7a also indicates that with the temperature rising from 40 to 50 °C, the permanent strain of unmodified sample increased by 61%, while this increase was 5% for the SBR-modified sample. This indicate that in contrast to the unmodified sample, rising temperature has a slight negative effect on the rutting resistance of SBR-modified asphalt mixtures. With rising temperature, the viscosity of binder will decrease and the asphalt mixtures undergo more and faster deformations. This decrease in viscosity is significantly more obvious in unmodified samples during rising temperature. While the binder is modified by polymeric additives like SBR, rising temperature had not remarkable effect on decreasing its viscosity due to the good temperature stability of polymer-modified bitumen. This is due to creation of polymeric network in the bitumen structure, which is more temperature-resistant. The confirmation of this is shown in Figure 7b: with 6% SBR addition, the permanent strain of asphalt mixtures decreased by 39 and 60% at 40 and 50 °C, respectively. This was due to a very low increase in permanent strain of SBR-modified mixtures (5%) against rising temperature, in comparison to that for unmodified ones (61%).

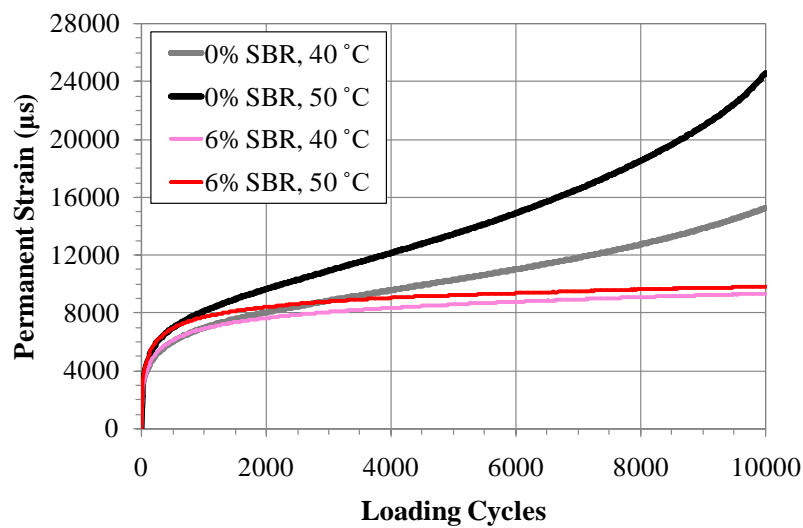


Figure 6. Permanent deformation curves of unmodified and SBR-modified asphalt mixtures at different ambient temperatures.

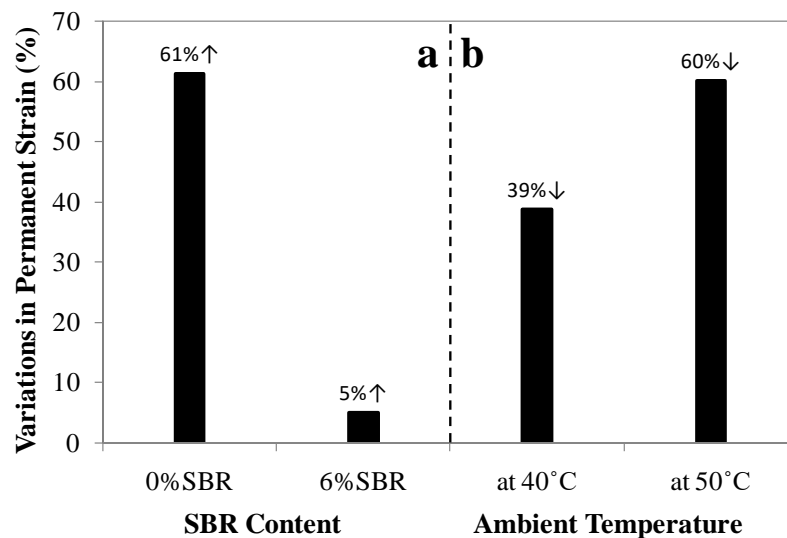


Figure 7. Increase and decrease in permanent strain of a) unmodified and modified asphalt mixture with 6% of SBR due to temperature rising from 40 to 50 °C, and b) asphalt mixtures with 6% SBR addition at 40 and 50 °C, respectively, at the end of 10000 loading cycles.

Figure 8 showed the resilient modulus of unmodified and modified samples versus the load repetition at both ambient temperatures of 40 and 50 °C. As indicated, the resilient modulus of modified samples was higher than that for unmodified ones at both ambient temperatures. The rising temperature caused a decrease in resilient modulus due to a drop in binder viscosity. In initial time of loading up to around 500 cycles, a sharp rise (about 60–70 MPa) was observed in resilient modulus of all of the tested samples. As reported by Khodaii and Mehrara [5], compactive deformation has a direct relation with resilient modulus, so that the more compactive deformation the more resilient modulus. Therefore, it can be said that all of the unmodified and modified samples experienced compactive deformations in initial cycles of loading. After that, as the loading cycles continued, a slight rising or a drop were observed in their resilient modulus trends. This means that the samples were gently compacted [5]. After 6000 cycles, the unmodified samples showed a downward trend in their resilient modulus curves, while the modified samples remained at a constant level. It can be concluded that in near-to-last cycles, the compactive deformation of unmodified samples seized and the shear flow tended to initiation. On the other hand, the general trends of resilient modulus of modified samples were at approximately the same level, which means the compactive deformation of modified samples was slowly progressing up to the last loading cycle. The main reason of this lies in the elastic properties of the SBR network, which preserved the stone materials and prevented and/or postponed the excessive deformations.

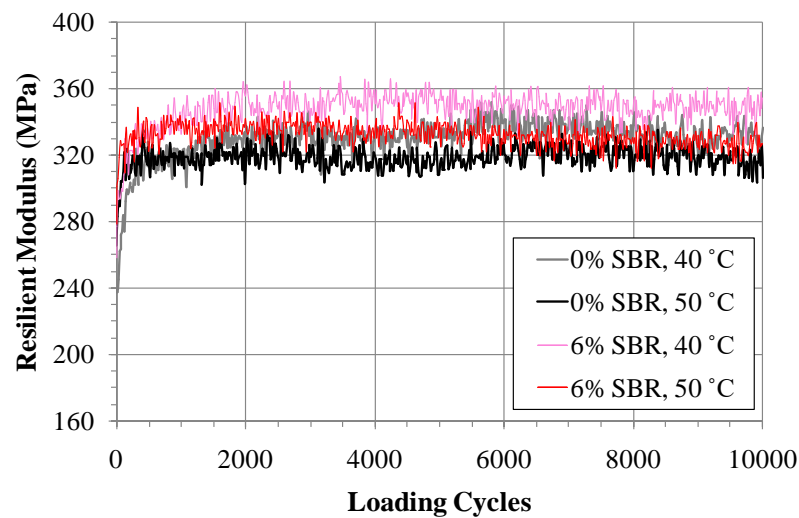


Figure 8. Resilient modulus of unmodified and SBR-modified asphalt mixtures at different ambient temperatures.

Figure 9 illustrates the variations of creep modulus of unmodified and modified samples versus the loading cycles at different ambient temperatures. As it can be seen, the creep modulus of all samples had a sharp drop (from 80–100 to around 30 MPa) in initial loading times up to around 500 cycles. This can be due to the compactive deformation of samples in initial loading cycles. After these drops, the creep modulus of SBR-modified samples reached an approximately constant level, while a 10 °C rise in ambient temperature had a negligible effect on their creep modulus. So that after 10000 loading cycles, the creep moduli of the samples modified by 6% of SBR at 40 and 50 °C, were about 21.3 and 20 MPa, respectively. On the other hand, the unmodified samples showed a decreasing trend in their creep modulus and a 10 °C rise in ambient temperature had a significant effect. So that the creep modulus of the sample tested at 50 °C (8.6 MPa) significantly decreased in comparison to the one tested at 40 °C (13 MPa). According to researches conducted by Gokhale et al. [4] and Khodaii and Mehrara [5], the dynamic creep test conducted by UTM device could not separate the compactive and shear deformations of asphalt mixtures from each other. But Gokhale et al. [4] reported that the compactive deformation mainly occurs in initial loading cycles while with the continuing load repetition, the compactive deformation tends to decrease and the shear deformation gradually appears. Therefore, in initial loading cycles, the UTM device considered the rising resilient modulus as permanent deformation and indicated a considerable drop in creep modulus curve [5]. As indicated in Figure 10a, with a 10 °C rise in temperature, the creep modulus of unmodified sample decreased by 34%. While this decrease was 6% for SBR-modified sample, which was due to the good stability of SBR-modified samples against rising temperature. Figure 10b indicates that with rising temperature, the positive effect of SBR becomes more obvious. So that at 40 °C, with the 6% SBR addition, the creep modulus of asphalt mixture increased by 64%. Whereas the same increase at 50 °C was 133%. As mentioned earlier, this can be due to the better stability of SBR-modified bitumen against rising temperature in comparison to the unmodified samples.

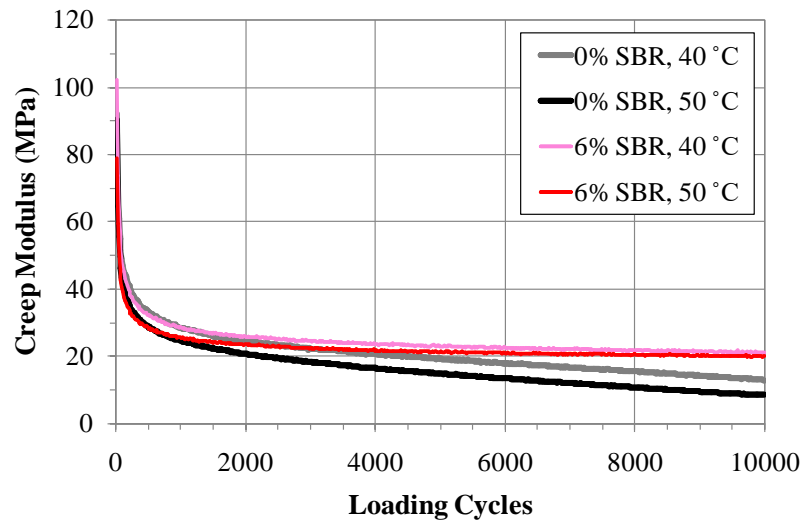


Figure 9. Creep modulus of unmodified and SBR-modified asphalt mixtures at different ambient temperatures.

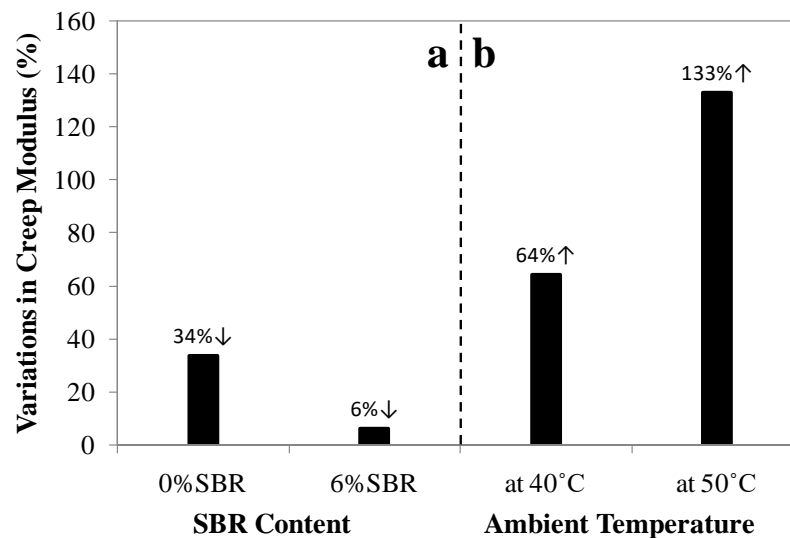


Figure 10. Decrease and increase in creep modulus of a) unmodified and modified asphalt mixture with 6% of SBR due to temperature rising from 40 to 50 °C, and b) asphalt mixtures with 6% SBR addition at 40 and 50 °C, respectively, at the end of 10000 loading cycles.

Figure 11 illustrated the variations in the ratio of creep modulus (M_c) to resilient modulus (M_r) versus the number of loading cycles. A sharp drop (about 0.18–0.29) is observable in all of the tested samples up to around 500 cycles due to the decrease of creep modulus and increase of resilient modulus (see Figures 8 and 9). This confirms the samples compaction in the initial loading cycles. As the loading cycles continued, the M_c/M_r had an approximately constant value in SBR-modified samples and rising temperature had no effect on this ratio. As shown in Figure 12a, with the temperature rising from 40 to 50 °C, the M_c/M_r of the unmodified sample decreased by 27%. Whereas this decrease was only 0.1% for SBR-modified sample. At 40 and 50 °C, with the 6% SBR addition, the M_c/M_r of the modified samples increased by 59 and 118%, respectively. The variations of M_c and M_r , as well as shear deformation were negligible and the SBR-modified samples were compacted, considering a slight increase in their resilient modulus [5]. The unmodified samples demonstrated a decreasing trend in M_c/M_r up to the last loading cycle. In view of the downward trend in their resilient modulus, it can be concluded that the proportion of compactive deformation to shear deformation is dropping [4], [5] with the shear deformation occurring in unmodified samples [5].

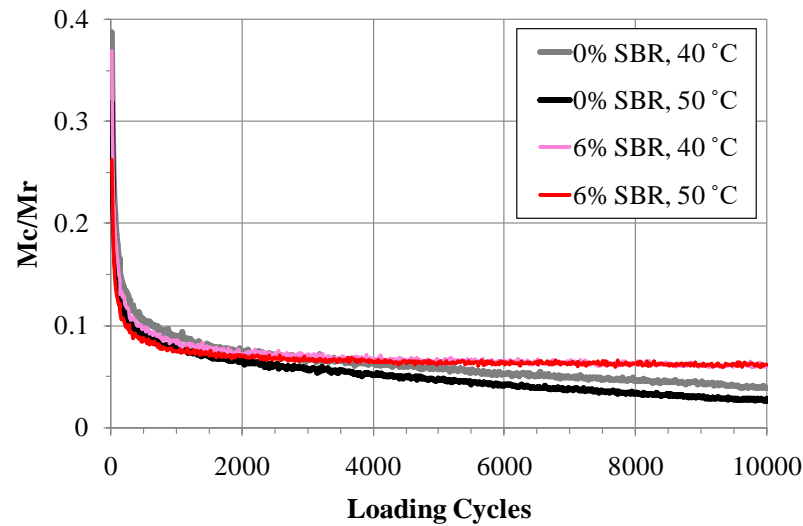


Figure 11. The ratio of creep to resilient modulus (M_c/M_r) of unmodified and SBR-modified asphalt mixtures at different ambient temperatures.

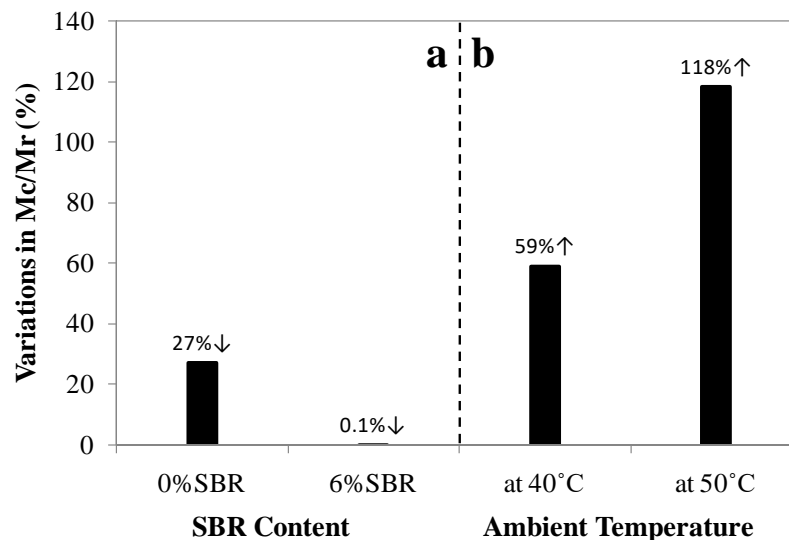


Figure 12. Decrease and increase in M_c/M_r of a) unmodified and modified asphalt mixture with 6% of SBR due to temperature rising from 40 to 50 °C, and b) asphalt mixtures with 6% SBR addition at 40 and 50 °C, respectively, at the end of 10000 loading cycles.

3.1. Determination of flow number (FN)

The permanent deformation curve of asphalt mixtures can be divided into the following three stages: First, the primary stage or primary flow that initiates from the coordinate origin and can be modeled using Power-law [22] or logarithmic functions [27]. Secondly, the secondary flow that initiates from the end point of the primary stage and continues in the form of a simple linear function; and thirdly, the tertiary stage or tertiary flow that initiates from the end point of the secondary stage which is called flow number (FN). The FN is a critical point in which the linear trend of the secondary stage is substituted with an ascending non-linear trend that indicates that the permanent strain increases dramatically from each cycle to the next one. From FN point, the pure plastic shear deformation begins [23] and the individual aggregates that make up the skeleton of asphalt mixture move past each other [28]. According to literature, the FN has a strong correlation to the Traffic Force Index (TFI) [29] and field rutting performance [21], and is a rutting indicator for asphalt mixtures [21, 22].

In this stage, the Goh and You method [23] was used in order to determine the FN of samples. In this method, the minimum value of strain rate (SR) curve versus the loading cycles is considered as FN. It is worth noting that if the minimum value of SR matches the last loading cycle, the FN is not determined

and the sample does not experience the tertiary flow up to the last loading cycle [23]. Equation (1) indicated the SR formula, where ε and N are the permanent strain and the number of loading cycle, respectively.

$$SR = \frac{\varepsilon}{N} \quad (1)$$

Figure 13 shows the SRs of the selected samples versus the number of loading cycles. Based on the calculated SR values for different samples, it must be said that the minimum SRs for unmodified samples were obtained in loading cycles of 9728 and 8416 as FNs at the ambient temperatures of 40 and 50 °C, respectively. This indicates that the tertiary flow or pure shear deformation occurred in unmodified samples. Also with rising temperature, the FN value decreased due to decrease in viscosity of the binder. Under this condition, the occurrence of shear deformation was accelerated and the sample experienced a higher permanent deformation. On the other hand, the minimum SRs for samples modified by 6% of SBR under both ambient temperatures were obtained in the last loading cycle. As mentioned recently, this means that the SBR-modified samples had higher rutting resistance than unmodified samples, so that the tertiary flow did not occur up until the last loading cycle.

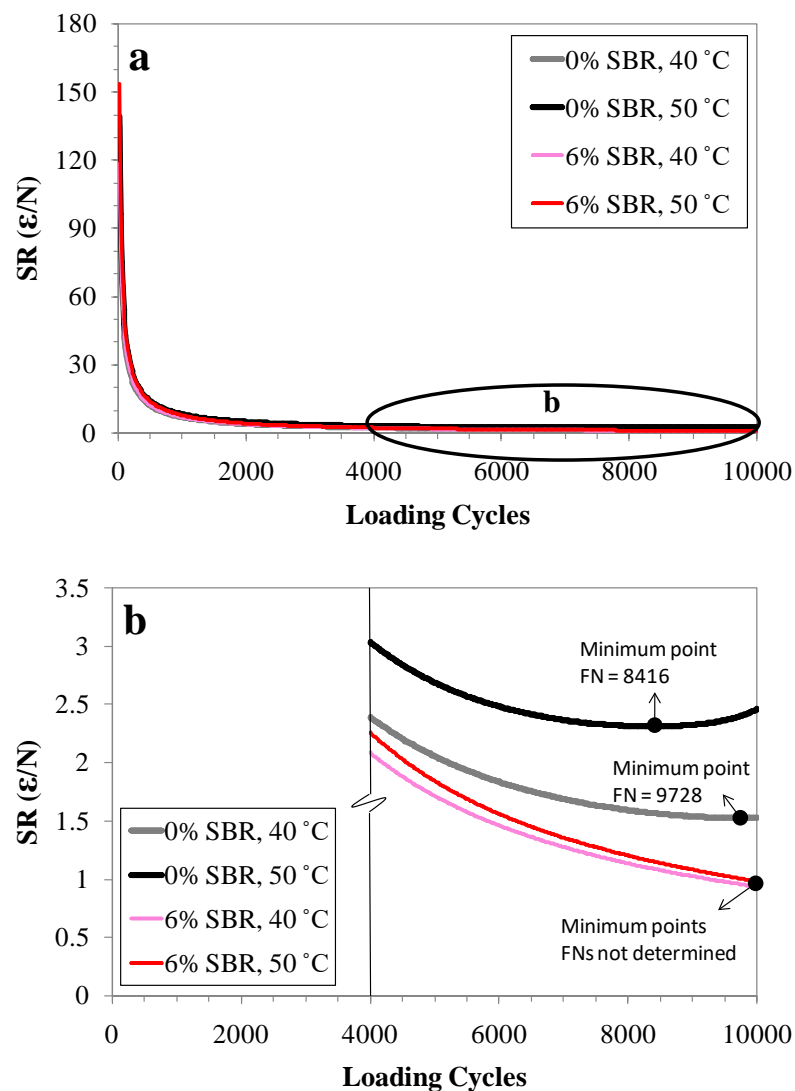


Figure 13. The flow number (FN) of unmodified and SBR-modified asphalt mixtures.

Figure 14 illustrated the triple flows of permanent deformation curves. As it can be seen, the secondary flow of SBR-modified samples continued up to the last loading cycle. Thus, the tertiary flow did not occur at desired loading cycles. While in unmodified samples, the linear trend of secondary flows stopped in their FNs, and the tertiary flows with the origin of FNs started with a dramatic slope increase. It must also be noted that line 1, as a border of primary and secondary flows, was drawn hypothetically to show the approximate location of this border in permanent deformation curves in terms of the changes in their trends.

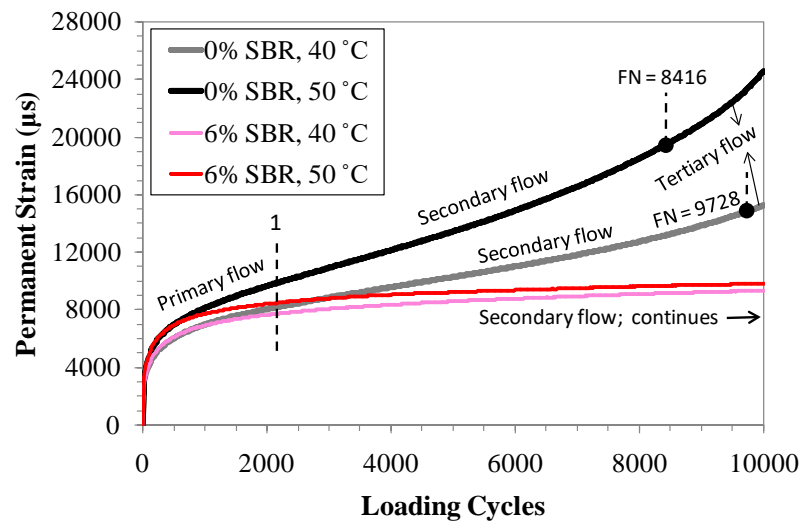


Figure 14. The triple stages of permanent deformation curves of unmodified and SBR-modified asphalt mixtures.

4. Conclusions

This study aimed to evaluate the effect of SBR on permanent deformation of asphalt mixtures. Based on the test results, the following conclusions were obtained:

1. With addition the optimum content (6%) of SBR to the bitumen, the permanent deformations of asphalt mixtures decreased by 39 and 60% at 40 and 50 °C, respectively. In addition, with the temperature rising from 40 to 50 °C, the permanent strain of unmodified asphalt mixture increased by 61%. Whereas the same property only increased by 5% in SBR-modified sample. This shows the effectiveness of SBR on enhancing the rutting resistance of asphalt mixtures, especially under the condition of rising temperature.

2. The resilient modulus trends and the creep modulus of SBR-modified samples were at a higher level than those for unmodified samples at the same ambient temperatures. Moreover, after around 6000 cycles, the general trend of resilient modulus curves of unmodified samples tends to decrease. While the general trends of resilient modulus of SBR-modified samples were at an approximately constant level. It can be concluded that in near-to-last load cycles, the compactive deformation of unmodified samples seized and the shear flow tended to initiation. However, in the SBR-modified samples, the compactive deformation was slowly progressing up until the last loading cycle. The main reason of this lies in the elastic properties of the SBR network, which preserved the stone materials and prevented and/or postponed the excessive plastic deformations.

3. Modification of bitumen with SBR enhances the creep modulus of asphalt mixtures. With the 6% SBR addition, the creep modulus of the samples increased by 64 and 133% at 40 and 50 °C, respectively. Also with the temperature rising from 40 to 50 °C, the creep modulus of the unmodified mixture decreased by 34%. Whereas the same reduction for the SBR-modified sample was only 6%. As mentioned earlier, this shows better stability of the SBR-modified samples against rising temperature compared to the unmodified ones.

4. Modification of bitumen with appropriate amount of SBR can be a suitable method for construction of durable roads particularly in the regions with hot climate. The SBR has lower price than another common polymeric product, SBS. Therefore, using it as a binder modifier, along with meeting the technical requirements for durable asphalts, can decrease the total cost of road construction.

References

1. Al-Khateeb, G.G., Al-Suleiman Obaidat, T.I., Khedaywi, T.S., Elayan, M.S. Studying rutting performance of Superpave asphalt mixtures using unconfined dynamic creep and simple performance tests. *Road Materials and Pavement Design*. 2018. 19(2). Pp. 315–333. DOI: 10.1080/14680629.2016.1261722
2. Mirzapour Mounes, S., Karim, M.R., Khodaii, A., Almasi, M.H. Evaluation of permanent deformation of geogrid reinforced asphalt concrete using dynamic creep test. *Geotextiles and Geomembranes*. 2016. 44(1). Pp. 109–116. DOI: 10.1016/j.geotextmem.2015.06.003
3. Tayfur, S., Ozen, H., Aksoy, A. Investigation of rutting performance of asphalt mixtures containing polymer modifiers. *Construction and Building Materials*. 2007. 21(2). Pp. 328–337. DOI: 10.1016/j.conbuildmat.2005.08.014
4. Gokhale, S., Choubane, B., Byron, T., Tia, M. Rut Initiation Mechanisms in Asphalt Mixtures as Generated under Accelerated Pavement Testing. *Transportation Research Record*. 2005. 1940(1). Pp. 136–145. DOI: 10.1177/0361198105194000115

5. Khodaii, A., Mehrara, A. Evaluation of permanent deformation of unmodified and SBS modified asphalt mixtures using dynamic creep test. *Construction and Building Materials*. 2009. 23(7). Pp. 2586–2592. DOI: 10.1016/j.conbuildmat.2009.02.015
6. Baumgardner, G.L., Hardee, J.R., Negulescu, I.I., Williams, E.R., Howard, I.L., St. John, R.C. Quantitative analysis of functional polymer in recycled tire rubber used in modified asphalt binders. *Asphalt Paving Technology: Association of Asphalt Paving Technologists-Proceedings of the Technical Sessions*. 2014. 83(January). Pp. 583–611. DOI: 10.1080/14680629.2014.927413
7. Vamegh, M., Ameri, M., Chavoshian Naeni, S.F. Experimental investigation of effect of PP/SBR polymer blends on the moisture resistance and rutting performance of asphalt mixtures. *Construction and Building Materials*. 2020. 253. Pp. 119197. DOI: 10.1016/j.conbuildmat.2020.119197
8. Ameri, M., Yeganeh, S., Erfani Valipor, P. Experimental evaluation of fatigue resistance of asphalt mixtures containing waste elastomeric polymers. *Construction and Building Materials*. 2019. 198. Pp. 638–649. DOI: 10.1016/j.conbuildmat.2018.11.017
9. Abdel-Goad, M.A.H. Waste polyvinyl chloride-modified bitumen. *Journal of Applied Polymer Science*. 2006. 101(3). Pp. 1501–1505. DOI: 10.1002/app.22623
10. Zhai, R., Ge, L., Li, Y. The effect of nano-CaCO₃/styrene-butadiene rubber (SBR) on fundamental characteristic of hot mix asphalt. *Road Materials and Pavement Design*. 2018. 21(4). Pp. 1006–1026. DOI: 10.1080/14680629.2018.1532924
11. Ming, L.Y., Feng, C.P., Siddig, E.A.A. Effect of phenolic resin on the performance of the styrene-butadiene rubber modified asphalt. *Construction and Building Materials*. 2018. 181. Pp. 465–473. DOI: 10.1016/j.conbuildmat.2018.06.076
12. Cong, Y., Liao, K., Huang, W., Zhai, Y. Performance of SBR-modified asphalt. *Petroleum Science and Technology*. 2006. 24(10). Pp. 1187–1194. DOI: 10.1081/LFT-200053905.
13. Zhang, B., Xi, M., Zhang, D., Zhang, H., Zhang, B. The effect of styrene-butadiene-rubber/montmorillonite modification on the characteristics and properties of asphalt. *Construction and Building Materials*. 2009. 23(10). Pp. 3112–3117. DOI: 10.1016/j.conbuildmat.2009.06.011
14. Zhang, F., Hu, C. The research for SBS and SBR compound modified asphalts with polyphosphoric acid and sulfur. *Construction and Building Materials*. 2013. 43. Pp. 461–468. DOI: 10.1016/j.conbuildmat.2013.03.001.
15. Hossein Hamed, G., Ghalandari Shamami, K., Mazhari Pakenari, M. Effect of ultra-high-molecular-weight polyethylene on the performance characteristics of hot mix asphalt. *Construction and Building Materials*. 2020. 258. Pp. 119729. DOI: 10.1016/j.conbuildmat.2020.119729
16. Kuttah, D.K., Sato, K., Koga, C. Evaluating the dynamic stabilities of asphalt concrete mixtures incorporating plasterboard wastes. *International Journal of Pavement Engineering*. 2015. 16(10). Pp. 929–938. DOI: 10.1080/10298436.2014.973023
17. Hao, P., Zhai, R., Zhang, Z., Cao, X. Investigation on performance of polyphosphoric acid (PPA)/SBR compound-modified asphalt mixture at high and low temperatures. *Road Materials and Pavement Design*. 2019. 20(6). Pp. 1376–1390. DOI: 10.1080/14680629.2018.1447503
18. Ren, S., Liang, M., Fan, W., Zhang, Y., Qian, C., He, Y., Shi, J. Investigating the effects of SBR on the properties of gilsonite modified asphalt. *Construction and Building Materials*. 2018. 190. Pp. 1103–1116. DOI: 10.1016/j.conbuildmat.2018.09.190
19. Jiang, J., Ni, F., Zheng, J., Han, Y., Zhao, X. Improving the high-temperature performance of cold recycled mixtures by polymer-modified asphalt emulsion. *International Journal of Pavement Engineering*. 2020. 21(1). Pp. 41–48. DOI: 10.1080/10298436.2018.1435882
20. Liu, B., Liang, D. Influence of SBS and SBR on the properties of emulsified asphalt. *Petroleum Science and Technology*. 2017. 35(10). Pp. 1008–1013. DOI: 10.1080/10916466.2017.1303720
21. Witczak, M. Specification Criteria for Simple Performance Tests for Rutting, Volume I: Dynamic Modulus (E*) and Volume II: Flow Number and Flow Time. The National Academies Press. 2007. Washington, DC. DOI: 10.17226/23120
22. Zhou, F., Scullion, T., Sun, L. Verification and modeling of three-stage permanent deformation behavior of asphalt mixes. *Journal of Transportation Engineering*. 2004. 130(4). Pp. 486–494. DOI: 10.1061/(ASCE)0733-947X(2004)130:4(486)
23. Goh, S.W., You, Z. A simple stepwise method to determine and evaluate the initiation of tertiary flow for asphalt mixtures under dynamic creep test. *Construction and Building Materials*. 2009. 23(11). Pp. 3398–3405. DOI: 10.1016/j.conbuildmat.2009.06.020
24. Behnood, A., Modiri Gharehveran, M. Morphology, rheology, and physical properties of polymer-modified asphalt binders. *European Polymer Journal*. 2019. 112. Pp. 766–791. DOI: 10.1016/j.eurpolymj.2018.10.049
25. Gong, M., Yang, B., Zhang, H., Sun, Q. Comparative study on durability of different composite modified asphalt mixtures. *Road Materials and Pavement Design*. 2019. Pp. 1–20. DOI: 10.1080/14680629.2019.1688672
26. Ahari, A.S., Forough, S.A., Khodaii, A., Nejad, F.M. Modeling the Primary and Secondary Regions of Creep Curves for SBS-Modified Asphalt Mixtures under Dry and Wet Conditions. *Journal of Materials in Civil Engineering*. 2014. 26(5). Pp. 904–911. DOI: 10.1061/(asce)mt.1943-5533.0000857
27. Kanitpong, K., Bahia, H. Relating adhesion and cohesion of asphalts to the effect of moisture on laboratory performance of asphalt mixtures. *Transportation Research Record*. 2005. (1901). Pp. 33–43. DOI: 10.3141/1901-05
28. Faheem, A.F., Bahia, H.U., Ajideh, H. Estimating results of a proposed simple performance test for hot-mix asphalt from superpave gyratory compactor results. *Transportation Research Record*. 2005. (1929). Pp. 104–113. DOI: 10.3141/1929-13

Information about authors:

Navid Lotfi Omran

ORCID: <https://orcid.org/0000-0002-6438-132X>

E-mail: navid.lotfii.omran@gmail.com

Komeil Rajaei

ORCID: <https://orcid.org/0000-0001-6449-874X>

E-mail: rajaei.geotech@gmail.com

Seyed Morteza Marandi, PhD

ORCID: <https://orcid.org/0000-0003-0044-1781>

E-mail: marandi@uk.ac.ir

Received 30.12.2020. Approved after reviewing 13.10.2021. Accepted 17.10.2021.



Research article

UDC 691.32 : 666.9.03

DOI: 10.34910/MCE.113.10



Aerated dry mix concrete for remote northern territories

L.V. Ilina^a , A.I. Kudyakov^b, M.A. Rakov^a 

^a Novosibirsk State University of Architecture and Civil Engineering (Sibstrin), Novosibirsk, Russia

^b Tomsk State University of Architecture and Building, Tomsk, Russia

✉ nsklika@mail.ru

Keywords: aerated concrete, dry raw mix, Portland cement, clinker, mineral additives, joint grinding, compressive strength, porosity, frost resistance, thermal conductivity

Abstract. The study results on aerated concrete based on imported long-term storage clinker and mineral additives for northern remote construction sites are presented here. The relevance of the research is due to the need for cement composites of stable quality to install enclosing structures at remote northern construction sites. It is impossible to ensure stable quality and safety of construction objects using imported cement due to a significant decrease in its activity during transportation and long-term storage. This problem is shown to be solved by organizing the production of aerated concrete from imported Portland cement clinker using a mechano-chemical technological platform, including: scientific substantiation of the components' choice, mechanical or mechano-chemical activation of clinker by joint grinding with additives and obtaining a dry mixture, preparing aerated concrete mixture and hardening aerated concrete in molded products. Modern physicochemical methods for studying cement compositions are used in this scientific work. Ensuring the required characteristics of aerated concrete on imported Portland cement clinker is provided by introducing activated mineral additives of wollastonite and diopside, which have a chemical affinity with cement minerals and hydrosilicates. It was found that the activity of the binder increased by 30 % and 59 %, respectively when 7 % wollastonite and diopside with a specific surface area of 309 and 323 m²/kg were added to cement from imported clinker for long-term storage. At the same time, the initial activity of cement (43 MPa) is restored even with the 2 % content of diopside of a specific surface area of 323 m²/kg. An increase in the activity of cement from imported clinker was explained by the formation of an additional amount of low-basic hydrosilicates and a decrease in stone porosity. Aerated concrete from cement, based on imported clinker, has a homogeneous structure of evenly distributed pores with an average diameter of 6.81 microns, which provides a 10–15 % increase in strength with a compression variability coefficient of 5.4. The obtained aerated concrete had the strength of B2 class, F75 grade frost resistance and thermal conductivity coefficient of 0.14–0.15 W/(m·°C). The developed aerated concrete and the technology of its preparation from imported Portland cement clinker are intended for the construction of buildings in the remote northern territories.

Citation: Ilina, L.V., Kudyakov, A.I., Rakov, M.A. Aerated dry mix concrete for remote northern territories. Magazine of Civil Engineering. 2022. 113(5). Article No. 11310. DOI: 10.34910/MCE.113.10

1. Introduction

When forecasting the development of the economy, much attention is paid to the northern construction and climatic zone. It is necessary to develop technologies and methods of resource provision of construction facilities with materials, taking into account the peculiarities of these remote areas. Modern economic conditions suggest new approaches to the selection and justification of production and use of efficient construction materials [1–5]. Energy efficiency and predicted payback period of construction projects in the northern regions significantly depend on the thermophysical characteristics of the enclosing structures and the rational use of material resources [2, 6–8].

Regional industry of building materials is developing with the use of local and imported raw materials for effective resource support and safety of buildings construction in remote northern territories of Russia. The main material is cement aerated concrete for the purpose and scope of use for the enclosing structures of energy-saving buildings. The technical characteristics of aerated concrete, as well as the operational reliability of the structures made from it, significantly depend on the level and stability of the quality parameters of the used Portland cement [9–13]. Cement is delivered to the regions only in the summer period. It is practically impossible to organize the production of cellular concrete products with the required quality parameters for remote construction sites, due to the significant loss of Portland cement activity during long-term transportation and storage [14–17].

Previously, the scientific substantiation of technological processes for the cement hardening mixtures manufacture in the northern territories by joint wet grinding of imported clinker from the Achinsk cement plant with natural mineral additives and waste from the metallurgical industry was carried out by the scientists of the Leningrad Civil Engineering Institute under the leadership of P.I. Bozhenov, the Academician of the Russian Academy of Architecture and Construction Sciences and introduced at the Norilsk Mining and Metallurgical Plant for laying mine workings. The available scientific results and practical recommendations for the joint wet grinding of clinker with mineral additives do not allow effectively controlling the structure formation processes of non-autoclaved aerated concrete in the wall structures manufacture with the required characteristics under extreme conditions. In order to solve this problem, the most effective is the dry method of joint grinding of imported Portland cement clinker with modifying additives, a dry mixture production, followed by a cellular concrete mixture preparation and molding products, using prefabricated products of wall structures (wall blocks) or directly at construction sites. (monolithic structures) [13, 15, 16, 18].

The technological processes of dry grinding of Portland cement clinker for long-term storage together with modifying mineral additives and the aerated concrete mixture production, as well as the structure formation control and aerated concrete properties, based on the prepared dry mixtures in relation to the production of wall products have not been previously studied. This is relevant for the construction industry development and resource provision of facilities construction in remote northern clusters, including the Arctic zone of Russia, as well Canada, Finland, Norway, Sweden and Iceland.

The purpose of the scientific work is to scientifically substantiate the technological processes for the manufacture of cement from imported Portland cement clinker with mineral modifying additives, dry building mixtures and effective and stable in quality aerated concrete wall materials on their basis.

2. Methods and Materials

During laboratory research, we used Portland cement clinker of Joint Stock Company "Iskitimcement" (Novosibirsk region). The chemical composition of clinker is given in Table 1. Mineralogical composition, % by weight: C₃S–63, C₂S–16, C₃A–8 and C₄AF–13. In order to regulate the timing of the initial structure formation of cement from imported clinker, we used "A" gypsum class with CaSO₄·2H₂O –content of 80.6 %. Wollastonite and diopside were used as mineral additives (Table 2), and the silica component was fine quartz sand (Size module SM – 1.8) with a content of dusty, silty and clay particles of 0.5 % of "Kamnerechensky Stone Quarry" production, Novosibirsk. Aluminum suspension was used, including PAP-1 aluminum powder and sulfanol, as well as grade II lime of Joint Stock Company Iskitimizvest, Iskitim, to form the porous structure of the aerated concrete mixture.

Table 1. Chemical composition of Portland cement clinker, wt. %

SiO ₂	Al ₂ O ₃	Fe ₂ O ₃	CaO	MgO	SO ₃	Loss on Ignition
21.95	5.73	4.27	65.95	1.62	0.26	0.22

Table 2. Chemical composition of mineral additives

Additive	Mine	Chemical composition, % wt.					Loss on Ignition
		SiO ₂	CaO	MgO	Al ₂ O ₃	Fe ₂ O ₃	
Diopside	Aldansk, Republic of Sakha, Yakutia	50.99	24.78	15.78	4.63	3.58	0.24
Wollastonite	Mine "Vesely", Altai Republic	53.43	34.63	0.30	3.06	2.34	6.24

During the research, real conditions were simulated in transporting and storage the clinker at construction sites in the Russian northern territories, the used clinker was stored for 12 months at 80 % of

humidity. The clinker was used after 7 days of storage in normal conditions and fineness modulus for long-term storage in northern conditions and Portland cement for the manufacture of reference samples (control).

In order to establish the structure formation regularities of binders, as well as to determine the quality parameters of aerated concrete, standard methods of mechanical testing, modern physicochemical research methods, verified instruments and certified equipment were used.

Mineral additives were ground in an AGO-3 mill to a given specific surface area.

The analysis of the granulometric composition of the additives was carried out using PRO-7000 laser dispersion analyzer from SeishinEnterpriceCo., LTD, Tokyo.

The activity of cement (ultimate compressive strength) was determined by testing standard specimens-beams 40x40x160 mm in size, made from a cement-sand mortar of normal consistency with a composition of 1: 3 by weight with a water-cement ratio of 0.42. The samples were solidified under normal conditions (above water for the first day and in water at a temperature of (20 ± 2) °C, for 27 days), and they were also subjected to steam curing at atmospheric pressure according to the following mode: temperature-rise period to 85 °C – 3 hours, isothermal curing – 8 hours, temperature reduction to 20 °C – 3 hours.

The ultimate compressive strength of aerated concrete was determined by testing concrete samples on a hydraulic press at a constant loading rate until failure. The aerated concrete samples were hardened under normal conditions in a chamber with a temperature of (20 ± 2) °C and relative air humidity (95 ± 5) %, and they were also subjected to steam curing at atmospheric pressure according to the mode: 4 hours – preliminary curing, temperature-rise period to 85 °C – 3 hours, isothermal curing – 8 hours at this temperature and 3 hours – temperature reduction to 20 °C.

The density of aerated concrete was determined in the dry state and frost resistance, due to the values of strength loss in compression and weight reduction of samples subjected to alternate freezing in water saturation state at a temperature of minus (18 ± 2) °C and their thawing at a temperature of plus (18 ± 2) °C and relative humidity (95 ± 2) %.

Differential thermal studies of hardened cement paste were carried out using a DTG 60H analyzer from Shimadzu, Japan. The rate of temperature rise was 10 °C/min. The measurements were carried out with NETZSCH software from Proteus.

The structural characteristics of aerated concrete samples (macro-V_{ma}, S_{ma} and mesopores – V_{me}, S_{me}) were investigated using AutoPoreV 9520 automated mercury porosimeter (Micromeritics, USA). The experimental research process was controlled by a computer using a special program Milestone-100-software from Fisons.

3. Results and Discussion

In order to improve the quality of cement from long-term storage clinker, the authors proposed to use mineral additives wollastonite and diopside, which had similar chemical composition and thermodynamic characteristics with clinker minerals (alite and belite), as well as the main products of their hydration (calcium silicate hydrates).

The establishment of patterns in the influence of type and amount of mineral additives on the cement composites' properties was carried out in the following sequence:

1. determination of the effect of the specific surface area and the content of mineral additives on the clinker binder activity and the structure of the hardened cement paste;
2. influence of all mineral additives and joint grinding of raw mixture components on aerated concrete properties.

At the initial stage 2.1, their optimal specific surface was established to ensure the efficiency of adding mineral additives into cement [16–19]. The maximum strength of the hardened cement paste was achieved with a minimum intergranular void between the grains of the mineral additive and the binder. The specific surface of particles and their content are taken as parameters for controlling the quality of cement from clinker with mineral additives.

The studies were carried out at the specific surface area of the used wollastonite powder after grinding – 309, 764, 888 and 982 m²/kg, diopside powder – 323; 635; 979 and 1157 m²/kg. The granulometric composition of the diopside and wollastonite powders is given in Table. 3.

Table 3. The studies' results of the granulometric composition of mineral additives

Specific surface, m ² /kg	Volumetric average particle size, μm	Volume fraction of particles with sizes	
		≤ 4 μm	≤ 12 μm
diopside			
323	27.0	19.5	31.9
635	12.8	32.2	48.4
979	4.3	49.2	66.6
1157	2.9	58.2	74.7
wollastonite			
309	28.6	13.3	27.9
746	9.0	36.4	57.6
888	5.9	43.6	65.1
982	4.3	49.0	68.6

3.1. Influence of the specific surface and dosage of mineral additives on the activity of Portland cement clinker and the structure of the hardened cement paste

We used cement, obtained by grinding Portland cement clinker with 5 % gypsum, studying the effect of specific surface and content of mineral additives on the activity and structure of hardened cement paste. The specific surface of the cement was 280 m²/kg.

The studies' results on changes in the cement activity with the adding of wollastonite and different specific surface are shown in Fig. 1. It was found that the adding of wollastonite into cement from clinker increased the strength characteristics of the hardened cement paste:

- in order to use clinker, stored for 7 days under normal conditions, and the adding of wollastonite with a specific surface area of 309 m²/kg into the cement during hardening under normal conditions, the hardened cement paste in compression increased by 30 %, and with steam curing at atmospheric pressure – by 31 %;
- in order to use clinker, stored for 12 months in humid conditions and introducing wollastonite with a specific surface area of 309 m²/kg during hardening under normal conditions, the compressive strength increased by 20 %, and during steam curing at atmospheric pressure – by 35 %.

The changes' results in the activity of the binder with the diopside and different specific surface areas adding are shown in Fig. 2.

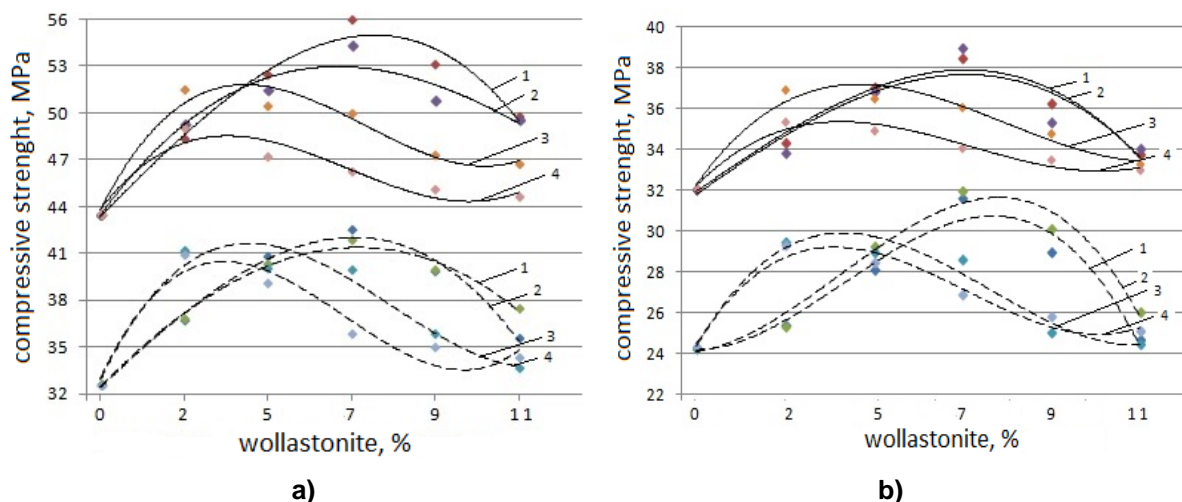


Figure: 1. Influence of the wollastonite amount and specific surface and quantity on cement activity made from ground clinker stored: a) 7 days under normal conditions; b) 12 months in humid conditions
1 – wollastonite with a specific surface of 309 m²/kg; 2 – 746 m²/kg; 3 – 888 m²/kg; 4 – 982 m²/kg

The dotted line indicates the curves for specimen hardening under the conditions of steam curing at atmospheric pressure, the solid line indicates 28 days under normal conditions.

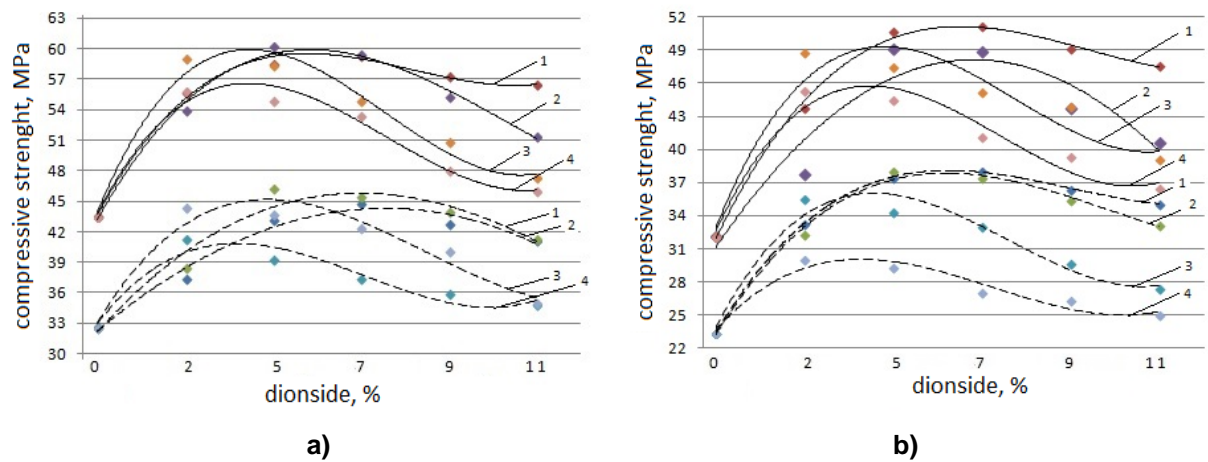


Figure 2. Influence of specific surface and diopside amount on the binder activity made from ground clinker stored: a) 7 days under normal conditions; b) 12 months in humid conditions 1 – diopside with a specific surface of 323 m²/kg; 2 – 635 m²/kg; 3 – 979 m²/kg; 4 – 1157 m²/kg

The dashed line indicates curves during the hardening of the samples under the conditions of steam curing at atmospheric pressure, the solid line – 28 days under normal conditions.

The compressive strength increased by 30 %, and during steam curing at atmospheric pressure – by 37 %, using clinker stored for 7 days under normal conditions and adding of diopside with a specific surface area of 323 m²/kg during cement paste hardening under normal conditions.

The cement paste compressive strength made of cement, based on clinker, stored for 12 months in humid conditions with the diopside addition of a specific surface area of 323 m² / kg, increased by 59 % during cement paste hardening under normal conditions, and increased by 62 % during steam curing at atmospheric pressure. At the same time, the initial activity of cement (43 MPa) is restored even at the diopside content with a specific surface area of 323 m²/kg – only 2 %.

It can be noted that the activation of Portland cement clinker, stored for 7 days under normal conditions and for a long time under humid conditions, by adding finely dispersed diopside leads to an increase in the binder activity, analyzing the research data in Fig. 1 and 2. The greatest increase in the strength of the binder is achieved with the addition of milled diopside, which has a high hardness value (7 on the Mohs scale), i.e. the highest value of the modulus of elasticity containing calcium and silicon oxides, as well as the specific surface area equal to that of ground clinker. Wollastonite has a lower hardness (4.5–5.0 on the Mohs scale). An increase in the strength of the hardened cement paste with additives is explained by micro-reinforcement and redistribution of stresses between the components of the cement stone, while the greatest efficiency is provided by the use of diopside.

With an increase in the content of the mineral additive over 7 % and an increase in the specific surface areas of wollastonite to 982 m²/kg and diopside to 1157 m²/kg, the effect of hardened cement paste decreases as a result of additives' aggregation, in addition, the energy consumption for their grinding increases significantly.

Thereby, in the process of conducting further studies of aerated concrete on cement from imported clinker (point 2.2), we used additions of wollastonite with a specific surface area of 309 m²/kg and diopside with a specific surface area of 323 m²/kg, i.e. close to the dispersion of ground clinker. The content of additives was 7 %.

We conducted a complex thermal analysis (Fig. 3 and 4) and porosimetry to explain the structure formation processes of hardened cement paste with the addition of dispersed wollastonite and diopside.

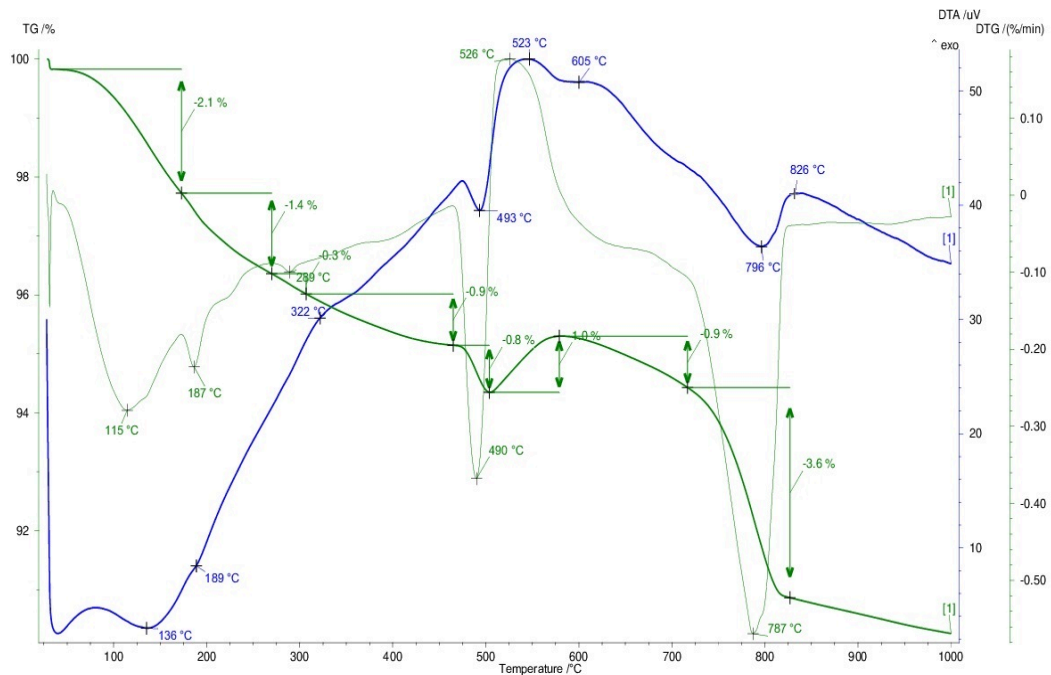


Figure 3. Thermal analysis' results of hardened cement paste made on ground clinker with gypsum without mineral additives introduction.

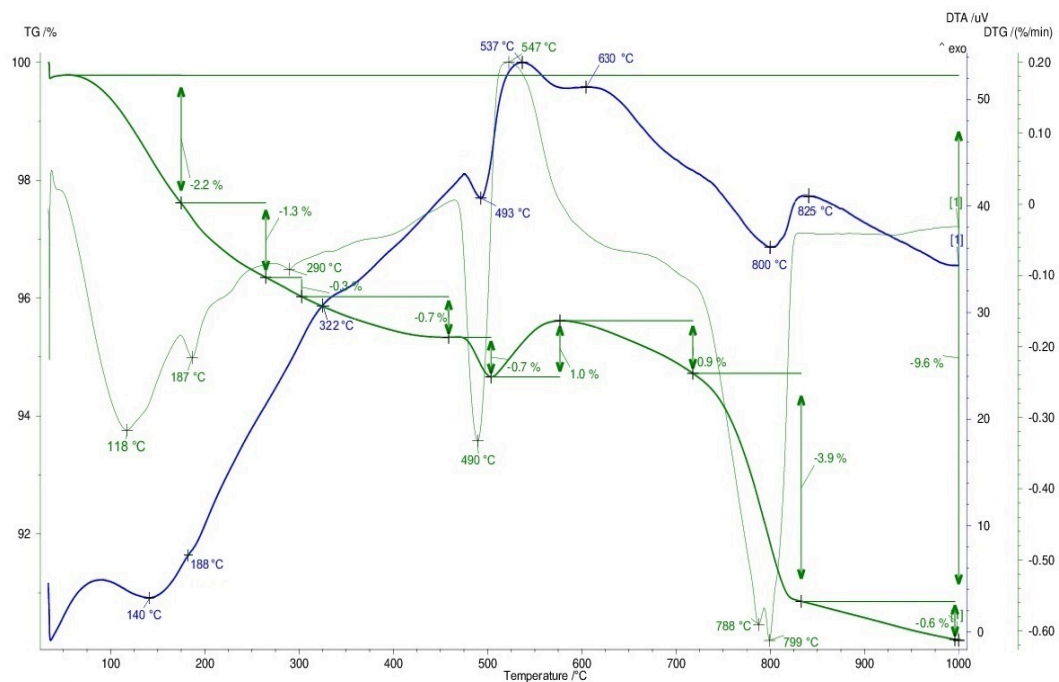


Figure 4. Thermal analysis' results of hardened cement paste made on ground clinker with gypsum and 7% diopside.

According to the results of a comprehensive thermal analysis, there is no significant change in the phase composition during the cement paste hardening with diopside. A change in the temperature of the thermal effect and a transition to a higher temperatures zone (from 605 to 630 °C) are observed, which can be caused by the structure strengthening due to the interaction of diopside with portlandite, which is released during the hydration of alite, and the additional amount of low-basic calcium silicate hydrates.

The study's results of the hardened cement paste porosity from clinker with 7% dispersed diopside are given in Table 4.

Table 4. Porosity of hardened cement paste with the dispersed diopside addition

Average pore diameter, μm	Type of cement			
	from clinker without additives		from clinker with 7% diopside	
	pore volume, ml/g	pore volume, %	pore volume, ml/g	pore volume, %
73.1 – 361.0	0.0919	33.53	0.0275	12.72
15.4 – 73.1	0.0115	4.19	0.0106	4.9
1.2 – 15.4	0.0164	5.96	0.0165	7.63
0.15 – 1.2	0.0513	56.32	0.0560	74.75
0.003-0.15	0.1030		0.1056	
Total	0.2741	100	0.2162	100

Analyzing mercury porosimetry results, the following can be noted:

- the total pore volume decreases from 0.274 to 0.216 ml/g in hardened cement paste from 7 % diopside in comparison with hardened cement paste from clinker without additives;
- the pores volume with a diameter of more than 73.1 microns is reduced by 2.6 times;
- the pores content with a diameter of less than 1.2 microns increases significantly.

A decrease in the total porosity of hardened cement paste with a dispersed addition of diopside, as well as a decrease in large-diameter pores, is one of the factors explaining an increase in the hardened cement paste strength. Increase in the pores number (capillaries) of small diameter (less than 1.2 μm), forming partitions structure (matrix) in aerated concrete, which can contribute to an increase in frost resistance of the developed aerated concrete.

3.2. Influence of mineral additives and joint grinding of raw mix components on the aerated concrete properties

A number of scientists' researches have shown the effectiveness of cellular concrete preparation for wall products and structures from a dry mixture [20, 21]. Manufacturability of construction processes significantly increases, mixing the dry mixture with water and pouring the aerated concrete mixture into molds or formwork directly on the construction site. In the study of aerated concrete based on dry mixtures, the data specified in paragraph 2.1 on the optimal specific surface area and the content of mineral additives in the cement from clinker, providing the maximum increase in strength, were used. Since the greatest increase in the strength of the hardened cement paste was obtained with the addition of diopside and wollastonite with a specific surface area close to that of Portland cement, then at stage 2.2 the joint grinding of all raw materials was studied. The dry mixture was prepared by joint grinding of clinker with gypsum, natural gypsum, mineral additive, silica and lime components.

3.2.1. Influence of mineral additives on the density and strength of aerated concrete

The tests' results of the density and strength of aerated concrete obtained on the basis of a dry raw mixture are presented in Table 5.

Table 5. Dependence of the density and aerated concrete strength on a type and number of additives

Type of cement	Density of aerated concrete, kg/m^3	Compressive strength of aerated concrete, MPa
Clinker stored for 7 days under normal conditions		
Cement without mineral additives	610	2.8
Cement with wollastonite, 7 %	600	3.1
Cement with diopside, 7 %	580	3.3
Clinker stored for 12 months in humid conditions		
Cement without mineral additives	610	2.1
Cement with wollastonite, 7 %	605	2.3
Cement with diopside, 7 %	590	2.4

The density does not significantly decrease in aerated concrete with mineral additions of wollastonite and diopside. Thus, we have obtained structural and heat-insulating aerated concrete of D600 brand.

The strength characteristics of aerated concrete on normal storage clinker cement increase with the adding of wollastonite by 11 %, and diopside – by 18 %.

The strength of aerated concrete from imported long-term storage clinker without mineral additives is reduced by 25 %. The strength characteristics of aerated concrete increase by 10 and 14 %, respectively, using clinker cement with additions of wollastonite and diopside. The strength indicators of aerated concrete decreased to 0.6 MPa (2.5 times) and the density of aerated concrete increased by 30 %, using Portland cement from the same composition, prepared in the factory and stored for 12 months.

The coefficient of variation in determining the compressive strength of aerated concrete from a dry mix, based on imported clinker is 5.4 %, the density of samples is 4.2 %, which characterizes the high stability of the aerated concrete's quality indicators. Compressive strength class of aerated concrete is B2. Thus, the preliminary preparation of the dry mixture by joint grinding of long-term storage clinker with gypsum, mineral additives, silica and lime components, followed by the aerated concrete mixture production, makes it possible to form products for building structures that meet regulatory documents.

3.2.2. Influence of mineral additives on the pore structure of aerated concrete

The properties of aerated concrete are greatly influenced by the microstructure and porosity, as well [22–25]. The type and content of pores in aerated concrete, based on long-term storage clinker cement, were studied using mercury-vacuum porosimetry. The total pore volume of the developed aerated concrete on cement from long-term storage clinker with diopside addition was 7.26 sm³/g. Differential curve of pores distribution in aerated concrete are shown in Fig. 5.

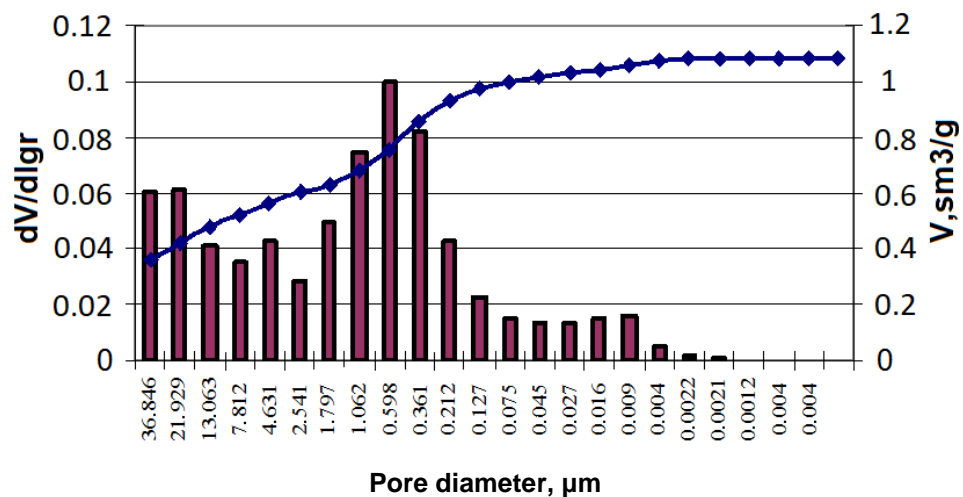


Figure 5. Differential pore distribution curve in aerated concrete, made from a dry mix, based on clinker stored for 12 months in humid conditions and diopside

The average pore diameter in aerated concrete is 6.81 microns. Aerated concrete has uniformly distributed porosity in the range of pores with a size of 0.0012 – 0.075 and 1.062 – 13.063 microns.

Mineral additives influence on frost resistance of aerated concrete

Change in strength and weight of aerated concrete, tested for frost resistance, is given in Table 6.

Table 6. Changes in the properties of aerated concrete, tested for frost resistance (as a percentage of the original value)

Binder composition in dry mix	Reduction of strength after testing, depending on the number of cycles,%				Reduction of mass after testing, depending on the number of cycles,%				Frost resistance grade
	50	75	100	125	50	75	100	125	
Prefabricated Portland Cement	-14.1	-21.2	-	-	-3.5	-6.3	-	-	F50
Ground clinker	-14.3	-21.4	-	-	-3.8	-6.1	-	-	F50
Ground clinker with 50 % siliceous component	-7.6	-11.2	-22.7	-	-3.1	-4.5	-7.0	-	F75
Ground clinker with 50 % siliceous component and 7 % wollastonite	-7.0	-9.6	-16.4	-	-2.8	-4.2	-6.7	-	F75
Ground clinker with 50 % siliceous component and 7 % diopside	-6.0	-10.0	-17.1	-	-2.7	-4.0	-6.7	-	F75

For aerated concrete sample, made on the basis of ground clinker without additives, a noticeable decrease in strength (14.3 %) was noted after 50 test cycles. Compressive strength of such aerated concrete decreased by 21.4 % after 75 cycles. The mass of the samples decreased after 50 cycles by 3.8 %, after 75 cycles by 6.1 %. Frost resistance grade was F50. The decrease in strength after 75 test cycles was 9.6–10.0 % with adding of 7 % wollastonite or diopside and the weight of the samples decreased by 4.0–4.2 %. The frost resistance grade of aerated concrete rose to F75. The increase in frost resistance of aerated concrete with additions of wollastonite or diopside was explained by the increased content of small pores in the structure, which degree of filling with water and transformation into ice slowed down.

The thermal conductivity coefficient of the developed aerated concrete from a dry mixture, based on imported clinker with mineral additions of wollastonite and diopside in a dry state at a temperature of 25 °C was 0.14–0.15 W/(m °C).

4. Conclusion

1. A scientifically based technology has been developed for the manufacture of aerated concrete from a pre-prepared dry mixture, obtained by joint grinding of imported clinker with mineral additives wollastonite or diopside, gypsum, silica and lime components, which make it possible to mechanically activate the components surfaces and significantly intensify the physicochemical processes of structure formation of the porous cement composition that makes it possible to ensure a homogeneous structure, to increase the strength of interpore partitions and aerated concrete.

2. It was found that 7 % wollastonite and diopside with a specific surface area of 309 and 323 m²/kg, which have chemical affinity, added to cement, prepared from imported clinker for long-term storage, as well as the similarity of thermodynamic characteristics with clinker minerals and products of their hydration, the activity of the binder increased by 30 % and 59 %, respectively. At the same time, the initial activity of cement (43 MPa) was restored even at the content of diopside with a specific surface area of 323 m²/kg – 2 %.

3. An increase in the cement activity from imported clinker with dispersed additions of wollastonite and diopside, occurred mainly due to the interaction of mineral additives with portlandite, released during hydration of alite and the formation of an additional amount of low-basic calcium silicate hydrates, as well as a decrease in the pore content from 0.274 to 0.216 ml/g.

4. In the aerated concrete of non-autoclave hardening, made by a two-stage technology on cement from imported clinker with additions of wollastonite and diopside at 28 days of age, the strength increased by 10 and 15 %, which made it possible to produce goods with the required B2 strength class.

5. The average pore diameter was 6.81 microns in aerated concrete on cement from long-term storage clinker with mineral additives. Pores with a size of 0.0012 – 0.075 and 1.062 – 13.063 microns were evenly distributed over the volume, which ensured high stability of quality parameters. The index of variability in average density was 4.2, in compressive strength – 5.4, grade for frost resistance – F75, thermal conductivity coefficient – 0.14 – 0.15 W/(m °C).

6. The developed technology of aerated concrete is recommended for industrial use in wall structures molding from imported clinker at construction sites in the remote northern territories.

Thus, the authors have formed a set of technological principles for managing the processes of improving the non-autoclaved aerated concrete quality for organizing the facilities construction in remote hard-to-reach areas, taking into account the complexities of resource provision and maintaining the technical characteristics of the concrete – cement's main component, namely:

- aerated concrete production of the required stable quality from a dry construction mixture, by joint grinding (mechanical activation) of the base components that form the matrix of porous concrete (interpore partitions) with the physicochemical processes intensification of structure formation and ensuring the specified porosity;
- scientific substantiation of the components choice and the sequence of introduction into the construction composition, based on their functional purpose in the manufacture of dry mix and aerated concrete mix with subsequent participation in the structure formation of porous cement concrete;
- taking into account the degree of hydration and the activity loss of Portland cement clinker in long-term storage, as well as the synergistic effect from the activation effect during joint or separate grinding of components in the scientific substantiation of the type and processes sequence.

References

1. Suleymanova, L.A., Kolomatsky, A.S., Pogorelova, I.A., Marushko, M.V. Improving the efficiency of production and use of cellular concreteo Bulletin of the Belgorod State Technological University named after V.G. Shukhov. 2017. 11. Pp. 34–42. DOI: 10.12737/article_5a001aae2035d9.25914342
2. Roberz, F., Loonen, R.C.G.M., Hoes, P., Hensen, J.L.M. Ultra-lightweight concrete: Energy and comfort performance evaluation in relation to buildings with low and high thermal mass. Energy and Buildings. 2017. 138. Pp. 432–442. DOI: 10.1016/j.enbuild.2016.12.049
3. Tasdemir, C., Sengul, O., Tasdemir, M.A. A comparative study on the thermal conductivities and mechanical properties of lightweight concretes. Energy and Buildings. 2017. 151. Pp. 469–475. DOI: 10.1016/j.enbuild.2017.07.013
4. Drochytka, R., Zach, J., Korjenic, A., Hroudová, J. Improving the energy efficiency in buildings while reducing the waste using autoclaved aerated concrete made from power industry waste. Energy and Buildings. 2013. 58. Pp. 319–323. DOI: 10.1016/j.enbuild.2012.10.029
5. Maoduš, N., Agarski, B., Kočetov Mišulić, T., Budak, I., Radeka, M. Life cycle and energy performance assessment of three wall types in south-eastern Europe region. Energy and Buildings. 2016. 133. Pp. 605–614. DOI: 10.1016/j.enbuild.2016.10.014
6. Gorshkov, A., Murgul, V., Oliynyk, O. Forecasted Payback Period in the Case of Energy-Efficient Activities. MATEC Web of Conferences. 2016. 53. DOI: 10.1051/mateconf/20165301045
7. Korniyenko, S. Complex analysis of energy efficiency in operated high-rise residential building: Case study. E3S Web of Conferences. 2018. 33. DOI: 10.1051/e3sconf/20183302005
8. Gorshkov, A.S., Vatin, N.I., Rymkevich, P.P., Kydrevich, O.O. Payback period of investments in energy saving. Magazine of Civil Engineering. 2018. 78(2). Pp. 65–75. DOI: 10.18720/MCE.78.5
9. Poole, J.L., Riding, K.A., Juenger, M.C.G., Folliard, K.J., Schindler, A.K. Effects of supplementary cementitious materials on apparent activation energy. Journal of ASTM International. 2010. Vol. 7. No. 9. Pp. 46–51. DOI: 10.1520/JAI102893
10. Ermilova, E.Yu., Bulanov, P.E., Rakhimov, R.Z., Stoyanov, O.V. Kompozicionnye portlandcementy s kompleksnymi dobavkami dlja remontnyh rabot [Composite Portland cements with complex additives for repair works]. Remont. Vosstanovlenie. Modernizacija [Repair. Recovery. Modernization]. 2019. No. 1. Pp. 35–41. DOI: 10.31044/1684-2561-2019-0-1-35-41. (rus)
11. Steshenko, A. B., Kudryakov, A. I., Ryabtseva, N. E. Cement based foam concrete with hardening accelerators. IOP Conference Series: Materials Science and Engineering. 2020. 911. 012003. DOI: 10.1088/1757-899X/911/1/012003
12. Mestnikov, A.E., Kudryakov, A.I., Rozhin, V.N. Portlandcement s prirodnyimi aktivnymi mineral'nymi dobavkami [Portland Cement with natural active mineral additives]. Vestnik Tomskogo gosudarstvennogo arhitekturno-stroitel'nogo universiteta [Journal of Construction and Architecture]. 2019. No. 2. Pp. 192–201. DOI: 10.31675/1607-1859-2019-21-2-192-201. (rus)
13. Berdov, G.I., Il'ina, L.V., Mukhina, I.N., Rakov, M.A. Aerated concrete with mineral dispersed reinforcing additives. IOP Conf. Series Materials Sci. and Engineering. 2015. 71. 012017. DOI: 10.1088/1757-899X/71/1/012017
14. Mestnikov, A.A. Heat-insulating highly porous insulating materials from mineral raw materials. Conference IOP. Ser.: Mater. Sci. English. 2015. Vol. 71. No. 012014. Pp. 1–4. DOI: 10.1088/1757899X/71/1/012014
15. Ilina, L., Rakov, M., Velichko, B., Mukhina, I. Technology and Automation of Non-Autoclave Aerated Concrete Production, IOP Conf. Series Materials Science and Engineering. 2020. 953. 012050. DOI: 10.1088/1757-899X/953/1/012050
16. Il'ina, L., Mukhina, I., Teplov, A. Dry building mixture with complex dispersed mineral additives. AIP Conference Proceedings. 2016. 1698(1). 070001. DOI: 10.1063/1.4937871
17. Mashkin, N., Bartenjeva, E. Research of structuring processes of non-autoclave foam concrete with introduction of mineral additives. IOP Conference Series: Materials Science and Engineering. 2018. 451(1). 012018. DOI: 10.1088/1757-899X/451/1/012018
18. Belov, V.V., Kuryatnikov, Yu.Yu. Aeroconcrete of non-autoclave curing on the basis of reactionary and powder dry blends. Sbornik nauchnykh trudov RAASN [Collection of scientific papers of the Russian Academy of Architecture and Building Sciences]. 2018. Vol. 2. Pp. 63–70. (rus)
19. Akhverdiyeva, T.A., Dzhfarov, R. Vliyanie tonkomolotyh mineral'nyh dobavok na svojstva betona [Impact of Fine Ground Mineral Additives on Properties of Concrete]. Stroitel'nye Materialy. 2019. No. 3 (768). Pp. 73–76. DOI: 10.31659/0585-430x-2019-768-3-73-76. (rus)
20. Hozin, V.G., Krasnikova, N.M., Yeruslanova, E.V. Lightweight porous concrete based on dry mixes, Construction Materials. 2018. 9. Pp. 40–45. DOI: 10.31659/0585-430X-2018-763-9-40-45
21. Qu, X., Zhao, X. Previous and present investigations on the components, microstructure and main properties of autoclaved aerated concrete – A review. Construction and Building Materials. 2017. 135. Pp. 505–516. DOI: 10.1016/j.conbuildmat.2016.12.208
22. Lesovik, V.S., Glagolev, E.S., Voronov, V.V., Absimetov, M.V., Elistratkin, M.Y. Non-autoclaved aerated concrete on the basis of composite binder using technogenic raw materials. Materials Science Forum. 2018. Vol. 945. Pp. 205–211. DOI: 10.4028/www.scientific.net/MSF.945.205
23. Korniyenko, S.V., Vatin, N.I., Gorshkov, A.S. Thermophysical field testing of residential buildings made of autoclaved aerated concrete blocks. Magazine of Civil Engineering. 2016. 64 (4). Pp. 10–25. DOI: 10.5862/MCE.64.2
24. Leontev, S., Saraykina, K., Golubev, V., Shamanov, V., Senkov, S., Yakovlev, G., Rakhimova, N., Urkhanova, L. Research into influence of ultra- and nanodisperse size additives on the structure and properties of heat insulating autoclaved aerated concrete. Procedia Engineering. 2017. Pp. 649–656. DOI: 10.1016/j.proeng.2017.02.076
25. Kasymova, M.T., Dyikanbaeva, N.A. Study of the structure and phase composition of non-autoclave aerated concrete // News of higher educational institutions. Construction. 2019. No. 7(727). Pp. 16–24.

Information about authors:

Lilia Ilina,

Doctor of Technical Science

ORCID: <https://orcid.org/0000-0002-8520-4453>

E-mail: nsklika@mail.ru

Alexander Kudyakov,
Doctor of Technical Science
E-mail: kudyakow@mail.tomsknet.ru

Mikhail Rakov,
PhD of Technical Science
ORCID: <https://orcid.org/0000-0001-9032-8138>
E-mail: westcoast89@mail.ru

Received 07.04.2021. Approved after reviewing 08.10.2021. Accepted 12.10.2021.



Research article

UDC 666.962

DOI: 10.34910/MCE.113.11



Magnesia cement in the MgO-CO₂-H₂O system

N.A. Mitina^a , I.B. Revva^a , A. Mitina^b 

^a National Research Tomsk Polytechnic University, Tomsk, Russia

^b National Research Tomsk State University, Tomsk, Russia

✉ mitinana@tpu.ru

Keywords: magnesium oxide, water resistance, thermoanalysis, carbonation, microstructure

Abstract. A detailed study of the MgO-CO₂-H₂O system allows creating new inorganic binders. The present research is focused on the process of structure formation during hydration and curing of magnesia composition from active magnesium oxide and magnesium bicarbonate solution. Magnesium hydroxide and magnesium hydrocarbonates, basically hydromagnesite and dypingite are the products of MgO interaction with solution of magnesium bicarbonate Mg(HCO₃)₂. This was established by means of complex thermal analysis using thermogravimetry (TG), differential scanning calorimetry (DSC), mass spectrometry (MS), and electron microscopy. These methods allowed us to define the influence of the curing environment of magnesia composition. Results show that processes of hydration and curing of composition of magnesium oxide with magnesium bicarbonate solution proceed most effectively in water conditions at the course of cyclic reactions of magnesium hydrocarbonate formation. The magnesia composition transforms magnesia cement into the state of hydraulic magnesia cement.

Acknowledgements: Research was carried out using the core facilities of TPU's "Physical and chemical methods of analysis".

Citation: Mitina, N.A., Revva, I.B., Mitina A. Magnesia cement in the MgO-CO₂-H₂O system. Magazine of Civil Engineering. 2022. 113(5). Article No. 11311. DOI: 10.34910/MCE.113.11

1. Introduction

Due to the unique combination of properties, magnesia cement is one of the most sufficient materials for creating compositions for construction and technological purposes. A robust hardening structure of magnesia compositions is created by the synthesis of such crystalline hydrates as magnesium hydroxychlorides and hydroxysulfates [1, 2]. At the same time, these substances entail low water resistance due to their supersolubility in water conditions. The phase of magnesium oxychloride (oxysulfate) is unstable upon prolonged contact with water, which leads to leaching through the dissolution of magnesium chloride (sulfate) from the cement phase, leaving magnesium hydroxide as a binder that is unable to form hardening structures [1]. Scientists use various methods to solve the issue. The positive effect of chemical additives, sulfates, phosphates, and iron compounds has been established [3, 4]. Mineral additives of natural [5, 6] and technogenic origin [7–10] also increase the water resistance of the compositions.

The following methods for increasing the water resistance of magnesia cement do not exclude the formation of water-soluble substances in the products of hydration and hardening, since they are based on the use of magnesium salt solutions as a mixing liquid. A radical way to increase the water resistance of magnesia cement is the synthesis of water-insoluble compounds in the hardening products of magnesia binder, it is possible only on condition of a complete replacement of the mixing fluid.

Analysis of compounds in the MgO-CO₂-H₂O system showed their insolubility in water or low solubility. Characteristic compositions in the MgO-CO₂-H₂O system are hydrocarbonate groups of minerals with the general formula xMgCO₃·yMg(OH)₂·zH₂O and MgCO₃·xH₂O [1, 11–12], and also brucite Mg(OH)₂

and magnesite $MgCO_3$. Hydrocarbonate groups include barringtonite $MgCO_3 \cdot 2H_2O$, nesquehonite $MgCO_3 \cdot 3H_2O$, lansfordite $MgCO_3 \cdot 5H_2O$, pokrovskite $Mg_2(CO_3)(OH)_2 \cdot 0.5H_2O$, artinite $Mg_2(CO_3)(OH)_2 \cdot 3H_2O$, hydromagnesite $Mg_5(CO_3)_4(OH)_2 \cdot 4H_2O$, dypingite $Mg_5(CO_3)_4(OH)_2 \cdot 5H_2O$, giorgiosite $Mg_5(CO_3)_4(OH)_2 \cdot 5-6H_2O$, shelkovite $Mg_7(CO_3)_5(OH)_4 \cdot 24H_2O$. Hydrocarbonates with general formula $xMgCO_3 \cdot yMg(OH)_2 \cdot zH_2O$ are subdivided into a light form with content of H_2O up to 4 molecules and a heavy one with content of H_2O from 4 up to 5 molecules.

Researches in the field of the $MgO-CO_2-H_2O$ system are focused on studying natural and artificial magnesium hydrocarbonate phases [11, 13–21]. Study of natural magnesium hydrocarbonates [14, 19–21] allows to trace history of genesis and metamorphism of carbonate and magnesium silicate rocks. Purposeful synthesis of magnesium hydrocarbonates allows to obtain pure products, without impurity, for different fields of application [13, 18, 22–23]. The researches dedicated to CO_2 removal from the atmosphere (sequestration) are also actual nowadays. These processes perform well involving the components of the $MgO-CO_2-H_2O$ system, for instance, original elements as well as compound substances [24–26].

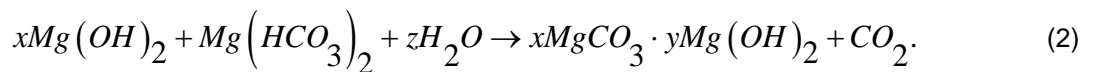
The $MgO-CO_2-H_2O$ system has great interest as the curable system which products are capable to create strong curing structures and to be used to produce new types of binders. Some scientists have already used synthesized magnesium hydrocarbonates for the purpose of hardening and creation of binding compositions [25–30]. The process of hardening is also performed with the help of external carbonization both natural one using CO_2 of environment air, and artificial one at the elevated pressure of CO_2 gas in the special chamber [11–18, 29–30]. Binding compositions have been obtained by gaging of caustic magnesite with special solutions [31–32] which essentially differ from classical magnesia Sorel cement. The compositions have high water resistance.

In this research the binding composition has been presented by mixture of caustic magnesium oxide MgO with water solution of magnesium bicarbonate (MBC) [31]. The interaction of active powder of magnesium oxide with MBC solution takes place in accordance with the following reactions (1, 2) [33]. This is consistent with studies of the carbonization magnesium compounds [22, 29–30, 32].

At first the hydration reaction proceeds:



Further formed magnesium hydroxide interacts with MBC in accordance with the reaction:



With formation of magnesium hydrocarbonate and carbon dioxide which entering the interaction with excess of magnesium hydroxide forms secondary MBC:



Secondary magnesium bicarbonate interacts with magnesium hydroxide again in accordance with the reaction (2) creating new portion of magnesium hydrocarbonate. Thus, three main crystal phases – magnesium hydroxide, magnesium carbonate and magnesium hydrocarbonates, which quantitative ratio is predetermined by content of magnesium bicarbonate in gauging liquid, are formed in cement stone as the result of proceeding consequent and parallel reactions (1, 2, 3). At that, composition and quantity of magnesium hydrocarbonate phase changes permanently and depends on the time of interaction and humidity of environment. Hydrocarbonate phases in the composition of hardening products make it possible for magnesia compositions to harden in water.

The goal of the research is determination of conditions for structuration and specification of types for new crystal formations of binding compositions using MBC solution when hardening in air-dry conditions and in water.

In connection with this goal, the tasks of studying the formation and change of hydrocarbonate phases depending on the hardening medium are solved using combined thermal analysis, differential scanning calorimetry (TG/DSC) and mass-spectrometric analysis of the interaction products.

2. Materials and Methods

2.1. Materials

The research has been performed using factory caustic magnesite of LLC "Sibirskiye poroshki" (Irkutsk) produced by roasting of magnesite rocks of the Savinsky deposit (Irkutsk region) in the rotating furnaces at a temperature of 800 °C. The chemical composition of initial and ignited rock is presented in Table 1.

Table 1. The chemical composition of caustic magnesite and initial magnesite rock

Material	Content, wt. %							Total
	MgO	SiO ₂	Al ₂ O ₃	CaO	Fe ₂ O ₃	MnO	Loss on ignition	
Initial magnesite	47,21	1.61	0.59	0.86	0.81	0.29	48.63	100.00
Caustic magnesite	75.64	3.18	0.62	4.24	0.83	0.32	15,17*	100.00

*- losses of caustic magnesite burned at 800 °C are connected with existence of undecomposed MgCO₃ with defect structure.

MBC solution has been obtained with artificial carbonization of caustic MgO suspension in the 5 l autoclave with a stirrer. The ratio of caustic powder and water was 10 g of MgO for 1 l of H₂O. Carbonization has been performed under CO₂ gas pressure of 0.9 MPa within 20 min. Concentration of MBC solution on bicarbonate ions was 6224.0 mg/l [33].

2.2. Methods

To study processes of hydration and curing of magnesia composition with the curing time up to 28 days we prepared mixtures of caustic magnesia powder and MBC solution with ratio of L/S = 0.5, and formed samples. After air curing within 24 hours these samples were located in different environments. Curing environments of the samples differed on humidity: 1) air humid – humidity was about 70 %, air temperature was 22–25 °C; 2) air moist – humidity was 95 ± 5 %, air temperature was 22–25 °C; 3) water (the samples were dipped into water, water layer over the sample was 2 cm). The samples cured within 3, 7, 14, and 28 days. After certain curing term the samples were taken from environment, dried up to the constant weight at temperature not more than 60 °C and tested.

To carry out thermal analysis we used the device for synchronous thermal analysis STA 449 F3 *Jupiter*® NETZSCH (Germany). The samples were heated in the air from 25 to 1000 °C with speed of 10 °C/min. Analysis of evolved gaseous products was performed with the QMS-403D quadrupole mass spectrometer of NETZSCH firm (Germany) production.

Microstructure of the samples was observed by means of the scanning electron microscope JEOL JSM 6000.

3. Results and Discussion

3.1. Microstructure

The curing environment of magnesia composition exercises considerable influence on composition and microstructure of products. After 28 days of curing in various kinds of environments different degrees of crystallinity, new crystal formation size and character of microstructure are registered during the experiment (Fig. 1).

The storage in humid and water conditions causes a big number of aggregations of foliated crystal formations: dypingite [25] and hydromagnesite [26]. They are formed at the edges of lamellar crystals of magnesium hydroxide Mg(OH)₂ that confirms theoretical assumptions about primary formation of magnesium hydroxide, and then its interaction with bicarbonate ions creating hydrocarbonates. There are no such processes in the samples, which were exposed to air with low humidity. Most new formations are light crystallized particles of magnesium hydroxide and magnesium hydrocarbonates, and also residues of unreacted magnesium oxide. This difference is caused by beneficial effect of water environment where magnesium oxide is constantly and actively hydrated and conditions for its interaction with bicarbonate ions are created. There is no supply of reacting components, in particular H₂O, during air curing after mixing of magnesium oxide with MBC solution. Thus, intensity of magnesia composition curing with MBC solution depends on the degree of MgO hydration.

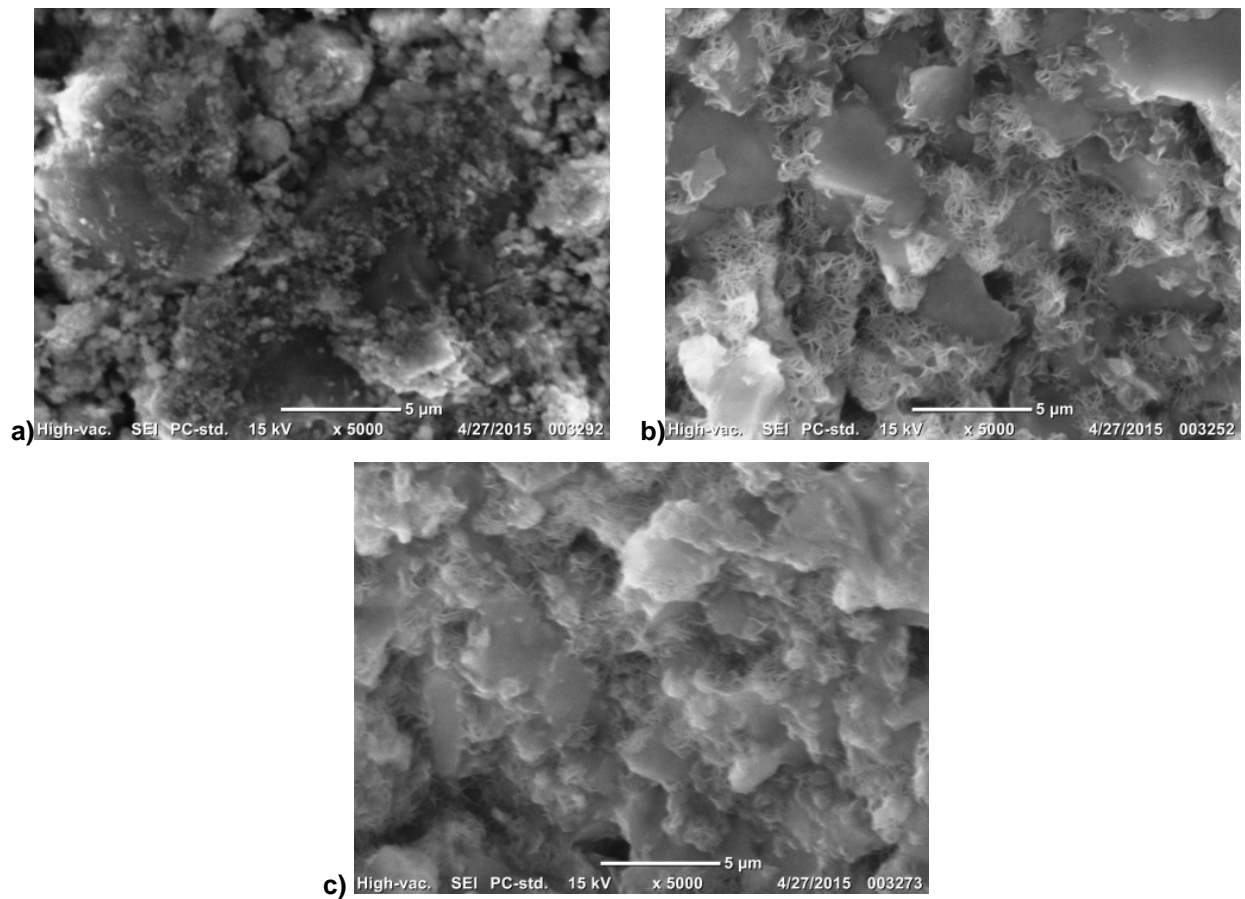
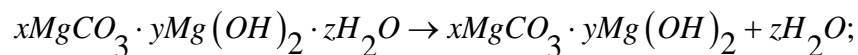


Figure 1. Microstructure of magnesia compositions after curing within 28 days in: a) air humid environment; b) air moist environment; c) in water.

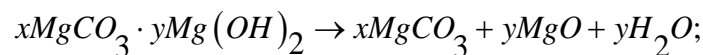
3.2. Simultaneous thermal analysis

The main processes of heating hydration products and curing the magnesia composition [12, 29, 32] are:

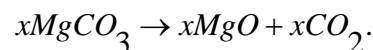
- dehydration, that is removal of crystallization water



- dehydroxylation, that is removal of hydroxyl group with decomposition of $Mg(OH)_2$ on MgO and H_2O



- decarbonization



Influence of curing environment of magnesia compositions is well traced by results of thermal analyses. TG and DSC curves of magnesia compositions cured on air and in water within 7 days (Fig. 2a) and 28 days (to Fig. 2b) are presented in Fig. 2. Results of thermogravimetric analysis of the magnesia composition samples at the age of 3, 7, 14, and 28 days when curing on air and in water are shown in Table 2. It is clear that weight losses at curing magnesia compositions in water exceed these values while curing them on air. Endothermic effects of DSC curves at average temperatures of 240, 400, and 590 °C correspond to processes of dehydration, dehydroxylation, and decarbonization of the magnesia composition samples at heating [12]. The endothermic effect at the temperature of 720–740 °C is well showed in Fig. 2 (b) and corresponds to the decarbonization of magnesium carbonate $MgCO_3$. The presence of magnesium carbonate is explained by underburned in the original caustic magnesite.

Table 2. Weight losses and TG of magnesia compositions

Peak	Age of 3 days		Age of 7 days		Age of 14 days		Age of 28 days	
	Temperature peak, °C	Weight losses, %						
1	86.6/113.3	5.1/5.9*	149.8/97.6	4.5/4.6	122.9/107.1	5.4/6.3	92.9/92.9	4.6/5.9
	240.3/240.0		252.7/245.3		242.2/245.3		246.3/245.0	
2	388.2/414.3	10.3/15.5	406.2/400.1	10.8/16.9	396.8/403.2	11.3/16.6	397.5/405.2	11.3/17.4
3	586.8/614.2	14.1/14.9	617.7/584.5	14.1/13.2	593.1/587.1	16.3/14.9	588.6/585.9	14.1/13.0

*- in numerator data for air environment, in denominator data for water environment

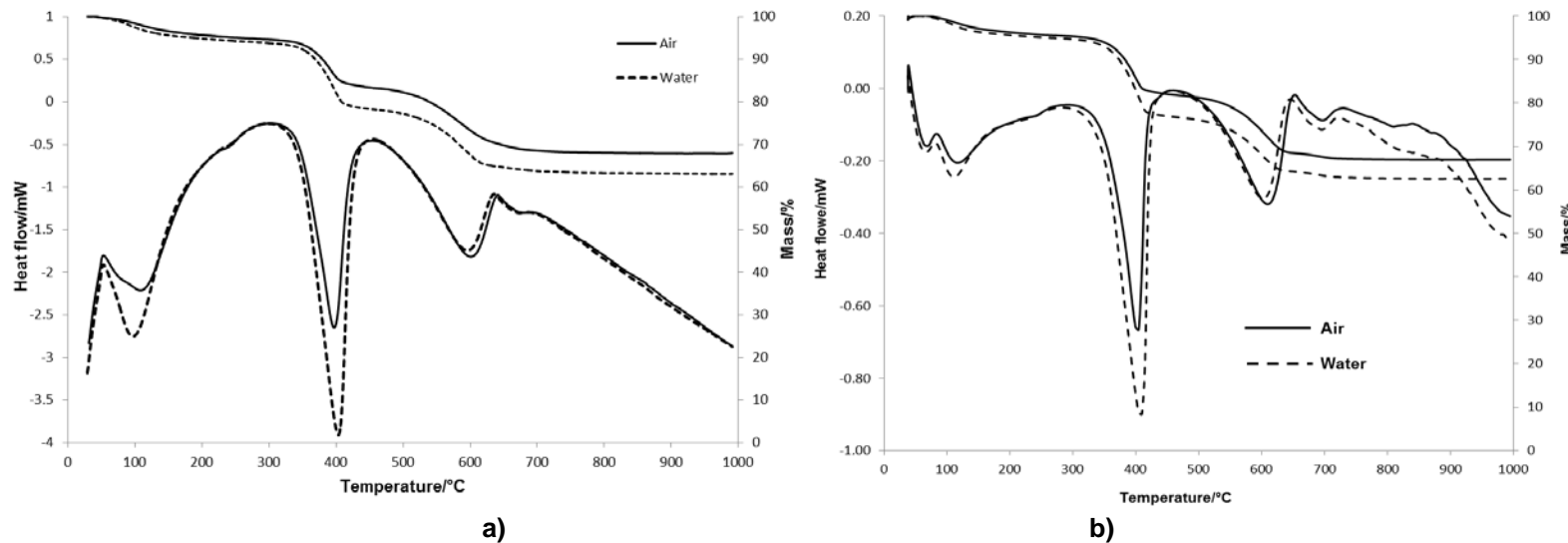


Figure 2. Thermograms of magnesia compositions at the age of 7 (a) and 28 (b) days.

The greatest difference in weight loss of magnesia compositions while curing in different conditions is registered during dehydroxylation process at the temperature of 400 °C. There is decomposition of $Mg(OH)_2$ both as component of magnesium hydrocarbonates crystallohydrates, and as initial magnesium hydroxide, which is formed in the reaction (1). Therefore, this thermal effect has been chosen to assess intensity of hydrocarbonate product formation at curing magnesia compositions with MBC solution (Fig. 3).

Data of Fig. 3 testify the different level of weight loss size at heating magnesia compositions in accordance with curing environment. The weight losses are increased on 50–70 % in the process of curing composition in water conditions. It implies that the quantity of magnesium hydrocarbonates is bigger in comparison with their quantity during formation in air environment. In addition, it is noted that if curing time of magnesia binding samples in water increases, the quantity of magnesium hydrocarbonates crystallohydrates increases, so that causes continuous increase of weight losses at dehydration and dehydroxylation. Such phenomenon is not observed during air curing because of lack of liquid component and the practical cessation of formation of magnesium hydroxide and, consequently, of magnesium hydrocarbonates.

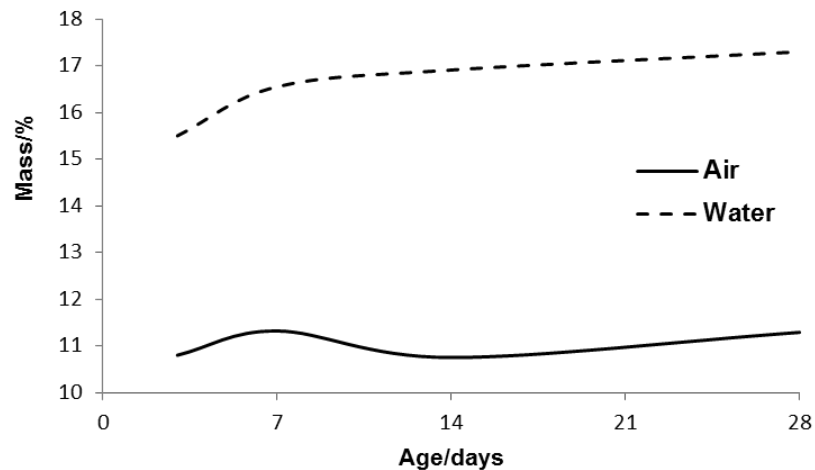


Figure 3. Dependence of weight losses during magnesia compositions' heating on curing time in different conditions.

In case of continuous presence of liquid phase while dipping and exposure in water of "the caustic magnesium oxide – MBC solution" system, continuous hydration of MgO takes place and cyclic process of magnesium hydrocarbonate formation in accordance with the reactions (1-3) occurs with the maximum intensity.

To confirm data of TG/DSC interaction products of caustic magnesite with MBC solution (Fig. 2b) we carried out analysis of gaseous products of the cyclic reactions 1-2 (Fig. 4) evolving during heating of the samples that were cured within 28 days in different conditions. Thermogravimetric and differential thermal analysis shows that total weight loss in the case of long presence of the reacting system on air is 33.01 %, during long presence in water – 37.5 %.

Ion current curves show that water vapors with the charge-mass ratio of 18 are removed at temperatures of 112, 242 (small amount) and at 405 °C [14]. The OH ion current curve (charge –mass ratio of 17) has the characteristic peaks corresponding to exudation of water. The beginning of CO₂ emission (charge-mass ratio of 12) is observed already at the temperature of 405 °C, the main process of magnesium hydrocarbonates decarbonization takes place at 606 °C. Emission of CO₂ at 696 °C occurs due to magnesium carbonate as an underburnt in the original caustic magnesia powder [34, 35].

Ion current curves with charge-mass ratio of 18 and 12 characterize the processes of thermal decomposition of magnesium hydrocarbonates (Table 3). Comparing curing conditions of magnesia compositions with MBC solution on the area of DSC thermograms peaks and ion current curves can indirectly inform about quantity of new formations. For this purpose, we chose characteristic peaks at maximum temperature of 405 °C, that are responsible for removal of water, hydroxyl ion and partial decarbonization and at 600 °C, according to decarbonization.

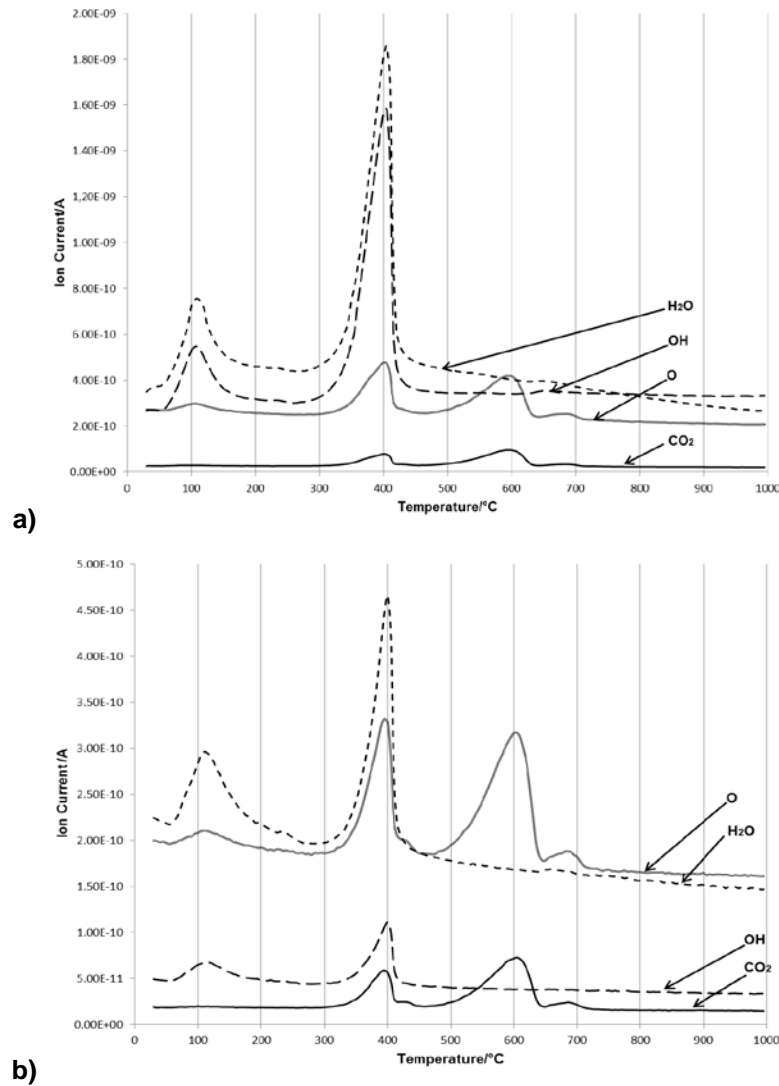


Figure 4. Ion current curves of gas emission at heating of magnesia compositions cured in air conditions (a) and in water conditions (b).

Table 3. Area of characteristic peaks of curves of thermal analysis and ion current

Peak temperature, °C	Processes	Area of peaks of DSC, J/g		Area of peaks of ion current curves, A	
		Air environment	Water	Air environment	Water
405	Removal of H ₂ O Removal of OH Removal of CO ₂	344.8	559.2	$1.35 \cdot 10^{-7}$	$8.08 \cdot 10^{-7}$
606	Decarbonization	331.9	337.3	$0.07 \cdot 10^{-7}$	$0.16 \cdot 10^{-7}$

Data of DSC and ion current curves show that the water environment provides formation of larger quantity of magnesium hydrocarbonates. The area under the integral sign of peak characterizes quantitatively the processes of thermal decomposition of the studied products and emission of gases. At the temperature of 405 °C, which causes the removal of water and hydroxyl ion, the peak area on thermogram is practically twice as much at curing magnesia composition in water, in comparison with curing one in air conditions. It is confirmed by data of mass spectroscopy on H₂O. During the decarbonization process at 606 °C by thermogram there was no difference in number of evolved CO₂, the area of peaks in air and water environment is almost identical – 331.9 and 337.3 J/g. However, according to mass spectrometry data the area of peak at the given temperature in water conditions is much bigger than one in air conditions that implies higher efficiency of magnesium hydrocarbonate formation during curing magnesia composition in water.

4. Conclusions

The results obtained confirm that:

1. In the interaction between magnesia caustic powder and solution of magnesium bicarbonate magnesium hydroxide and hydrocarbonate phases, dypengite and hydromagnesite, are formed.
2. The hardening of the magnesia composition under moist conditions after preliminary exposure to air contributes to a more intense structure formation, which is confirmed by thermal analysis methods. The formation of an increased amount of magnesium hydroxide is observed, since the hydration process in water conditions is continuous. $Mg(OH)_2$ in a highly dispersed state is the basis for new phases of magnesium bicarbonates. Thus, the bicarbonate magnesia binder is capable of hardening in water.
3. Structures generated from magnesium bicarbonates are insoluble in water. Therefore, magnesia binders relating to the $MgO-CO_2-H_2O$ system may be classified as hydraulic magnesia binders.

References

1. Shand, Mark A. The Chemistry and Technology of Magnesia. John Wiley & Sons. New York, 2006. 266 p.
2. Svit, T.F. Termogravimetricheskoe issledovanie produktov gidratatsii i tverdenija sulfomagnezial'nyh vjashushhih veshhestv [Thermogravimetric study of hydration and hardening products of sulfomagnezian binders]. Polzunovskij vestnik. 2010. No. 3. Pp. 100–103.
3. Li, Y., Li, Z., Pei, H., Yu, H. The influence of $FeSO_4$ and KH_2PO_4 on the performance of magnesium oxychloride cement. Construction and Building Materials. 2016. No. 102. Pp. 233–238. DOI: 10.1016/j.conbuildmat.2015.10.186
4. Zimich, V.V., Kramar, L.Ja., Trofimov, B.Ja. Reduced hygroscopicity and improved water resistance hlormagnezial'nogo stone by introducing ferric [Reduced hygroscopicity and improved water resistance hlormagnezial'nogo stone by introducing ferric]. Stroitel'nye materialy. 2009. No. 5. Pp. 58–61.
5. Vereshchagin, V.I., Smirenskaya, V.N., Érdman, S.V. Water-resistant blended oxychlorate cements. Glass and Ceramics. 1997. 54 (11-12). Pp. 368–372.
6. Zyrjanova, V.N., Lytkina, E.V., Berdov, G.I. Povyshenie mehanicheskoy prochnosti i vodostojkosti magnezial'nyh vjashushhih veshhestv pri vvedenii mineral'nyh napolnitelej [Increasing the mechanical strength and water resistance of magnesia binders with the introduction of mineral fillers]. Izvestija vysshih uchebnyh zavedenij. Stroitel'stvo. 2010. No. 3. Pp. 21–26.
7. Sam, A. Walling, John, L. Provis Magnesia-Based Cements: A Journey of 150 Years, and Cements for the Future? Chemical Reviews. 2016. No. 116. Pp. 4170–4204. DOI: 10.1021/acs.chemrev.5b00463
8. He, P., Poon, C.S., Tsang, D.C.W. Effect of pulverized fuel ash and CO_2 curing on the water resistance of magnesium oxychloride cement (MOC). Cement and Concrete Research. 2017. No. 97. Pp. 115–122. DOI: 10.1016/j.cemconres.2017.03.005
9. He, P., Poon, C.S., Tsang, D.C.W. Using incinerated sewage sludge ash to improve the water resistance of magnesium oxychloride cement (MOC). Construction and Building Materials. 2017. No. 147. Pp. 519–524. DOI: 10.1016/j.conbuildmat.2017.04.187
10. Zimich, V.V., Kramar, L.Ja., Chernyh, T.N., Pudovikov, V.N., Perminov, A.V. Osobnosti vlijanija dobavki zolja gidroksida zheleza na strukturu i svojstva magnezial'nogo kamnja [Features of the effect of the addition of iron hydroxide sol on the structure and properties of magnesia stone] Vestnik JuUrgU. Serija Stroitel'stvo i arhitektura. 2011. 13 (35). Pp. 25–32.
11. Hopkinson, L., Kristova, P., Rutt, K., Cressey, G. Phase transitions in the system $MgO-CO_2-H_2O$ during CO_2 degassing of Mg-bearing solutions. Geochimica et Cosmochimica Acta. 2012. No. 76. Pp. 1–13. DOI: 10.1016/j.gca.2011.10.023
12. Unluer, C., Al-Tabbaa, A. Characterization of light and heavy hydrated magnesium carbonates using thermal analysis. Journal of Thermal Analysis and Calorimetry. 2014. No. 115. Pp. 595–607. DOI: 10.1007/s10973-013-3300-3
13. Ballirano, P., De Vito, C., Mignardi, S., Ferrini, V. Phase transitions in the $Mg-CO_2-H_2O$ system and the thermal decomposition of dypingite, $Mg_5(CO_3)_4(OH)_2 \cdot 5H_2O$: Implications for geosequestration of carbon dioxide. Chemical Geology. 2013. 340 (24). Pp. 59–67. DOI: 10.1016/j.chemgeo.2012.12.005
14. Frost, R.L., Bahfenne, S., Graham, J., Reddy, B.J. The structure of selected magnesium carbonate minerals – A near infrared and mid-infrared spectroscopic study. Polyhedron. 2008. No. 27. Pp. 2069–2076. DOI: 10.1016/j.poly.2008.03.019
15. Zhao, Y., Zhu, G. A technology of preparing honeycomb-like structure MgO from low-grade magnesite. International Journal of Mineral Processing. 2014. No. 126. Pp. 35–40. DOI: 10.1016/j.minpro.2013.11.006
16. Ferrini, V., De Vito, C., Mignardi, S. Synthesis of nesquehonite by reaction of gaseous CO_2 with Mg chloride solution: Its potential role in the sequestration of carbon dioxide. Journal of Hazardous Materials. 2009. No. 168. Pp. 832–837. DOI: 10.1016/j.jhazmat.2009.02.103
17. Xiong, Y., Snider Lord, A. Experimental investigations of the reaction path in the $MgO-CO_2-H_2O$ system in solutions with various ionic strengths, and their applications to nuclear waste isolation. Applied Geochemistry. 2008. No. 23. Pp. 1634–1659. DOI.org/10.1016/j.apgeochem.2007.12.035
18. Hovelmann, J., Putnis, C.V., Ruiz-Agudo, E., Austrheim, H. Direct Nanoscale Observations of CO_2 Sequestration during Brucite $[Mg(OH)_2]$ Dissolution. Environmental Science and Technology. 2012. No. 46. Pp. 5253–5260. DOI: 10.1021/es30-0403n
19. Chelnokov, G.A., Haritonova, N.A. Uglekislye mineral'nye vody yuga Dal'nego Vostoka Rossii [High PCO_2 Mineral Waters of the South of Far East of Russia]. Vladivostok: Dalnauka, 2008. 165 p.
20. Diaying, Chen, Eric, H. Jordan Synthesis of porous, high surface area MgO microspheres. Materials Letters. 2009. No. 63. Pp. 783–785. DOI: 10.1016/j.matlet.2009.01.014
21. Frost, R.L., Bahfenne, S., Graham, J., Martens, W.N. Thermal stability of artinite, dypingite and brugnatellite – Implications for the geosequestration of greenhouse gases. Thermochimica Acta. 2008. No. 475. Pp. 39–43. DOI: 10.1016/j.tca.2008.06.007
22. Guocai, Z., Zhang, H., Zhao, Y. A novel recirculating reactor for the leaching of magnesia by CO_2 . Hydrometallurgy. 2008. No. 92. Pp. 141–147. DOI.org/10.1016/j.hydromet.2008.01.011

23. Hollingbery, L.A., Hull, T.R. The thermal decomposition of natural mixtures of huntite and hydromagnesite. *Thermochimica Acta*. 2012. No. 528. Pp. 45–52. DOI: 10.1016/j.tca.2011.11.002
24. Frost, R.L., Bahfenne, S., Graham, J., Martens, W.N. Thermal stability of artinite, dypingite and brugnatellite – Implications for the geosequestration of greenhouse gases. *Thermochimica Acta*. 2008. No. 475. Pp. 39–43. DOI: 10.1016/j.tca.2008.06.007
25. Kuenzel, C., Zhang, F., Ferrándiz-Mas, V., Cheeseman, C.R., Gartner, E.M. The mechanism of hydration of MgO-hydromagnesite blends. *Cement and Concrete Research*. 2018. No. 103. Pp. 123–129. DOI.org/10.1016/j.cemconres.2017.10.003
26. Vlasopoulos, N. Process for producing cement binder compositions containing magnesium. Patent US no. 20130213273A1, 2013.
27. Kelemen, P.B., McQueen, N., Wilcox, J., Renforth, Ph., Dipple, Gr., Vankeuren, A.P. Engineered carbon mineralization in ultramafic rocks for CO₂ removal from air: Review and new insights. *Chemical Geology*. 2020. No. 550. Pp. 119628. DOI.org/10.1016/j.chemgeo.2020.119628
28. Morrison, J., Jauffret, G., Galvez-Martos, J.L., Glasser, F.P. Magnesium-based cements for CO₂ capture and utilization. *Cement and Concrete Research*. 2016. No. 85. Pp. 183–191. DOI.org/10.1016/j.cemconres.2015.12.016
29. Dung, N.T., Unluer, C. Improving the performance of reactive MgO cement-based concrete mixes. *Construction and Building Materials*. 2016. No. 126. Pp. 747–758. dx.doi.org/10.1016/j.conbuildmat.2016.09.090
30. Ruan, S., Unluer, C. Influence of mix design on the carbonation, mechanical properties and microstructure of reactive MgO cement-based concrete. *Cement and Concrete Composites*. 2017. No. 80. Pp. 104–114. dx.doi.org/10.1016/j.cemconcomp.2017.03.004
31. Guo, Y., Tan, Ch., Wang, P., Sun, J., Li, W., Zhao, Ch., Lu, P. Magnesium-based basic mixtures derived from earth-abundant natural minerals for CO₂ capture in simulated flue gas. *Fuel*. 2019. No. 243. Pp. 298–305. DOI.org/10.1016/j.fuel.2019.01.108
32. Unluer, C., Al-Tabbaa, A. Impact of hydratedmagnesium carbonate additives on the carbonation of reactive MgO cements. *Cement and Concrete Research*. 2013. No. 54. Pp. 87–97. DOI.org/10.1016/j.cemconres.2013.08.009
33. Mitina, N.A., Lotov, V.A., Sukhushina, A.V. ZHidkost' zatvoreniya dlya magnezial'nogo vyazhushchego. [Fluid mixing for magnesia binder]. *Stroitel' nye Materialy*. 2015. No. 1. Pp. 64–68.
34. Vágvölgyi, V., Hales, M., Frost, R.L., Locke, A., Kristóf, J., Horváth, E. Conventional and controlled rate thermal analysis of nesquehonite Mg(HCO₃)(OH)·2(H₂O). *Journal of Thermal Analysis and Calorimetry*. 2008. 94 (2). Pp. 523–528. DOI: 10.1007/s10973-007-8844-7
35. Vágvölgyi, V., Frost, R.L., Hales, M., Locke, A., Kristóf, J., Horváth, E. Controlled rate thermal analysis of hydromagnesite. *Journal of Thermal Analysis and Calorimetry*. 2008. 92 (3). Pp. 893–897. DOI: 10.1007/s10973-007-8845-6

Information about authors:

Natalia Mitina

PhD of Technical Science

ORCID: <https://orcid.org/0000-0002-1032-6077>

E-mail: mitinana@tpu.ru

Inna Revva

PhD of Technical Science

ORCID: <https://orcid.org/0000-0003-4184-1554>

E-mail: revva@tpu.ru

Anna Mitina

ORCID: <https://orcid.org/0000-0003-0670-5143>

E-mail: mit1na4n@yandex.ru

Received 25.02.2021. Approved after reviewing 13.10.2021. Accepted 15.10.2021.



Research article

UDC 626

DOI: 10.34910/MCE.113.12



The calculation of the dynamic characteristics of the spillway of the dam

G.L. Kozinetc , **P.V. Kozinetc**

Peter the Great St. Petersburg Polytechnic University, St. Petersburg, Russia

 kozinets_gl@spbstu.ru

Keywords: concrete spillways, earthquake, natural frequencies, mode shapes, finite element method, deformation

Abstract. The object of the presented studies is a concrete spillway dam of a run-of-river hydroelectric power station. The modes of vibrations are determined on the basis of a solid model, which is necessary to take into account possible resonant phenomena in the structure. A review of publications on the method of calculating the dynamic responses of structures is made. Computational studies were carried out by the finite element method based on the calculated three-component accelerogram. When processing the results, the possibilities of modal temporal calculation were used. The response of structures excited by forces, time-varying or earthquake is calculated. Based on the calculation results, the natural frequencies and vibration modes of the concrete spillway dam were determined. The description of the oscillations of the dam is made. According to the obtained response spectrum, the maximum horizontal accelerations were achieved. Based on the response spectra, a calculated three-component accelerogram was synthesized at the equipment installation marks.

Funding: Thanks the Ministry of Science and Higher Education of the Russian Federation for financial support of numeric simulations under the Strategic Academic Leadership Program "Priority 2030" (Agreement 075-15-2021-1333 dated 30.09.2021).

Citation: Kozinetc, G.L., Kozinetc, P.V. The calculation of the dynamic characteristics of the spillway of the dam. Magazine of Civil Engineering. 2022. 113(5). Article No. 11312. DOI: 10.34910/MCE.113.12

1. Introduction

When designing hydroelectric power plants in zones of seismic activity, an indispensable condition is the analysis of natural frequencies and forms of vibrations of structures. A feature of the seismic design of HPPs is the consideration of two levels of seismic impact, referred to in Russia as a design earthquake (DE) and a maximum design earthquake (MPE).

The first of them is the strongest earthquake that can actually occur during the estimated period of operation of the HPP, equal to 100 years; the second is the strongest earthquake, generally potentially possible at this site.

In the recommendations of the IAEA, the design basis earthquake is designated as SL1, and MSE as SL2.

American designations are widely used in the world: for OBE - OBE (Operating Basis Earthquake - safe stop earthquake).

The intensities of PZ and MSE are established on the basis of historical information about past earthquakes, as well as (primarily MSE) with the help of geophysical surveys. There are two main approaches to determining these intensities. (The first used in Russia and a number of other countries) -

probabilistic: an earthquake with a recurrence interval of 1 time in 100 years is taken as a PZ, and 1 time in 10,000 years as an MPS.

Under seismic action, the structure begins to oscillate. For the analysis of vibration modes and resonance phenomena, a prerequisite is the determination of natural frequencies and vibration modes or the dynamic characteristics of the structure.

The task of the research was to determine the natural frequencies and analyze the vibration modes of the spillway dam of the run-of-river hydroelectric power station, Fig. 1.

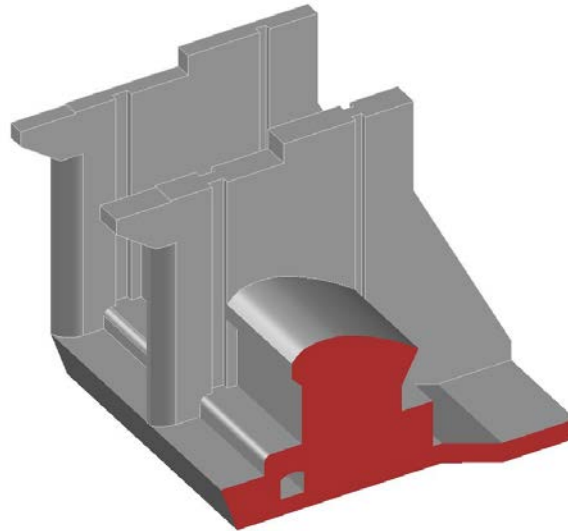


Figure 1. Volumetric geometric model of the spillway dam of a run-of-river HPP with a section along the spillway.

The initial data for the calculation are the geometric parameters of the spillway dam of the Nizhne-Bureya HPP on the Bureya River, the physical characteristics of the concrete material and the base soil, as well as the accelerogram of the dynamic seismic impact.

The spillway structure is designed to release water in case of overflow of the reservoir in front of the dam. The spillway structure consists of a dam divided across by concrete abutments (steers), which can serve as bridge supports for medium-pressure run-of-river hydroelectric power plants. Lifting mechanisms are mounted on the bulls, designed to maneuver the hydraulic gates that block the spillways.

Since there is equipment on the spillways, it is necessary to calculate the load on it during an earthquake. The elevation of the equipment supports is higher than the base surface, so the seismic load at the elevation of the supports is always greater than at the elevation of the spillway base.

Determining the seismic response or response spectrum at the equipment installation level is an actual dynamic problem.

The spillway dam of the run-of-river hydroelectric power station is a five-span concrete structure. Each spillway is limited by bulls, one of which is monolithic, and the other has an expansion joint in the middle of the bull. The spillway operation is provided by segment gates with smooth flow control.

The physical characteristics of B20 class concrete of the spillway dam are as follows: concrete density $p_b = 2.36 \text{ t/m}^3$. Design resistance of concrete in compression R_b and tension R_{bt} for the limit states of the first group: $R_b = 11700 \text{ kPa}$; $R_{bt} = 900 \text{ kPa}$. The initial modulus of elasticity of concrete in compression and tension $E_b = 3.0 \times 10^7 \text{ kPa}$. The coefficient of transverse deformation of concrete (Poisson's ratio) for massive structures $\nu = 0.15$.

The rocky base is composed of granites. Physical and mechanical properties and thermophysical characteristics of a rocky base made of granite:

Density $p_{gr} = 2.65 \text{ t/m}^3$.

Modulus of elasticity $E = 1.30 \times 10^7 \text{ kPa}$.

Poisson's ratio $\nu = 0.35$.

Adhesion $c = 400 \text{ kPa}$. Angle of internal friction $\varphi = 39^\circ$.

Thermal expansion coefficient $\alpha_{gr} = 1.4 \times 10^{-5} \text{ } ^\circ\text{C}^{-1}$.

Thermal conductivity coefficient $K_{gr} = 1.81 \text{ W / (m * K)}$.

Studies of the dynamic characteristics of concrete structures is the first stage in the calculation of structures for seismic resistance.

Among scientists [1–24], who study seismic resistance and dynamic characteristics of structures, it is necessary to note the works of Ya.N. Aizenberg, A.N. Birbraer, S.P. Timoshenko, V.V. Lalin and others [1, 2, 10, 15, 20].

Many articles and books [8–14], [17–24] are devoted to methods for numerically solving problems of structure dynamics.

The theory of the finite element method is covered in the works of O Zenkevich, K. Morgan, G. Strang [4–6], and many other authors.

In studies [18], an analysis was made of comparing the dynamic parameters calculated from the processed experimental data with the parameters obtained from seismic data, and close values were obtained. A numerical modal analysis of the rockfill dam has been carried out, and the correspondence of the vibration parameter with the experimental data has been obtained.

The article [19] analyzes the modal and harmonic characteristics for the design of the power plant at the Kenir Dam in Terengganu, Malaysia. Modal analysis was carried out to obtain the dynamic characteristics of the power plant, which include natural frequencies and mode shapes. A real-scale three-dimensional (3D) model of the Kenyir Dam power plant was built using SolidWorks software and imported into ANSYS software for finite element analysis (FE). According to the results, the six most significant natural frequencies and modes of oscillation are selected, the phenomenon of resonance from external disturbing forces is checked.

Article [20] is devoted to substantiating the magnitude of the calculated dynamic loads on the process equipment of nuclear power plants in the event of an aircraft impact. A technique for calculating PS with the required probability is given. The place and angle of impact, the distance from it to the equipment are taken into account. A technique for probabilistic substantiation of calculated dynamic loads on equipment in the event of an intentional aircraft crash at a nuclear power plant (terrorist act) is proposed.

Paper [21] presents the results obtained during the first six months of operation of the dynamic monitoring system, which include the characterization of acceleration levels for opening weirs after heavy rain, and the change in the modal properties of the Baixo Sabor arch dam in northeastern Portugal. At the end of the article, a comparison of the results of natural frequencies obtained with external excitation and the results obtained in a forced vibration test, as well as predicted using a numerical model, is presented.

In the study [22], the control of damage and the behavior of the structure of an earthen dam during an earthquake was performed. Important factors such as plane stress, plane strain, data monitoring, application of the finite element method, analysis of free vibrations, seismic cracks are identified. It is noted that earth dam structures have an integrated response to an increase in acceleration or displacement on the crest.

In [23], a method is proposed for analyzing the time-varying dynamic reliability for a concrete gravity dam under seismic action, based on the generalized probability density evolution method (GPDEM). The method can be used to predict the time-varying seismic performance of concrete dams in terms of probability. The effectiveness of the proposed method and its suitability for complex non-linear structures subjected to seismic loads have been confirmed.

In [24], a 2D non-linear dynamic analysis (NDA) was performed for an Austrian dam during the 1989 Loma Prieta earthquake. up to 859 mm. The engineering properties of compacted fill materials are evaluated based on available test data for isotropically compacted undrained triaxial compressions and resonant columns.

The validity of the research is due to the fact that in order to calculate the seismic resistance of equipment, it is necessary to calculate the response spectrum at the dam elevations.

The purpose of the study is to calculate the seismic load for equipment standing on the elevations of the structure.

The strength and stability of the concrete dam was not included in this study, but was carried out when determining the geometric dimensions of the structure.

Research objectives:

1. Construction of a mathematical dynamic model "dam-foundation" of a spillway dam, including partitioning into finite elements, setting material properties, setting boundary conditions;

2. Calculation of natural frequencies and vibration modes of the spillway dam;
3. Dynamic calculation of the structure for the calculated accelelogram;
4. Generation of response spectra at given nodes at the elevations of the spillway dam;
5. At the 5th stage, graphs of the response spectra at given nodes and tables of digitization of spectral curves are constructed.

2. Methods

Computational studies were carried out within the framework of the spatial formulation of the problem by the Finite Element Method (FEM) using the SolidWorks program. The method and its application in structural calculations are presented in [17-24]. The construction of the calculation model was carried out on the basis of the geometric parameters of the spillway dam. The design model of the dam with symmetry conditions for a continuous bull is shown in Figure 2.

The “structure-base” model was divided into three-dimensional 4-node elements of the tetrahedron -TETRA, interconnected at the nodes. Coordinate system: OX axis - along the flow, OY axis - across the flow, OZ axis - vertically upwards.

The opposite bull has free movement within the expansion joint. The results of the calculation are presented in the form of a table of natural frequencies and fields of relative deformations (modes of oscillation) of the structure.

When processing the results, the possibilities of modal time calculation (Modal Time History Analysis) were used. The response of structures excited by forces, time varying or earthquake is calculated. Independent (uncoupled) modal equations of motion are solved using Newmark's step-by-step integration method. Response Spectra Generation. The response spectrum curves at the specified node are calculated using the previously obtained modal time responses of the structure for that node. This variant of dynamic calculation allows generating curves of the response spectrum in any node of the structure for any degree of freedom of movement. A curve is generated and represents the maximum response amplitudes as a function of frequency for a given damping factor. The initial excitation for this version of the calculation is the accelerogram, which specifies the acceleration relative to time at the specified point of the structure. To generate the curve of the response spectrum, the results obtained from the modal calculation of the temporal characteristics were used. Thus, the response spectrum is generated after modal timing is performed.

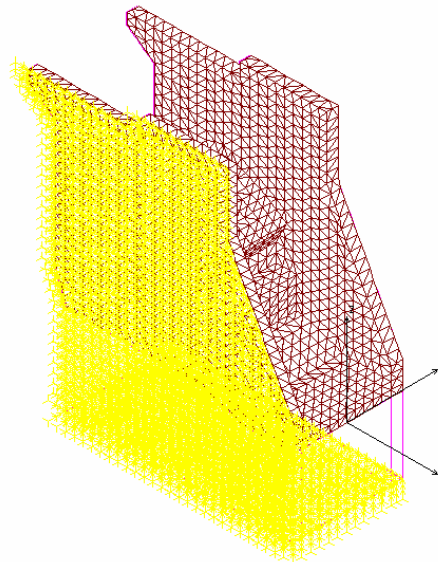


Figure 2. Calculation model of a spillway dam with boundary conditions.

3. Results and Discussion

In the work of A.I. Savich [25] carried out similar studies of the Sayano-Shushenskaya dam, including the behavior of the dam under static loads and seismic impacts. At the same time, the authors did not determine the response spectra on equipment marks.

As a result of solving problems 1 and 2 of our research, 15 first natural frequencies of the dam-foundation were obtained, ranging from 4.11 to 29.7 Hz (from 25.82 to 186.8 rad/sec), Table 1.

Table 1. Forms and frequencies of natural oscillations of the structure.

Form No.	Frequency	Frequency	Period
	Hz	Rad/sec	seconds
1	4.11076	25.8287	0.243264
2	5.48924	34.4899	0.182175
3	8.02316	50.4110	0.124639
4	10.6378	66.8391	0.0940046
5	12.0677	75.8234	0.0828660
6	14.4089	90.5337	0.0694016
7	16.4201	103.170	0.0609011
8	17.9924	113.050	0.0555789
9	18.9998	119.379	0.0526322
10	20.4634	128.575	0.0488677
11	23.1945	145.735	0.0431137
12	24.5038	153.962	0.0408100
13	25.6340	161.063	0.0390106
14	27.3885	172.087	0.0365117
15	29.7395	186.859	0.0336253

3.1. Analysis of the forms and frequencies of vibrations

The first form of oscillations with a frequency of 4.11 Hz (25.8287 rad/sec) shows local horizontal oscillations along the flow along the OX axis of one bull with a deformation joint, (Figure 3). The second continuous bull is not involved in oscillations, since the model symmetry conditions are set on its boundary.

The spillway is not involved in the oscillatory process due to the rigidity of the monolithic spillway dam. Gobies are relatively thin high spillway elements, so they experience large deformations during an earthquake.

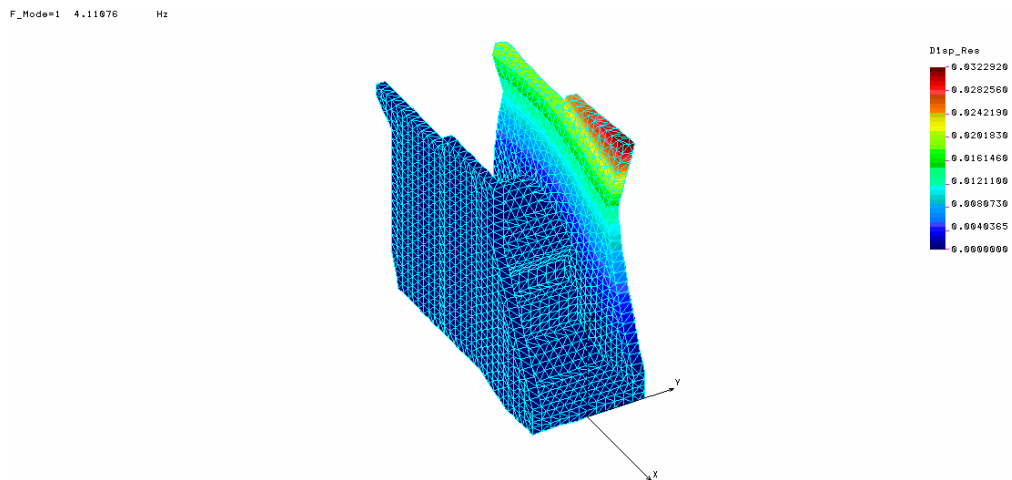


Figure 3. The first form of oscillation with a frequency of 4.11 Hz (25.8287 rad/s).

The second form of oscillations with a frequency of 5.48 Hz shows local horizontal oscillations with torsion across the flow along the OY axis of one bull with a deformation joint, (Figure 4). The main concrete of the spillway and the continuous steer do not participate in the vibrations.

The torsion of the steer occurs with the simultaneous action of longitudinal and transverse deformations of the relatively thin wall of the steer.

F_Mode=2 5.48924 Hz

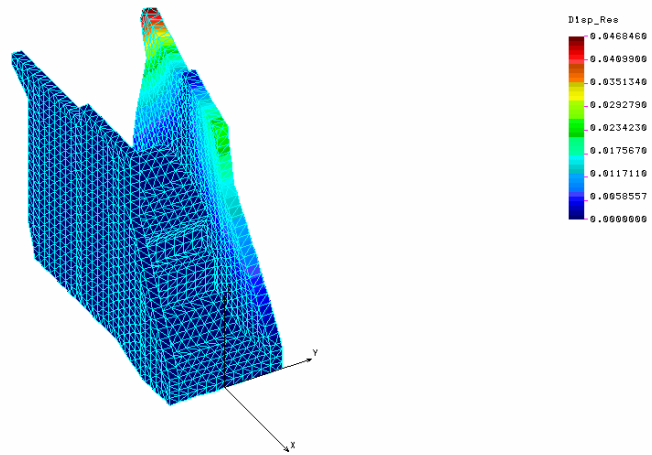


Figure 4. Second waveform with a frequency of 5.48 Hz (34.5 rad/s).

The third form of vibrations with a frequency of 8.02 Hz (50.4 rad/sec) represents the general horizontal vibrations of the dam along the flow along the OX axis; the entire weir is included in the oscillatory process. The steers of the structure experience the greatest relative deformations.

The spillway also oscillates along the horizontal axis OX. This form of oscillation is the most dangerous for the construction of the spillway dam as a whole.

F_Mode=3 8.02318 Hz

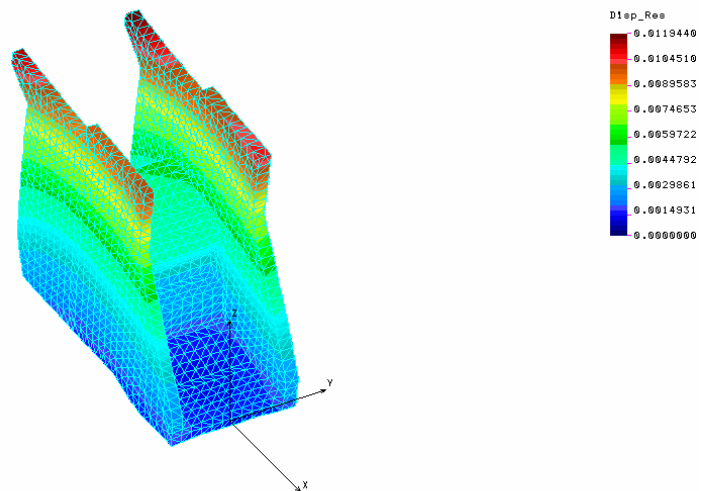


Figure 5. The third form of oscillation with a frequency of 8.02 Hz (50.4 rad/s).

The dynamic seismic impact on the structure is specified using a three-component calculated accelerogram, shown in Figure 6. The duration of the accelerogram is 8 seconds. Peak values of accelerations for each of the components are 1 m/s². The damping factor values for concrete are 0.05.

To evaluate the resonance phenomena, the response spectra were generated using the solution of the Duhamel integral:

$$F(t) = \frac{1}{\omega_0} \int_0^t F(\tau) e^{-\xi\omega(t-\tau)} \sin[\omega(t-\tau)] dt$$

where $F(t)$ is the force perturbation given by the accelerogram, ω is the natural circular frequency (rad/sec), $\xi = 0.05$ is dimensionless damping factor.

As an example of the assessment of resonance phenomena, an analysis of the spectrum of the response obtained at the upper elevation of the dam bull was performed.

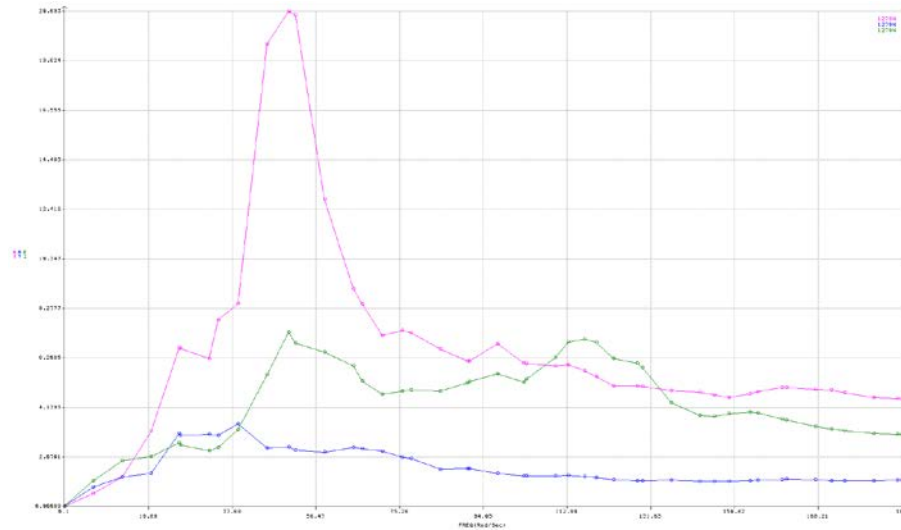


**Figure 6. Response spectra at the top mark of the spillway dam bull (dependence of accelerations m/s² on frequencies rad/s)
red line – horizontal accelerations AX (along the flow);
blue line – horizontal accelerations AY (across the flow);
green line – vertical accelerations AZ.**

The most dangerous is the horizontal component of the spectrum along the flow. According to the response spectrum obtained, the maximum horizontal accelerations of 20.693 m/s² correspond to a frequency of 50.01 rad/s and do not coincide with the first natural frequency of 25.8287 rad/s, so there will be no resonant phenomena during an earthquake.

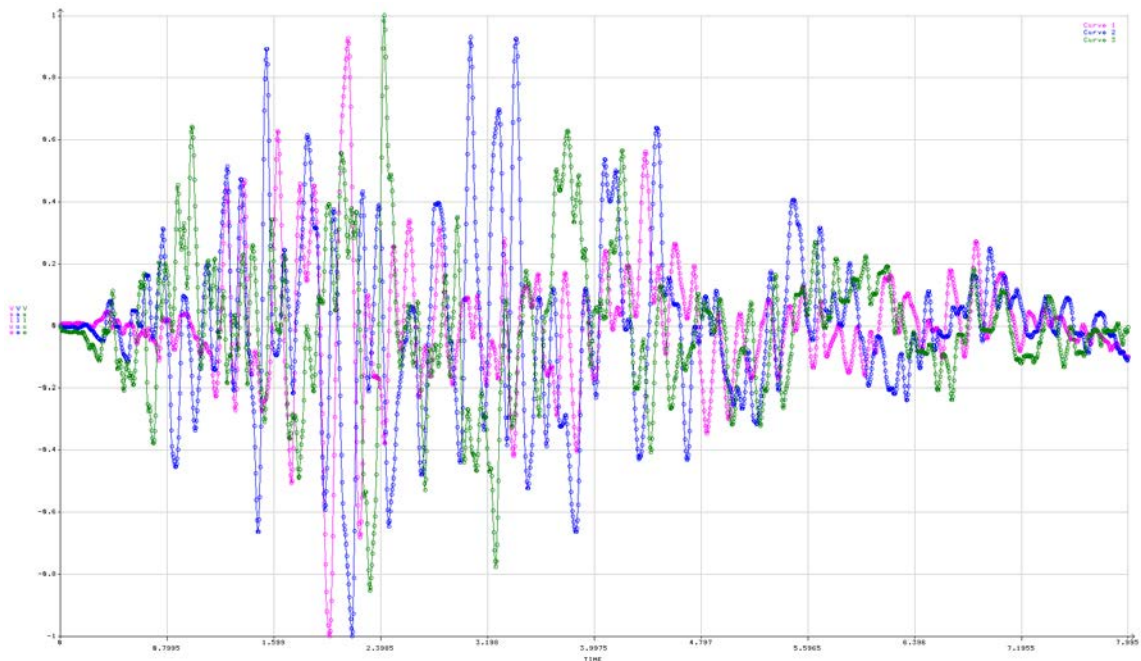


Figure 7. Estimated three-component accelerogram at equipment installation marks.

4. Conclusion

1. As a result of the dynamic calculation of the spillway dam-foundation system of the spillway HPP, the values of the natural vibration frequencies of the structure were obtained and the response spectra were plotted at the marks of the installation of mechanical equipment corresponding to the seismic impact of the MPE level of 8 points (Novobureysky settlement) [26].

2. Dynamic calculations are performed on the basis of the calculated three-component accelerogram.

3. Comparison of the frequency values of the response spectrum with the first natural frequency indicates the absence of resonant phenomena in the structure during an earthquake.

4. The response spectra obtained as a result of the calculation on the steers of the spillway dam can be set as a dynamic effect on the equipment installed on the steers of the spillway.

5. Based on the response spectra, a calculated three-component accelerogram was synthesized at the equipment installation marks.

6. Equipment installed on bullheads must be designed for seismic resistance according to the calculated response spectra or a three-component accelerogram.

References

1. Ayzenberg Ya.M., Kodysh E.N., Nikitin I.K., Smirnov V.I., Trekin N.N. Seysmostoykiye mnogoetazhnyye zdaniya s zhelezobetonnyim karkasom [Seismic-resistant multi-storey buildings with reinforced concrete frame]. Izdatelstvo Assotsiatsii stroitelnykh vuzov (ASV). 2012. Pp. 18.
2. Birbrayer A.N. Raschet konstruksiy na seysmostoykost [Calculation of structures for seismic resistance]. SPb: Nauka. 1998. S. 254.
3. Zenkevich O., Morgan K. Konechnyye elementy i approksimatsiya [Finite Elements and Approximation]. M.: Mir. 1986. S. 318.
4. Streng G., Fiks Dzh. Teoriya metoda konechnykh elementov. M.: Mir, 1977. S. 349 .
5. Zienkiewicz, O.C., Taylor, R.L. Finite Element Method: Volume 1. The Basis. Butterworth-Heinemann, 2000. 712 p.
6. Zienkiewicz O.C., Taylor, R.L. Finite Element Method: Volume 2. Solid Mechanics. Butterworth-Heinemann, 2000. 480 p.
7. Doyev V.S., Doronin F.A., Indeykin A.V. Teoriya kolebaniy v transportnoy mekhanike (pod red. A. V. Indeykina) [Theory of vibrations in transport mechanics (under the editorship of A. V. Indeykin)]. M.: FGOU «Uchebno-metodicheskiy tsentr po obrazovaniyu na zheleznodorozhnom transporte». 2011. S. 352.
8. Gorelov Yu.N. Chislennyye metody resheniya obyknovennykh differentsialnykh uravneniy (metod Runge – Kutta): ucheb. Posobiye [Numerical Methods for Solving Ordinary Differential Equations (Runge-Kutta Method): Tutorial]. Samara: Samarskiy universitet. 2006. S. 48.
9. Barshteyn M.F., Ilichev V.A., Korenev B.G. Dinamicheskiy raschet zdaniy i sooruzheniy [Dynamic calculation of buildings and structures]. M.: Stroyizdat, 1984.
10. Bertyayev V.D. Teoreticheskaya mekhanika na baze Mathcad. Praktikum [Theoretical mechanics based on Mathsad. Workshop.]. SPb: BKhV-Peterburg. 2005. 752 s.
11. Konstantinov I.A., Lalina I.I. Stroitel'naya mekhanika. Raschet sterzhnevnykh sistem [Structural mechanics. Design of bar systems]. Spb.: Izd-vo Politekh. un-ta. 2005. S.155.
12. Kiselev V.A. Stroitel'naya mekhanika: Spetsialnyy kurs (dinamika i ustoychivost sooruzheniy) [Structural mechanics: Special course (dynamics and stability of structures)]. M.: Stroyizdat. 1980.
13. Rozin L.A., Konstantinov I.A., Smelov V.A. Raschet staticheskii opredelimykh sistem [Calculation of statically determinate systems.]. L.: Izd-vo LGU, 1984. S. 228.
14. Zarubin P.Ye., Baranovskiy M.Yu., Tarasov V.A. Teklastructures – innovatsiya v sozdanii konstruksiy [Tekla structures – innovatsiya v sozdanii konstruksiy]. Stroitelstvo unikalnykh zdaniy i sooruzheniy. 2013. № 5. S.1-8.
15. Timoshenko S.P. Kolebaniya v inzhenernom dele [Fluctuations in engineering]. M.: Nauka, 1967. S. 444.
16. Abdikarimov, R.A., Eshmatov, Kh., Bobanazarov, Sh.P., Khodzhayev, D.A., Eshmatov, B.Kh. Mathematical modelling and calculation of hydraulic engineering constructions such as dam-plate in view of hydrodynamical pressure of water and seismic loading. Magazine of Civil Engineering. 2011. No. 3. Pp. 59–70.
17. Kozinec, G.L. Generalization of the Methodology of Studying the Durability of Segmental Gates. Power Technology and Engineering. 2018. Vol. 52. No. 4. Pp. 395–399.
18. Verret, D., LeBoeuf, D. Dynamic characteristics assessment of the Denis-Perron dam (SM-3) based on ambient noise measurements. Earthquake Engineering & Structural Dynamics. 2022. 51(3). Pp. 569–587.
19. Arbain, A., Ahmad Mazlan, A.Z., Zawawi, M.H., Mohd Radzi, M.R. Vibration analysis of Kenyir dam power station structure using a real scale 3D model. Civil and Environmental Engineering Reports. 2019. 29(3). Pp. 48–59.
20. Chernukha, N.A., Lalin, V.V., Nikitich, B.A. Probabilistic justification of dynamic loads on NPP equipment caused by aircraft impact. Peter the Great St. Petersburg polytechnic university journal of engineering sciences and technology. 2017. 23(4). Pp. 159–171. DOI: 10.18721/JEST.230416
21. Pereira, S., Magalhães, F., Gomes, J.P., Cunha, Á., Lemos, J.V. Dynamic monitoring of a concrete arch dam during the first filling of the reservoir. Engineering Structures. 2018. 174. Pp. 548–560.
22. Gordan, B., Raja, M.A., Armaghani, D.J., Adnan, A. Review on Dynamic Behaviour of Earth Dam and Embankment During an Earthquake. Geotechnical and Geological Engineering. 2021. Pp. 1–31.
23. Chen, J., Jia, Q., Xu, Q., Fan, S., Liu, P. The PDEM-based time-varying dynamic reliability analysis method for a concrete dam subjected to earthquake. Structures. 2021. Vol. 33. Pp. 2964–2973.
24. Boulanger, R.W. Nonlinear dynamic analyses of Austrian dam in the 1989 Loma Prieta earthquake. Journal of Geotechnical and Geoenvironmental Engineering. 2019. 145(11). 05019011.
25. Savich, A. I., et al. "Sticheskiye i dinamicheskiye povedeniye Sayano-Shushenskoy arochno-gravitatsionnoy plotiny." [Static and dynamic behavior of the Sayano-Shushenskaya arch-gravity dam] Gidrotekhnicheskoye stroitelstvo 3 (2013): 2-13.
26. Seismic building design code 14.13330.2018

Information about authors:

Galina Kozinets

Doctor of Technical Science

E-mail: kozinets_gl@spbstu.ru

Pavel Kozinets

E-mail: pavelkozinets@yandex.ru



Research article

UDC 699.866

DOI: 10.34910/MCE.113.13



Calculation of heat resistance of external enclosing structures with heat-conducting inclusions

A.N. Belous^a , G.A. Kotov^a , O.E. Belous^a , I.M. Garanzha^b  

^a Donbass National Academy of Civil Engineering and Architecture (DNACEA), Makeevka, Donetsk People Republic

^b Moscow State University of Civil Engineering (National Research University) (MGSU), Moscow, Russia

 garigo@mail.ru

Keywords: heat exchangers, heat transfer coefficients, flow resistance, non-stationary mode, temperature field

Abstract. The paper is devoted to the development of a method for calculating the thermal stability of external enclosing structures with heat-conducting inclusions. Based on the analysis of existing methods and methodologies for solving the problem of heat resistance of enclosing structures with heat-conducting inclusions, the solution of the one-dimensional problem of heat resistance was established to be characteristic for all these works. One of the possible methods for determining the amplitude of temperature fluctuations on the inner surface of the enclosing structure with heat-conducting inclusions is the simulation of non-stationary temperature conditions in software systems. However, this solution causes great difficulties, since it transfers the indicated calculation from engineering to scientific and, therefore, cannot be recommended for direct practical application. The second solution to this problem is to use the convergence coefficient α , which can be obtained empirically. By choosing the value of the coefficient α , one can take into account the effect of a heat-conducting inclusion on the weighted average value of the surface temperature depending on the design of the fence. The paper presents values of the convergence coefficient α for six most common cases of heat-conducting inclusions in enclosing structures. When analyzing the design solutions of external enclosing structures, the features of the influence of heat-conducting inclusions on the averaged amplitude of oscillations on the inner surface were revealed. In the schemes with outer edge or through location of the heat-conducting inclusion, there is a slight influence of the amplitude of the oscillation of the heat-conducting inclusion on the averaged amplitude over the surface of the structure. The greatest degree of influence is exerted by the scheme with the through arrangement of heat-conducting inclusion. On the basis of the comparative analysis, it was found that when constructing harmonics of average temperature fluctuations on the inner surface, preference is given to the methodology with the convergence coefficient.

Citation: Belous, A.N., Kotov, G.A., Belous, O.E., Garanzha, I.M. Calculation of heat resistance of external enclosing structures with heat-conducting inclusions. Magazine of Civil Engineering. 2022. 113(5). Article No. 11313. DOI: 10.34910/MCE.113.13

1. Introduction

Modern outdoor enclosing structures, in most cases, are multilayer systems with a large number of heat-conducting inclusions. In this case, the main attention in the design and calculation of energy indicators is given to the reduced resistance to heat transfer [1–7]. For the theoretical determination of the reduced resistance to heat transfer are developed various methodologies [8–12], which are confirmed and tested in full-scale and laboratory conditions.

This approach to the design of enclosing structures is economically justified from the point of view of saving energy, but do not forget that buildings, first of all, are built for people and comfort conditions should be put at the forefront of the design. Proceeding from the second condition of comfort [13], the regulatory documents put forward restrictions on the change in the amplitude of temperature fluctuations on the inner surface of the external enclosing structures in the summer. This problem was dealt with in detail by A.M. Shklover in the sixties of the twentieth century. Based on his researches many problems were solved related to the thermal stability of enclosing structures and premises. In particular was determined the relationship between the constructive solution of walls and heat resistance [14], but these works and problems were investigated only for multilayer structures without heat-conducting inclusions.

The development of the methodology for calculating thermal stability was continued in their works by Russian scientists [15–18], who proposed various approaches to this problem. Foreign scientists [19–24] dealt with separate problems of the non-stationary regime of the enclosing structures in their works [19–23, 25]. But all these works are characterized by the solution of a one-dimensional problem of heat resistance, which is not correct for modern enclosing structures with numerous heat-conducting inclusions, since for such cases it is necessary to solve problems in a two-dimensional formulation under non-stationary heat transfer conditions. Most of the proposed methods require revision or comparison with the results of field or laboratory studies.

The relevance of the study lies in the fact that the cost of electricity for the air conditioning system in the southern regions of Russia and Ukraine often exceeds the cost for the heating period. This is partly due to the overloading of the air conditioning system, the load for which is calculated according to the methods of calculating the enclosing structures with partial consideration of heat-conducting connections, or, in most cases, ignoring them. The new methodology will make it possible to calculate the thermal stability of enclosing structures with heat-conducting inclusions, which will make it possible to more accurately assess the thermal parameters of structures in the summer period of the year.

The goal of the study is to develop a method for calculating the thermal stability of external enclosing structures with heat-conducting inclusions. To achieve this goal, a number of tasks were set:

- to analyze external enclosing structures and identify the most common structural schemes with heat-conducting inclusions;
- to carry out studies of the distribution of the temperature field inside the enclosing structures with heat-conducting inclusions under non-stationary conditions of heat transfer;
- to determine the numerical values of the convergence coefficients, which make it possible to find the average temperature of the inner surface of the enclosing structure with heat-conducting inclusions.

2. Materials and Methods

The heat resistance of homogeneous multilayer enclosing structures in warm season is normalized by the amplitude indicator of temperature fluctuations on the inner surface and is determined by the ratio of the amplitude A of fluctuations in the outside air temperature to the attenuation coefficient ν in the enclosing structure. The amplitude of fluctuations in the outdoor air depends on two climatic factors: outdoor temperature and solar radiation. Their combined effect on the outer surface of the enclosing structure can be expressed through the effective air temperature at the outer surface of the enclosure T_{con} , K, which is calculated by the equation (1):

$$T_{con} = T_{out} \cdot \sqrt[4]{\frac{G(\alpha)}{G_m(\alpha)} + r \frac{I(\alpha, \beta) + i(\alpha, \beta)}{\alpha_{out}}}, \quad (1)$$

where α and β are, respectively, the angular height and azimuth of the normal to the surface at a given point; T_{out} is outdoor temperature, K; G , I , i are irradiance of the surface at a given point, respectively by thermal, direct solar and scattered solar radiation, W/m^2 ; G_m is spatial intensity of thermal radiation, W/m^2 ; r is surface albedo in fractions of a unit; α_{out} is heat transfer coefficient between the outer surface of the fence and the outside air $W/(m^2 \cdot K)$.

Thus, the amplitude of the outdoor temperature fluctuation is calculated as the difference between the temperature at 3 o'clock in the afternoon and 3 o'clock in the morning solar time according to the equation (1).

The damping coefficient ν depends on the thermal performance of the layers of the enclosing structure (thermal inertia D and heat assimilation S , $W/(m^2 \cdot K)$), and also on the index of heat absorption of the surface Y , $W/(m^2 \cdot K)$ and is found by the equation (2) [13]:

$$\nu = 0.9e^{\frac{D}{\sqrt{2}}} \frac{(s_1 + \alpha_{out})(s_2 + Y_1) \dots (s_n + Y_{n-1})(\alpha + Y_n)}{(s_1 + Y_1)(s_2 + Y_2) \dots (s_n + Y_n)\alpha}. \quad (2)$$

This calculation methodology is valid only for multilayer homogeneous structures, since in the presence of heat-conducting inclusions is observed a change in the temperature field in the thickness of the enclosing structure.

In a homogeneous structure the temperature isotherms are parallel and the heat flux vector is perpendicular to the outer and inner surfaces.

In the presence of a heat-conducting inclusion for the heat flux vectors is observed a change of their directions from the outer surface to the heat-conducting inclusion and, in some cases, heat propagation occurs parallel to the inner surface of the enclosing structure. Thus, when calculating the value of the temperature amplitude's damping of fluctuations in the thickness of the structure, it is not possible to choose the design section along the vector of the heat flux.

One of the possible methods for determining the amplitude of temperature fluctuations on the inner surface of the enclosing structure with heat-conducting inclusions is the simulation of non-stationary temperature conditions in software systems. However, this solution causes great difficulties, since it transfers the indicated calculation from engineering to scientific and, therefore, cannot be recommended for direct practical application.

The second solution to this problem is to use the convergence coefficient α , which can be obtained based on the results of numerical simulation. By choosing the value of the coefficient α , one can take into account the effect of a heat-conducting inclusion on the weighted average value of the surface temperature, depending on the design of the fence, using the relation (3):

$$t_m = \alpha \cdot t_{h,i} + (1 - \alpha) \cdot t_h, \quad (3)$$

where t_m is weighted average value of temperature on the inner surface of the enclosing structure with heat-conducting inclusions, K, α is convergence coefficient, $0 \leq \alpha \leq 1$; $t_{h,i}$ is temperature on the inner surface in the zone of heat-conducting inclusion, K, t_h is homogeneous zone temperature, K.

To determine the coefficient of convergence α , it is necessary to simulate the design scheme of the external enclosing structure with heat-conducting inclusions in an unsteady thermal regime. The measurement results are harmonics of temperature fluctuations $t_{h,i}$ on the inner surface of the enclosing structure at the point of heat-conducting inclusion and temperature t_h of a homogeneous zone, as well as harmonics of the average temperature t_m , calculated using the model. At known temperatures included in equality (3), the convergence coefficient α is found from it.

Thus, computer modeling of the unsteady temperature regime must be carried out for a certain number of typical enclosing structures, for each of them to obtain the values of the convergence coefficient α , and then in subsequent studies, when finding the averaged temperature t_m over the surface, use the ready-made formula (3), substituting only the input data $t_{h,i}$ and t_h .

Computer simulation allows obtaining arrays of temperature values t_m , $t_{h,i}$ and t_h , which are used to plot harmonics. The process of finding the values of α can be based on the approximation of the harmonics of temperature fluctuations by periodic functions, for example, using Fourier series, then Eq. (3) for α is solved analytically and the obtained value of the convergence coefficient is unique for specific specified parameters of the enclosing structure. This approach is applicable even in the case when the initial values of temperatures t_m , $t_{h,i}$ and t_h are small (about 10 values), since this number of points is quite enough for interpolation of a periodic function on one interval of the period length. The estimation of the interpolation error is not performed in this article.

Another way to determine the value of α is iterative, i.e. equation (3) is written in the form (4):

$$t_m^i = \alpha_i \cdot t_{h,i}^i + (1 - \alpha_i) \cdot t_{i_h}, \quad (4)$$

where $i = 1, 2, 3, \dots, n$, and is solved for each corresponding i^{th} value t_m , $t_{h,i}$ and t_h . Thus, an array of values α_i is formed, and the convergence coefficient itself is defined as the arithmetic mean over all values of α_{app} (5):

$$\alpha_{app} = \frac{1}{n} \sum_{i=1}^n \alpha_i. \quad (5)$$

Then a dependency graph is built (6):

$$t_{m,app}^i = \alpha^{app} \cdot t_{h,i}^i + (1 - \alpha^{app}) \cdot t_{i_h}, \quad (6)$$

which serves as an approximation of the temperature graph t_m . The article uses an iterative approach, since the number of points in the arrays is 864, which makes it possible to determine the convergence coefficient α with sufficient accuracy.

3. Results and Discussion

Thermally conductive inclusions by their shape and location can be conditionally divided into six types [13]. These types of heat-conducting connections are most typical for residential buildings of low and medium storey (see Fig. 1). For further analysis, we will take foam concrete as the main material of external enclosing structures, and heavy reinforced concrete as heat-conducting inclusions. In this case, the calculations considered several options for each design scheme with a change in the thickness of the enclosing structure from 300 to 500 mm and a density of 500 ... 800 kg/m³. Let us take climatic conditions for the Donetsk city as the calculated parameters of the summer period.

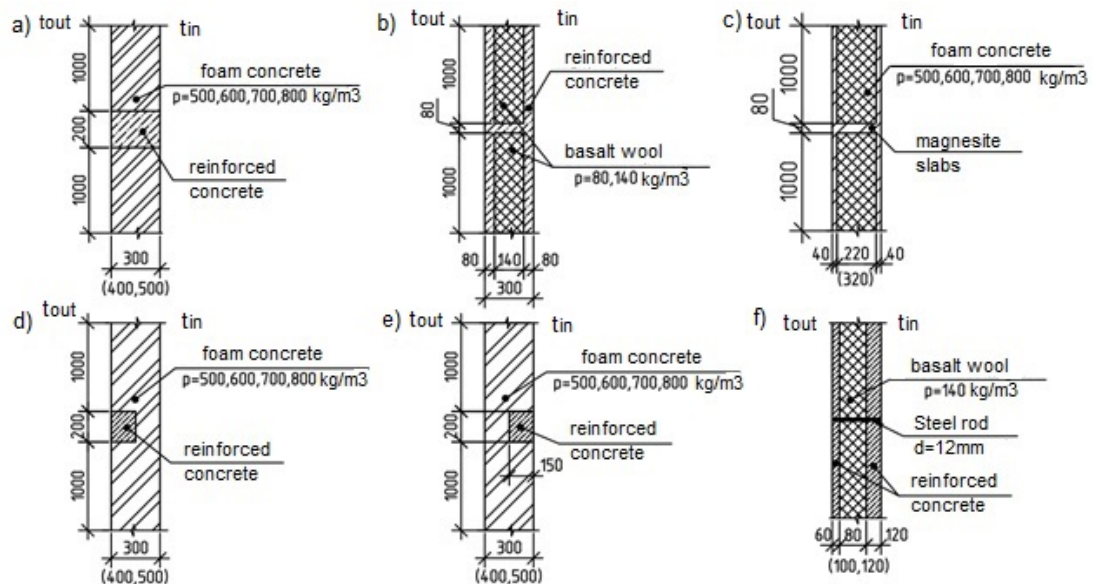


Figure 1. Schematic of heat-conducting inclusions: a) end-to-end; b) a thick-walled shell; c) a thin-walled shell; d) at the inner edge; e) at the outer edge; f) steel through the bar.

In the ELCUT6.4 software package the non-stationary temperature regime was simulated for an external wall scheme with a through heat-conducting connection (Fig. 1a). As the analysis result of changes in the temperature field of a homogeneous zone in time was found the effect of "buffering" of heat. Let us consider in more detail the distribution of the temperature flow in time for this case (Fig. 2). The cycle of temperature fluctuations inside the enclosing structure is divided into several stages, depending on the effect of outdoor air and solar radiation. The countdown of the first stage starts from reaching the maximum temperature in the thickness of the building envelope (Fig. 2a). The next stage begins with the beginning of cooling of the outer surface, while is noted the continuation of penetration and maintenance of the maximum temperature in the structure (Fig. 2b).

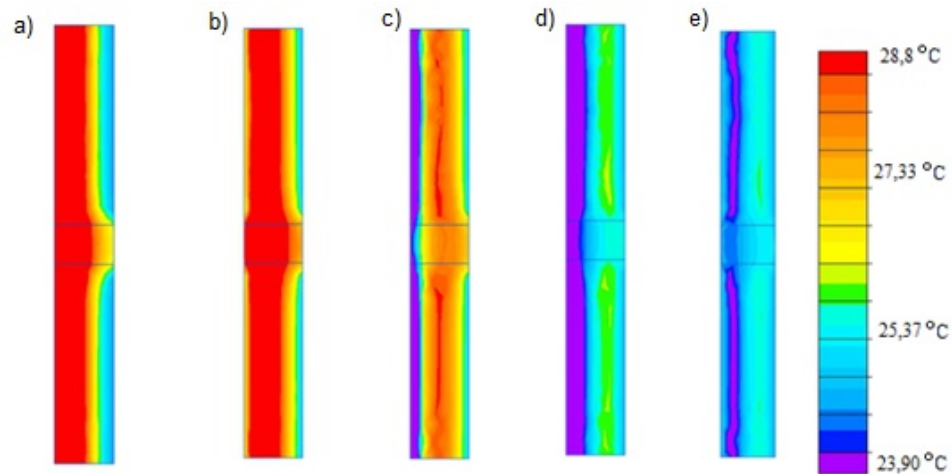


Figure 2. Distribution of the temperature field in the thickness of the enclosing structure during the period: a) the initial phase of heating; b) maximum temperatures; c) the beginning of cooling; d) minimum temperature; e) final cooling phase.

In the third stage, there is a simultaneous cooling on the outer surface and a decrease in the zone of maximum temperatures due to the transfer of heat to colder zones (Fig. 2c), while heat spreading is observed both towards the interior of the room and towards the outer zone of the wall. The fourth stage is characterized by the spread of the minimum temperature deep into the structure (Fig. 2d), however, the zone with an increased temperature in the thickness of the wall prevents the penetration of low temperatures and partially continues to heat the inner zone of the wall. At the fifth stage, the outer surface begins to warm up (Fig. 2e). However, a zone with low temperatures is formed near the outer surface, which later, when the structure warms up, is similar in its behavior to the zone of maximum temperatures from the third stage with a difference in temperatures: the third stage did not "pass" low temperatures, and the fifth – increased ones. When considering the temperature distribution in the zone of heat-conducting inclusion (Fig. 2), the phenomenon of "buffering" of heat is not observed. The temperature change in the thickness of the heat-conducting inclusion is described by the harmonic (curve 2, Fig. 3), similar to the harmonic of the temperature change on the outer surface (curve No. 1, Fig. 4), proportional to the damping coefficient.

When comparing the harmonics of temperature fluctuations on the inner surface in the zone of the heat-conducting inclusion and the homogeneous zone (curves 2 and 3, Fig. 3) were found large differences in amplitudes (in 3 times) and insignificant period shifts for circuit a) Fig. 1. When analyzing the harmonics on the inner surface of the homogeneous zone and the weighted average temperature on the inner surface (curves 1 and 3, Fig. 4), obtained in the ELCUT6.4 software package were found insignificant deviations of the amplitude and period. Thus, it becomes possible to obtain temperatures on the inner surface using the proposed methodology through the coefficient α .

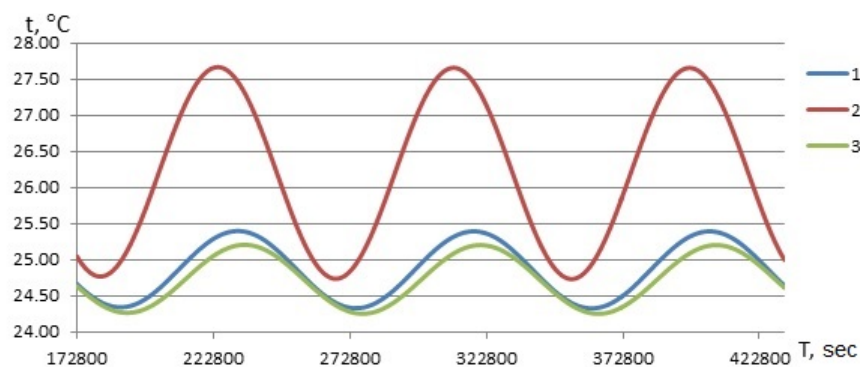


Figure 3. Harmonics of the amplitudes of temperature fluctuations on the inner surface in the place: 1 – averaged over the surface; 2 – heat-conducting inclusion; 3 – homogeneous surface.

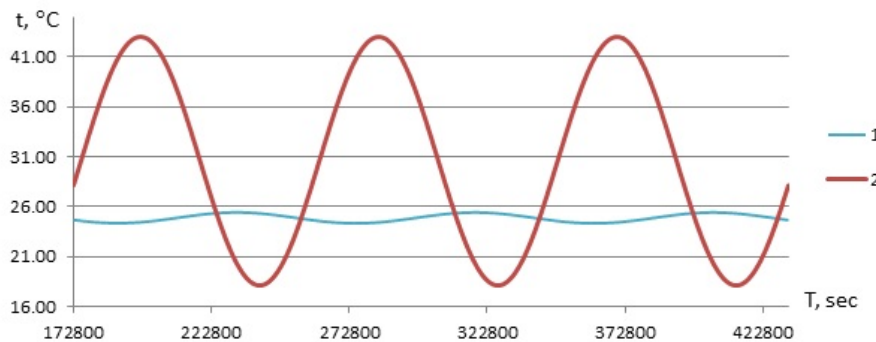
For scheme a) Fig. 1 were calculated the coefficients α , which, depending on the density and thickness of the material, are given in Table 1. When comparing the values of the coefficient α with the resistance to heat transfer, thermal inertia, and the coefficient of heat assimilation, no were found simple dependencies with a high degree of convergence.

Table 1. Convergence coefficient α values for the scheme a) Fig. 1

Thickness, mm	Density, kg/m ³			
	500	600	700	800
300	0.1911	0.0884	0.0998	0.0935
400	0.0597	0.1231	0.1640	0.1338
500	0.0696	0.1230	0.1563	0.1049

Analysis of the amplitudes of fluctuations in the external temperature (curve 2, Fig. 4) and on the inner surface shows that for this scheme, the vibration amplitude for a heat-conducting inclusion decreases from 13 to 40 times for the averaged surface.

In [13, 25] are presented the calculations for reducing the amplitude of temperature fluctuations on inner surface of the enclosing structure in summer through the damping coefficient, but is not considered the movement of heat from the inner zone to the outer surface. Due to this, the values of V.N. Bogoslovskii more by 40 % from those obtained as the result of numerical simulation of the circuit e) (Fig. 1).



**Figure 4. Harmonics of averaged amplitudes of temperature fluctuations:
1 – on the outer surface; 2 – on the inner surface.**

As a result of modeling scheme b) (Fig. 1), convergence coefficients α were obtained equal to 0.1911 and ≈ 0.000 for insulation thicknesses of 80 mm and 140 mm, respectively. The convergence coefficient for thickness of 140 mm is close to zero, but nonzero, since the harmonics of temperature fluctuations on the inner surface in a homogeneous zone and averaged over the surface practically coincide (curves 1 and 3, Fig. 5). At the place of the heat-conducting inclusion, although a large amplitude of oscillations is observed (curve 2, Fig. 5), due to the small thickness of the heat-conducting inclusion, it does not affect the average value of the amplitude over the entire inner surface of the enclosing structure.

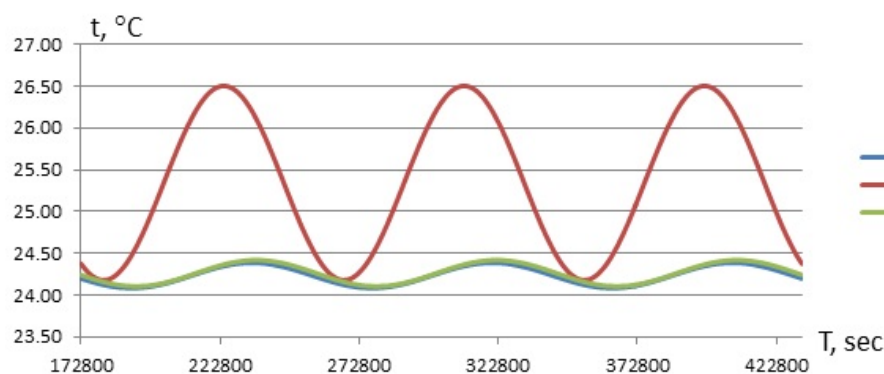


**Figure 5. Harmonics of the amplitudes of temperature fluctuations
on the inner surface in the place: 1 – averaged over the surface; 2 – heat-conducting inclusion;
3 – homogeneous surface.**

When analyzing the results of modeling the structure with a heat-conducting connection according to scheme c) (Fig. 1) were found the convergence factors α (Table 2). It was also found that due to the small proportion of heat-conducting inclusion, there is a slight difference in the amplitudes of oscillations (Fig. 6) on the inner surface. In this case, the heat-conducting inclusion can be neglected.

Table 2. Convergence coefficient α values for the scheme c) Fig. 1

Thickness, mm	Density, kg/m ³			
	500	600	700	800
300	0.4902	0.1663	0.2696	0.4174
400	0.0195	0.0195	0.6818	0.0906

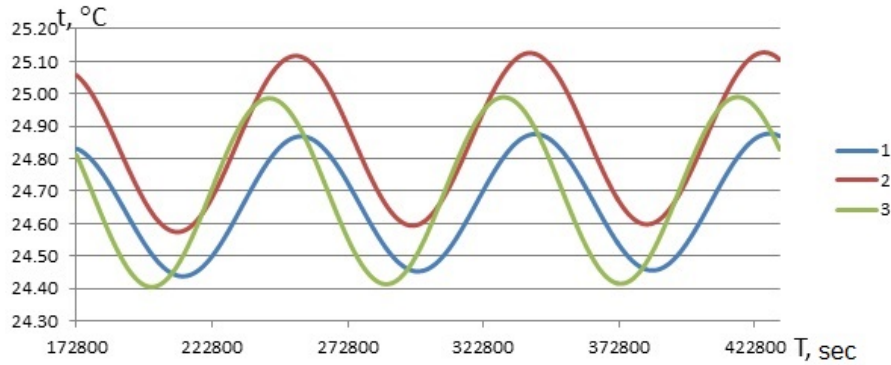


Figure 6. Harmonics of the amplitudes of temperature fluctuations on the inner surface in the place: 1 – averaged over the surface; 2 – heat-conducting inclusion; 3 – homogeneous surface.

The simulation results of circuit d) (Fig. 1) are similar to the simulation results of circuit a), but with a structure thickness of 500 mm, it was found that the heat-conducting connection has practically no effect on the averaged amplitude of temperature fluctuations on the inner surface. Table 3 shows the values of the convergence coefficient α .

Table 3. Convergence coefficient α values for the scheme d) Fig. 1

Thickness, mm	Density, kg/m ³			
	500	600	700	800
300	0.1964	0.2517	0.1601	0.1787
400	0.1559	0.0718	0.2801	0.0010

With an external blind arrangement of a heat-conducting inclusion, as in diagram e) (Fig. 1), a change in the amplitude of oscillations was recorded only at a thickness of 300 mm, at large values of the thickness, the harmonic of the temperature of the homogeneous zone is close to the average (Fig. 7). The obtained convergence coefficients α for a thickness of 300 mm are presented in Table 4.

Table 4. Convergence coefficient α values for the scheme e) Fig. 1

Thickness, mm	Density, kg/m ³			
	500	600	700	800
300	0.0493	0.0862	0.0141	0.0890

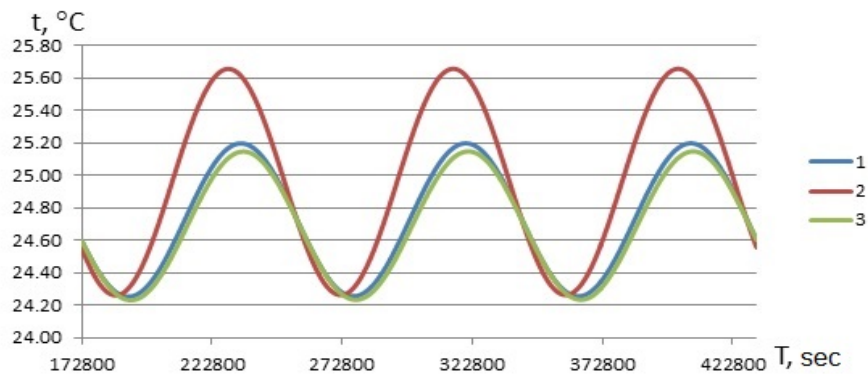


Figure 7. Harmonics of the amplitudes of temperature fluctuations on the inner surface in the place: 1 – averaged over the surface; 2 – heat-conducting inclusion; 3 – homogeneous surface.

The cardinal difference is the scheme f) (Fig. 1) with a through heat-conducting connection: even with a small diameter of a steel rod ($\varnothing 12$ mm) it causes significant disturbances in the amplitude of temperature fluctuations on the inner surface. With an amplitude in the homogeneous zone 0.46 °K and 5.94 °K for heat-conducting inclusion (Fig. 8), the average amplitude over the surface is 3.44 °K, i.e., the degree of influence of the heat-conducting inclusion is 12.91 . For the previous schemes this value ranges from 3.0 to 5.0 . Also, the values of the convergence coefficient were calculated for various thicknesses of the enclosing structure, which were: $\alpha = 0.4451$ for 80 mm; $\alpha = 0.7040$ for 100 mm and 120 mm.

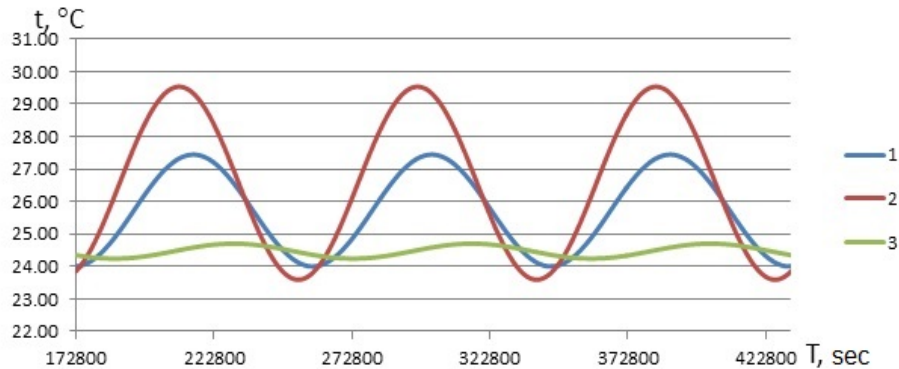


Figure 8. Harmonics of the amplitudes of temperature fluctuations on the inner surface in the place: 1 – averaged over the surface; 2 – heat-conducting inclusion; 3 – homogeneous surface.

4. Conclusions

The revealed "buffering" effect of the heat flow in the thickness of the enclosing structure will allow, when designing, to reduce the amplitude of oscillations on the inner surface by $2 \dots 3$ K due to the selection of the optimal density and heat resistance of materials. Additionally, it is necessary to study this effect in the winter period of the year and its degree of influence on the temperature of the inner surface of the enclosing structure during the period of daily fluctuations of the outer air or uneven operation of the heating system.

When analyzing the design solutions of external enclosing structures were revealed the features of the influence of heat-conducting inclusions on the averaged vibration amplitude on the inner surface. In circuits with the location of the heat-conducting inclusion at the outer edge or through, there is a slight influence of the amplitude of the vibration of the heat-conducting inclusion on the averaged amplitude over the structure surface. In structures in which a heat-conducting inclusion plays the role of a shell or is located at the outer edge, the degree of influence is insignificant, and at maximum thicknesses is absent. The greatest degree of influence is exerted by a scheme with a through arrangement of a heat-conducting inclusion in the form of a steel rod $\varnothing 12$ mm. This heat-conducting inclusion has a 4 times greater effect on the amplitude of fluctuations in the temperature of the inner surface than in circuits with a through heat-conducting inclusion in the form of a 200 mm thick concrete lintel. Based on this diagram, it can be concluded that structures with a high percentage of reinforcement or the presence of transverse reinforcement will not meet design standards in the summer season.

As a result of a comparison of the two methods for constructing harmonics of average temperature fluctuations on the inner surface (Fig. 9), preference is given to the method with a convergence coefficient.

This methodology showed the convergence of the obtained harmonic from the theoretical one to 95% . The mean square method showed high convergence in the average temperature zone of the curve, but in the peak part of the harmonics, this method reduces the maximum and minimum temperatures. This underestimation of temperature values sharply reduces the normalized coefficient – the amplitude of oscillations on the inner surface, thus the calculated values of the average amplitude of the surface are significantly reduced relative to the data obtained as a result of modeling the unsteady heat flow in the ELCUT 6.4 software package.

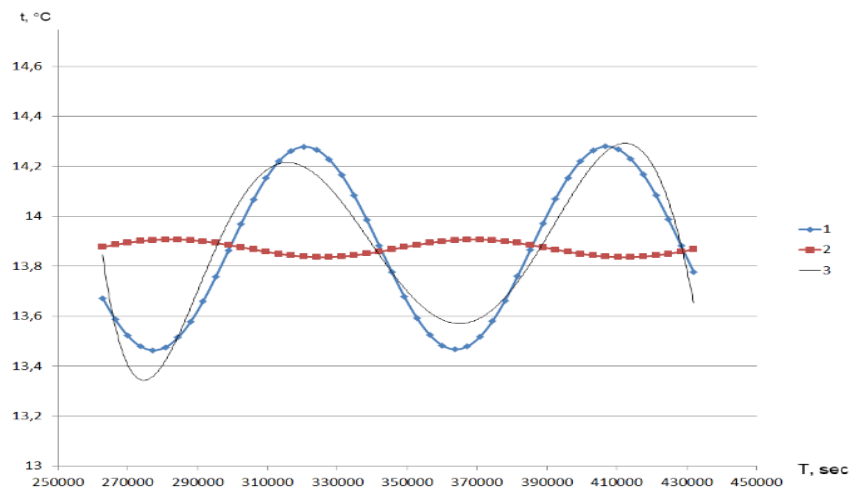


Figure 9. The fragment of the harmonic of temperature fluctuations on the inner surface obtained: 1 – using the convergence factor; 2 – least squares method; 3 – as a result of numerical simulation.

References

1. Samarin, O.D., Shevchenkova, I.S. Otsenka teplotekhnicheskoi neodnorodnosti naruzhnoi steny pri izmenenii tolshchiny uteplitel'ya [Assessment of the heat engineering heterogeneity of the outer wall when changing the thickness of the insulation]. S.O.K. 2016. 3. Pp. 42–43.
2. Samarin O.D., Makeshin D.A. Obosnovanie teplozashchity neodnorodnykh ograzhdenii [Substantiation of thermal protection of non-uniform enclosures]. S.O.K. 2015. 4. Pp. 52–54.
3. Golubev, S.S. Opredelenie privedennogo soprotivleniya teploperedache ograzhdayushchikh konstruksii na osnove chislennogo rascheta raspredeleniya temperaturnykh polei [Determination of the reduced resistance to heat transfer of enclosing structures based on a numerical calculation of the distribution of temperature fields]. Nauchno-tekhnicheskii vestnik Povolzh'ya. 2011. 5. Pp. 93–97.
4. Makarov, R.A., Mureev, P.N., Makarov, A.N. Opredelenie popravki k termicheskomu soprotivleniyu pri kvazistatsionarnom rezhime teploperedachi v naruzhnykh stenakh, vypolnennykh iz kirpicha [Determination of the correction to thermal resistance for a quasi-stationary heat transfer mode in external walls made of bricks]. Sovremennye problemy nauki i obrazovaniya. 2015. 1–1. Pp. 1992–1992.
5. Makarov, A.N., Mureev, P.N., Makarov, R.A. Reshenie zadachi regulirovaniya temperatury vnutrennei poverkhnosti naruzhnykh sten rekonstruirovemykh zdaniy postroiki 60-80-kh godov XX veka [Solving the problem of regulating the temperature of the inner surface of the outer walls of reconstructed buildings constructed in the 60s-80s of the XX century]. Fundamental'nye issledovaniya. 2016. 6-1. Pp. 83–87. (rus)
6. Mikov, A.V., Balushkin, A.L. Vliyaniye teploprovodnykh vklyuchenii na raschet privedennogo soprotivleniya teploperedache fasada zhilogo zdaniya s ispol'zovaniem raschetov temperaturnykh polei [Influence of heat-conducting inclusions on the calculation of the reduced resistance to heat transfer of the facade of a residential building using calculations of temperature fields]. Mezhdunarodnaya nauchno-prakticheskayakonferentsiya: sbornik statej [International scientific and practical conference]. Ufa: 2020. Pp. 38–45.
7. Belous, A.N., Kotov, G.A., Saprionov, D.A., Novikov, B.A. Opredelenie soprotivleniya teploperedache pri nestatsionarnom teplovom rezhime [Determination of resistance to heat transfer in non-stationary thermal conditions]. Vestnik Tomskogo gosudarstvennogo arkhitekturno-stroitel'nogo universiteta. 2020. 22 (6). Pp. 83–93.
8. Gagarin, V.G., Neklyudov, A.Yu. Uchet teplotekhnicheskikh neodnorodnostei ograzhdenii pri opredelenii teplovoi nagruzki na sistemu otopeniya zdaniya [Accounting for heat engineering inhomogeneities of fences when determining the heat load on the heating system of a building]. Zhilishchnoe stroitel'stvo. 2014. 6. Pp. 3–7.
9. Gagarin, V.G., Plyushchenko, N.Yu. Opredelenie termicheskogo soprotivleniya ventiliruemoi prosloiki NFS [Determination of the thermal resistance of the ventilated layer of the hinged facade system]. Stroitel'stvo: nauka i obrazovanie. 2015. 1. Pp. 1–1.
10. Gorshkov, A.S. Predlozheniya po sovershenstvovaniyu normativnykh trebovaniy k ograzhdayushchim konstruksiyam [Proposals for improving the regulatory requirements for enclosing structures]. Stroitel'nye materialy, oborudovanie, tekhnologii XXI veka. 2017. 1-2. Pp. 49–52.
11. Mikheev, D.A. Sravnitel'nyi analiz otmenennogo i predlozhenogo metodov rascheta privedennogo soprotivleniya teploperedache ograzhdayushchikh konstruksii [Comparative analysis of the canceled and the proposed methods for calculating the reduced resistance to heat transfer of enclosing structures]. Nauchnyi zhurnal stroitel'stva i arkhitektury. 2017. 3 (47). Pp. 11–20.
12. Tushina, O.A. Teplotekhnicheskii raschet konstruksii chislennymi metodami [Heat engineering calculation of structures by numerical methods]. Vestnik MGSU. 2013. 11. Pp. 91–99.
13. Bogoslovskii, V.N. Stroitel'naya teplofizika (teplofizicheskie osnovy otopeniya, ventilyatsii i konditsionirovaniya vozdukh) [Building thermal physics (thermophysical basics of heating, ventilation and air conditioning)]. Moscow: Vysshaya shkola, 1982. 415 p.
14. Koshlatyi, O.B. Zavisimost' teploustoichivosti naruzhnykh sten ot ikh konstruktivnogo resheniya [Dependence of the heat resistance of external walls on their design solution]. Materialy mezhdunarodnoi nauchnoi konferentsii FAD TOGU [Materials of the international scientific conference FAD TOGU]. Khabarovsk: TOGU, 2013. V. 2. Pp. 357–360.
15. Malyavina, E.G., Usmanov, Sh.Z. Ogranichenie amplitudy kolebaniy temperatury pomeshcheniya v teplyi period goda [Limiting the amplitude of room temperature fluctuations during the warm season]. Vestnik grazhdanskikh inzhenerov. 2017. 2 (61). Pp. 188–194.

16. Gorshkov, A.S., Rymkevich, P.P. Diagrammnyi metod opisaniya protsessa nestatsionarnoi teploperedachi [Diagrammatic method for describing the process of unsteady heat transfer]. Inzhenerno-stroitel'nyi zhurnal. 2015. 8 (60). Pp. 68–82.
17. Panferov, V.I., Panferov, S.F. Primeniye metoda chastotnykh peredatochnykh funktsii dlya resheniya odnoi zadachi teploustoichivosti ograzhdeniya. [Primeneniye metoda chastotnykh peredatochnykh funktsiy dlya resheniya odnoy problemy termostoykosti ograzhdeniya]. Vestnik Yuzhno-Ural'skogo gosudarstvennogo universiteta. Seriya: stroitel'stvo i arkhitektura. 2015. 15 (1). Pp. 48–51.
18. Kutuev, M.D., Manapbaev, I.K. Ispol'zovanie metoda interpolirovaniya dlya rascheta teploustoichivosti ograzhdayushchikh konstruksii v usloviyakh Kyrgystana [Using the interpolation method for calculating the thermal stability of enclosing structures in the conditions of Kyrgyzstan]. Vestnik KRSU. 2017. 17 (5). Pp. 157–159.
19. Deconinck, A., Roels, S. The as-built thermal quality of building components: characterising non-stationary phenomena through inverse modelling. Energy Procedia. 2017. 132. Pp. 351–356. DOI: 10/1016/j.egypro.2017.09.748
20. Rulik, S., Wróblewski, W., Majkut, M., Stozik, M., Rusin, K. Experimental and numerical analysis of heat transfer within cavity working under highly non-stationary flow conditions. Energy. 2020. 190. 116303. DOI: 10/1016/j.energy.2019.116303
21. Stolarska, A., Strzałkowski, J. Modelling of Edge Insulation Depending on Boundary Conditions for the Ground Level. IOP Conference Series Materials Science and Engineering. 2017. 245 (4). 042003.
22. Adilhodzhaev, A.I., Shaumarov, S.S., Shipacheva, E.V., Kandahorov, S.I. Complex approach at thermalization external walls of residential buildings. International Journal of Advanced Research in Science, Engineering and Technology. 2019. 6 (1). Pp. 71–77. DOI:10/35940/ijeat.A2993.109119
23. Shaumarov, S.S. On the issue of increasing energetic efficiency of buildings in railway transport. Transport Problems – 2016: VIII International Conference. Katowice, 2016. Pp. 522–532.
24. Petrichenko, M.R., Nemova, D.V., Kotov, E.V., Tarasova, D.S., Sergeev, V.V. Ventilated facade integrated with the HVAC system for cold climate. Magazine of Civil Engineering. 2018. 77 (1). Pp. 47–58. DOI: 10.18720/MCE.77.5
25. Samarin, O.D. Thermal mode of a room with integrated regulation of cooling systems. Magazine of Civil Engineering. 2021. 103(3). Article No. 10312. DOI: 10.34910/MCE.103.12

Information about author:

Alexey Belous,

PhD of Technical Science

ORCID: <https://orcid.org/0000-0003-4662-6650>

E-mail: a.n.belous@donnasa.ru

German Kotov,

PhD of Physical and Mathematical Sciences

ORCID: <https://orcid.org/0000-0002-4534-7302>

E-mail: g.a.kotov@donnasa.ru

Olga Belous,

ORCID: <https://orcid.org/0000-0002-4109-5742>

E-mail: o.e.belous@donnasa.ru

Igor Garanzha,

PhD of Technical Science

ORCID: <https://orcid.org/0000-0002-6687-7249>

E-mail: garigo@mail.ru

Received 16.03.2021. Approved after reviewing 27.09.2021. Accepted 01.10.2021.



Research article

UDC 539.3

DOI: 10.34910/MCE.113.14



Physically nonlinear shell deformation based on three-dimensional finite elements

Yu.V. Klochkov^a , A.P. Nikolaev^a , O.V. Vakhnina^a , T.A. Sobolevskaya^a  ,
M.Yu. Klochkov^b

^a Volgograd State Agricultural University, Volgograd, Russian Federation

^b Lomonosov Moscow State University, Moscow, Russian Federation

✉ moonway13@rambler.ru

Keywords: physical nonlinearity, three-dimensional finite element, shell, stress increment deviator, strain increment deviator

Abstract. The aim of the study is to determine the stress-strain state of the shell under step loading beyond the elastic limit. At the loading step, relations between strain increments and stress increments are obtained without accepting the hypothesis of a straight normal. For the numerical implementation of the algorithm in the calculation of the shell without using a straight normal, a prismatic finite element has been developed. We consider the physically nonlinear deformation of the shell, an arbitrary point of which is represented by a radius vector defined by the curvilinear coordinates of the reference surface and the distance from the reference surface to the point under consideration. By differentiating the radius-vector function, the basis vectors of the point under consideration are determined, the scalar products of which are the components of its metric tensor. The increments of deformations at the loading step are defined as the differences of the corresponding components of the metric tensors. The defining equations at the loading step are obtained in two versions. In the first version, they are determined by differentiating the stress functions of the deformation theory of plasticity, which are obtained on the basis of dividing deformations into elastic and plastic parts using the hypothesis of material incompressibility during plastic deformation. In the second version, they are obtained without using the operation of dividing the strain increments into elastic and plastic parts on the basis of the proposed hypothesis that the components of the deviator of the stress increments are proportional to the components of the deviator of the increments of deformations. For the numerical implementation, a three-dimensional prismatic finite element with a triangular base was used for nodal unknowns in the form of displacements and their first derivatives with respect to curved coordinates. The correctness of the proposed variant of obtaining physically nonlinear defining equations at the loading step of the deformable shell is confirmed by a numerical example. On the example of calculating a cylindrical shell under the action of internal pressure, clamped at one end and free at the other, the values of normal stresses in the embedment turned out to be approximately 14% lower in the case of using the proposed variant of obtaining the constitutive equations at the loading step. The developed algorithm for determining the stress-strain state in the physically nonlinear deformation of elements of technospheric objects can be used in the practice of engineering calculations.

Funding: The study was carried out with the financial support of the Russian Foundation for Basic Research and the Administration of the Volgograd Region in the framework of the research project No. 19-41-340005 r_a.

Citation: Klochkov, Yu.V., Nikolaev, A.P., Vakhnina, O.V., Sobolevskaya, T.A., Klochkov, M.Yu. Physically nonlinear shell deformation based on three-dimensional finite elements. Magazine of Civil Engineering. 2022. 113(5). Article No. 11314. DOI: 10.34910/MCE.113.14

1. Introduction

Currently, technospheric objects are subject to rather stringent requirements to minimize their material consumption, without reducing the criterion of their strength, stability, durability, etc. The above requirements are fully met by shell-type structures with curved surfaces. The analysis of the stress-strain state (SSS) of such objects by classical analytical methods of calculation is difficult, especially in a nonlinear setting. The theory of the stress-strain state of a solid has received quite sufficient development [1–5]. To solve the problems of strength of objects of engineering practice, approximate calculation methods were developed both in a linear formulation [6–10] and in a nonlinear one [11–15]. Due to the complexity of solving the equations of deformation mechanics as applied to specific elements of engineering objects, the task of developing numerical methods for determining the stress-strain state has become urgent [16–20]. Among the numerical methods for calculating the constituent parts of engineering objects, the finite element method (FEM) has become widespread [20–22]. It has been applied to cylindrical shells of circular and elliptical sections [13, 14], as well as to plates and shells with finite deformations [15, 23, 24]. FEM was also widely used to calculate nonlinear elastic bodies and shells taking into account the Kirchhoff hypothesis [25–29]. Composite shells were calculated based on the FEM [30–33]. Volumetric finite elements were also used to calculate the shells without taking into account Kirchhoff's hypothesis [34–37]. Volumetric finite elements were used to calculate elastic and inelastic solids based on the method of virtual components [38, 39].

In the case of deformation of shell structures under various combinations of loads, it becomes possible for zones of significant stress concentrations to appear, in which the relationships between stresses and deformations become nonlinear. When solving problems of this class, the method of step loading [36] is widely used to obtain the governing physically nonlinear equations at the loading step, the method of decomposing the increments of deformations into elastic and plastic parts is used [37, 38].

When analyzing the SSS of shells of arbitrary configuration and thickness, the most promising are three-dimensional sampling elements without reduction to two-dimensional ones based on any hypothesis. Despite the wide range of computing systems of foreign and domestic production, the problem of improving the finite element algorithms for analyzing the SSS of technospheric shell-type objects based on three-dimensional discretization elements, taking into account the elastic-plastic stage of the material used, remains very urgent.

In this paper, at the loading step, an algorithm for the formation of the stiffness matrix of a prismatic discretization element is presented, intended for calculating structures from shells of arbitrary thickness and configuration, taking into account the physical nonlinearity of the material used. A distinctive feature of the study is the developed method for obtaining the constitutive equations at the loading step based on the hypothesis that the components of the deviator of the deformation increments are proportional to the components of the deviator of the stress increments without dividing the increments of deformations into elastic and plastic parts.

When implementing the proposed hypothesis, the proportionality coefficient of the constitutive equations turned out to be a function of the chord modulus of the material deformation diagram, which opens up prospects for using the constitutive equations obtained by this method even in the presence of unloading zones of the calculated structures.

2. Methods

The reference surface, which is the curvilinear boundary of the object under study, is determined by the radius vector [40] (Fig. 1).

$$\vec{R}^0 = x(\theta^1, \theta^2) \vec{i} + y(\theta^1, \theta^2) \vec{j} + z(\theta^1, \theta^2) \vec{k}, \quad (1)$$

where \vec{i} , \vec{j} , \vec{k} are unit vectors of the Cartesian coordinate system, θ^p ($p=1, 2$) are curvilinear coordinates of the reference surface.

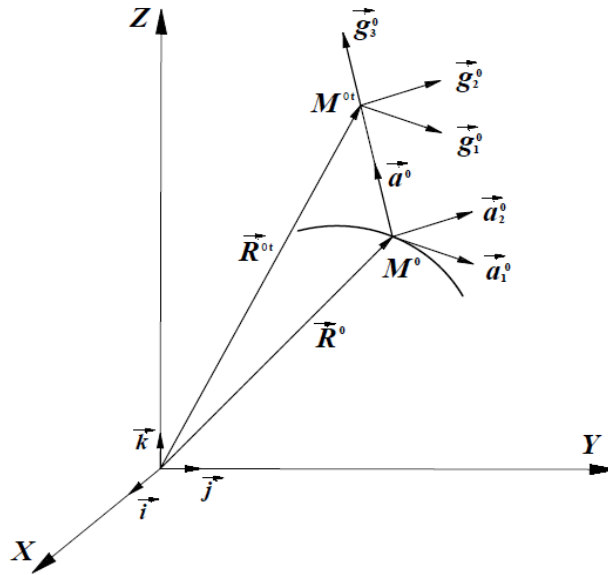


Figure 1. Geometry of the shell: – an arbitrary point of the reference surface of the shell; – arbitrary point of the shell.

The position of an arbitrary point M^{0t} of the object located at a distance of t , measured along the normal to the reference surface, is determined by the radius vector of the form

$$\vec{R}^{0t} = \vec{R}^0 + t\vec{a}^0, \quad (2)$$

where $\vec{a}^0 = \vec{a}_1^0 \times \vec{a}_2^0 / |\vec{a}_1^0 \times \vec{a}_2^0|$ is the unit vector of the normal to the reference surface [41]; $\vec{a}_1^0 = \vec{R}_{,\theta^1}^0$; $\vec{a}_2^0 = \vec{R}_{,\theta^2}^0$. Here and below, the comma means the operation of differentiation by the corresponding coordinate, for example, θ^p ($p = 1, 2$).

The basis vectors of point M^{0t} are determined by differentiating (2) with respect to θ^p and t .

$$\vec{g}_1^0 = \vec{R}_{,\theta^1}^{0t}; \dots \vec{g}_2^0 = \vec{R}_{,\theta^2}^{0t}; \dots \vec{g}_3^0 = \vec{R}_{,t}^{0t}. \quad (3)$$

1. or in matrix form

$$\{\vec{g}^0\} = [l]\{\vec{i}\}; \{\vec{i}\} = [l]^{-1}\{\vec{g}^0\}, \quad (4)$$

where $\{\vec{g}^0\} = \{\vec{g}_1^0 \vec{g}_2^0 \vec{g}_3^0\}$, $\{\vec{i}\}^T = \{\vec{i} \ \vec{j} \ \vec{k}\}$.

2. Differentiation (3) with allowance for (4) determines the derivatives of the basis vectors by the components in this basis

$$\{\vec{g}_{,i}^0\} = [Z_i][l]^{-1}\{\vec{g}^0\} = [m_i]\{\vec{g}^0\}, \quad (5)$$

where $\{\vec{g}_{,i}^0\}^T = \{\vec{g}_{1,i}^0 \vec{g}_{2,i}^0 \vec{g}_{3,i}^0\}$; ($i = \theta^1, \theta^2, t$).

When studying the stress-strain state of technospheric objects in a nonlinear formulation, a step-by-step loading procedure is usually used, during which an arbitrary point of object M^{0t} will move to point M^t in j loading steps, and to point M^{*t} in the $(j+1)^{\text{th}}$ loading step.

The positions of points M^t and M^{*t} are determined by the corresponding radius vectors

$$\vec{R}^t = \vec{R}^{0t} + \vec{V}; \vec{R}^{*t} = \vec{R}^t + \vec{W}, \quad (6)$$

where $\vec{V} = v^i \vec{g}_i^0$ and $\vec{W} = w^i \vec{g}_i^0$ are the total and step vectors of displacement of point M^{0t} .

The vectors of bases at points M^t and M^{0t} can be determined by differentiating (6) with respect to θ^p and t .

$$\begin{aligned}\vec{g}_1 &= \vec{R}_{,\theta^1}^t = \vec{g}_1^0 + \vec{V}_{,\theta^1}; \dots \vec{g}_2 = \vec{R}_{,\theta^2}^t = \vec{g}_2^0 + \vec{V}_{,\theta^2}; \dots \vec{g}_3 = \vec{R}_{,t}^t = \vec{g}_3^0 + \vec{V}_{,t}; \\ \vec{g}_1^* &= \vec{R}_{,\theta^1}^{*t} = \vec{g}_1 + \vec{W}_{,\theta^1}; \dots \vec{g}_2^* = \vec{R}_{,\theta^2}^{*t} = \vec{g}_2 + \vec{W}_{,\theta^2}; \dots \vec{g}_3^* = \vec{R}_{,t}^{*t} = \vec{g}_3 + \vec{W}_{,t}.\end{aligned}\quad (7)$$

The covariant components of the metric tensors at points M^{0t} , M^t , and M^{*t} can be obtained by scalar products of vectors (3), (7).

$$g_{mn}^0 = \vec{g}_m^0 \cdot \vec{g}_n^0; \quad g_{mn} = \vec{g}_m \cdot \vec{g}_n; \quad g_{mn}^* = \vec{g}_m^* \cdot \vec{g}_n^*.\quad (8)$$

The covariant components of the deformation tensor at point M^t in j loading steps and the increment tensor at the $(j+1)^{\text{th}}$ loading step at point M^{*t} can be calculated using the classical relations of continuum mechanics [42]

$$\varepsilon_{mn} = 0.5 \cdot (g_{mn} - g_{mn}^0); \quad \Delta \varepsilon_{mn} = 0.5 \cdot (g_{mn}^* - g_{mn}),\quad (9)$$

which are represented in matrix form

$$\begin{Bmatrix} \varepsilon \end{Bmatrix} = \begin{bmatrix} L_1 \end{bmatrix} \begin{Bmatrix} v \end{Bmatrix}; \quad \begin{Bmatrix} \Delta \varepsilon \end{Bmatrix} = \begin{bmatrix} L_2 \end{bmatrix} \begin{Bmatrix} w \end{Bmatrix},\quad (10)$$

where $\begin{Bmatrix} \varepsilon \end{Bmatrix}_{1 \times 6}^T = \{\varepsilon_{11} \varepsilon_{22} \varepsilon_{33} 2\varepsilon_{12} 2\varepsilon_{13} 2\varepsilon_{23}\}$; $\begin{Bmatrix} \Delta \varepsilon \end{Bmatrix}_{1 \times 6}^T = \{\Delta \varepsilon_{11} \Delta \varepsilon_{22} \Delta \varepsilon_{33} 2\Delta \varepsilon_{12} 2\Delta \varepsilon_{13} 2\Delta \varepsilon_{23}\}$;

$\begin{Bmatrix} v \end{Bmatrix}_{1 \times 3}^T = \{v^1 v^2 v^3\}$; $\begin{Bmatrix} w \end{Bmatrix}_{1 \times 3}^T = \{w^1 w^2 w^3\}$; $\begin{bmatrix} L_1 \end{bmatrix}$ and $\begin{bmatrix} L_2 \end{bmatrix}$ matrices of algebraic and differential operators.

3. Matrix of elastic-plastic deformation at the $(j+1)^{\text{th}}$ step of loading

At the $(j+1)^{\text{th}}$ loading step, it is necessary to have a relationship between the stress increment tensor and the strain increment tensor.

To obtain ratios in a curvilinear coordinate system between the components of stress and strain tensors, the hypothesis of proportionality of the stress deviator components to the strain deviator components is used [43]

$$\sigma^{mn} - \frac{1}{3} g^{mn} I_1(\sigma) = \frac{2}{3} E_c \left(\varepsilon^{mn} - \frac{1}{3} g^{mn} I_1(\varepsilon) \right),\quad (11)$$

where σ^{mn} is contravariant component of the stress tensor; g^{mn} is contravariant component of the metric tensor; $\varepsilon^{mn} = g^{mi} g^{nj} \varepsilon_{ij}$ is contravariant component of the strain tensor; $I_1(\varepsilon) = g^{ij} \varepsilon_{ij} = g_{ij} \varepsilon^{ij}$ is the first invariant of the strain tensor; $I_1(\sigma) = \sigma^{ij} g_{ij} = \sigma_{ij} g^{ij}$ is the first invariant of the stress tensor; E_c is secant module of the deformation diagram.

The relationship between the first invariants of the stress and strain tensors is [43]

$$I_1(\sigma) = \frac{E}{1-2\nu} I_1(\varepsilon) = K \cdot I_1(\varepsilon),\quad (12)$$

where E is the modulus of elasticity of the material; ν is coefficient of transverse deformation.

Using (12) from (11), expressions for the contravariant components of the stress tensor are determined

$$\sigma^{mn} = \frac{2}{3} E_c g^{mi} g^{nj} \varepsilon_{ij} + \frac{1}{3} g^{mn} I_1(\varepsilon) \left(K - \frac{2}{3} E_c \right). \quad (13)$$

The relationships between the increments of the stress tensor components and the increments of the components of the deformation tensor are determined by differentiation (13)

$$\Delta\sigma^{mn} = \frac{\partial\sigma^{mn}}{\partial\varepsilon_{ij}} \Delta\varepsilon_{ij}, \quad (14)$$

or in matrix form

$$\left\{ \Delta\sigma \right\}_{6 \times 1} = \left[C_1^{\Pi} \right]_{6 \times 6} \left\{ \Delta\varepsilon \right\}_{6 \times 1}, \quad (15)$$

where $\left\{ \Delta\sigma^{mn} \right\}^T = \left\{ \Delta\sigma^{11} \Delta\sigma^{22} \Delta\sigma^{33} \Delta\sigma^{12} \Delta\sigma^{13} \Delta\sigma^{23} \right\}$.

The implementation of relations (14) in a three-dimensional formulation involves a significant amount of analytical calculations due to the variability of the components of the metric tensors, which significantly complicates the programming procedure. Therefore, in this work, we propose a layout of the constitutive equations at the $(j+1)^{\text{th}}$ step of loading based on the proposed hypothesis of proportionality of the components of the deviator of the stress increments to the components of the deviator of the increments of deformations, according to which the following expression can be written

$$\Delta\sigma^{mn} - \frac{1}{3} g^{mn} I_1(\Delta\sigma) = \frac{2}{3} E_x \left(\Delta\varepsilon^{mn} - \frac{1}{3} g^{mn} I_1(\Delta\varepsilon) \right), \quad (16)$$

where $\Delta\sigma^{mn}$ is contravariant component of the stress increment tensor; $\Delta\varepsilon^{mn} = g^{mi} g^{nj} \Delta\varepsilon_{ij}$ is contravariant component of the strain increment tensor; $I_1(\Delta\varepsilon) = g^{ij} \Delta\varepsilon_{ij} = g_{ij} \Delta\varepsilon^{ij}$ is the first invariant of the strain increment tensor; $I_1(\Delta\sigma) = \Delta\sigma^{ij} g_{ij} = \Delta\sigma_{ij} g^{ij}$ is the first invariant of the stress increment tensor; E_x is chordal module of the material deformation diagram.

Taking the relationship between the first invariants $I_1(\Delta\sigma)$ and $I_1(\Delta\varepsilon)$ according to (12), based on (16), the governing equations at the loading step can be written in the form

$$\Delta\sigma^{mn} = \frac{2}{3} E_x g^{mi} g^{nj} \Delta\varepsilon_{ij} + \frac{1}{3} g^{mn} I_1(\Delta\varepsilon) \left(K - \frac{2}{3} E_x \right), \quad (17)$$

which are represented in matrix form

$$\left\{ \Delta\sigma \right\}_{6 \times 1} = \left[C_2^{\Pi} \right]_{6 \times 6} \left\{ \Delta\varepsilon \right\}_{6 \times 1}. \quad (18)$$

4. Stiffness matrix of the prismatic discretization element at the $(j+1)^{\text{th}}$ loading step

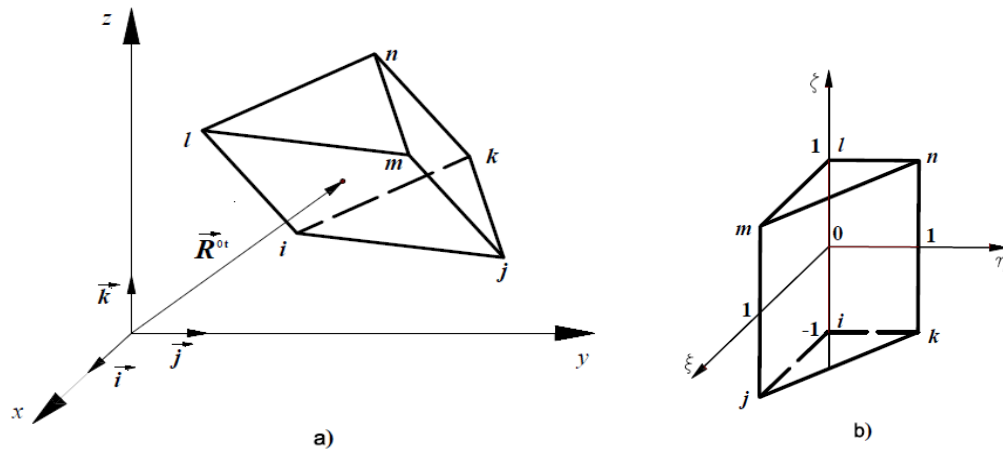


Figure 2. Finite element geometry: a) in the global coordinate system; b) in the local coordinate system.

A prismatic fragment with triangular bases with nodes i, j, k (lower base) and l, m, n (upper base) (Fig. 2a) was chosen as the sampling element for the investigated technospheric object of the shell type. To perform numerical integration, the prismatic fragment was mapped onto a local prism with a triangular base in the form of a right-angled triangle with local coordinates varying within $0 \leq \xi, \eta \leq 1$ and with a local coordinate in height varying within $-1 \leq \zeta \leq 1$ (Fig. 2b). The nodal variable parameters of this element are the increments of the displacement vector components and their first-order partial derivatives. The columns of the required step nodal unknowns in the local ξ, η, ζ and global θ^1, θ^2, t coordinate systems can be represented in the following form

$$\left\{ W^L \right\}_{1 \times 72}^T = \left\{ \left\{ w^{1L} \right\}_{1 \times 24}^T \left\{ w^{2L} \right\}_{1 \times 24}^T \left\{ w^{3L} \right\}_{1 \times 24}^T \right\}; \quad (19)$$

$$\left\{ W^G \right\}_{1 \times 72}^T = \left\{ \left\{ w^{1G} \right\}_{1 \times 24}^T \left\{ w^{2G} \right\}_{1 \times 24}^T \left\{ w^{3G} \right\}_{1 \times 24}^T \right\}, \quad (20)$$

where $\left\{ q^L \right\}_{1 \times 24}^T = \left\{ q^i q^j q^k q^l q^m q^n q_{,\xi}^i \dots q_{,\xi}^n q_{,\eta}^i \dots q_{,\eta}^n q_{,\zeta}^i \dots q_{,\zeta}^n \right\};$

$\left\{ q^G \right\}_{1 \times 24}^T = \left\{ q^i \dots q^n q_{,\theta^1}^i \dots q_{,\theta^1}^n q_{,\theta^2}^i \dots q_{,\theta^2}^n q_{,t}^i \dots q_{,t}^n \right\};$ q is understood as the component of the step

motion vector $\vec{w} = w^1 \vec{a}_1^0 + w^2 \vec{a}_2^0 + w^3 \vec{a}^0$.

When approximating the components of the displacement vector at the loading step, we used the products of two-dimensional polynomials of the third degree in the planes of triangular bases and Hermite polynomials of the third degree in the direction of the height of the local prism

$$\{w\} = [A] \{W^L\} = [A] [P_R] \{W^G\}, \quad (21)$$

where $[P_R]$ is transformation matrix between columns of nodal unknowns in local and global coordinate systems.

Taking into account (21), the strain increments are determined by the following expression

$$\{\Delta \varepsilon\} = [L_2] [A] \{W^L\} = [B] [P_R] \{W^G\}. \quad (22)$$

For the arrangement of the stiffness matrix and the column of nodal forces of the prismatic discretization element at the $(j+1)^{\text{th}}$ loading step, the Lagrange functional was used

$$\Phi_L = \int_V \{\Delta \varepsilon\}^T (\{\sigma\} + \{\Delta \sigma\}) dV - \int_S \{w\}^T (\{P\} + \{\Delta P\}) dS, \quad (23)$$

where $\{P\}$; $\{\Delta P\}$ are columns of the external load in j loading steps and increments of this load at the $(j+1)^{\text{th}}$ loading step; $\{\sigma\}$, $\{\Delta\sigma\}$ are columns containing contravariant components of stress tensors accumulated over j loading steps and increments of these stresses at the $(j+1)^{\text{th}}$ loading step; V is volume; S is load application surface.

Functional (23), taking into account (22), can be transformed to the form

$$\begin{aligned} \Phi_L = & \{W^G\}^T [P_R]^T \int_V [B]^T \{\sigma^{mn}\} dV + \\ & + \{W^G\}^T [P_R]^T \int_V [B]^T [C_{II}] [B] dV [P_R] \{W^G\} - \\ & - \{W^G\}^T [P_R]^T \int_S [A]^T \{P\} dS - \{W^G\}^T [P_R]^T \int_S [A]^T \{\Delta P\} dS. \end{aligned} \quad (24)$$

By minimizing (24) by $\{W^G\}^T$, one can obtain the following matrix expression

$$[K] \{W^G\} = \{f\} - \{R\}, \quad (25)$$

where $[K] = [P_R]^T \int_V [B]^T [C_{II}] [B] dV [P_R]$ is stiffness matrix of the prismatic sampling element at the $(j+1)^{\text{th}}$ loading step; $\{f\} = [P_R]^T \int_S [A]^T \{\Delta P\} dS$ is column of nodal forces of the sampling element at the $(j+1)^{\text{th}}$ loading step; $\{R\} = \left([P_R]^T \int_V [B]^T \{\sigma\} dV - [P_R]^T \int_S [A]^T \{P\} dS \right)$ is Newton-Raphson correction.

3. Results and Discussion

In order to verify the developed algorithm, a test problem was solved to determine the stress-strain state of a circular cylinder rigidly clamped along the right end and having a left end free of fixings (Fig. 3). The cylinder was loaded with an internal pressure of intensity $q = 3.5$ MPa. Geometrical dimensions of the cylinder: generatrix length $L = 0.8$ m; the radius of the inner surface of the cylinder is $R = 0.895$ m; wall thickness $t = 0.01$ m. Duralumin alloy $E = 7.5 \cdot 10^4$ MPa was used as a material; $\nu = 0.32$. The deformation diagram was selected with linear hardening determined by the formula

$$\sigma_i = 18087 (\varepsilon_i - \varepsilon_i^T) + \sigma_i^T, \quad (26)$$

where $\varepsilon_i^T = 0.00295$ is the intensity of deformations corresponding to the yield point; $\sigma_i^T = 200$ MPa is stress intensity corresponding to the yield point.

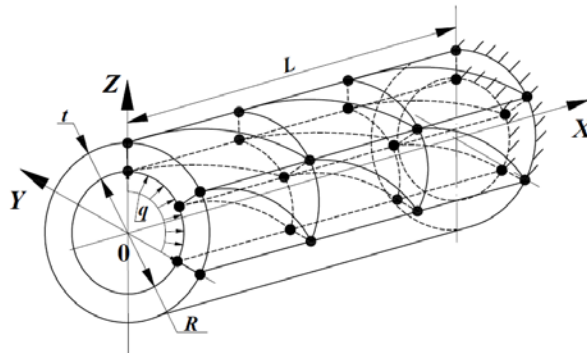


Figure 3. Design scheme of the shell.

Along the generatrix, the cylinder was divided into 25 finite elements. The shell was crushed into 8 sampling points along the thickness.

The results of finite element calculations are summarized in a table, which shows the values of "physical" normal stresses on the outer σ^{out} and inner σ^{in} surfaces of the cylinder in a rigid embedment and at the free end, depending on the number of loading steps.

It should be noted that the stress values obtained using the constitutive relations according to (14) and (16) turned out to be quite close.

Table 1. Values of normal stresses in the rigid termination and at the free end of the cylinder.

Cross section	Stress, MPa	Number of loading steps				Analytical stress values
		12	22	32	42	
Rigid termination	σ_{11}^{in}	421.4	436.1	434.7	434.0	–
	σ_{11}^{out}	–440.1	–436.5	–433.6	–432.7	–
	σ_{22}^{in}	198.3	205.2	204.6	204.2	–
	σ_{22}^{out}	–207.1	–205.4	–204.0	–203.6	–
Free end	σ_{11}^{in}	0.003	0.003	0.002	0.0019	0.000
	σ_{11}^{out}	–0.003	0.000	0.001	0.001	0.000
	σ_{22}^{in}	310.6	313.8	314.9	315.4	315.0
	σ_{22}^{out}	317.3	315.4	314.8	314.5	315.0
	σ_{33}^{in}	–3.50	–3.50	–3.50	–3.50	–3.50
	σ_{33}^{out}	0.003	0.003	0.003	0.004	0.000

Analysis of the numerical values of the stresses presented in Table 1 shows that there is a stable convergence of the computational process with an increase in the number of loading steps. The numerical values of the stresses at the free end of the cylinder practically coincide with the values obtained from the static equations. The meridional stresses (σ_{11}) at the end of the cylinder must be zero, because the external load, represented by the internal pressure q , acts along the normal to the inner surface of the cylinder and its projection onto the generatrix of the cylinder is zero. Hoop stresses (σ_{22}) can be obtained from the equilibrium condition of $\sigma_{22} = \frac{qR}{t} = \frac{3.5 \cdot 0.9}{0.01} = 315.0$ MPa. The stresses acting along the normal to the inner surface must coincide in absolute value with the intensity of the inner pressure, i.e. $\sigma_{33} = -q = -3.5$ MPa.

Analyzing the numerical values of normal stresses σ_{11} in a rigid termination, it can be noted that they correspond to the condition of static equilibrium, namely: the sum of internal longitudinal forces should be zero, since there are no external longitudinal forces. The sum of internal longitudinal forces can be determined by calculating the areas of the diagrams of compressive and tensile stresses σ_{11} , approximately taking the area in the form of the sums of triangular and trapezoidal fragments (Fig. 4).

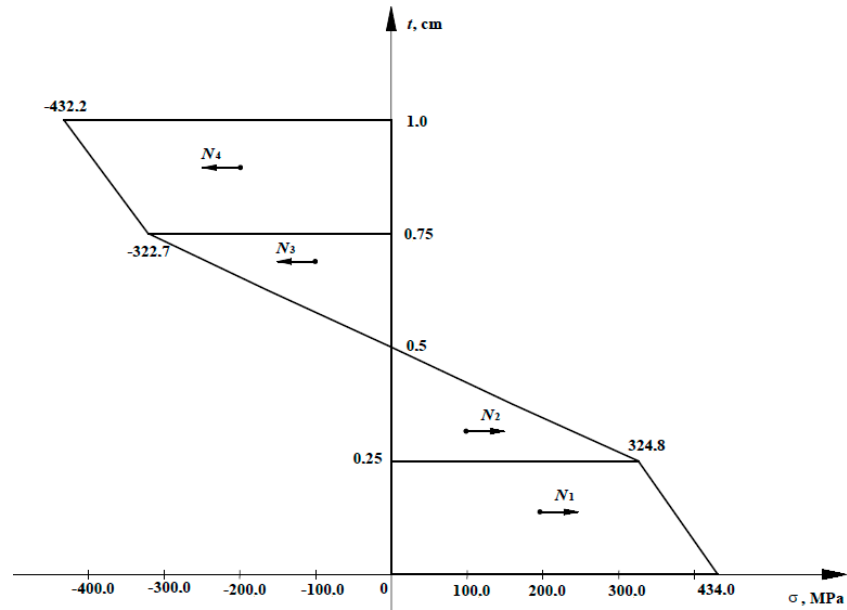


Figure 4. Stress diagram σ_{11} in a rigid termination with the number of steps $n_s = 42$

The total tensile force is $N_t = N_1 + N_2 = 1354.5$ kN and the total compressive force is $N_c = N_3 + N_4 = 1347.0$ kN.

The difference between N_t and N_c is negligible (about 0.16 %).

In the numerical implementation of the developed algorithm on the considered test problem, a calculation was performed based on the relationships between stress increments and strain increments obtained by differentiating the governing equations of the deformation theory of plasticity (10) in accordance with formula (11). The use of this differentiation approach is widespread [44, 45]. The numerical values of normal stresses in a rigid seal based on formula (11) turned out to be 15.6 % less for σ_{11}^{in} and 14.2 % less for hoop stresses σ_{22}^{in} .

Fig. 5 shows graphs showing changes in normal stresses σ_{11} and σ_{22} in a rigid seal on the inner σ^{in} and outer σ^{out} surfaces of the cylinder, depending on the number of prismatic elements along the generatrix of the cylinder. As can be seen from Fig. 5, there is a stable convergence of the computational process when the discretization grid is refined, which is an additional criterion for the adequacy of the developed calculation algorithm.

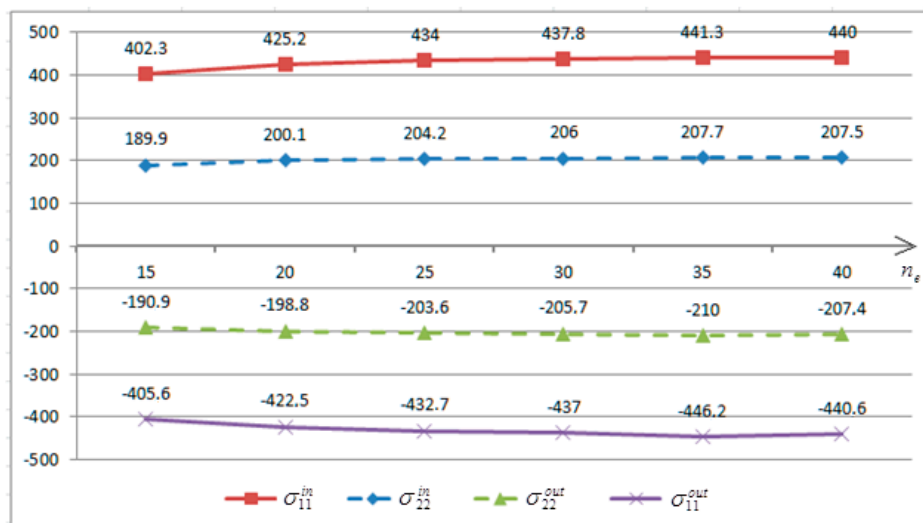


Figure 5. Stresses σ_{11} and σ_{22} in a rigid termination depending on the number of finite elements along the generatrix.

4. Conclusion

Based on the research performed, the following conclusions can be drawn:

1. The difference in the numerical values of the normal stresses in the embedding of the cylindrical shell from the effect of internal pressure, obtained on the basis of the constitutive equations (10) and (11), turned out to differ by about 14 %. Consequently, in the case of elastic-plastic deformation, it is physically more reasonable to obtain the governing equations between stress increments and strain increments on the basis of the proposed hypothesis that the components of the deviator of the stress increments are proportional to the components of the deviator of the increments of deformations.
2. For strength calculations of shells of various shapes and thicknesses, it is preferable to use the developed volumetric finite element without using additional hypotheses about deformation along the thickness of the shell structures.
3. A numerical example confirmed the accuracy of determining the parameters of strength during deformation beyond the elastic limit, sufficient for solving shell-type engineering objects.

References

1. Novozhilov, V.V. *Teoriya tonkikh obolochek* [Theory of thin shells]. St. Petersburg: Publishing House of the St. Petersburg University, 2010. 378 p. (rus)
2. Kabrits, S.A., Mikhailovsky, E.I., Tovstik, P.E., Chernykh, K.F., Shamina, V.A. *Obshchaya nelineynaya teoriya uprugikh obolochek* [General nonlinear theory of elastic shells]. St. Petersburg: Publishing House of the St. Petersburg University, 2002. 388 p. (rus)
3. Rozin, L.A. *Zadachi teorii uprugosti i chislennyye metody ikh resheniya* [Problems of the theory of elasticity and numerical methods for their solution]. St. Petersburg: Publishing house of SPbSTU, 1998. 531 p. (rus)
4. Pikul, V.V. *Mekhanika obolochek* [Mechanics of shells]. Vladivostok: Dalnauka, 2009. 536 p. (rus)
5. Paimushin, V.N. On the forms of loss of stability of a cylindrical shell under an external side pressure. *Journal of Applied Mathematics and Mechanics*. 2016. 80 (1). Pp. 65–72.
6. Rozin, L.A., Terpugov, V.N. *Variatsionnyye zadachi uprugogo ravnovesiya s odnovremenno zadannymi skachkami napryazheniy i peremeshcheniy* [Variational problems of elastic equilibrium with simultaneously given jumps of stresses and displacements]. Scientific and technical statements of the St. Petersburg State Polytechnic University. 2009. 1 (74). Pp. 65–72. (rus)
7. Lalin, V.V., Zdanchuk, E.V., Kushova, D.A., Rozin, L.A. *Variatsionnyye postanovki nelineynykh zadach s nezavisimymi vrashchatelnymi stepenyami svobody* [Variational formulations for non-linear problems with independent rotational degrees of freedom]. *Magazine of Civil Engineering*. 2015. 56(4). Pp. 54–65. (rus)
8. Postnov, V.A. Use of Tikhonov's regularization method for solving identification problem for elastic systems. *Mechanics of Solids*. 2010. 1 (45). Pp. 51–56.
9. Postnov, V.A., Tumashik, G.A., Moskvina, I.V. On the stability of the reinforced cylindrical shell. *Strength and Ductility Problems*. 2007. 69. Pp. 18–23.
10. Karpov, V., Maslennikov, A. Methods for solving non-linear tasks for calculating construction structures. *World Applied Sciences Journal*. 2013. 13 (23). Pp. 178–183.
11. Klochkov, Yu.V., Nikolaev, A.P., Fomin, S.D., Vakhnina, O.V., Klochkov, M.Yu. Application of volume final elements in strength calculations of engineering objects of agricultural complex. *Proceedings of Lower Volga Agro-University Complex: Science and Higher Education*. 2019. 4 (56). Pp. 227–237. DOI: 10.32786/2071-9485-2019-04-27
12. Magisano, D., Liang, K., Garcea, G., Leonetti, L., Ruess, M. An efficient mixed variational reduced-order model formulation for nonlinear analyses of elastic shells. *International Journal for Numerical Methods in Engineering*. 2018. 113 (4). Pp. 634–655.
13. Storozhuk, E.A., Maksimyyuk, V.A., Chernyshenko, I.S. Nonlinear elastic state of a composite cylindrical shell with a rectangular hole. *International Applied Mechanics*. 2019. 55 (4). Pp. 504–514. DOI: 10.1007/s10778-019-00972-0
14. Storozhuk, E.A., Chernyshenko, I.S., Yatsura, A.V. Stress–strain state near a hole in a shear-compliant composite cylindrical shell with elliptical cross-section. *International Applied Mechanics*. 2018. 54 (5). Pp. 559–567. DOI: 10.1007/s10778-018-0909-8
15. Leonetti, L., Magisano, D., Madeo, A., Garcea, G., Kiendl, J., Reali, A. A simplified Kirchhoff–Love large deformation model for elastic shells and its effective isogeometric formulation. *Computer Methods in Applied Mechanics and Engineering*. 2019. 354. Pp. 369–396. DOI: 10.1016/j.cma.2019.05.025
16. Badriev, I.B., Paimushin, V.N. Refined Models of Contact Interaction of a Thin Plate with Positioned on Both Sides Deformable Foundations. *Lobachevskii Journal of Mathematics*. 2017. 38 (5). Pp. 779–793.
17. Neto, M.A., Amaro, A., Roseiro, L., Cirne, J., Leal, R. *Engineering computation of structures: The finite element method*. Springer, Cham. 2015. 314 p. DOI: 10.1007/978-3-319-17710-6
18. Klochkov, Yu.V., Nikolaev, A.P., Sobolevskaya, T.A., Fomin, S.D., Klochkov, M.Yu. Finite-element models of discretization of thin-walled structures of enterprises of agro-industrial complex. *Proceedings of Lower Volga Agro-University Complex: Science and Higher Education*. 2019. 1 (53). Pp. 255–264. DOI: 10.32786/2071-9485-2019-01-34
19. Garcea, G., Liguori, F.S., Leonetti, L., Magisano, D., Madeo, A. Accurate and efficient a posteriori account of geometrical imperfections in Koiter finite element analysis. *Int. J. Numer. Methods Eng.* 2017. 112 (9). Pp. 1154–1174.
20. Neto, M.A., Amaro, A., Roseiro, L., Cirne, J., Leal, R. *Finite element method for plates/shells. in: engineering computation of structures: The finite element method*. Springer, Cham. 2015. Pp. 195–232. DOI: 10.1007/978-3-319-17710-6_6
21. Maslennikov, A.M., Kobelev, E.A., Maslennikov, N.A. Solution of stability problems by the finite element method. *Bulletin of Civil Engineers*. 2020. 2(79). Pp. 68–74.
22. Lalin, V.V., Yavarov, A.V., Orlova, E.S., Gulov, A.R. Application of the finite element method for the solution of stability problems of the Timoshenko beam with exact shape functions. *Power Technology and Engineering*. 2019. 4(53). Pp. 449–454.

23. He, X. Finite element analysis of torsional free vibration of adhesively bonded single-lap joints. *Int. J. Adhes. and Adhes.* 2014. 48. Pp. 59–66.
24. Paznanova, S.L., Vasilev, G.P., Dineva, P.S., Manolis, G.D. Dynamic analysis of nanoheterogeneities in a finite-sized solid by boundary and finite element methods. *Int. J. Solids and Struct.* 2016. 80. Pp. 1–18.
25. Javili, A., Mc Bride, A., Steinmann, P., Reddy, B.D. A unified computational framework for bulk and surface elasticity theory: a curvilinear-coordinate based finite element methodology. *Comput. Mech.* 2014. 54 (3). Pp. 745–762. DOI: 10.1007/s00466-014-1030-4
26. Nguyen, N., Waas, A.M. Nonlinear, finite deformation, finite element analysis. *ZAMP. Z. Angew. Math. and Phys.* 2016. 67 (3). Pp. 35/1–35/24. DOI: 10.1007/s00033-016-0623-5
27. Hansbo, P., Larson Mats G., Larson, F. Tangential differential calculus and the finite element modeling of a large deformation elastic membrane problem. *Comput. Mech.* 2015. 56(1). Pp. 87–95. DOI: 10.1007/s00466-015-1158-x
28. Ren, H. Fast and robust full-quadrature triangular elements for thin plates/ shells, with large deformations and large rotations. *Trans. ASME. J. Comput. and Nonlinear Dyn.* 2015. 10 (5). Pp. 051018/1–051018/13.
29. Magisano, D., Liang, K., Garcea, G., Leonetti, L., Ruess, M. An efficient mixed variational reduced-order model formulation for nonlinear analyses of elastic shells. *International Journal for Numerical Methods in Engineering.* 2018. 113(4). Pp. 634–655.
30. Sartorato, M., De Medeiros, R., Tita, V. A finite element formulation for smart piezoelectric composite shells: Mathematical formulation, computational analysis and experimental evaluation. *Compos. Struct.* 2015. 127. Pp. 185–198. DOI: 10.1016/j.compstruct.2015.03.009
31. Li, S., Lu, G., Wang, Z., Zhao, Longmao, Wu, G. Finite element simulation of metallic cylindrical sandwich shells with graded aluminum tubular cores subjected to internal blast loading. *Int. J. Mech. Sci.* 2015. 96-97. Pp. 1–12.
32. Chi, H., Talischi, C., Lopez-Pamies, O., Paulino, G.H. A paradigm for higher order polygonal elements in finite elasticity. *Comput. Methods Appl. Mech. Engrg.* 2016. 306. Pp. 216–251.
33. Zucco, G., Groh, R.M.J., Madeo, A., Weaver, P.M. Mixed shell element for static and buckling analysis of variable angle tow composite plates. *Compos. Struct.* 2016. 152 (Suppl. C). Pp. 324–338.
34. Talischi, C., Pereira, A., Menezes, I.F., Paulino, G.H. Gradient correction for polygonal and polyhedral finite elements. *Internat. J. Numer. Methods Engrg.* 2015. 102 (3). Pp. 728–747. DOI: 10.1002/nme.4851
35. Manzini, G., Russo, A., Sukumar, N. New perspective on polygonal and polyhedral finite element method. *Math. Models Methods Appl. Sci.* 2014. 24 (08). Pp. 1665–1699. DOI: 10.1142/S0218202514400065
36. Gain, A.L., Talischi, C., Paulino, G.H. On the virtual element method for three-dimensional linear elasticity problems on arbitrary polyhedral meshes. *Computer Methods in Applied Mechanics and Engineering.* 2014. 282. Pp. 132–160.
37. Klochkov, Yu.V., Nikolaev, A.P., Fomin, S.D., Vakhnina, O.V., Sobolevskaya, T.A., Klochkov, M.Yu. A finite elemental algorithm for calculating the arbitrarily loaded shell using three-dimensional finite elements. *ARNP Journal of Engineering and Applied Sciences.* 2020. 15(13). Pp. 1472–1481.
38. Beirão da Veiga, L., Lovadina, C., Mora, D. A virtual element method for elastic and inelastic problems on polytope meshes. *Comput. Methods Appl. Mech. Engrg.* 2015. 295. Pp. 327–346.
39. Antonietti, P.F., Beirão da Veiga, L., Scacchi, S., Verani, M. A C1 Virtual element method for the Cahn–Hilliard equation with polygonal meshes. *SIAM J. Numer. Anal.* 2016. 54 (1). Pp. 34–56.
40. Klochkov, Yu.V., Nikolaev, A.P., Sobolevskaya, T.A., Vakhnina, O.V., Klochkov, M.Yu. The calculation of the ellipsoidal shell based FEM with vector interpolation of displacements when the variable parameterisation of the middle surface. *Lobachevskii Journal of Mathematics.* 2020. 41 (3). Pp. 373–381. DOI: 10.1134/S1995080220030117
41. Pogorelov, A.V. *Differentsial'naya geometriya [Differential geometry]*. 6th ed., stereotype. Moscow: Nauka, 1974. 176 p. (rus)
42. Sedov, L.I. *Mekhanika sploshnoy sredy [Mechanics of a continuous medium]*. v. 1. Moscow: Nauka, 1976. 536 p. (rus)
43. Zubchaninov V.G. *Ustoychivost' i plastichnost'. Tom 2. Plastichnost' [Stability and plasticity. Volume 2. Plasticity]*. Moscow: Fizmatlit, 2007. 336 p. (rus)
44. Chi, H., Beirão da Veiga L., Paulino, G.H. Some basic formulations of the virtual element method (VEM) for finite deformations. *Comput. Methods Appl. Mech. Engrg.* 2017. 318. Pp. 148–192.
45. Roehl, D., Ramm, E. Large elasto-plastic finite element analysis of solids and shells with the enhanced assumed strain concept. *International Journal of Solids and Structures.* 1996. 33. Pp. 3215–3237.

Contacts:

Yury Klochkov,

Doctor of Technical Science

ORCID: <https://orcid.org/0000-0002-1027-1811>

E-mail: Klotchkov@bk.ru

Anatoliy Nikolaev,

Doctor of Technical Science

ORCID: <https://orcid.org/0000-0002-7098-5998>

E-mail: anpetr40@yandex.ru

Olga Vakhnina,

PhD of Technical Science

ORCID: <https://orcid.org/0000-0001-9234-7287>

E-mail: ovahnina@bk.ru

Tatyana Sobolevskaya,
PhD of Technical Science
ORCID: <https://orcid.org/0000-0002-9167-075X>
E-mail: moonway13@rambler.ru

Michael Klochkov,
E-mail: m.klo4koff@yandex.ru

Received 29.04.2021. Approved after reviewing 15.11.2021. Accepted 19.11.2021.

